The Thesis Committee for Laurie Christine O'Neill
Certifies that this is the approved version of the following thesis:

REE-Be-U-F Mineralization of the Round Top Laccolith, Sierra Blanca Peaks, Trans-Pecos Texas

APPROVED BY
SUPERVISING COMMITTEE:

Supervisor:

J. Richard Kyle

Brent Elliott

James Gardner

REE-Be-U-F Mineralization of the Round Top Laccolith, Sierra Blanca Peaks, Trans-Pecos Texas

by

Laurie Christine O'Neill, B.S.

Thesis

Presented to the Faculty of the Graduate School of

The University of Texas at Austin

in Partial Fulfillment

of the Requirements

for the Degree of

Master of Science in Geological Sciences

The University of Texas at Austin

May 2014

Dedication

To the Oms

Acknowledgements

I would like to thank the people and organizations that have helped me to conduct and complete this research. Thank you to the Texas Rare Earth Resources Corporation for permission and assistance in conducting fieldwork at Round Top, and for allowing me access to existing maps, the RC drill hole data, and previous studies of the area. I would especially like to thank Stan Korzeb, Rob Otto, Nichole Kyger, and Ben Geller for their assistance and for sharing their knowledge of the deposit.

I would like to thank my committee members, Drs. J. Richard Kyle, Brent Elliott, and James Gardner for their support and guidance through this process. Dr. Kyle provided me with this opportunity to complete a Masters degree, and has contributed his guidance and knowledge throughout this process. Dr. Elliott has provided exceptional insight into the geochemical aspects of this research in addition to support and encouragement. Dr. Gardner has provided considerable insight into the magmatic and mineralogical aspects of this study. Additionally, I would like to thank Nick DeChant my trusty field assistant, who provided support to me in the field and the lab. Elizabeth Bloch was instrumental in beginning an initial portion of this research for her senior honors thesis.

Thank you to the Jackson School of Geosciences, the West Texas Geologic Association, the Society of Economic Geologists, and the Association of Environmental and Engineering Geologists for providing funding support for this research.

Stefanie Frelinger and Matt Ledvina have been supportive friends and wonderful officemates. Dr. Lex Lambeck has been a helpful mentor and friend throughout this process.

I would like to thank my friends and colleagues for their endless support and encouragement. Finally, I would like to thank my family for their unwavering support and belief in me during it all. Especially my parents, it is with your love and inspiration I have made it this far.

Abstract

REE-Be-U-F Mineralization of the Round Top Laccolith, Sierra Blanca Peaks, Trans-Pecos Texas

Laurie Christine O'Neill, M.S.GeoSci

The University of Texas at Austin, 2014

Supervisor: J. Richard Kyle

The Round Top laccolith is considered to be one of the youngest laccoliths in a series of five known as the Sierra Blanca peaks, located in Hudspeth county, Texas. The laccolith is anomalous within the region in that it is peraluminous and enriched in HREEs, F, and U, and is comprised of intermingled discrete packages of various rhyolite types. The laccolith rhyolite varies in color from gray, purple, red, and tan, which combine locally to form distinct geometric mottled textures. The general composition of the rhyolite is 48-52% potassium feldspar, 28-30% quartz, 8-14% plagioclase feldspar, 4-5% annite biotite, 2-3% magnetite-hematite, 1% zircon, and 1% trace phases. The morphology of the trace phases suggests quenching of a late-stage volatile-rich vapor phase at the time of the laccolith formation. The rhyolite displays a wide array of unique mineralogical characteristics indicative to rapid emplacement and metastable crystallization conditions, including three-part quartz phenocrysts, hourglass sector-zoned

potassium feldspars, and late-stage anhedral zircons. Unique accessory and trace phases include cassiterite, cerianite-(Ce), changbaiite, columbite, cryolite, tantalite, thorite, yttrofluorite, yttrocerite, and two unidentified minerals named (W) and (X).

Initial alteration of the laccolith by high temperature volatile-rich vapor during the late stages of crystallization caused the partial dissolution of the feldspars and quartz. Subsequent quenching of this high temperature vapor phase produced the abundant interstitial, and pore filling REE-fluorides common to the laccolith. The variation in rhyolite color and the presence of the mottled textures are a direct result of partial oxidation of the laccolith by secondary fluids. The oxidizing fluids migrated within the laccolith along an extensive fracture network, altering the adjacent wallrock by oxidizing magnetite phenocrysts to hematite. The gray, purple, and red rhyolite types reflect an increase in turbidity caused by hematitic inclusions primarily within the pore spaces of the potassium feldspar portions of the groundmass. The tan rhyolite is locally restricted to the base of the laccolith and has been subjected to an intense degree of alteration independent of the other rhyolite types, primarily indicated by the conversion of feldspars to clay.

Petrographic, microbeam, and geochemical studies have determined little variation in REE concentration between the three rhyolites of similar alteration intensity, but have indicated a depletion in LREEs within the more altered tan

rhyolite. The average REE+Y content for the rhyolites sampled (n=11) ranges between 249 ppm and 518 ppm. The REE+Y concentrations between rhyolite samples of the same type show some variation, possibly indicating a correlation between alteration and REE+Y abundance and/or innate heterogeneity in the vapor phase during the initial laccolith formation.

The magma emplaced at Round Top underwent a prolonged evolutionary process of fractionation/differentiation as evident by the unusual mineral assemblage and geochemical enrichment associated with the laccolith (e.g. extremely negative europium anomaly, and the positive La/Yb correlation). Future exploration for Round Top style REE-deposits should center within long-lived, tectonically active and complex regions where laccoliths are likely to exist. Specifically, exploration should focus on identifying the youngest laccolith in a felsic series, as this is the most likely to contain the greatest abundance of incompatible elements within the laccolithic group. The early alteration of feldspars by the high temperature vapor phase was crucial in the development of the REE+Y enrichment at Round Top. The feldspar dissolution provided abundant open pore space that was subsequently filled by the REE-fluorides. Thus, exploration should additionally seek laccoliths that have undergone a similar early alteration process, and expand to potential laccolith groups not yet exposed by erosional processes.

Table of Contents

List of Tables

List of Figures

CHAPTER 1: INTRODUCTION AND PURPOSE OF RESEARCH

Introduction

Laccoliths are concordant, mushroom-shaped igneous bodies emplaced at shallow depths into relatively undeformed sedimentary units (Corry, 1988; Blatt & Tracey, 1997). Their shape and size vary greatly but generally range from less than a half to five miles (1-8 km) in diameter and are typically less than 2,500 feet (750 m) thick (Blatt & Tracey, 1997). Corry (1988) estimated the existence of approximately 1,000 laccoliths within the United States and perhaps as many as 10,000 laccoliths globally. Of these occurrences, the geology of only a small number have been described in detail and fewer still are known to host mineral occurrences. Within the Texas portion of the Trans-Pecos Magmatic Province (TPMP), there are approximately 100 laccoliths and laccolithic complexes (Henry & McDowell, 1986; Corry, 1988). The subject of this study is the Round Top laccolith, a peraluminous rhyolite laccolith enriched in rare earth elements (REEs), beryllium (Be), uranium (U), and fluorine (F) (Rubin et al., 1987; Price et al., 1990). Round Top is one of five rhyolite laccoliths comprising the Sierra Blanca peaks located northwest of the town of Sierra Blanca in Hudspeth County, Texas.

Economic interest in Round Top peak has grown over the past several years due to the noted enrichment in REEs associated with the laccolith. The

REEs are a set of 17 highly incompatible elements comprised of the Lanthanide Series (atomic numbers 57-71). Yttrium (atomic number 39) Scandium (atomic number 21) are occasionally included in this group. The REEs are subcategorized into light rare earth elements (LREEs), atomic numbers 57-63, and the heavy rare earth elements (HREEs), atomic numbers 64-71 and 39 (Henderson, 1984; Long et al., 2010). Yttrium does not fall within the Lanthanide Series, but is commonly included with the HREEs due to similar chemical behaviors (Henderson, 1984). Interest in the production of REEs as an economic commodity has increased over the past decade due to their unique properties in luminescence, magnetism, and strength; properties that are essential in the production of a number of technologies, clean energies, and defense weapons (Long et al., 2010).

The demand for REEs in the United States and global markets has fluctuated over the past decade due to several factors: a monopoly in mining and production of REEs by China, a slow U.S. recovery from the economic lull, and a general lack of REE producers within the American market (Long et al., 2010). This has driven interest in exploration and development of potential REE deposits within the continental United States due to the desire to secure a local, more reliable resource (Long et al, 2010).

Few REE enrichments have been described in association with peraluminous, subalkaline rhyolitic laccoliths. Therefore, the Round Top laccolith presents a unique opportunity to describe and investigate this type of REE

mineralization, including the potential to further understand the unique associated enrichment of a number of other elements, including F, U, and Be. REE deposits are presently known to be associated with peralkaline igneous suites, carbonatite, pegmatite, placer, iron-oxide copper-gold, and metamorphosed geologic settings (skarn to high grade), and encompass a wide array of mineralogical forms and concentrations (Long et al., 2010).

The Texas Rare Earth Resources Corporation (TRER, http://trer.com) is currently conducting exploration and an economic assessment at Round Top to determine the viability of the laccolith as a potential new REE deposit, specifically a HREE resource. Previous work at this site began in the 1980s as a joint drilling campaign by the Cabot Corporation and the Cyprus Metals Company to evaluate the laccolith as a beryllium resource. The Standard Silver Corporation, which later became TRER, resumed exploration in 2007. This current exploration in conjunction with past investigation has produced a wealth of new data in the form of reverse circulation chips (RC), drill road exposures, and opportunities for study that were not previously available (Hulse et al., 2012, 2013).

Purpose

This investigation was conducted to determine and describe the geologic, mineralogical, morphological, and geochemical characteristics of the REE-Be-U-F enriched Round Top laccolith. Petrographic, electron microbeam, and geochemical methods, in addition to cross-section construction were conducted

as a means to examine and document these characteristics. From this investigation, a detailed summation of this unique geologic feature is presented to better understand the evolution and formation of enriched laccoliths, including morphology, magma chemistry, crystallization history, and accompanying alteration processes. Documenting and understanding such characteristics will aid in the further understanding of the laccoliths' association with regional, tectonic, and magmatic controls: in addition to increasing the ability and potential for future economic exploration of similar deposits.

CHAPTER 2: GEOLOGIC SETTING AND BACKGROUND OF THE SIERRA BLANCA PEAKS

Location and Access

The Sierra Blanca peaks are a series of five rhyolite laccoliths located approximately seven miles northwest of the town of Sierra Blanca, Hudspeth County, Texas, and four miles northeast of Texas Interstate 10 (Figure 2.1). Access to Round Top peak and the surrounding area was granted by TRER for the purpose of research and sample collection. Site visit duration totaled two weeks over two different periods in March and August 2012. The peaks are located within the Gunsight Hills South and Lasca Texas-Hudspeth County USGS 7.5-minute quadrangle maps. The peaks are bounded by 31°12’30”N and 31°21’00”N latitudes and 105°22’30”W and 105°30’00”N longitudes.

History of Activity and Exploration, Sierra Blanca Peaks

Initial economic interest of Round Top began in 1969 when W.N. McAnulty Sr. noted the occurrence of anomalous fluorspar in the vicinity of the laccoliths (Cyprus Sierra Blanca Inc., 1988). Between 1971-1980, McAnulty, in conjunction with other associates, drilled a total of 22 holes and conducted limited trenching at Round Top, Little Round Top, and Little Sierra Blanca (Cyprus Sierra Blanca Inc., 1988; Hulse et al., 2012, 2013). During this period, several uranium companies also noted anomalous occurrences of uranium associated with the

site (Hulse et al., 2012, 2013). In 1982, the Cabot Corporation became interested in the laccoliths after the United States Geological Survey led a nationwide Be-geochemical reconnaissance survey, which indicated anomalous Be associated with the peak (Cyprus Sierra Blanca Inc., 1988). The Cabot Corporation gained the land position in 1984, and commenced a rotary drill program at Round Top that same year (Cyprus Sierra Blanca Inc., 1988). In 1987, the Cyprus Metals Company entered into a joint venture with the Cabot Corporation and continued exploration by drilling a total of 82,000 feet (24,994 m) and sinking a 1,115 foot (340 m), 10 by 10 foot (3 by 3 m) test decline into the west side of the peak, culminating in a mine and mill feasibility study in June 1988 (Cyprus Sierra Blanca Inc., 1988; Hulse et al., 2012, 2013). From 1987 through 1990 the Texas Bureau of Economic Geology (BEG) conducted a series of studies on Round Top and the surrounding area; these include Rubin et al. (1987, 1989, 1990, 1993), and Price et al. (1987, 1990) (Hulse et al., 2012, 2013). During the 1990s a lack of interest in the site lead to the property reverting back to the Texas General Land Office, until the Standard Silver Company established a land position in late 2007. The Standard Silver Company became Texas Rare Earth Resources in 2010, and is the current owner and potential developer of Round Top. The company released a Preliminary Economic Assessment in June 2012 and December 2013. TRER is currently conducting an evaluation of the economic potential for developing Round Top as a REE mine (Hulse et al., 2012, 2013).

Climate and Vegetation

The Sierra Blanca area is typical of a semiarid desert climate. Daily temperatures in the summer months (June through August), range from the 60-90°F, with days commonly reaching over 100°F (Southern Regional Climate Center, 2013). During the winter months (November through January), temperatures range from the 20-50°F (Southern Regional Climate Center, 2013). The rainy season for the area spans July through September with average monthly precipitation of 5 centimeters (cm), and an annual average of 28 cm, which typically falls as local and abrupt thunderstorms (Albritton & Smith , 1965; Southern Regional Climate Center, 2013). Annual humidity averages 75% (U.S. Climate Data Webpage, 2013). High winds are common to the area with an average wind speed of 13 mph and occasional gusts surpassing 20 mph (U.S. Climate Data Webpage, 2013).

Vegetation in the region is typical of the west Texas desert; small but numerous lechuguilla, ocotillo, yucca, and agave (century plants) blanket the ground and hill slopes. The peaks are relatively steep and covered in rubbly scree, limiting the number of in-situ rock exposures and in some areas making access impossible.

Geologic Setting

TECTONIC SETTING

The Sierra Blanca peaks are located within the western portion of the Texas segment of the Trans-Pecos Magmatic Province (Figure 2.2). The province has no definite border, but is approximately bounded by southern New Mexico to the north, the Pecos River to the east, and the Mexico-America border to the west (Henry & McDowell, 1986; Barker 1987; Price et al., 1987, 1990). The southern portion extends south into Mexico for an unknown extent (McAnulty, 1980; Barker, 1977).

Volcanism within the region is bimodal, encompassing both mafic to highly evolved silicic magmatism (Barker, 1977; Henry & McDowell, 1986; Price et al., 1990; Rubin et al., 1993). Igneous bodies range from voluminous caldera-sourced pyroclastics, intrusive sills and dikes, small volume cones and ring dikes, to shallowly emplaced laccoliths (Barker, 1979; Price et. al., 1987, 1990). The region is roughly divided into two distinct geochemical sections, a predominantly alkali-calcic volcanic suite to the west (the region in which the Sierra Blancas are located), and alkalic volcanism to the east (Figure 2.2; Henry & Price, 1984; Barker, 1987; Price et al., 1987).

Magmatic activity in the region was emplaced in a continental arc environment, and was associated with the subduction of the Farallon plate beneath the North American plate to the west 100-40 Ma, which produced of

wave of bimodal volcanism extending easterly from the western coast (Price et al., 1990; Henry et. al, 1991).

Trans-Pecos magmatism occurred approximately 48-17 Ma and is divided into two main phases, termed early and late (Henry & McDowell, 1986; Price 1990 sensu Henry et al. 1989; Rubin et al., 1993). The early phase (48-38 Ma) is characterized by numerous small silicic-to-mafic igneous intrusions, mafic lava flows, and two minor caldera eruptions (Henry & McDowell, 1986; Price et al., 1990). The late phase (38-32 Ma) spanned both the alkalic-calcic and alkalic regions and comprises the most voluminous episode of Trans-Pecos magmatism (Henry & Price, 1984; Henry & McDowell, 1986; Price et al., 1990). Volcanism during this period is characterized by numerous silicic-to-mafic intrusions, and large-volume caldera eruptions and associated ash-tuff flows (Henry & Price, 1984; Henry & McDowell, 1986; Price et al., 1990). Basin and Range extension and subsequent normal faulting in the region began approximately 24 Ma and continues through to the present, initiated by a change in regional stresses at approximately 31 Ma (Price et al., 1990). Small volume mafic volcanism accompanied the early stages of rifting with the youngest dated at 17 Ma (Price et al., 1990).

Prior to Trans-Pecos magmatic activity, the region underwent Laramide deformation including predominately north-northwest folding and thrusting (Wilson, 1980; Price et al., 1990). This tectonic activity is responsible for the gentle dip (~15°SW) of the Cretaceous units, into which the Sierra Blanca peaks

were later emplaced (Price et al., 1990). This region was also volcanically active during this time as indicated by recent research. Notable geologic occurrences that predate the Trans-Pecos arc magmatism included the formation of the Red Hills Cu-Mo porphyry system south of the Chinati Mountains and episodic phreatomagmatic style volcanism within the Big Bend region of west Texas (Gilmer et al., 2003; Breyer et al., 2007; Befus et al., 2008). Before recent discoveries, Laramide magmatism had not been recognized within the region during this period (Wilson, 1980; Price et al., 1990).

Transecting the TPMP is the Texas Lineament Zone (TLZ); a regional series of large-scale parallel geologic features, spanning a width of approximately 50 miles (80 km) within the western portion of Texas and continuing into Mexico (Muehlberger, 1980). The zone represents long-term and ongoing periodic tectonic activity, dominated by dip-slip movement, beginning approximately 1.4 Ga, and continuing through to the present (Muehlberger, 1980). The Sierra Blanca and Van Horn area is the type locality for this regional trend as defined by Albritton and Smith (1965). Muehlberger (1980) positioned the Sierra Blanca complex along the proposed northern boundary of the TLZ within the downthrown portion of a tectonic block. The downthrown block in which the laccoliths are situation is bounded by the regionally N-S trending dip-slip Rim Rock Fault to the north and an unnamed, more minor dip-slip fault to the south (Muehlberger, 1980). Contrary to this, Albritton and Smith (1965) and Price et al. (1990) placed the Sierra Blanca group along the eastern footwall side of a large

regional scale thrust fault (Figure 2.2). The Trans-Pecos region has undergone a complex tectonic history, which most likely includes the reactivation of numerous faults during different tectonic episodes, thus obscuring the exact nature of fault movement in the area. These tectonic episodes have contributed to the formation and location of many of the igneous features within the province, including the Sierra Blancas. The area of the Sierra Blancas has been the site of regional scale thrusting and orogenic activity during the Proterozoic, high-angle normal faulting during the Late Paleozoic, folding and thrusting during the Laramide, in addition to on-going Basin and Range extension.

Sierra Blanca Peak, and presumably the rest of the Sierra Blanca laccoliths were emplaced during the main phase of Paleogene bimodal Trans-Pecos magmatic activity, as indicated by a biotite K-Ar date of 36.2 ± 0.6 Ma (Henry & McDowell, 1986).

CRETACEOUS SEDIMENTARY UNITS

The Sierra Blanca laccoliths were emplaced along limestone and shale bedding planes within the Cretaceous Washita Group (Figure 2.3; Albritton & Smith, 1965; Price et al., 1987). Exposures in this area are discontinuous and typically occur in arroyos where erosion has produced outcrops. The Washita Group consists of limestone interbedded with clay and shale and has an approximate maximum thickness in this region of 1,020-1,400 feet (310-425 m), (Albritton & Smith, 1965). An exposure of marl and clay facies of the upper

Washita Group at the northern flank of Round Top is most likely equivalent to the Buda Limestone and Del Rio Clay recognized elsewhere in the district (Albritton & Smith, 1965). The sedimentary beds dip gently 10-15° to the southwest, except for along the laccolith contact where they dip more steeply due to doming (Albritton & Smith, 1965; Price et al., 1990). Further to the east, the Triple Hill laccolith was emplaced into the Fredericksburg Group (Albritton & Smith, 1965).

SILLS AND DIKES

Several sills, dikes, and possible plugs occur near and stratigraphically below the Sierra Blanca laccoliths. These features appear to predate the emplacement of the laccoliths and are typically of andesite, hornblende andesite porphyry, hornblende diorite porphyry, or latite porphyry in composition (Albritton & Smith, 1965; Henry et al., 1986; Matthews & Adams, 1986; Rubin et al., 1990). Three dike and sill samples, diorite to andesitic in composition, collected from Sierra Blanca Peak and Round Top laccolith produced a collective K-Ar age of 40.6 ± 0.1 Ma (Mathews & Adams, 1986). The sill exposed at the northern flank of Round Top was described by Matthews and Adams (1986) as a diorite, but can be more precisely characterized as a hornblende diorite porphyry. Compositionally, the sill is classified as a syeno-diorite as defined by TAS Plutonic classification diagram (Figure 3.64; Cox et al., 1979; adapted by Wilson, 1989). Where exposed at Round Top, the sill sits unconformably at the base of the laccolith, above the upper portion of the exposed Washita Group (Figure 2.4).

Portions of the sill and the underlying sedimentary units are fluoritized. Near Sierra Blanca Peak, dikes, sills and possible plugs occur to the north and west of the laccolith. The exact nature of the relationship between the dikes and sills to Round Top mineralization is unclear. Although, it is probable that the same conduits utilized by the magmas that formed the sill were subsequently utilized during emplacement of both the Round Top and Sierra Blanca laccoliths.

SIERRA BLANCA LACCOLITHS

The Sierra Blanca Peaks are a series of five peraluminous rhyolite and rhyolite porphyry laccoliths emplaced in an arcuate pattern. All of the laccoliths are aphanitic to slightly porphyritic, thus the common use of rhyolite (cf. microgranite) for their general description. The peaks encompass an area of approximately 35 square miles southwest of the Finley Mountains (47 Ma) and to the north of the Quitman Mountains (35 Ma) (Figure 2.1; Henry & McDowell, 1986). The largest of the peaks, Sierra Blanca, was emplaced 36.2 ± 0.6 Ma (Henry & McDowell, 1986). Emplacement ages of the four other laccoliths have not been determined, but a relative emplacement sequence can be interpreted through trace-element differentiation patterns. Based on the increasing enrichment of REEs, especially the increasing ratio of HREEs to LREEs between the five laccoliths, Triple Hill was emplaced first, followed sequentially by Sierra Blanca Peak, Little Sierra Blanca, Round Top, and Little Round Top (Figure 2.5; Shannon, 1986; Shannon & Goodell, 1986; Price et al., 1990). The timing

between emplacement and duration of emplacement is unknown. Attempts to recover zircon from Round Top and Sierra Blanca samples for (U/Th)/He geochronology have been unsuccessful.

SIERRA BLANCA PEAK

Sierra Blanca Peak is the largest of the five Sierra Blanca laccoliths, and the namesake for the group. The peak is the most southerly of the five, and encompasses an area of approximately two square miles (3.2 km^2) (Figure 2.1). The base of the laccolith is exposed on the west side, indicating a preserved thickness approaching 4,000 feet (1,220 m). It is the tallest of the peaks at 8,868 feet (2,701 m) and is a distinct geographically recognizable feature within the region. RCL Rocks LLC currently operates the Sierra Blanca Quarry on the northeast flank of the peak. Material quarried is used for railroad ballast and is transported utilizing the Union Pacific Railway that parallels Interstate 10 in this portion of the state. The morphology of the peak is that of a convex mushroom in sectional view and is circular with a peaked dome.

Sierra Blanca is composed of a quartz rhyolite porphyry, typically gray to pink in color. Based on observations of the RCL Rocks LLC quarry faces, alteration of the rhyolite appears to be minimal versus that of Round Top, but discoloration does occur locally along fractures and is most likely the result of meteoric water flow through the jointed and faulted portions of the laccolith.

ROUND TOP LACCOLITH

Round Top peak is the most westerly of the five laccoliths and encompasses an area of approximately one by one and half square miles (1.6-2.4 km^2) (Figure 2.1). The peak has an elevation of 5,731 feet (1,747 m) with an approximate maximum laccolith thickness of 1,300 feet (396 m). The laccolith is comprised of four variations of peraluminous, subalkaline rhyolites that differ by color, mineralogy, and texture and combine to form geometric mottled textures.

The laccolith has an asymmetrical convex or mushroom morphology in cross-section, and is circular in outline with a peaked dome. On the northern flank the northeast portion has been eroded to expose the underlying diorite and limestone units. The northeast flank grades abruptly into a saddle that connects to Little Round Top peak. The southern flank is of equal steepness as the other flanks in the upper portion but grades into a shallow slope at the base that extends laterally onto the desert floor (Figure 2.6 A-B). The slopes of the peak are covered in a mixture of scree and west Texas vegetation that impedes access to the upper portion of the peak. The rhyolite is blocky and fragmented, and locally cemented by multiple generations of fluorite, calcite, microcrystalline silica, and clay (Figures 2.7-2.8).

Access to the upper portion is achieved through a network of switchbacks on the northwestern flank, initially constructed for drilling conducted in the 1980s and that have since been improved and expanded by TRER for a recent drilling campaign (Figure 2.6 B). One road located on the eastern flank allows access to

the middle portion of the peak on the east side. On the southern flank, two drill roads provide access to two saddles approximately halfway up the peak.

Previous Work

King (1949) mapped the Sierra Blanca peaks as part of a USGS regional geologic map of Culberson and Hudspeth counties, Texas. Albritton and Smith (1965) conducted extensive mapping and descriptions of the geology of the Sierra Blanca area, culminating in the USGS Professional Paper 479. It is key to note that a geologic map produced by King (1949) refers to Round Top as “McNulty Peak” and Little Sierra Blanca at “Everatt Peak,” but the geologic map produced by Albritton and Smith (1965) refers to the two peaks by their current nomenclature. It is unclear when the change in naming came about or by what means.

McAnulty (1971, 1980) was the first to describe samples from the peaks in detail, and recognized the area as a potential economic resource. Barker (1980) further described the igneous units in the area, including samples from the Cox and the Quitman Mountains. Shannon and Goodell (1986) and Shannon (1986) conducted whole-rock and trace geochemical analyses on the Sierra Blancas and surrounding igneous bodies. Matthews and Adams (1986) characterized the geochemistry, age, and structures associated with the Sierra Blanca peaks. Rubin et al. (1987, 1989a, 1989b, 1990, 1993) and Price et al. (1987, 1990) conducted extensive research within their positions at the BEG on Round Top

and the Sierra Blanca peaks, producing a series of papers on the mineralogy, alteration, and geochemistry of Sierra Blanca Peak and Round Top laccolith.

A group with the University of Texas at El Paso (UTEP) has recently produced a number of abstracts and one paper outlining research being conducted on Round Top in coordination with TRER. These include Goodell et al. (2013), Pingitore et al. (2013), Negron et al. (2013), and Pingitore et al. (2014).

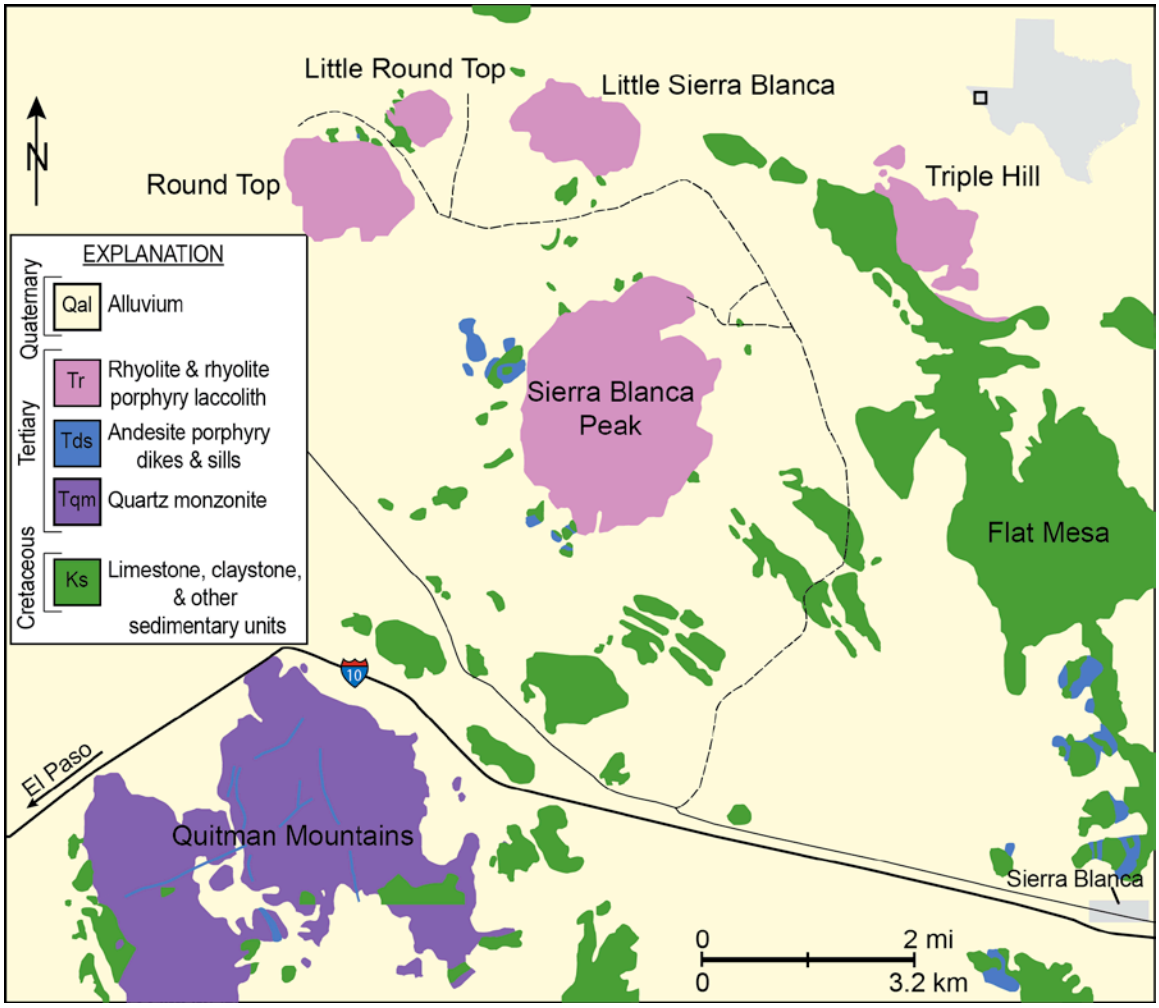

Figure 2.1: Geologic map of the Sierra Blanca peaks, modified after McAnulty (1980). Clockwise, the laccolith group consists of Sierra Blanca Peak the largest of the five peaks, Round Top, Little Round Top, Little Sierra Blanca, and Triple Hill.

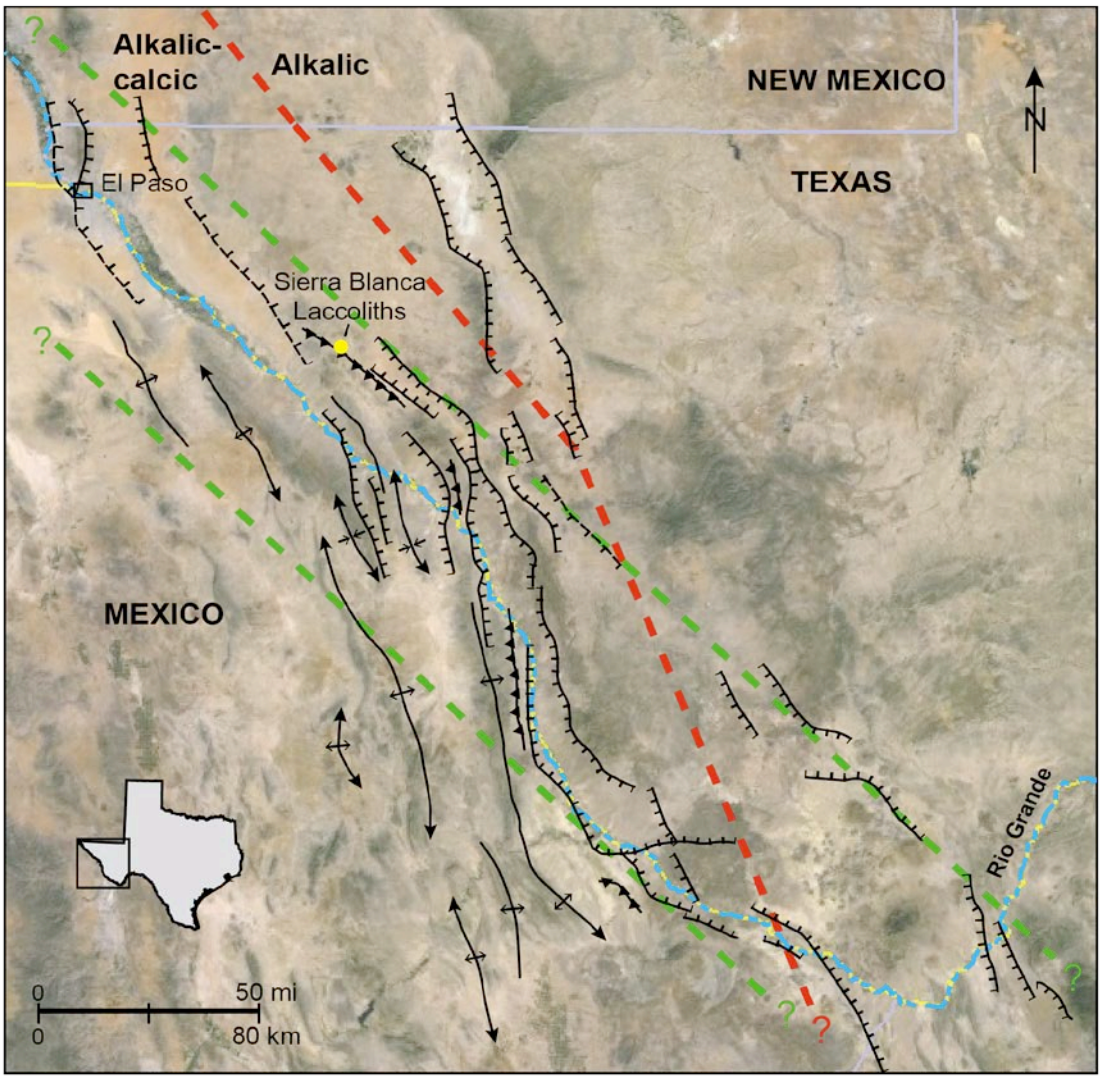

Figure 2.2: Location map of the Sierra Blanca peaks relative to major geologic structures within the Trans-Pecos Magmatic Province (TPMP). The TPMP has no finite border but is roughly bounded by southern New Mexico to the north, the Pecos River to the east, the Mexico-America boarder to the west, and continues for an unknown distance into Mexico to the south. The region is roughly divided into two distinct geochemical sections: a predominantly alkali-calcic volcanic suite to the west (the region in which the Sierra Blancas are located), and alkalic volcanism to the east (red-dashed line). Cutting across the Trans-Pecos Magmatic Province is the Texas Lineament Zone (TLZ), a regional series of large-scale parallel features spanning a width of approximately 50 miles within the western portion of Texas and continuing into Mexico (green-dashed lines). Map modified after Muehlberger (1980), Price et al. (1990), and Google Earth (2013).

Era	System	Series	Formation
Cenozoic	Quaternary	Recent to Pleistocene	alluvium, colluvium, windblown sand, caliche, gypsite; landslide, lacustrine, & alkali-flat deposits
	Quaternary-Tertiary	Pleistocene to Miocene	bolson & valley-fill deposits; terrace & pediment gravels
	Tertiary	Miocene, Oligocene, & Eocene	volcanic & intrusive igneous rocks, mostly Oligocene in age; volcanic sedimentary rocks
		Paleocene	Black Peaks Formation
Mesozoic	Cretaceous	Upper	El Picacho & Javelina Formations
			San Carlos Sandstone, Aguja Formation
			Pen Chalk Formation, Teringua Clay, Austin Chalk
			Boquillas, Ojinaga, Eagle Ford, & Chispa Summit Formations
		Lower (Washita Group)	Buda Limestone
			Del Rio Clay, Grayson Formation, Eagle Mountains Sandstone
			Santa Elena, Devils River, Espy, Loma, Plata, & Boracho Limestones; Georgetown Formation
			Sue Peaks, Benevides, & Kiamichi Formations
			Del Carmen, Finley, & Edwards Limestones (Fredericksburg Group)
			Telephone Canyon Formation
			Maxon Sandstone
			Cox Sandstone; Shafter & Glen Rose Formations
			Campground, Bluff Mesa, Yearwood, & Presidio Formations
			Yucca & Mountain Formations
			Etholen Conglomerate
			Torcer Formation

Figure 2.3: Stratigraphic column of the Cenozoic and Cretaceous units within the Trans-Pecos region. Formations highlighted in blue correlate with the Washita Group and are the units exposed at the base of the Round Top laccolith. Column modified after Albritton and Smith (1965) and Price et al. (1986).

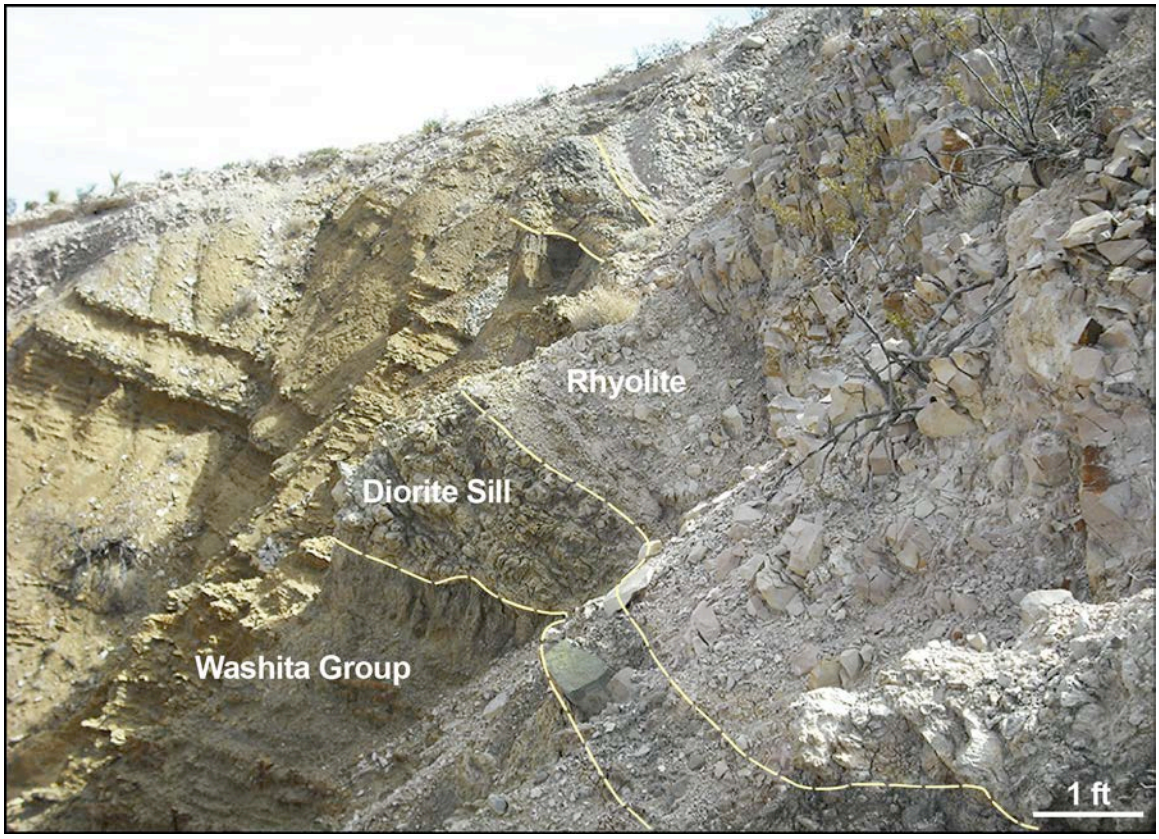

Figure 2.4: Photo of exposed contact between the Round Top rhyolite and the underlying hornblende diorite porphyry sill and Cretaceous strata of the Washita Group. The outcrop formed in an arroyo on the northern flank of Round Top and is the only known exposure of the rhyolite, sill, and limestone contact. Arroyo located at 31°16'56.7"N, 105°28'40.1"W. Photo by C. O'Neill, 2012.

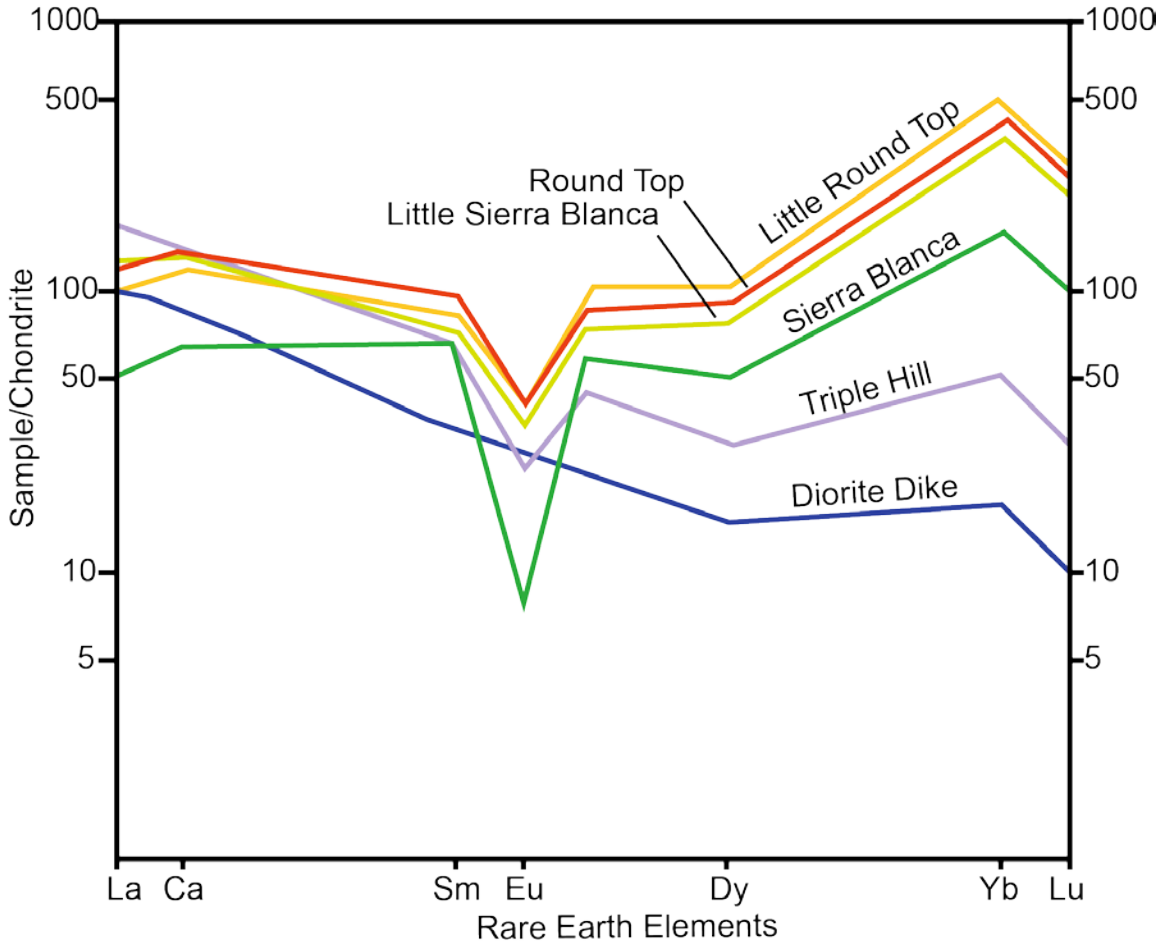

Figure 2.5: Rare earth element enrichment diagram for the Sierra Blanca peaks and associated diorite dike. The peaks sequentially become more enriched in HREEs beginning with Triple Hill, Sierra Blanca, Little Sierra Blanca, Round Top, and Little Round Top. This enrichment sequence may indicate an emplacement order and increasing differentiation. Plots represent the mean values of 5 samples for Little Round Top, 8 for Round Top, 10 for Little Sierra Blanca, 2 for Sierra Blanca, and 6 for Triple Hill. Data and figure modified after Shannon and Goodell (1986).

Figure 2.6A: Photo of Round Top and Little Round Top peaks. Looking northwest, Round Top is on the left and Little Round Top is the smaller peak to the right. Note the shallowing of the southern flank of Round Top as it grades out onto the desert floor. A hidden fault possibly crosses the saddle between the two peaks. West Texas vegetation blankets the landscape and includes abundant lechuguilla, ocotillo, yucca, and agave. Photo by C. O'Neill, 2012.

Figure 2.6B: Photo of Round Top laccolith looking southwest from Little Round Top. The test decline constructed in the late 1980s by the Cyprus Metals Company and the Cabot Corporation is just out of view on the west side on the peak. A network of switchback drill roads is visible on the northwest flank, and are the main areas of sample collection due to the limited natural exposure of the laccolith. Photo courtesy of R. Kyle, 2010.

Figure 2.7: Photos of blocky and fragmented Round Top rhyolite in outcrop. A) Blocky gray rhyolite located along a drill road. Note long continuous fractures that are characteristic to the laccolith. The rhyolite is blocky and highly fragmented, forming abundant scree along the roads and slopes. B) Photo of blocky and rubble-like red rhyolite outcrop along a drill road on the west side of the laccolith. Note the abundant blocks and scree piles accumulating at the base and characteristic to the Round Top laccolith. Caliche forms a white coating on many of the blocks as seen on the rocks in the foreground. Photos by C. O'Neill, 2012.

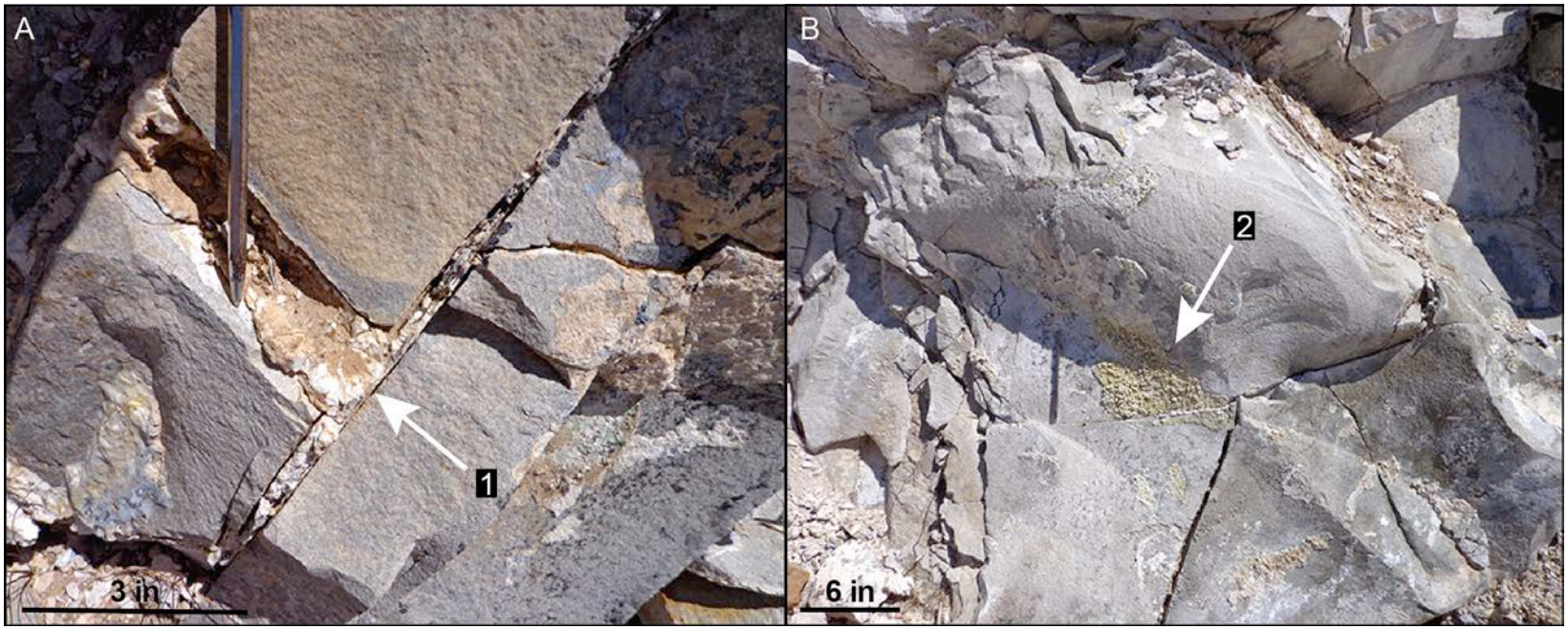

Figure 2.8: Photos of fractured blocky gray rhyolite in outcrop cemented by multiple generations of fracture fill. The fracture fill is typically a mix of calcite (1), fluorite (2), microcrystalline silica, and caliche. Cementation of the large rhyolite blocks is common along the fractures and joints throughout the laccolith. Photo by C. O'Neill, 2012.

CHAPTER 3: METHODS AND RESULTS

Methods

FIELDWORK

During March and August 2012, 373 samples were collected from locations at Round Top, Little Round Top, and Sierra Blanca Peak (Figures 3.1-3.4; Appendix A). Samples were collected from outcrops, road cuts, and from reverse circulation (RC) cuttings from drilling provided by TRER. Materials sampled included unaltered rhyolite, altered rhyolite, fluorite, calcite, and rhyolite breccia cemented with fluorite, calcite, and microcrystalline silica. Samples were collected to procure a representative sample suite for this deposit, for if mining does proceed little may be available of the original laccolith for future studies.

LACCOLITH MORPHOLOGIC STUDY

Reverse circulation chips collected from drilling conducted by TRER in 2012 were utilized to produce an accurate representation of the laccolith morphology and rhyolite associations at depth. Samples were collected from representative intervals from nine drill holes that form two perpendicular cross-sections across the laccolith (Figure 3.4; Appendix A.2). The cross sections form approximately northwest and northeast liner transects and represent a total of

5,097 feet (1,554 m) of drilling. RC chips from representative intervals were selected for further petrographic study.

PETROGRAPHY

Petrographic work was conducted using Zeiss Axioskop 40 transmitting light petrographic microscopes utilizing Sony Handycam E-mount NEX-VG10 cameras. These microscopes were provided by the Department of Geological Sciences for use in graduate research. A total of 43 thin sections were produced for use in this study from samples collected during fieldwork. Twenty-eight thin sections were made by National Petrographic Services Inc., Houston Texas, 10 thin sections were produced by Quality Thin Sections, Tucson Arizona, and five were produced by the author utilizing the facilities within the Department of Geological Sciences. Eighteen of the thin sections were partially stained with sodium cobaltinitrite [$Na_3Co(NO_2)_6$] to illuminate the potassium-rich portions of the sections with a yellow tint. All thin sections were made to the standard thickness of 30-microns (gray quartz). A list of thin sections and their associated descriptions may be found in the Appendix A.3. All mineral estimates are modal percentages based on visual abundance.

ELECTRON MICROBEAM

Microbeam analyses were conducted on the four types of rhyolite, a mottled rhyolite, and a rhyolite breccia sample, an approach that was dictated by the fine-grained nature of the samples (Appendix A.4). Microbeam analyses were

conducted in the University of Austin at Texas, Department of Geological Sciences, Electron Microbeam Laboratories, supervised by Dr. Donggao Zhao. Analyses conducted utilized the Scanning Electron Microscope (SEM) JEOL JSM-6490LV, and the Environmental SEM (ESEM) Phillips/FEI XL30. SEM work included use of the scanning electron (SE) and backscatter electron (BSE) detectors for sample imaging, in conjunction with an energy dispersive X-ray detector (EDS) for qualitative and semi-quantitative elemental analysis of samples. ESEM analyses utilized cathodoluminescence (CL), BSE, and SEM detectors to image elemental and compositional incongruities within samples. Each sample was imaged using the SE and BSE detectors within the SEM. The EDS detector on the SEM was utilized to identify individual minerals and to map local areas based on elemental composition. Two of the rhyolite samples were further analyzed with the ESEM and imaged using the CL detector to document heterogeneity within the quartz and feldspar minerals. Samples were coated with carbon prior to study, utilizing a Ladd Carbon Evaporator. The SEM and ESEM results are described in one section due to their close relationship and corresponding results.

WHOLE-ROCK GEOCHEMISTRY

Fourteen samples were submitted to Acme Analytical Laboratories Inc., Vancouver British Columbia, including eleven samples of rhyolite, one sample of diorite sill, one sample of fluoritized limestone, and one sample of rhyolite breccia

cemented by visible fluorite (Figure 3.5; Appendix A.5). All samples were first crushed till 80% passed through a 10 mesh, then had a split of 250 g removed and the split was further pulverized till 85% passed through a 200 mesh. Whole-rock analysis for 11 major oxides and several minor elements was conducted by a lithium borate fusion and dilute acid digestion of a 0.2 g sample pulp followed by an ICP emission spectrometry finish. Total carbon and sulfur were analyzed by loss on ignition (LOI) by sintering at 1000°C and Leco analysis.

For the remainder of the analytes, two separate inductively coupled plasma mass spectrometry (ICP-MS) analyses were conducted. Rare earths and refractory elements were processed by a lithium borate fusion and dilute acid digestion of a 0.2 g sample of pulp to give total abundances. Precious metals, base metals, and remaining elements were processed by an aqua-regia digestion and finished with ICP-MS analyses.

Raw data is located in the Appendices B.1-B.3, data was processed using Microsoft Excel 2011 version 14.3.9 and ioGAS 5.0 REFLEX software.

Results

LACCOLITH MORPHOLOGY

A laccolith is an igneous body of a concordant mushroom shape emplaced at shallow depths into relatively undeformed sediments (Corry, 1988; Blatt & Tracey, 1997). Based on morphological construction of the laccolith through RC chip logging and field observation, the Round Top laccolith is of a domed convex shape, and most closely resembles that of a Christmas-tree type laccolith as described by Corry (1988) (Figure 3.6). Christmas-tree laccoliths are characterized by the ductile deformation of the overburden during emplacement of igneous material, allowing for the formation of a smooth dome on the upper portion of the laccolith similar to the appearance of the convex side of a shield (Corry, 1988). Prior to erosion the sedimentary units into which the laccoliths were emplaced would have appeared to be draped over the domes, possibly with the formation of small crestal grabens at the summit (Corry, 1988). At depth, Christmas-tree type laccoliths branch into multiple stratigraphic layers (Corry, 1988). Drilling at Round Top has only penetrated to just past the known base of the laccolith, and therefore it is unknown if multiple branches of the Round Top laccolith exist at depth and if it is of a true Christmas-tree type morphology. The Christmas Mountains of the Big Bend region in west Texas are of similar geologic provenance to that of the Sierra Blanca group and have been described by Corry

(1988) to represent some of the best examples of this Christmas-tree laccolith morphology.

Four known attempts to describe the morphology of Round Top and the rhyolite sequence at depth have been made by McAnulty (1980), Rubin et al. (1990), and TRER (2012, 2013) (Figure 3.7 A-D). McAnulty (1980) proposed the Round Top laccolith formed a cap to the underlying Cretaceous sediments, and continued as a feeder at depth (Figure 3.7 A). Rubin et al. (1990) utilized RC drill hole chips to approximate the morphology of the laccolith at depth for the northern portion of the peak near the Cyprus Beryllium Corporation test adit (Figure 3.7 B). In this model, the rhyolite forms a relatively smooth contact with the underlying dipping Cretaceous sediments and then abruptly steps down, at which point fluorspar mineralization occurs towards the center of the laccolith. The TRER geologic overview of Round Top on the company website presents the laccolith as a sequence of layered rhyolite packages stacked at depth, which form a sharp lateral contact within the underlying Cretaceous sediments (Figure 3.7 C). The TRER NI 43-101 report modified this previous laccolith model to represent Round Top as a single massive rhyolite body with no layered sequences and included a feeder system to the northern flank (Figure 3.7 D) (Hulse et al., 2013).

Utilizing RC chips obtained from TRER drilling, two perpendicular cross sections of the Round Top laccolith representing the sequence of rhyolites at depth were constructed to establish variations in morphology and rhyolite

occurrence (Plates 1 & 2). The laccolith is composed of discrete zones of rhyolite that are laterally and vertically discontinuous. These rhyolite zones do not represent an emplaced layered sequence caused by differing magmatic injection events, as represented in Figure 3.7 C, but rather are the product of alteration. The pocket-type morphology of the rhyolites was formed by the partial oxidation of the laccolith. Down hole, the rhyolite packages range greatly in thickness from 5 to 400 feet (1.5-120 m), and vary in occurrence from drill hole to drill hole. When viewed in outcrop, a rhyolite type may grade abruptly in and out of another type, including the mottled variations. On a laccolithic scale, the gray and purple rhyolite types occur in greater volumes towards the northern flank and center of the peak, whereas the red rhyolite is more voluminous towards the southern flank. Volumetrically the red and gray rhyolites appear to be the most abundant, each comprising perhaps 20-40% of the Round Top laccolith, as determined through RC chip logging. As the red rhyolite represents intense exposure to oxidizing fluids, it suggests a large portion of the laccolith has undergone oxidation, potentially from the interaction with meteoric fluids to produce abundant hematite. The tan variety occurs stratigraphically at the base of the laccolith, above the underlying fluoritized Cretaceous strata and locally within mottled varieties.

Reexamination of existing drilling information through relogging of RC chips did not constrain the location of a feeder system to the laccolith (Plates 1 & 2). A covered series of hidden high-angle normal faults potentially related to

Basin and Range extension transect the laccolith, forming topographic saddles and down dropping the laccolith blocks (Plates 1 & 2).

COMPARISON OF RESULTS WITH PREVIOUS STUDIES

The work conducted by Rubin et al. (1987, 1989a, 1989b, 1990, 1993) and Price et al. (1987, 1990) within their positions at the Texas Bureau of Economic Geology (BEG) focused primarily on the description and characterization of the mineralogy and geochemistry of rhyolite samples from the Round Top laccolith and the Sierra Blanca Peaks. Based on methodology cited within Rubin et al. (1987) and Price et al. (1990), collection of samples at Round Top for both studies was primarily limited to gray unaltered and altered rhyolite, although the definition of altered gray rhyolite is not clearly expressed. Analytical methods included petrographic, microbeam, and geochemical analyses conducted primarily at the BEG facilities. Price et al. (1990) reported several rhyolite samples from Round Top that are of peralkaline and metaluminous compositions, whereas Rubin et al. (1987) reports a strictly mild peraluminous composition. Both Rubin et al. (1987) and Price et al. (1990) specifically note the occurrence of cryolite within several samples, although fail to cite whether cryolite was identified within all samples analyzed. Price et al. (1990) notes that weathered samples lack apparent cryolite as discrete grains versus the unweathered samples, and defined fresh samples as gray with relatively abundant magnetite and little hematite. Rubin et al. (1987) notes 2.5% cryolite in

one relatively unweathered gray sample, identified through Energy Dispersive Analysis. Price et al. (1990) cites the occurrence of cryolite within the groundmass of the rhyolite, ranging from 0-3%, and as inclusions within quartz. Both studies note the common association of cryolite with rutilated quartz phenocrysts.

Within this study, two crystals of cryolite were definitively identified through EDS point analysis as inclusions within the groundmass of a relatively unaltered gray rhyolite sample. Additionally, one occurrence of rutilated quartz was identified petrographically within a different unaltered gray rhyolite sample. The apparent lack within the scope of this study of relatively abundant cryolite and rutilated quartz as noted by Rubin et al. (1987) and Price et al. (1990) is most likely the product of differing sampling methods. Within this study, samples of rhyolite were chosen to include a wide spectrum of weathering/alteration intensities, and therefore comprised samples that are unlikely to contain preserved cryolite (Price et al., 1990). Additionally, rhyolite breccias and samples with apparent secondary coatings (e.g. fluorite, calcite, microcrystalline silica, caliche, and manganese oxides) were avoided, whereas it is unclear if these coatings were considered within the sampling of Rubin et al. (1987) and Price et al. (1990).

Rubin et al. (1987) noted the concentric inclusion ring common to quartz phenocrysts as vapor-rich. The inclusions observed within this study lack discernable crystal solids or clear vapor bubbles that would be indications of

vapor-rich inclusions. When imaged using SEM and the petrographic microscope, the polish across the inclusions appears to be continuous with no visible pockmarks, which would be expected if the inclusion had been vapor filled. Thus it is most likely that these inclusions represent a fully glass-solid endmember. The large range of findings made within this study and previous works highlights the complex nature of the Round Top laccolith and apparent need for continued examination.

RHYOLITE CHARACTERISTICS

The Round Top laccolith is composed of four major types of rhyolite that differ in color (gray, purple, red, and tan) and geochemically (Figure 3.8). Of these types, multiple mottled variations are formed from the natural combinations of two to three of the color variations (Figure 3.9). Along fractures, multiple generations of fluorite, calcite, microcrystalline silica, and caliche form the cement of the rhyolite breccias (Figure 3.10). Although visually dissimilar, all four of the rhyolite types, the mottled rhyolites, and the rhyolite that comprises the breccia clasts are classified as rhyolite (or subsolvus microgranite) and may be described as moderately homogeneous, aphanitic to microporphyritic, holocrystalline, hypidiomorphic, and locally glomeroporphyritic in texture. TRER (Hulse et al., 2012, 2013) described a fifth “brown” rhyolite located at depth, but this variety was not observed within outcrop or during RC chip logging by the author. When viewed with a transmitting light microscope the spectrum of rhyolite

from gray to tan appears to have an increasing “turbid-like” texture, producing a distinct red cloudiness (Figure 3.12 & 3.13). The turbid texture is caused by the increasing abundance of iron oxide inclusions within pore spaces of the potassium feldspar portions of the groundmass.

The Round Top rhyolites are composed of 48-52% potassium feldspar, 28-30% quartz, 8-14% plagioclase feldspar, 4-5% annite biotite, 2-3% opaques dominantly magnetite-hematite, 1% zircon, and 1% trace phases including REE-fluoride minerals, based on modal abundance estimates (Table 3.1). The petrogenetic sequence of mineralization and subsequent alteration is described in Figure 3.11. The mineral aeschynite has been cited by previous authors as being present within the rhyolite, and was also potentially observed within this study, but its occurrence could not be confirmed due to the limitations of the analytical process. This and other minerals identified by previous studies but not identified by the author are listed in Table 3.2. A list of minerals with their associated symbology used throughout this report is located in Table 3.3. A table of samples with corresponding analyses and minerals identified within each is located in Appendix A.6.

Phenocrysts typically range from 20-200 μm in diameter, and occur as individual disseminated crystals and within clusters. Minor phases comprise less than 1%, and include cassiterite, cerianite–(Ce), changbaiite, columbite, cryolite, tantalite, thorite, two unknown minerals labeled (W) and (X) respectively, yttrofluorite, and yttrocerite (Table 3.1). The groundmass consists of potassium

feldspar, quartz, and plagioclase feldspar. The accessory phases (commonly in conjunction with the trace phases) occur in groupings either near one another, as inclusions, or as adjoining phenocrysts.

Previous workers and current studies indicate enrichment of the rhyolite in Li, F, Be, Zn, Rb, Y, Zr, Nb, Sn, Ta, Pb, the REEs, especially HREEs, Th, and U, and depletion in Mg, Ca, Ti, Sr, and Ba, versus that of a typical calc-alkaline rhyolite (Rubin et al. 1987; Price et al. 1990). All four variations of the Round Top rhyolite are weakly peraluminous, except one sample that is strongly peraluminous, as defined by the Alumina Saturation Index of igneous rocks, which indicates an excess of alumina exceeding that required to form feldspars and defined by Al_2O_3>(CaO+Na_2O+K_2O) (Barton & Young, 2002). The rhyolite is additionally subalkaline as defined by the Volcanic Alkaline/Subalkaline classification Na_2O+K_2O versus SiO_2 (Irvine & Baragar, 1971).

RHYOLITE CLASSIFICATION

The rhyolite that comprises the Round Top laccolith may be broken into four subcategories based on distinct color variation: gray, purple, red, and tan. The gray, purple, and red rhyolites are very similar mineralogically but differ slightly in groundmass composition and texture. The tan rhyolite differs from the other three mineralogically and is less cohesive than the others, often with a chalk-like texture. Hand samples commonly have coatings of dendritic

manganese oxides, drusy green, white, brown, or purple fluorite, white to yellow calcite, white to brown microcrystalline silica, and chalky white caliche.

The color variation between the rhyolite is the result of increasing amounts of hematite within the pore spaces of the feldspar groundmass. The gray rhyolite typically has very little hematitic pore fill, giving the rhyolite a clear, non-red coloration in thin section. The purple rhyolite has more hematitic pore fill than the gray rhyolite, but less then the red. With the purple, hematite fill is visible in hand sample as red spots disseminated throughout the rhyolite. The red rhyolite contains the most hematitic pore fill, which leads to the distinct coloration. The tan rhyolite additionally has abundant hematitic fill but overall less feldspar groundmass.

It is key to note that classification of the Round Top rhyolite based on color variation took place in the field (prior to geochemical or mineralogical analyses), as a means to identify samples and as a geologic point of interest. Although subsequent analyses have shown mineralogical and geochemical similarities between the rhyolite types, the author believes the characteristic of highly variable color and texture within one laccolith is a significant indicator as to the processes that occurred to form such a deposit, and therefore the classification method is maintained.

Gray Rhyolite

The gray rhyolite in hand sample varies from medium to dark gray (Figure 3.8 A). The rhyolite is mostly aphanitic, although upon close inspection small (≤1 mm) magnetite phenocrysts are visible, especially along fresh and polished surfaces. The rhyolite is highly cohesive and difficult to fracture.

Purple Rhyolite

The purple rhyolite varies from light purple to light purplish-pink (Figure 3.8 B). Of the different types of rhyolite, the purple variation most closely resembles a rhyolite porphyry due to visible (≤5 mm) red hematitic “spots” that are dispersed throughout the rhyolite. Within some purple rhyolite samples the hematite appears larger and more prominent, whereas in others the spots are smaller (~1 mm) and less prominent. The rhyolite is highly cohesive and difficult to fracture.

Red Rhyolite

The red rhyolite is aphanitic and varies from light orangish-red to deep ox-blood red (Figure 3.8 C). A very few number of red rhyolite samples were noted to contain oblong vugs ranging from 1-2.5 cm in diameter. The rhyolite is highly cohesive and difficult to fracture.

Tan Rhyolite

The tan rhyolite is aphanitic and varies from tan to light brown (Figure 3.8 D). It differs from the other rhyolites in that it is chalky to the touch and less cohesive then the other three types, and easily fractured.

Mottled Rhyolite

A number of combinations of the mottled rhyolites have been observed, including texturally crosshatched, striped, and blob-like types. Each texture has been identified in a number of rhyolite color combinations, including red and gray, red gray and tan, purple and gray, purple and tan, and red and tan (Figure 3.9). The exact cause of the mottling is not known, but as the mineralogical composition does not change greatly between the differing rhyolite types, it is believed to not represent some form of magma mixing or assimilation. Rather, the mottled textures most likely represent the preferential movement of oxidizing fluids along microfractures. It is likely that with the migration of these fluids, the microfractures were subsequently annealed and are now invisible to observation, as petrographic and microbeam analyses failed to identified a set of these geometric microfractures.

Rhyolite Breccia

The rhyolite breccia typically occurs along fractures and within crevasses of the laccolith where rhyolite fragments have become entrained within a matrix

of fluorite, calcite, microcrystalline silica, and caliche (Figure 3.10). The matrix varies greatly and may be composed wholly of one material or any combination of many materials. The fluorite varies from drusy to massive and has been observed as purple, white, brown, and green. The calcite is typically a yellowish white and massive. The microcrystalline silica is additionally massive and ranges from white, to brown, to an orangish-brown color. The caliche is typically pale yellow to white and is found as a coating on most samples, including those that are not brecciated. The rhyolite fragments typically are angular to subangular and range from >0.5-5 cm in diameter. The coloration of the rhyolite clasts varies, and includes all of the main four-rhyolite types. Within one breccia sample multiple rhyolite types may be present.

PETROGRAPHY

The rhyolite types vary significantly in clarity when viewed with a transmitting light microscope due to the varying degrees of turbidity (Figures 3.12 & 3.13). The major phases and some of the accessory phases are visible using petrographic techniques alone, although the majority of the accessory and traces phases are not observable by this method. The minerals identifiable with the aid of a microscope are discussed in this section. All of the minerals, including the major, accessory, and trace phases are further discussed in the Electron Microbeam section.

Vapor-rich inclusions were observed within a number of phenocrysts, including quartz. These inclusions typically occur as single inclusions that do not align to the crystal structure of the host phenocryst, and are interpreted to be secondary in origin.

Mineralogy - Major Phases

Potassium Feldspar

Potassium feldspar constitutes 48-52% of the rhyolite, and is found in two forms, 1) as a rind mantling a more sodic plagioclase core, and 2) as euhedral to subhedral phenocrysts with distinct hourglass sector zonation (Figure 3.14). Of the 48-52%, 60% of the potassium feldspar occurs as overgrowths to sodic cores and approximately 40% occur as the hourglass-type phenocrysts. The clarity of the potassium feldspar phenocrysts and overgrowths in plain polarized light (PPL) and crossed polarized light (XPL) is often diminished due to a pervasive turbidity, causing the phenocrysts to appear opaque.

The mantling population of potassium feldspar ranges from 10-60 μm at the widest point. The overgrowths generally display a ragged, corroded appearance on the outer edges, and a smooth continuous contact with the interior plagioclase feldspar (Figure 3.15). They are commonly too turbid in appearance to view any form of extinction in XPL.

The hourglass phenocrysts have a maximum length from 75-200 μm. The hourglass feldspars display a range of internal symmetry and clarity varying from

highly discernable and well defined to poorly defined and irregular (Figure 3.16). This feldspar hourglass texture was first described to be an attribute of the Round Top rhyolite by Barker (1980). In crossed polarized light, discrete grains typically display a double undulatory extinction, sweeping inward through one opposing set of hourglass structures, then passing outward through the opposite pair, with continued rotation of the stage.

Quartz

Quartz comprises 28-30% of the rhyolite and occurs as colorless anhedral to subhedral phenocrysts that typically range from 20-150 μm in diameter (Figure 3.17). A large portion of the quartz phenocrysts demonstrate a pseudo-concentric ring of melt inclusions of a purplish hue, first noted by Barker (1980) (Figure 3.18). Through cathodoluminescence analyses, it was determined that quartz phenocrysts consist of a core, followed by a melt inclusion rim, and an outer late-stage quartz rim, discussed further in a later section. In crossed polarized light, the quartz displays a range of normal to undulatory extinction. One phenocryst of rutilated quartz was observed as an inclusion within a feldspar glomerocryst (Figure 3.19).

Plagioclase Feldspar

Plagioclase feldspar comprises 8-14% of the rhyolite, and occurs as subhedral to euhedral albite laths with potassic feldspar overgrowths. These laths with overgrowths occur in clusters, as penetrating twins, or as individual

phenocrysts (Figure 3.20). The potassic mantles may have an additional albitic overgrowth, although this is rare. The outer potion of the albite, before the potassium feldspar overgrowth, is equant and displays no reaction textures, indicating no dissolution of the albite before the formation of the potassic feldspar overgrowth (Figure 3.21). The plagioclase phenocrysts range from 50-100 μm in width and may vary from 20-120 μm in length. In crossed polarized light, the plagioclase commonly displays an array of albitic and/or Carlsbad twinning (Figure 3.21 B-C). No calcium-rich feldspar was observed.

Mineralogy - Accessory Phases

Accessory phases in total comprise 7-9% of the rhyolite, and include annite biotite, magnetite, hematite, and zircon. The annite biotite, zircon, and hematite are too small to be discernable without a microscope. The magnetite is typically larger than the other accessory phases and is therefore visible with the aid of a hand-lens, but is more easily observed with the aid of a petrographic microscope.

Annite Biotite

Li-rich annite biotite is the most abundant of the accessory phases, comprising 4-5% of the rhyolite. The annite typically occurs as subhedral to anhedral phenocrysts interstitial to the groundmass or adjacent to other more euhedral phenocrysts (Figure 3.22). Phenocrysts typically range from 10-100 μm in length at the longest point. The annite is easily identifiable due to prominent

basal cleavage and distinct birds-eye extinction when viewed in XPL (Figure 3.22 B). In PPL the annite displays a range of moderate pleochroism, alternating from a pale yellow-green to a dark brown-green as the stage is rotated. The outer edges of the phenocrysts are typically ragged, conforming to the shape of adjacent, earlier formed phenocrysts (Figure 3.22).

Magnetite

Magnetite and hematite combined comprise approximately 2-3% of the rhyolite (Figure 3.23). Magnetite and hematite commonly occur in conjunction with one another, and the hematite is believed to be predominantly a direct product of the oxidation of the magnetite (Figure 3.24). Transitioning from gray, purple, red, and tan rhyolites, the amount of magnetite decreases as the amount of hematite increases. This effect is visually apparent by the increasing turbidity of the rhyolite when viewed with a transmitting light microscope (Figures 3.12 & 3.13). Additionally, the integrity of the magnetite phenocrysts decreases transitioning from the gray to the red rhyolite, presumably due to the incomplete oxidization of the magnetite that is forming the hematite. Magnetite that is partially oxidized demonstrates a pock-like embayed texture, which is typically filled with or surrounded by a halo of hematite (Figure 3.25). This partial oxidation of the magnetite increases in abundance from the gray to red rhyolite types. Within the tan rhyolite the abundance of magnetite drops significantly to the point where no magnetite phenocrysts were observed, although small inclusions of

magnetite within the groundmass are moderately abundant and hematite is present within the groundmass and pore spaces (Figure 3.26).

The magnetite occurs as euhedral to subhedral phenocrysts that range from 10-150 μm at the maximum length, and as microcrysts within the groundmass. Approximately 70% of the magnetite occurs in close association with other accessary phases, including zircon, tantalite, columbite, cassiterite, and yttrofluorite. The trace phases that occur in conjunction with the magnetite are typically entrained as inclusions and/or just adjacent to the phenocryst. Within plain and crossed polarized light, the magnetite appears opaque and is therefore only visible in reflected light (RL) as a pale blue-gray color. Additionally, the magnetite is identifiable in reflected light by the distinct hematitic red halo commonly associated with the phenocryst.

Hematite

The hematite is visible in hand sample as red spots throughout the purple and occasionally the other rhyolite types. Hematite occurs in two forms, 1) as halos to magnetite phenocrysts, and 2) within the pore space of the potassium feldspar portions of the groundmass (Figure 3.27). These microcrysts range from <1-2 μm in diameter, and culminate to form hematitic halos up to 100 μm in length. The proportion of pore-filling hematite is the least abundant within the gray rhyolite, and increases from purple to red rhyolite. Within transmitted light, the hematite within the groundmass appears as red microinclusions scattered

throughout that cause the pervasive coloring of the red rhyolite (Figure 3.28). The hematite coronas to magnetite phenocrysts cause the distinct red spots characteristic of the purple rhyolite and visible in hand sample. Within PPL the hematite is a red-brown color and a distinct ox-blood red in RL.

Mineralogy - Groundmass

The rhyolite groundmass is composed of (in decreasing order), subhedral to anhedral potassium feldspar, plagioclase feldspar, and quartz (Figures 3.29-3.31). Staining reveals the pervasive abundance of potassium within the groundmass of all of the rhyolite types, although the red rhyolite has a notably higher abundance of potassium-rich mineralogy than the purple and gray varieties. Approximately 20% of the gray rhyolite groundmass appears yellow when stained, 30% for the purple, and 40% for the red (Figures 3.29-3.31). These percentages are approximate and attempt to omit the potassium-rich phenocrysts from the estimations. Within the gray rhyolite, the yellow portions of the groundmass appear as isolated pockets, surrounded by areas lacking abundant potassium (Figure 3.29). This varies greatly from the red rhyolite, in which the yellow stained areas (and therefore the potassium-rich portions) appear ubiquitous throughout the entirety of the groundmass (Figure 3.31). This is a surprising textural difference as the gray, purple, and red rhyolites all have an overall similar concentration of K_2O at approximately 4wt.%. In addition to emphasizing the potassium-rich pockets within the groundmass, staining

accentuates the potassium mantles of the plagioclase feldspar laths and the more potassium-rich quadrants of the hourglass feldspars (Figure 3.30).

ELECTRON MICROBEAM ANALYSES

The primary focus of the electron microbeam analysis was to determine the major similarities and differences between the rhyolite variations, to identify and document the specific mineralogy and textures of the rhyolites, and to determine if alteration of the rhyolites had occurred. Additionally, because identification of trace phases is nearly impossible with petrographic studies alone, a primary goal of this work was to identify the major trace phases within the rhyolites, including determine their compositions, abundance, textures, and relationships relative to other minerals.

Rhyolite Characteristics

Microbeam analyses indicate no major mineralogical differences between the gray, purple, and red rhyolite types. Each type contains approximately equivalent amounts of the major, accessory, and trace phases, respectively, a surprising result considering the strong visual differences between each. Additionally, no significant differences in the formation or crystal habits of the minerals were detected between the rhyolite types (e.g. all of the REE-fluorides appear to be late-stage and subhedral to anhedral).

The tan rhyolite varied from the other three-rhyolite types mineralogically and with porosity. The tan rhyolite appears to lack the prominent magnetite phenocrysts common in the other rhyolites, and has considerably greater porosity than the gray, purple, and red rhyolites.

Mineralogy - Major Phases

Potassium Feldspar

Potassium feldspar comprises the main portion of the phenocrysts and a major portion of the groundmass. EDS point analyses and mapping confirmed that the inner core of the feldspars laths is composed of sodium-rich feldspar, whereas the outer overgrowth is potassium-rich (Figure 3.32). The potassium feldspar portion of the feldspar laths varies greatly in width and length. Generally, the smaller the inner sodic core, the wider the outer potassic rim relative to the inner core. The potassic overgrowth typically ranges between 10-60 μm at the thickest point. CL imagining and EDS analyses suggest portions of the overgrowth are more sodic-rich versus potassic (Figure 3.32-3.33). In CL, these sodic portions appear as dark gray “stringers” in normal CL gray-scale, and typically match the coloration of the inner plagioclase core (Figure 3.33 A).

In addition, EDS analyses confirmed that the hourglass type phenocrysts are predominately composed of potassium feldspar, although one of the two hourglass sectors typically contains more sodium than the other. With CL, the two hourglass sections are visually evident as differing shades of gray caused by the slight compositional difference forming the sector zonation, although compositionally the sectors are too similar to be discerned with BSE or SE imaging (Figure 3.34).

Quartz

Quartz phenocrysts are typically subhedral to anhedral and are comprised of three parts, 1) an inner more euhedral core followed by, 2) a melt inclusion ring, and 3) an anhedral overgrowth of additional quartz (Figures 3.35 -3.36). The core is euhedral to subhedral equant high temperature beta quartz (hexagonal). Along the core outer boundary is a semi-concentric ring of potassium, sodium, and silica-rich melt inclusions, the main elemental components of the groundmass (Figures 3.35 A-B 2 & 3.48). Following, and intermingled with the inclusion ring is an overgrowth of late-stage anhedral magmatic quartz (Figure 3.35 A-B 3). The quartz overgrowth typically is highly embayed and undulatory along the outer edge, due to later corrosive processes (Figure 3.35-3). Further analyses with the CL detector on the ESEM determined that the inner core is typically oscillatory zoned and appears as a darker gray to the outer portion when viewed in normal CL mode (Figure 3.37). The differences in tone between the inner and outer portions of the quartz phenocrysts when viewed with CL suggest slight compositional and/or structural variations, which are not detectable with the EDS. When well formed, the inner portion of the quartz crystal is hexagonal. This hexagonal crystal form is indicative to beta quartz, the higher temperature form of the two primary types of quartz. Beta quartz, the higher symmetry and higher temperature quartz polymorph, forms at a minimum temperature of 573°C at normal atmospheric pressures (1 atm), although normal rhyolitic melt temperatures are above this range (Nesse, 2000). Due to subsequent decreased

pressure and temperature conditions, the quartz phenocrysts have presumably now pseudomorphed to the trigonal, lower temperature form of alpha quartz (trigonal) (Figure 3.35-1). The late-stage overgrowth of quartz varies greatly in thickness, and may range from 10-60 μm for phenocrysts of a similar size (Figure 3.37).

Melt inclusions along the quartz-to-quartz boundary occur within almost all quartz phenocrysts. These are most easily discernible with the CL detector (Figure 3.38 A-B). Additionally, the abundance of subhedral to anhedral quartz that comprises the groundmass is more readily apparent when viewed with the CL detector (Figure 3.38 C-D).

Plagioclase Feldspar

The plagioclase feldspar laths are composed of a sodic inner core surrounded by a more potassic overgrowth rim (Figure 3.32). The inner core portion of the feldspar varies in length, ranging between 20-120 μm along the longest axes (Figures 3.33 & 3.39). CL imaging and EDS analyses indicates a fairly homogenous plagioclase lath, with little compositional variation (Figures 3.33 & 3.39). The feldspar laths are typically the largest of the all of the phenocrysts, when both feldspar portions are considered. The morphology of the inner core is euhedral with no observable corrosion or embayment along the feldspar-to-feldspar transition (Figures 3.33 & 3.39).

Mineralogy - Accessory Phases

The accessory phases include annite biotite, magnetite, hematite, and zircon. Most of the accessory phases are observable with the aid of a transmitting light microscope, although not as clearly and as with microbeam techniques. Of the accessory phases, the magnetite is the only one that forms euhedral to anhedral phenocrysts. The annite, hematite, and zircon all form subhedral to anhedral crystals, interstitial to the groundmass and/or other phenocrysts.

Annite Biotite

Compositionally, the annite is the Li-rich iron-endmember form of biotite. The annite biotite is typically anhedral, displays strong basal cleavage, and ranges from 10-100 μm in the long direction. The crystals occur interstitial to, and along the grain boundaries of other phenocrysts, commonly incorporating surrounding crystals (Figure 3.40). Additionally, the outer edges of most of the annite crystals are highly irregular, embayed, and undulatory (Figure 3.40 A). This morphology suggests crystallization late in the petrogenetic sequence, potentially simultaneous to the crystallization of the groundmass and preexisting neighboring phenocrysts. In some instances, the annite displays rune-like edges, potentially further indicating rapid crystallization (Figure 3.40 B-2). Inclusions of quartz, magnetite, hematite, and yttrofluorite have been identified with EDS analyses within the annite (Figure 3.40 A-1 & B). The annite commonly displays

compositional zonation within a single crystal, visible by a darker gray color within the interior portion surrounded by a lighter gray portion when viewed with the BSE detector, although this compositional zonation is too minor to be detected with the EDS detector (Figure 3.40 B-3). Price et al. (1990) describes the presence of two micas within the Sierra Blanca rhyolites, a biotite and the lithium-rich trioctahedral mica (annite). EDS analyses of the micas only identified the Li-rich annite biotite, although this may be due to a lack of the biotite within the Round Top rhyolites and/or potential sampling bias.

Magnetite

The magnetite phenocrysts vary from euhedral to anhedral in form and range from 10-150 μm in diameter at the widest point (Figure 3.41). They are most commonly found in association with other accessory and traces phases, including hematite, zircon, tantalite, columbite, cassiterite, changbaiite, and the REE-fluorides. The associated accessory and trace phases occur as inclusions, or just adjacent to the magnetite phenocryst (Figure 3.41 B). This proximal relationship suggests that many of the accessory and trace phases formed conterminously to one another during crystallization. Inclusions within the magnetite vary greatly in size and have been observed to be from <1-10 μm in width (Figure 3.41 B-C). Additionally, magnetite commonly occurs as anhedral inclusions within other phenocrysts, ranging from 1-5 μm in size (Figure 3.40 B).

Hematite

The hematite occurs predominately within pore spaces of the potassium feldspar portion of the groundmass (Figure 3.42). It ranges from <1-2 μm in size, is anhedral and wispy in nature, conforming to the shape of the pore space in which it is enclosed. The abundance of hematite within the groundmass increases from the gray, purple, and red rhyolites. The hematitic pore-fill occurs most commonly near or in association to other accessory and trace phases, such as magnetite, annite biotite, zircon, and thorite (Figures 3.41 B, 3.42-3.43). The hematitic pore-fill is typically patchy throughout the groundmass, occurring in some areas and not in others when viewed with the BSE detector for all of the rhyolite types. The EDS detector cannot differentiate between magnetite and hematite, but the variation in BSE brightness, the morphology, and mineral association of the hematite, support that the iron oxide pore fill is hematite or goethite in composition.

Zircon

Zircon comprises approximately 1% of the rhyolite composition. Within the Round Top rhyolite, two populations exist, 1) a thorite inclusion-rich population, and 2) a thorite inclusion-poor population (Figure 3.43). The thorite inclusion-rich population appears to be the more abundant (Figure 3.42). Both populations range from 10-40 μm in length and are enriched in Hf, U, and Th. Most are anhedral, although a few instances of subhedral to euhedral phenocrysts have

been observed (Figure 3.44). These well-formed phenocrysts are rare, but when they do occur they are typically highly embayed with corroded irregular outer edges. Individual subhedral to anhedral crystals are typically amoeboid in appearance and have stinger-like tails (first noted by Rubin et al., 1989; Figure 3.43). The subhedral to anhedral zircons are late-stage, and typically occur in clusters with each other and other accessory and trace phases, such as magnetite, hematite, tantalite, and yttrocerite (Figures 3.41 B, 3.43-3.44). Many of the zircon phenocrysts observed contain abundant void spaces, presumably that represent thorite inclusions that were plucked during thin section preparation (Figure 3.45). Thorite inclusions (when present), may take up to approximately 20% of the zircon phenocryst. In addition to inclusions, thorite crystals commonly occur adjacent to many of the zircons (Figure 3.43-3.44).

Rubin et al. (1989) presented the hypothesis that the two populations of zircon represent an initial magmatic population (the thorite-rich), and a later population introduced by migrating hydrothermal fluids (the thorite-poor population). Rubin et al. (1989) noted the common presence of the late-stage hydrothermal zircons within the fluorspar replacement body of the underlying limestone but not within the Round Top rhyolites. Both populations (the thorite inclusion-rich and inclusion-poor) were observed in the Round Top rhyolites, commonly in close proximity to one another (Figure 3.43).

Mineralogy - Trace Phases

The fine size and limited abundance of the trace phases inhibits study of their formation and occurrence by transmitted light microscope techniques alone. The best method to effectively study and identify these minerals is with the aid of the BSE and CL detectors within the SEM and ESEM, respectively.

The trace phases are typically subhedral to anhedral, range from <1-40 μm in size, and include cassiterite, cerianite-(Ce), changbaiite, columbite, cryolite, tantalite, thorite, yttrocerite, yttrofluorite, (W) and (X)-unknown. All of the trace phases are late-stage and occur interstitial or adjacent to other phenocrysts, as growths along grain boundaries, and/or within microfractures and voids. Additionally, the trace phases are commonly intergrown with other major, accessory, and trace phases, such as magnetite. The combination of intergrown trace and accessory phases appears to occur with no discernable pattern, and may occur in any number of groupings. These characteristics imply late-stage and simultaneous crystallization in the petrogenetic sequence.

The abundance of trace phases appears to be approximately equal between the gray, purple, and red rhyolites. However yttrofluorite (a HREE-bearing fluoride) was only identified within the purple rhyolite, whereas yttrocerite (a HREE- and LREE-bearing fluoride) occurred within all four varieties. This discrepancy may represent mineral heterogeneity between the rhyolite types and/or a possible sampling bias.

REE-Fluorides - Yttrofluorite, Yttrocerite, & (X)-unknown

Yttrofluorite (a Y-HREE-Ca fluoride) and yttrocerite (a Y-HREE-LREE-Ca fluoride) are the two main REE-fluorides identified within the Round Top rhyolites. (X)-unknown, (a Ca-Th-Pb-REE fluoride) was also identified within the rhyolites, but in limited abundance and was first noted by Price et al. (1990). The variation in composition and concentrations of the REEs and additional elemental components observed within these minerals by EDS analyses varies greatly. Variations include yttrocerite rich in Ce-La-Y, Ce-Y-Th, Ce-Y, Y-Dy-Th, Ce-Y-Nd-La, and Y-Ce-Dy-Yb. For yttrofluorite, varieties rich in Y-Dy, Y-Yb-Lu, Y-Yb, Y-Dy-Er-Tm, and Y-Dy-Er-Yb. EDS mapping demonstrates the F- and Y-rich nature of the REE-fluoride (Figure 3.46). EDS analysis identified the main REE components of the (X)-unknown mineral as Ce-La-Nd. Additional REE minerals were observed, but their compositions could not be confirmed given the limited analytical nature of the EDS detector. These minerals include aeschynite, and an unknown Nb-REE fluoride labeled (W)-unknown. The aeschynite and other REE minerals have been described as being present within the rhyolites by previous authors but could not be confirmed within the scope of this study (Table 3.2; Shannon & Goodell, 1986; Rubin et al., 1987; Price et al., 1990; Hulse et al., 2012, 2013).

The REE-fluorides are typically anhedral and interstitial in nature, suggesting late-stage crystallization. They form as individually crystals or in

groups with multiple crystals. Their size may vary but is typically ~1-40 μm, although groups of crystals have been observed to be over 100 μm in length.

Yttrofluorite has been observed to occur in several forms, including along the outer potion of feldspar phenocrysts within the potassium overgrowths, as inclusions to other minerals, and within the potassium feldspar portion of the rhyolite groundmass (Figures 3.46-3.47). Yttrocerite has been observed to occur as individual crystals (Figure 3.41 B), as inclusions to other minerals, and within the groundmass of the rhyolite (Figure 3.48). (X)-unknown has been observed to occur as inclusions to other minerals (Figure 3.47).

Yttrofluorite and yttrocerite most commonly occur as a pore-filling type mineralogy within the outer boundaries of feldspar phenocrysts and within the feldspar-rich portions of the rhyolite groundmass (Figures 3.46-3.66). When in this pore-filling form the crystals are anhedral and wispy in nature, suggesting possible late-stage filling of the pore space by the REE-fluorides and/or contemporaneous crystallization with the outer portion of the feldspar or groundmass. They may form a singular crystal within the groundmass or overgrowth, or may occur as a group of multiple crystals within relatively close proximity.

The (X)-unknown mineral has only been observed as several inclusions within the same annite phenocryst. Crystals varied from semi-circular to elongate in habit (Figure 3.47). The size of the crystals varied from <5-10 μm in length.

As inclusions to other minerals, the REE-fluorides are typically anhedral and may range from very minor constituents of the overall phenocryst to large components of the host crystal (~1-40 μm). When in association with an annite phenocryst, the REE-fluorides typically partially conform to the direction of the basal cleavage, suggesting preferential substitution or contemporaneous crystallization with the biotite (Figure 3.47). When included within a quartz phenocryst, the REE-fluorides may take a wide range of forms including small (<1 μm) circular inclusions to larger (>5 μm) anhedral crystals (Figure 3.48).

Other Trace Phases - Cassiterite, Cerianite-(Ce), Changbaiite, Columbite, Cryolite, Thorite, Tantalite, & (W)-unknown

Cassiterite

Cassiterite is one of the more abundant of the non-REE-fluoride trace phases, although the total quantity is less than some of the other trace phases such as tantalite and changbaiite. It most commonly occurs as inclusions and in close association with other trace and accessory phases (Figures 3.49-3.50). Phenocrysts are typically subhedral to anhedral and may range from very small inclusions (≤5 μm) to relatively large crystals (50 μm). The contact edges of the cassiterite and adjacent crystals are typically irregular and undulatory (Figure 3.50).

Cerianite-(Ce)

Cerianite occurs within the pore spaces of the potassium feldspar-rich portions of the rhyolite groundmass and was identified by EDS point analysis to be enriched in cerium (Ce) (Figure 3.51). The crystals are anhedral and range from <1-5 μm in diameter. The cerianite occurs in clusters with 10s-100s of crystals. The form of the individual crystals appears to be similar to that of the adjacent pores within the groundmass (Figure 3.51 A). Additionally the edges of the cerianite are commonly wispy or tail like, conforming to the surrounding quartz and groundmass crystals (Figure 3.51 A). This potentially suggests the cerianite and the groundmass formed contemporaneously and/or the cerianite filled in pore spaces and fractures at a later stage. EDS analyses indicate the cerianite is rich in Th (Figure 3.51 B).

Changbaiite

Changbaiite occurs as fracture fill, along grain boundaries, and as inclusions in other accessory and trace phases, including columbite and magnetite (Figures 3.52-3.53). The crystals are typically anhedral and range from 5-10 μm in diameter. The inclusions of changbaiite are dispersed throughout and along the outer edges the host phenocryst (Figure 3.52). When the changbaiite occurs along microfractures and along grain boundaries the crystals appear to conform to the adjacent phenocrysts and groundmass, possibly suggesting concurrent or late-stage crystallization (Figure 3.53).

Columbite

Columbite occurs in close association with other trace and accessory phases, including magnetite, cassiterite, and changbaiite (Figure 3.50-3.52). Of the trace phases, the columbite is the most abundant, and typically is of the largest crystal size. Crystals are typically subhedral to anhedral and may range from 20-120 μm in length. The columbite commonly contains inclusions of other trace phases, particularly cassiterite and changbaiite. The contacts between the inclusions and the host columbite are undulatory and irregular (Figures 3.50-1 & 3.52).

Cryolite

Only two crystals of cryolite were observed within the scope of this study, and each occurred as an inclusion within the potassium feldspar portion of the rhyolite groundmass in proximity to one another (Figure 3.54). The inclusions are anhedral and wispy in nature, with a total width of <1 μm. EDS analyses indicates an anomalous enrichment of Ca within the two identified occurrences of cryolite (Figure 3.54 B). The surrounding potassium and plagioclase feldspar groundmass is known to be depleted in Ca, so it is unlikely this is an overlapping signal from the surrounding minerals. The anhedral shape of the inclusions and their occurrence within the groundmass suggests late-stage crystallization, either contemporaneous to, or subsequent to the formation of the groundmass.

Thorite

Thorite occurs in two forms within the rhyolite: 1) as inclusions within zircon phenocrysts, and 2) as individual crystals within the potassium feldspar portion of the groundmass (Figures 3.45 & 3.55). In both populations, the thorite is anhedral and irregular in shape. The size of the thorite varies greatly from <1-10 μm in diameter. And when many crystals occur in close proximity, the variation in size may be great (Figure 3.45). The thorite inclusions within the zircon phenocrysts indicate contemporaneous formation and/or exsolution of the thorite from the zircon (Figure 3.45). The occurrence of thorite along the grain boundaries and within fractures suggests either concurrent or subsequent crystallization of the thorite to the groundmass (Figure 3.55).

Tantalite

The tantalite typically occurs in two forms, 1) as phenocrysts associated with other trace and accessory phases including cassiterite and magnetite, and 2) as interstitial fracture fill (Figure 3.49 & 3.56). The tantalite is subhedral to anhedral and may range from pore size (≤5 μm) to phenocryst size (70 μm). When in phenocryst form the tantalite commonly contains inclusions of other minerals, such as cassiterite or changbaiite (Figure 3.49). As inclusions within the groundmass, the tantalite commonly appears to conform to the surrounding boundaries, commonly forming tail-like structures (Figure 3.56-1). This close association to other accessory and trace phases and to the groundmass

suggests probable late-stage crystallization of the tantalite in the petrogenetic sequence.

(W)-unknown

The (W)-unknown is a Nb-rich oxide with minor amounts of Ta, Fe, Mn, Pb, and F (Figure 3.53). The naming of the unknown mineral follows nomenclature utilized by Price et al. (1990), who named three unidentified minerals X, Y, and Z. The analytical precision of the EDS detector is too low to definitively quantify the elemental composition, but the relative percent abundance is given. Only one occurrence of the (W)-unknown mineral was identified, and that was in close proximity to two changbaiite inclusions within the groundmass (Figure 3.53). The (W)-unknown is anhedral and approximately 10 μm in length. Two tail-like structures protruding from one side of the unknown mineral suggest late-stage petrogenesis, conforming to the surrounding minerals as it crystallized.

Mineralogy - Groundmass

The groundmass of the rhyolite is dominated by intergrown anhedral patches of potassium and plagioclase feldspar with subhedral to anhedral quartz (Figure 3.57). With the BSE detector, the potassium feldspar, plagioclase, and quartz portions are easily distinguished based in differences in color tones and porosity. Given the variable working conditions of the SEM, the contrast and brightness between the groundmass figures may appear different, although the

relative color relationships are equivalent from figure to figure. Throughout the SEM images, the potassium feldspar is always the lightest gray tone between the three minerals, and is easily distinguished due to the abundance of pores visible within the feldspar (Figure 3.58-1). Plagioclase feldspar and quartz are a similar gray tone but are distinguished by differing porosity and smoothness. The plagioclase feldspar is a medium gray tone with moderate porosity, less than that of the potassium feldspar (Figure 3.58-2). The quartz is of an equivalent medium gray tone to that of the plagioclase but lacks any porosity and appears smooth (Figure 3.58-3). The pores within the potassium and plagioclase feldspars commonly appear in linear groupings (Figure 3.58).

The relative proportions of potassium feldspar to plagioclase and quartz are approximately even between the gray, purple, and red rhyolite (Figure 3.59). The tan rhyolite is highly porous compared to the other three and appears to contain a considerably less amount of potassium within the groundmass (Figure 3.59 D). The gray, purple, and red rhyolites all display a characteristic groundmass intermingled feldspar texture (Figure 3.59 A-C). Although compositionally very similar, there appears to be slight textural differences between the groundmass of the different rhyolites. The gray and tan rhyolites have slightly more quartz within the groundmass (25%) than the purple and red (15-20%) (Figure 3.59 A). Additionally, the groundmass of the purple rhyolite appears to contain slightly less of the intermingled feldspar texture, whereas the red rhyolite appears to contain the most amount of the intermingled feldspar

texture (Figure 3.59 B & D). Within all types of the rhyolite, the groundmass contains inclusions of accessory and trace phases, particularly within the potassium feldspar pore-spaces (Figure 3.58).

GEOCHEMICAL ANALYSES

Fourteen samples representing the major lithologic constituents that form the Round Top laccolith and the underlying units were selected for geochemical analysis. See the Methods section for details and analytical techniques.

Eleven samples of rhyolite were analyzed for geochemistry: two gray, two purple, three red, and two tan, representing the four rhyolite varieties, plus two samples of the mottled textures (Figure 3.5; Appendix A.5). Although only 11 rhyolite samples were selected for geochemical analyses, they were selected from localities that best represent the rhyolite varieties as a whole. All geochemical data referred to in this section may be found in Appendices B.1-B.3.

In addition to the 11 rhyolite samples, one sill, one fluoritized limestone, and one rhyolite breccia sample were analyzed for comparison purposes. These results are not discussed in detail as with the rhyolites, but data for these samples may be found in Figure 3.71 and Appendices A.5 & B.1-B.3.

The minimum and maximum concentrations for 21 elements from 2,340 samples as determined and published by TRER is available in Appendix B.4 (Hulse et al., 2013). Ideally, data produced for this study would be compared to data obtained by TRER as a means of establishing statistically similarity, but published data is not available for such a comparison.

Whole-rock Geochemistry

All of the samples are high-silica, peraluminous, subalkaline rhyolite in composition and defined as sourced from a within plate granite (Figures 3.60-3.63). Major element abundances are similar within representative rhyolite sample sets and between the rhyolite varieties as a whole, but do demonstrate enough variation to produce a slight spectrum of values within geochemical classifications. The sill that underlies the laccolith is syeno-diorite in composition (Figure 3.64).

Spider Diagrams

The values of select elemental abundances within the 11 rhyolite samples were compared to established values of a typical granite, the continental crust, the upper and lower portions of the crust, and chondrites. The results are as follows.

Compared to a typical granite composition determined by Levinson (1974), the Round Top rhyolites diverge by varying amounts from the determined abundances (Figure 3.65). All eleven rhyolite samples are slightly enriched in Ag, Cr, and W, and enriched by varying degrees in As, Pb, U, and Zn. Additionally, all are almost equally enriched by over an order of magnitude in Sn. The samples are depleted by varying amounts in Ba, Co, and Cu, and almost equally depleted by over a magnitude of order in Ti. The values for Mn and Ni span both enriched and depleted. The rhyolites are all not equal in the degree of enrichment or

depletion. The tan rhyolite demonstrates a greater degree of depletion and has lower levels of enrichment than the gray, purple, red, and mottled varieties (aside for U where the tan rhyolite is the most enriched). There is no clear correlation between enrichment and depletion relative to the gray, purple, red, and mottled rhyolites, each varies from element to element and from sample to sample.

The composition of the 11 rhyolite samples demonstrate both an enrichment and deletion relative to the established values of the average continental crust as determined by Weaver and Tarney (1984), (Figure 3.66). As with the last comparison to Levinson (1974), there appears to be little recognizable correlation to enrichment-depletion values relative to specific rhyolite types. When enriched in a specific element the 11 samples demonstrate a tighter correlation in concentration and are more tightly grouped then with the elements in which they are depleted, suggesting a tighter correlation in those elements representing enrichment than depletion (except for Tl). The data demonstrates a lack of correlation between rhyolite sample pairs, which may vary in concentration from one another. Of the sample pairs, the tan rhyolite is the most closely associated in values between samples and tends to follow a similar enrichment-depletion pattern. All eleven samples are enriched in Rb, Th, U, K, Nb, Hf, Zr, Tb, Y, Tm, and Yb and depleted in Ba, La, Sr, P, and Ti. The rhyolite values span both enrichment and depletion for the elements Ce, Nd, and Sm.

Relative to the average elemental abundances of upper and lower portions of the Earths' crust as established by Taylor and McLennan, (1981) and

Weaver and Tarney (1984), respectively, the rhyolite samples demonstrate similar enrichment and depletion patterns but vary in the degree of the magnitude (Figures 3.67-3.68). The two graphs show an overall similar pattern to the average crustal abundance comparison discussed previously. Relative to the upper crust, the rhyolite samples are enriched in Rb, Th, U, K, Nb, Hf, Zr, Y, Tm, and Yb and depleted in Ba, La, Sr, P, and Ti. The rhyolite samples span both enrichment and depletion for the elements Ce, Nd, Sm, and Tb. When compared to the lower crust, the rhyolites are similarly enriched in Rb, Th, U, K, Nb, Hf, Zr, Y, Tm, and Yb and depleted in Ba, Sr, P, and Ti. Likewise, the rhyolites span both enrichment and depletion for Ce, Nd, and Sm. Unlike the upper crust and relative to the lower crust, the rhyolites are almost equal to, and depleted in, average La abundances. Additionally, they are greatly enriched in Tb versus the lower crust where they span both enriched and depleted.

REE Spider Diagrams

Normalized to chondrite values, the Round Top rhyolites demonstrate a distinct enrichment in HREEs, a strong negative europium anomaly, and a positive slope (Figures 3.69-3.71). Comparison of the Round Top data to that of previous studies Price et al. (1990) and Rubin et al. (1993) produces a strong correlation in the REE trends of both datasets (Figure 3.70). Both datasets when normalized to chondrite values produces similar enrichment patterns that demonstrate a positive slope and a strong europium anomaly.

Three additional samples from Round Top were compared to the rhyolite samples for their REE concentrations and relative trends (Figure 3.71). The rhyolite breccia closely follows the trend of the tan and one red rhyolite sample. The fluoritized limestone demonstrates an overall depletion in REEs relative to the rhyolite samples, and has a greater depletion in middle REEs versus HREEs and LREEs. The diorite sill is enriched in LREEs over HREEs producing a negative slope.

The average REE+Y content between the 11-rhyolite samples analyzed varied between 249 parts per million (ppm) and 518 ppm. The average REE+Y concentration between all eleven samples is 380 ppm, with an average abundance of 272 ppm HREEs, and 108 ppm LREEs. HREEs on average account for 72% of the REE content within a sample, but this value can vary greatly between samples, ranging from 58-86%. The rhyolite breccia sample contains similar REE+Y abundances to that of the rhyolite average at 337 ppm total REE+Y, although 300 ppm is comprised of HREEs+Y. The fluoritized limestone and diorite contain lower abundances of total REE+Y at 47 ppm and 178 ppm, respectively. The fluoritized limestone contains 38 ppm HREE+Y and 9 ppm LREE, whereas the diorite contains 37 ppm HREE+Y and 141 ppm LREEs.

The REE concentration between sample pairs varies from similar to greatly different. The gray rhyolite sample pairs span a large range of REE+Y concentrations, ORT262-01 was collected from an outcrop on the western portion of the peak, whereas ORT37-01 was collected from an outcrop on the

northwestern flank. ORT262-01 contains a total REE+Y abundance of 335 ppm and ORT33-01 contains an abundance of 461 ppm. The total HREE+Y content of sample ORT262-01 represents only 220 ppm whereas HREE+Y content of ORT37-01 is 326 ppm. Sample groups also demonstrate ranges of total REE+Y concentrations, as with the tan samples ORT44-20 and ORT44-21, which were both collected from the northern flank of the laccolith. ORT44-20 contains a REE+Y abundance of 262 ppm whereas ORT44-21 contains the lowest concentration of all 11 samples at 240 ppm. The tan samples demonstrate similar HREE+Y concentrations at 213 ppm and 220 ppm respectively.

Harker Diagrams and Bivariate Plot Comparisons

Harker diagrams of the major oxides, F, Sr, Ba, Be, and Zr in addition to the ratios La/Yb, Sr/Rb, and Eu^{2+}/Eu^{3+}* were compared to data of previous workers Price et al. (1990) and Rubin et al. (1993) to establish geochemical trends and relationships between the rhyolites (Figure 3.70; Appendix B.6). Data form these previous studies is located in Appendix B.5. As a whole, the data produced in this study contained higher silica values than that of the previous studies, causing the new data to fall outside of the standard deviation of the previous geochemical data.

Overall, the Harker diagrams demonstrate a progression from lower to higher silica indicating a successive evolution between samples. The gray, purple, red, and mottled rhyolites are all geochemically similar and demonstrate a

relative tight correlation between Harker diagrams. The tan and one sample of the red rhyolite generally do not correlate with the rest of the population, an indication of the separate alteration process that has affected this subgroup.

The CaO vs. SiO_2 plot may be grouped into three population sets, one of higher calcium and moderate silica, one of low calcium and low silica, and one of low calcium and high silica (Appendix B.6). The high calcium-moderate silica group includes the tan and mottled rhyolite samples. The higher calcium content of this group is most likely the result of remobilized Ca from the underlying limestone units during alteration, and thus it is reasonable that the Ca enrichment is localized to the units at the base of the laccolith.

The positive slope of the La/Yb plot closely corresponds to that of previous workers, and confirms the HREE to LREE enrichment of the gray, purple, red, and mottled rhyolite types. The tan rhyolite and one red rhyolite sample fall below this trend, demonstrating the relative depletion in LREEs relative to HREEs of this group. The separation in the two populations is additionally confirmed in the La/Yb vs. SiO_2 plot. The $Eu^{2+}/Eu^{3+}*$ plot indicates a strong depletion in Eu within the group, a characteristic indicative to highly evolved magmas, where early Ca-rich plagioclase has been removed from the system during crystal fractionation. $Eu^{3+}*$ was calculated utilizing the average of Sm and Gd values for both datasets.

The Sr vs. SiO_2 plot indicate a wide range of Sr abundance verses progressive evolution of the magma. Commonly two samples of the same type of

rhyolite will contain varying Sr concentrations. Anomalous strontium values and patterns were first noted by Price et al. (1990), who suggested that the Sr anomalies represent a population of weathered (high Sr-values) rhyolites, and unweathered (low Sr-values) rhyolites. The F vs. SiO_2 diagram has a slightly negative slope with little correlation of the rhyolite types to fluorine concentration relative to silica evolution. Transitioning from the gray to purple to red rhyolite sample groups, the difference in F content between the rhyolite pairs greatly diminishes. The fluorine concentrations for the gray rhyolite pair is 2,200 ppm and 9,000 ppm, for the purple 3,100 ppm and 5,500 ppm, and for the red sample trio the fluorine content ranges between 2,300 ppm to 2,400 ppm. The tan rhyolite sample pair has a fluorine content of 2,900 ppm and 3,900 ppm, the mottled sample pair 4,000 ppm and 4,800 ppm. The red rhyolite demonstrates the least variation in F content between samples, whereas the gray sample pair has the greatest. Being a composite of the different rhyolite types, it is unexpected that the mottled sample pair has a small range in F concentrations relative to the gray or purple rhyolite types.

Contrary to the variable F concentration of the rhyolite samples, the zirconium (Zr) content is fairly homogeneous across all rhyolite samples. The minor variation in Zr content between rhyolite sample pairs is greatest between the red rhyolites and the least between the gray. The red rhyolite Zr content ranges between 969 ppm to 1,083 ppm, the purple rhyolite sample pair has concentrations of 1,084 and 1,050 ppm, the gray 1,060 ppm and 1,046 ppm, the

mottled pair 1,041 ppm and 1,003 ppm, and the tan 999 ppm and 1,038 ppm. Only one sample of the rhyolite breccia was analyzed, but the Zr content of the breccia was considerably lower then the rhyolite samples at 166 ppm.

Elemental Correlation Comparisons

A correlation matrix and comparative charts were constructed to identify positive and negative relationships between 25 primary oxides and elements within the Round Top rhyolite samples (Table 3.4; Appendix B.7). The correlation table and charts were constructed using Microsoft Excel 14.3.9, syntax [CORREL(array1,array2)], based on the Pearson correlation coefficient and using the formula:

$$Correl(x,y) = \frac{\Sigma(x-\bar{x})(y-\bar{y})}{\sqrt{\Sigma(x-\bar{x})^2(y-\bar{y})^2}}$$

$where\ \bar{x}\ and\ \bar{y}\ are\ the\ sample\ means\ AVERAGE(array1)\ and\ AVERAGE(array2).$

Correlations that were ≥0.70 (+ or -) were categorized as strong, 0.50-0.69 (+ or -) as moderate, and those that were 0.49-30 (+ or -) as moderately weak. Those values ≤0.29 (+ or -) were considered weakly correlated. The categorical divides were based on observed trends and known associations between the elemental and oxide pairs including inferred reasonable geologic geochemical behaviors, and therefore represent approximations and not finite boundaries. The correlation matrix (Table 3.4) is color coded to aid in visual identification of

correlation trends, although these trends are probably best observed on an individual basis within the correlation charts (Appendix B.7)

Overall, the REEs+Y are negatively correlated to SiO_2 and a positively to F. The strength of the correlation varies from weak, moderately weak, and moderate in relation to SiO_2, and weak to no correlation for F. F is additionally moderately positively correlated with Sr and Th, and moderately negatively correlated with SiO_2. As expected, the HREEs in general demonstrate a stronger positive correlation to other HREEs versus LREEs, and the same is true in reverse with the LREEs. Fe_2O_3 and FeO demonstrate a range of weak to moderate positive correlations to the REE+Ys, as well as a positive weak correlation to F and a weak negative correlation to SiO_2. Zr is positively weakly correlated to both SiO_2 and F, although a little more strongly with F than with SiO_2. U is negatively weakly correlated to SiO_2 and moderately weakly to F, but is only just barely negatively correlated to SiO_2 versus near moderately negative with F. Additionally, U is strongly negatively correlated to Fe_2O_3 and moderately negatively correlated to FeO. Th is moderately positively correlated to F and moderately negatively correlated to SiO_2, Fe_2O_3, and FeO. Th is strongly positively correlated to a number of the REEs, Y, and Sr. Li is weakly positively correlated to SiO_2 and negatively to F. Relative to the other oxides and elements, Li is weakly correlated to all except Eu, which has a near moderate positive correlation and F which has a moderate negative correlation.

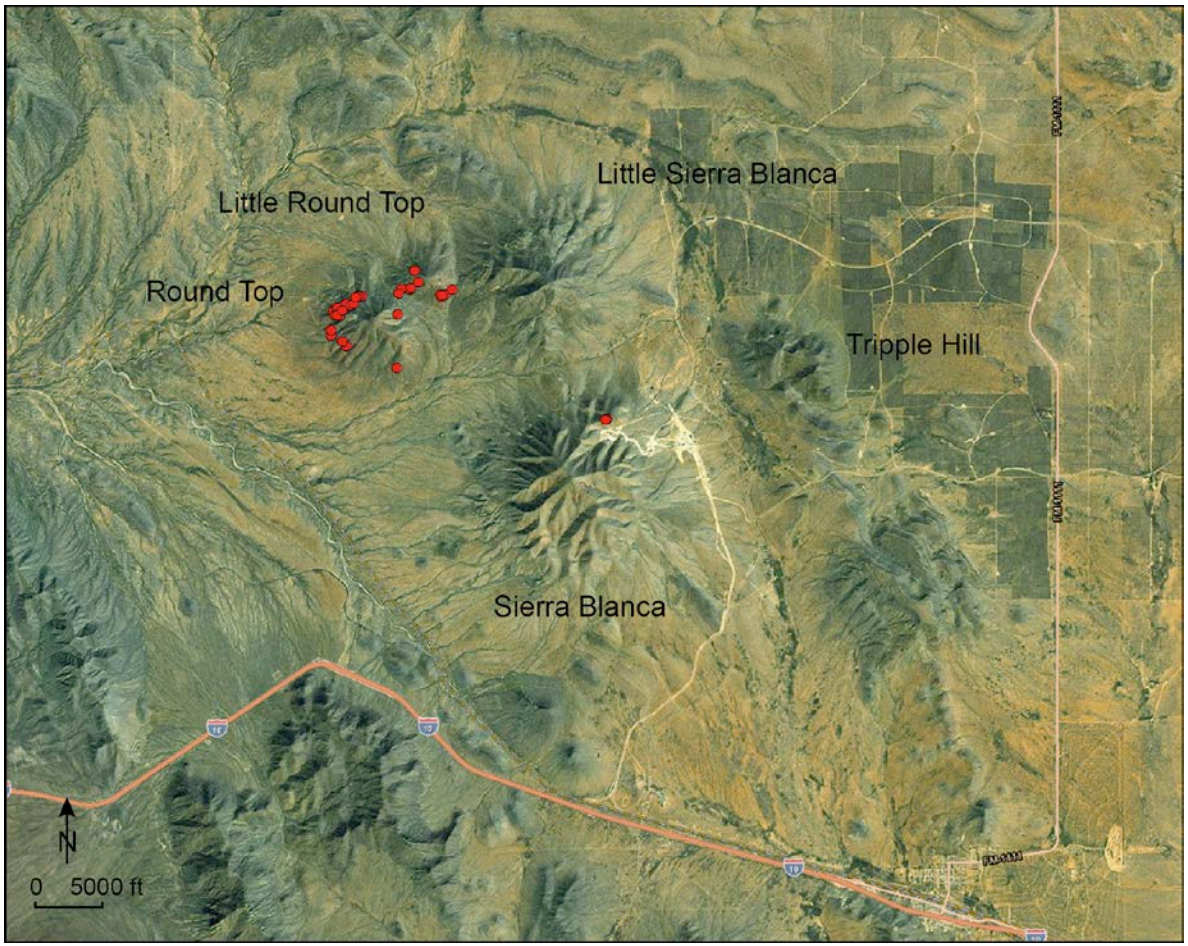

Figure 3.1: Aerial image of all sample locations. Samples were collected from Round Top, Little Round Top, and Sierra Blanca Peak (red markers). Aerial image modified after i-cubed 15 m eSAT imagery, ESRI AcrMAP 10.2 (2013).

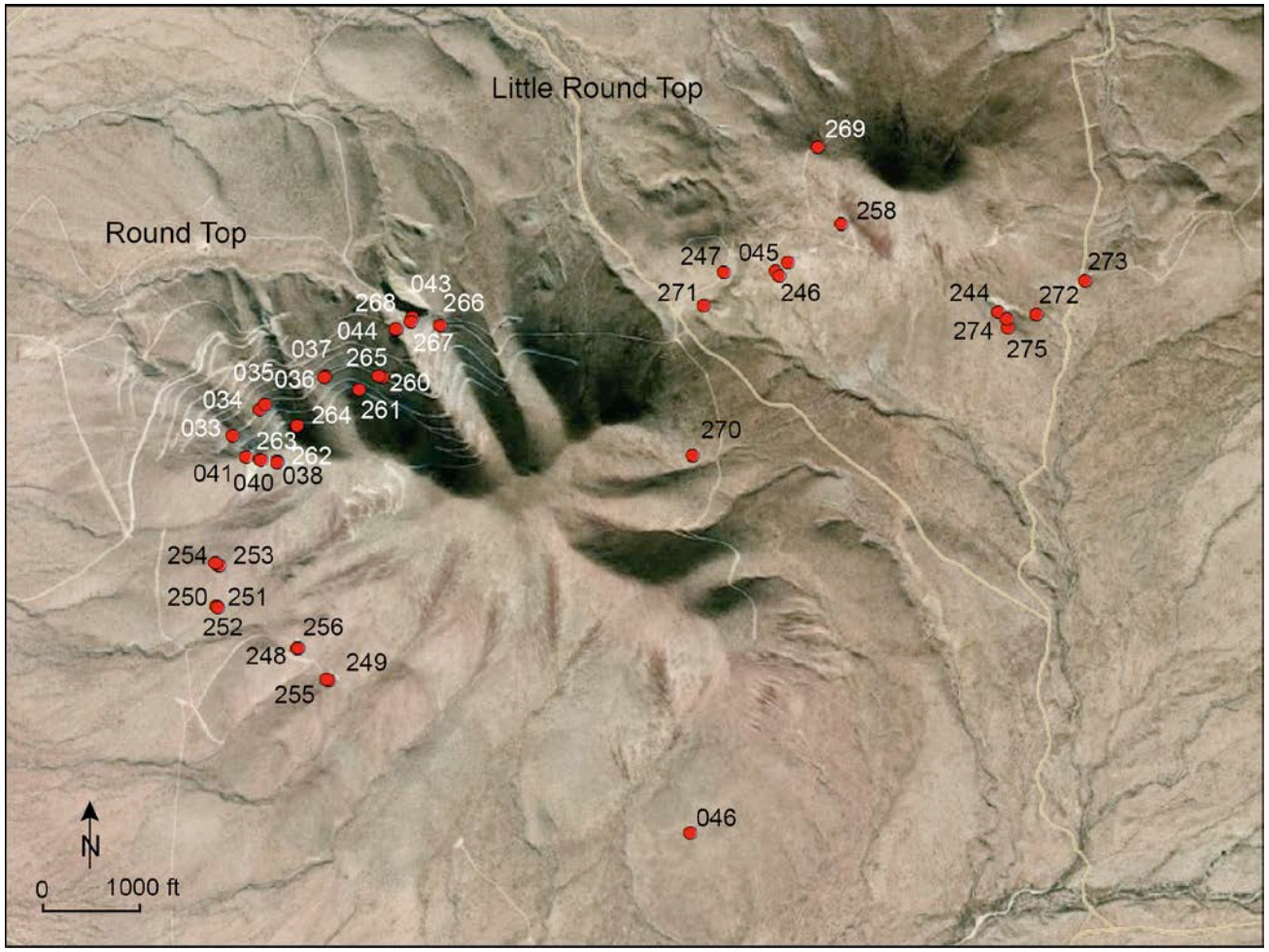

Figure 3.2: Aerial image of sample locations collected from Round Top and Little Round Top. Sample locations were primarily dictated by outcrop exposures produced from drill road construction (red markers). Aerial image modified after 0.3 m resolution imagery from Digital Globe, ESRI ArcMAP 10.2 (2013).

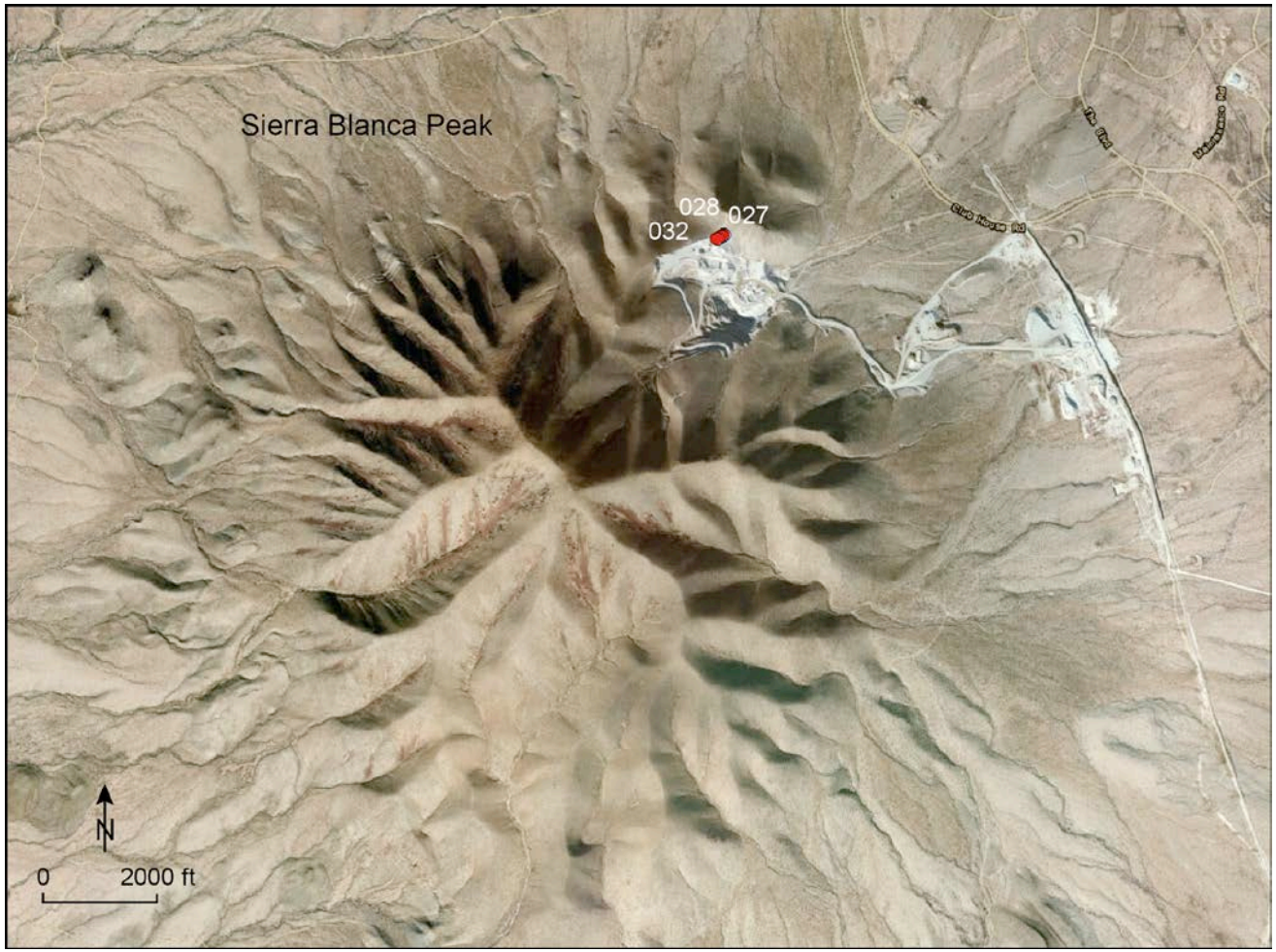

Figure 3.3: Aerial image of sample locations collected from the aggregate quarry at Sierra Blanca Peak. The quarry provided excellent exposure to the interior surface of the laccolith, sample locations indicated by red markers. Aerial image modified after 0.3 m resolution imagery from Digital Globe, ESRI ArcMAP 10.2 (2013).

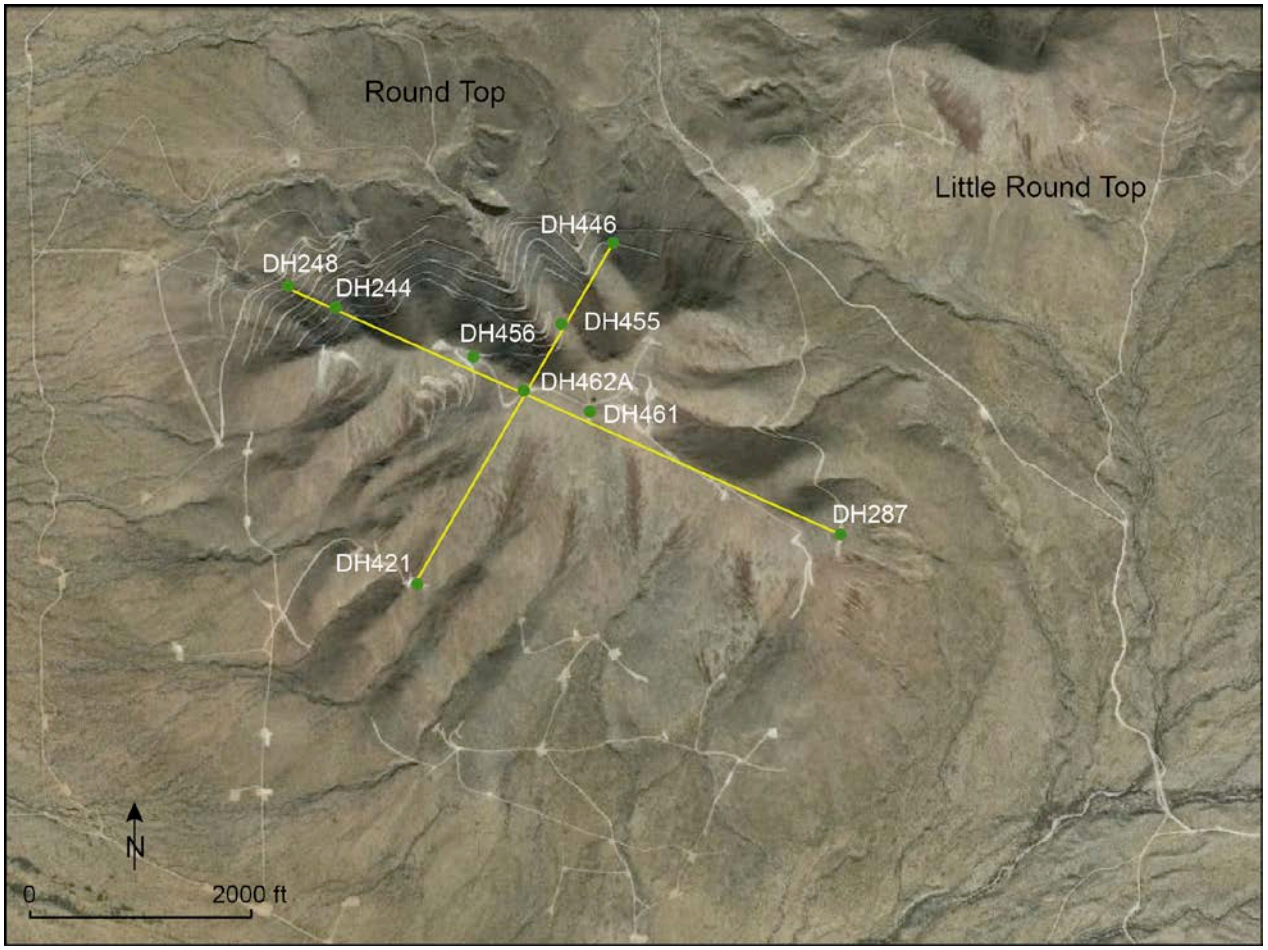

Figure 3.4: Aerial image of reverse circulation drill hole locations and cross section transects. Chip samples (green markers) were taken from each and utilized to construct the NE-SE and NW-SE cross-sections (yellow lines) through the laccolith. Image modified after Google 2012.

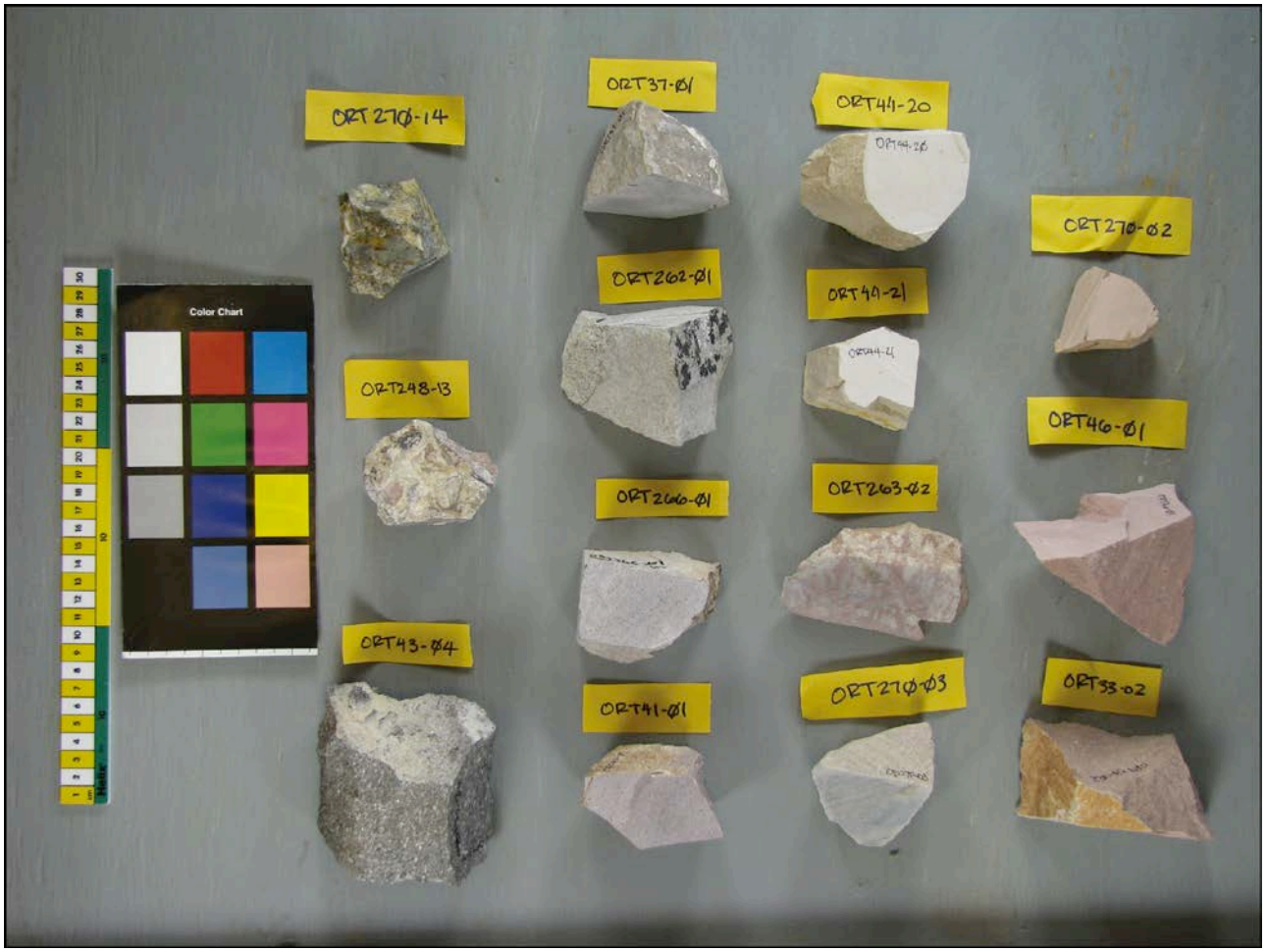

Figure 3.5: Photo of the fourteen samples submitted for geochemical analyses to ACME Analytical Laboratories Ltd. The samples include two gray rhyolites, two purple rhyolites, three red rhyolites, two tan rhyolites, two mottled rhyolites, one rhyolite breccia, one fluoritized limestone, and one diorite sill.

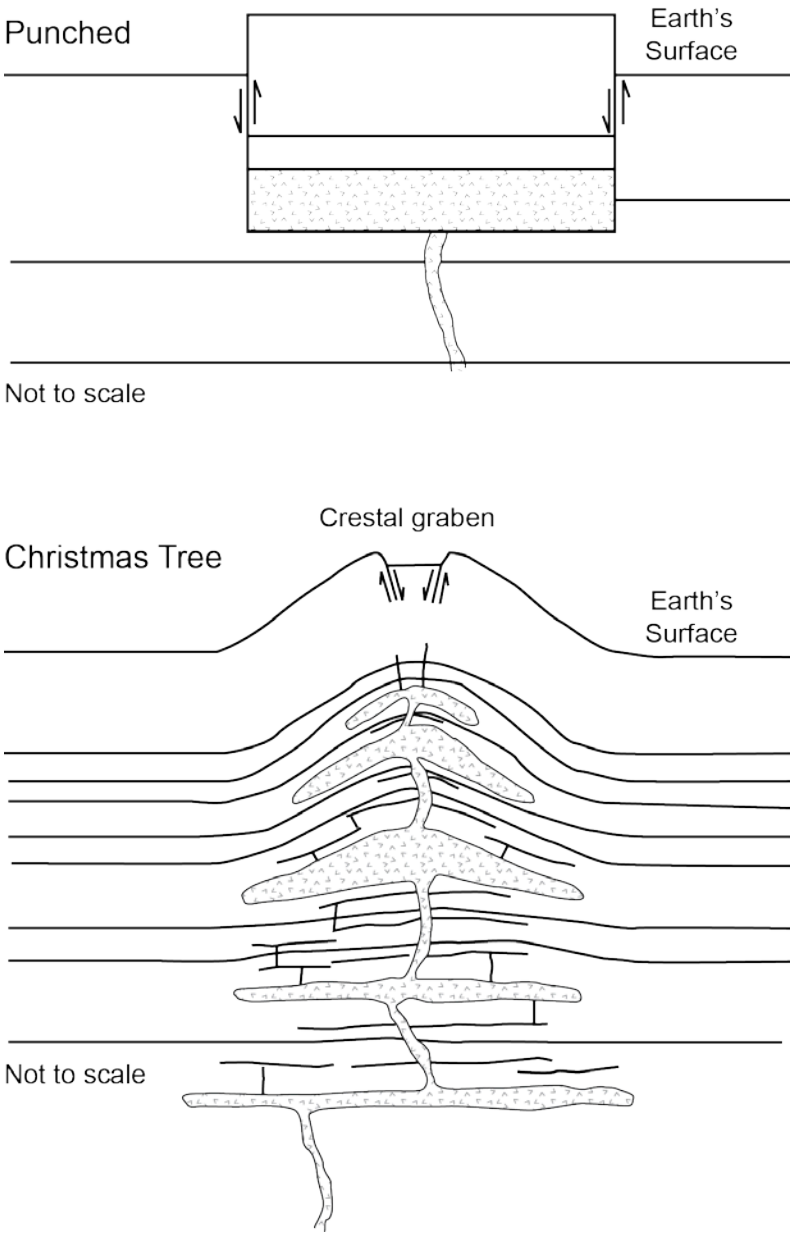

Figure 3.6: Corry (1988) models for Punched type laccolith formation (top) and Christmas-tree type laccolith formation (bottom). The Sierra Blanca group most closely resembles that of the Christmas-tree type model, where igneous material is injected into shallow sediments forming domed structures, which are then later exposed to the surface through erosion.

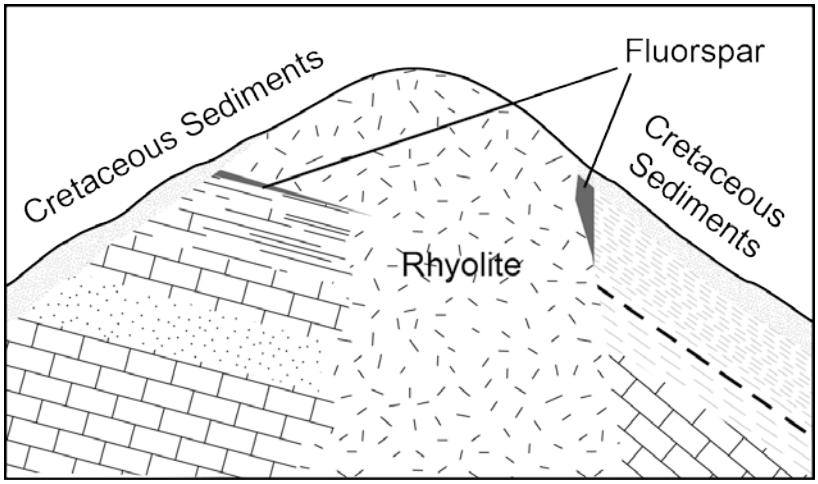

Figure 3.7A: McAnulty (1980) model of the morphology of the Round Top laccolith. Model includes a large feeder system capped by a rhyolite dome. Fluorspar deposits occur along the contact zones with the surrounding Cretaceous sediments. Diagram modified from McAnulty (1980).

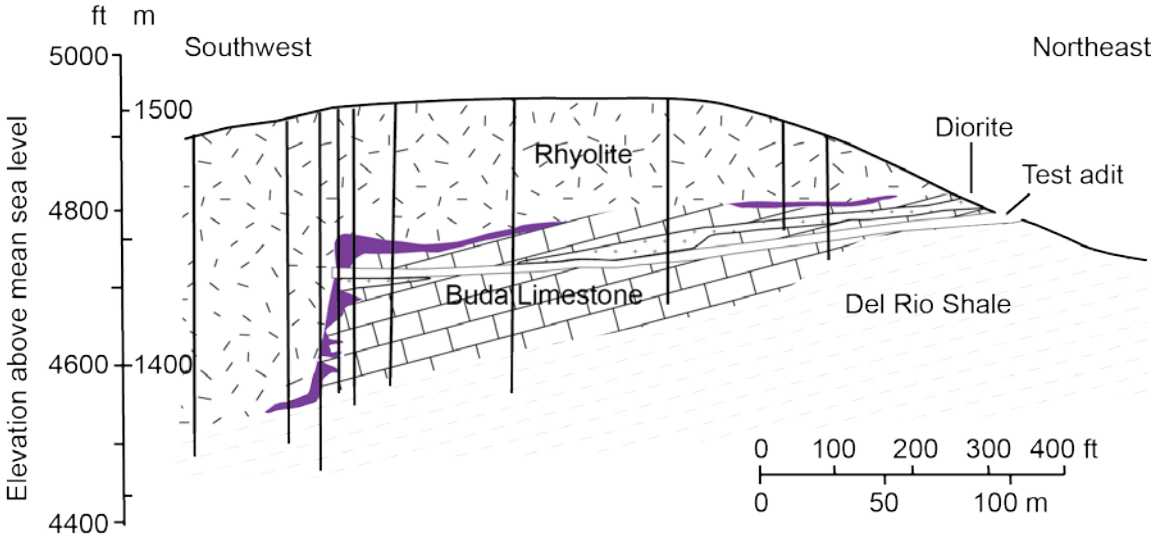

Figure 3.7B: Rubin et al. (1990) model for the morphology of the Round Top laccolith based on information collected from limited drilling and the test adit. The rhyolite forms a cap to the dipping Cretaceous sediments, which abruptly increases to the southwest. Fluorspar deposits occur along the contact between rhyolite and sediments. Diagram modified from Rubin et al. (1990).

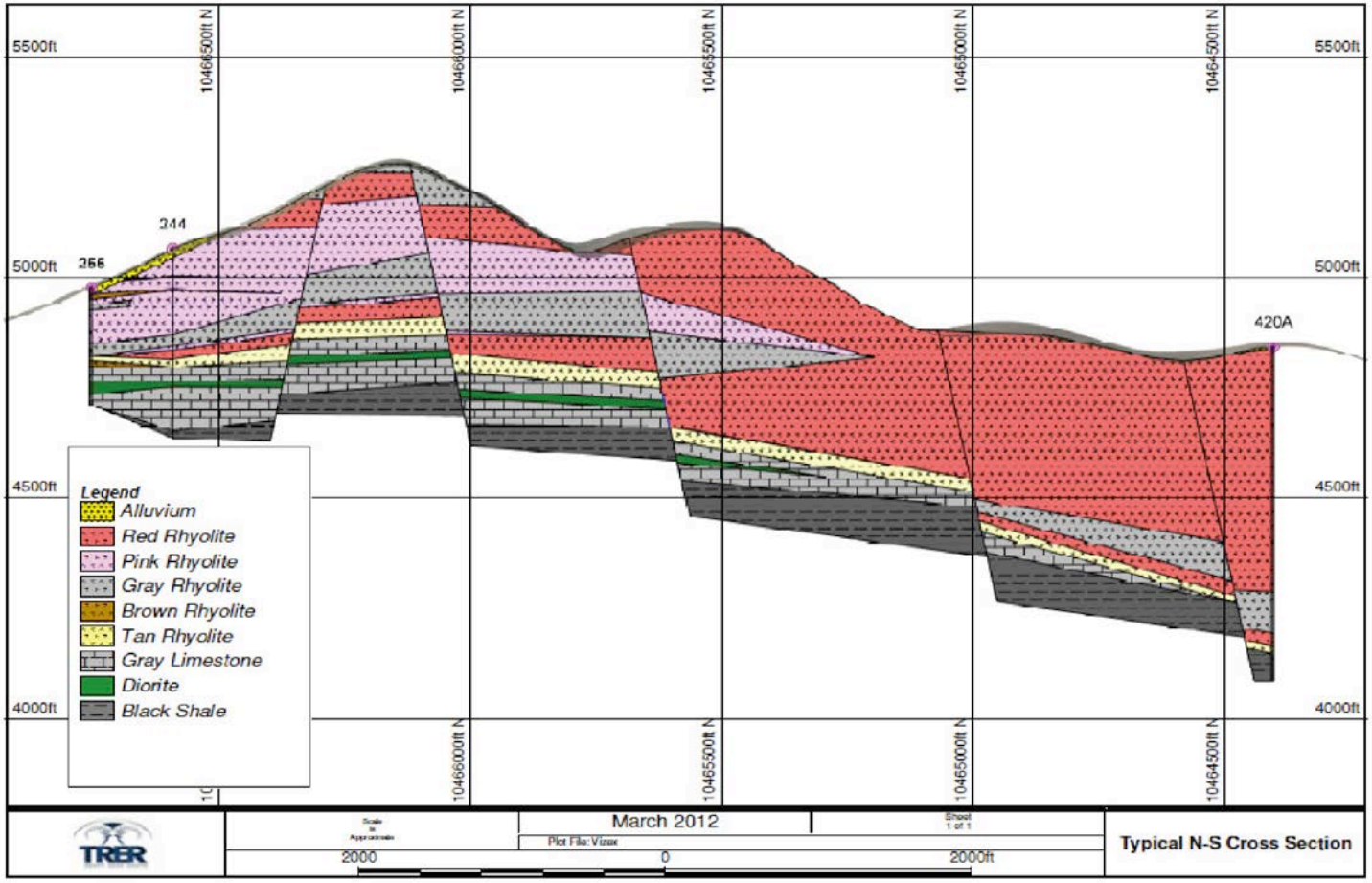

Figure 3.7C: TRER layered rhyolite model of the Round Top laccolith, 2012. Laccolith model from an online description provided by the company (www.TRER.com). The Round Top rhyolites form layered sequences, which are continuous across the length on the laccolith. Normal faulting has down dropped large blocks of the laccolith.

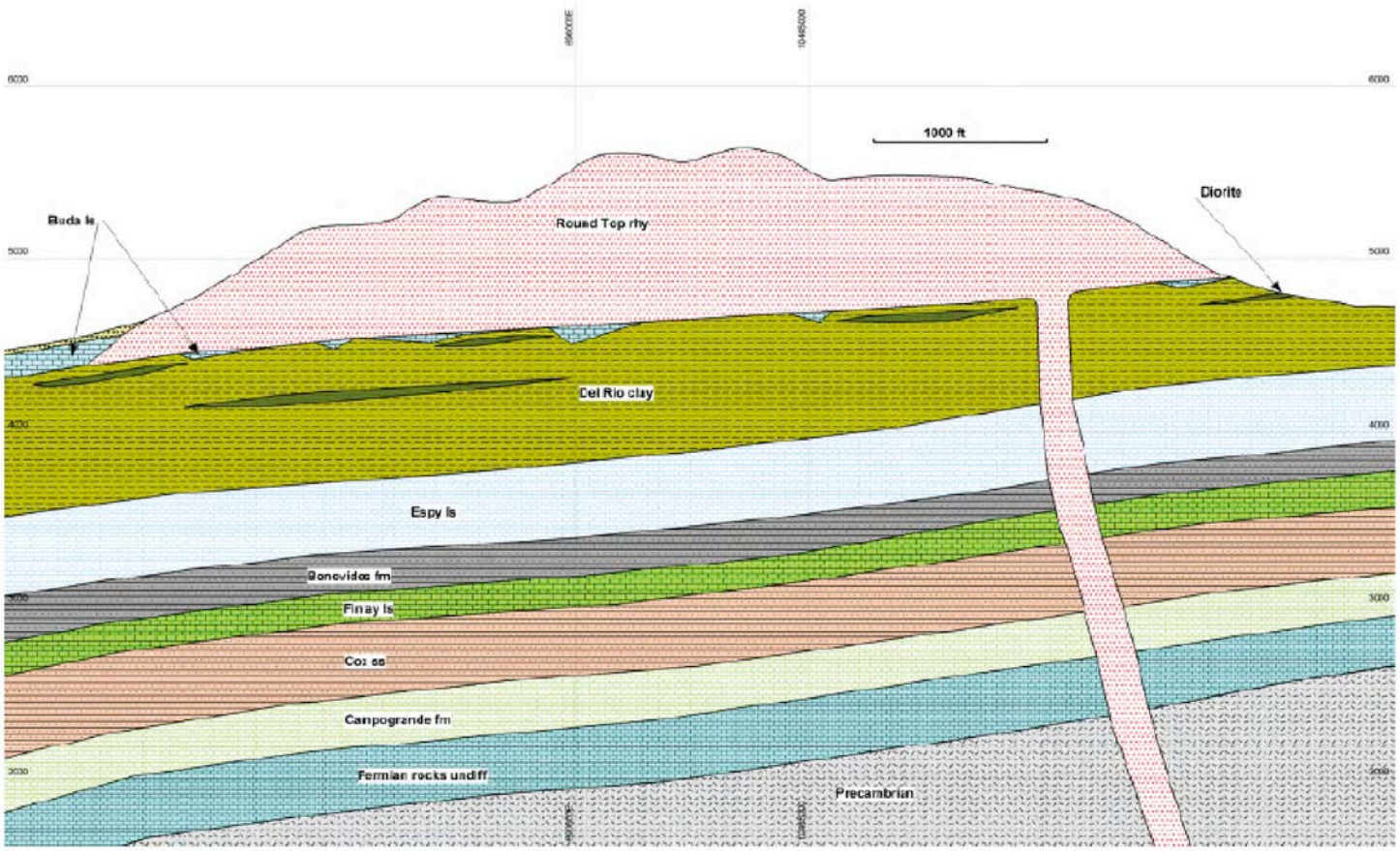

Figure 7-1 NW-SE Section Looking NE Through Round Top Mountain Showing the Underlying Sedimentary Rocks
(Source TRER)

Figure 3.7D: TRER single rhyolite model of the Round Top laccolith, 2013. The laccolith is represented as one homogenous rhyolite with a small single feeder system to the NW. Image from TRER NI 43-101 Preliminary Economic Assessment (Hulse et al., 2013).

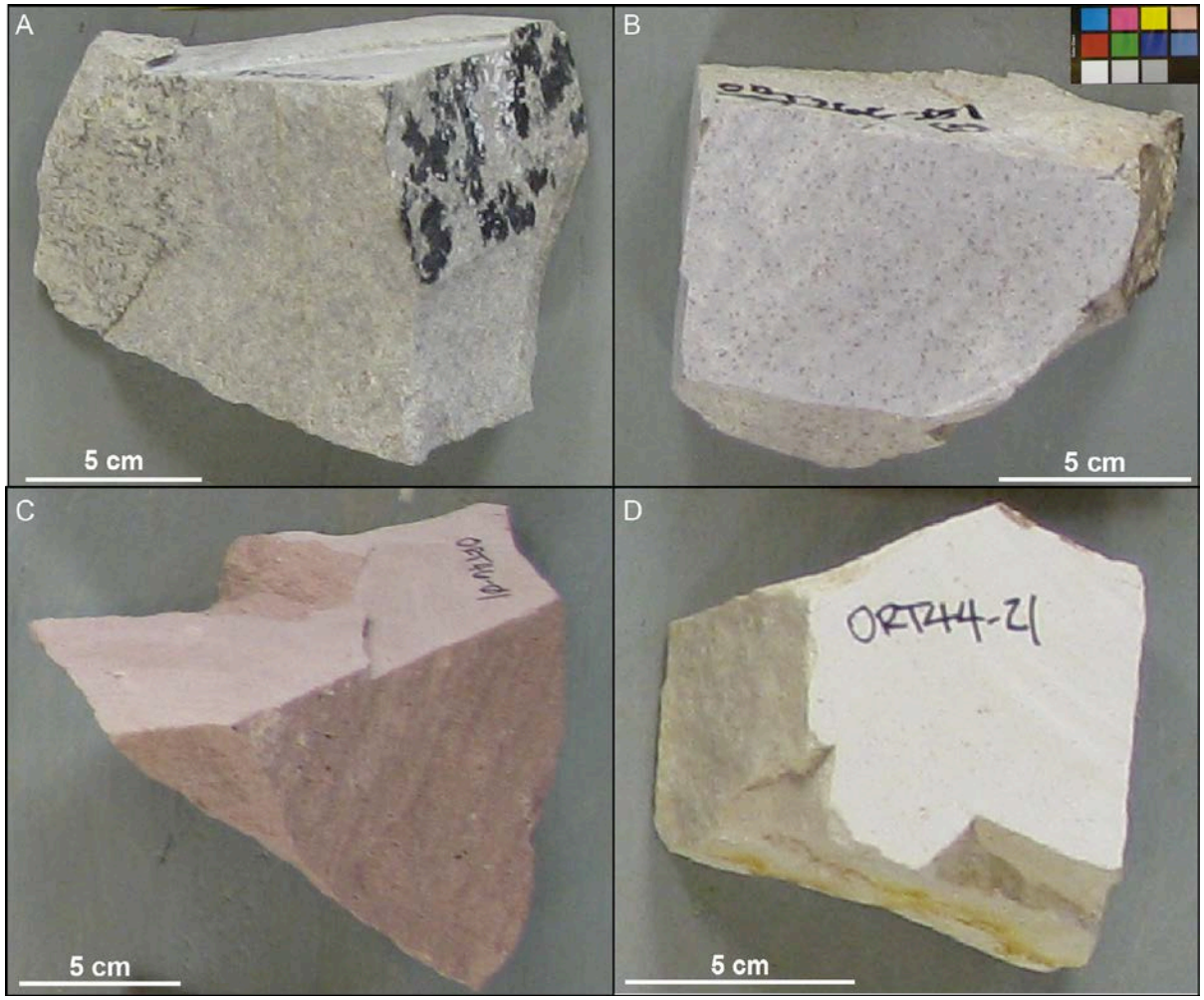

Figure 3.8: Photo of the four rhyolite types in hand sample. Figure 3.8 full caption, next page.

Figure 3.8 continued: A) The gray rhyolite is aphanitic and may range from a light gray (seen here) to a dark gray color. Many samples are covered in manganese oxide dendrites (top right). B) Photo of the purple rhyolite in hand sample. The purple rhyolite varies from light to medium in color and is typically micro-porphyritic, with fine red hematitic “splotches” visible throughout. C) Photo of the red rhyolite in hand sample. The red rhyolite is aphanitic and varies from an orangish-red to a deep red in color. Few samples have visible hematitic splotches, not pictured here. D) Photo of the tan rhyolite in hand sample. The tan rhyolite is aphanitic and is of a tan to light brown color. The tan rhyolite is typically less cohesive then the other types of rhyolites with a distinct chalky nature. Samples ORT262-01, ORT266-01, ORT46-01, and ORT44-21

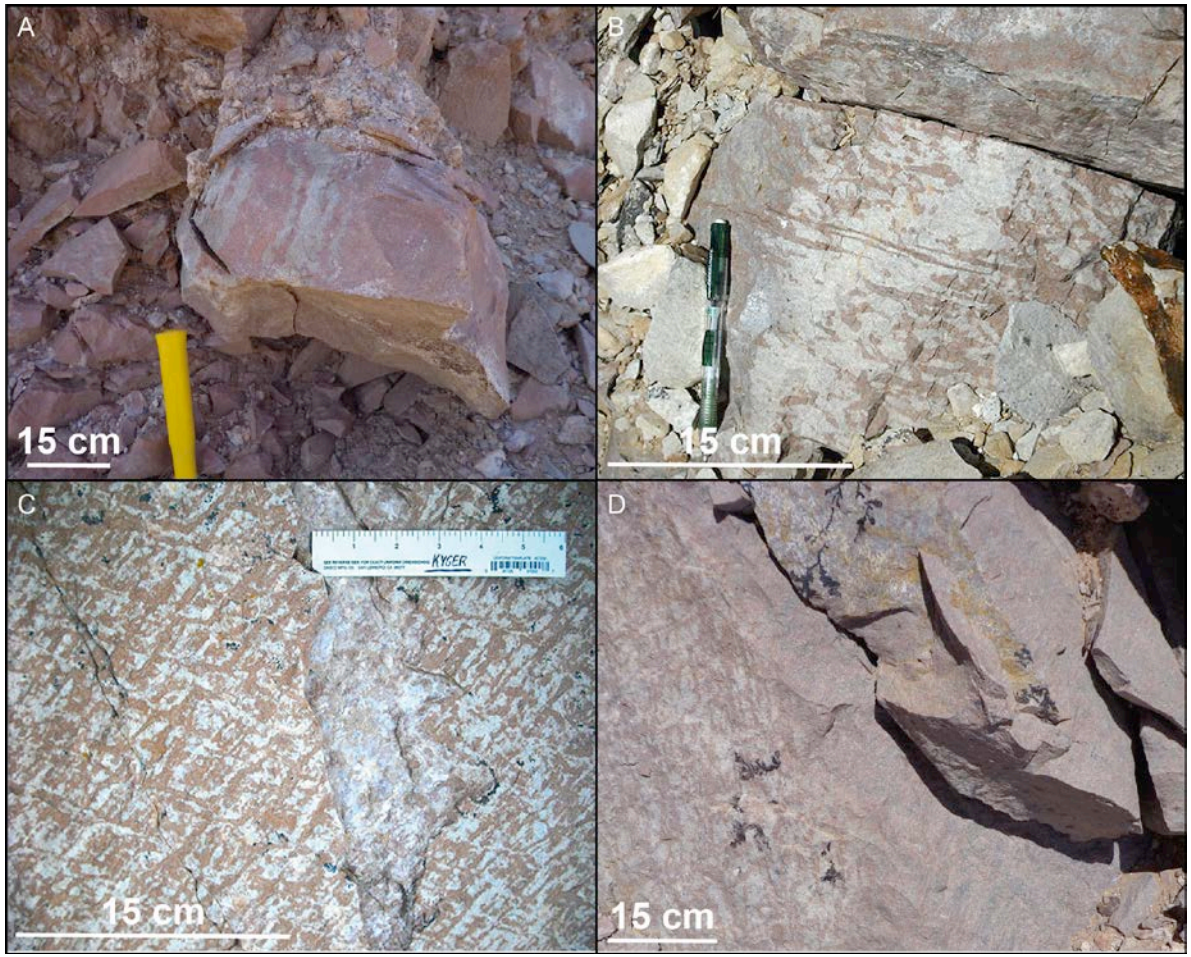

Figure 3.9: Photos of mottled rhyolite textures in outcrop. A) Striped mottled dark gray and red rhyolite in outcrop. Note the undulatory boundaries between the rhyolite types. B) A mixture of striped and amoeboid-like red and light gray rhyolites. C) Distinct crosshatch type texture with red and gray to tan rhyolite types. D) Red and tan crosshatched mottled texture transitioning into dark purplish-gray and red striped mottling.

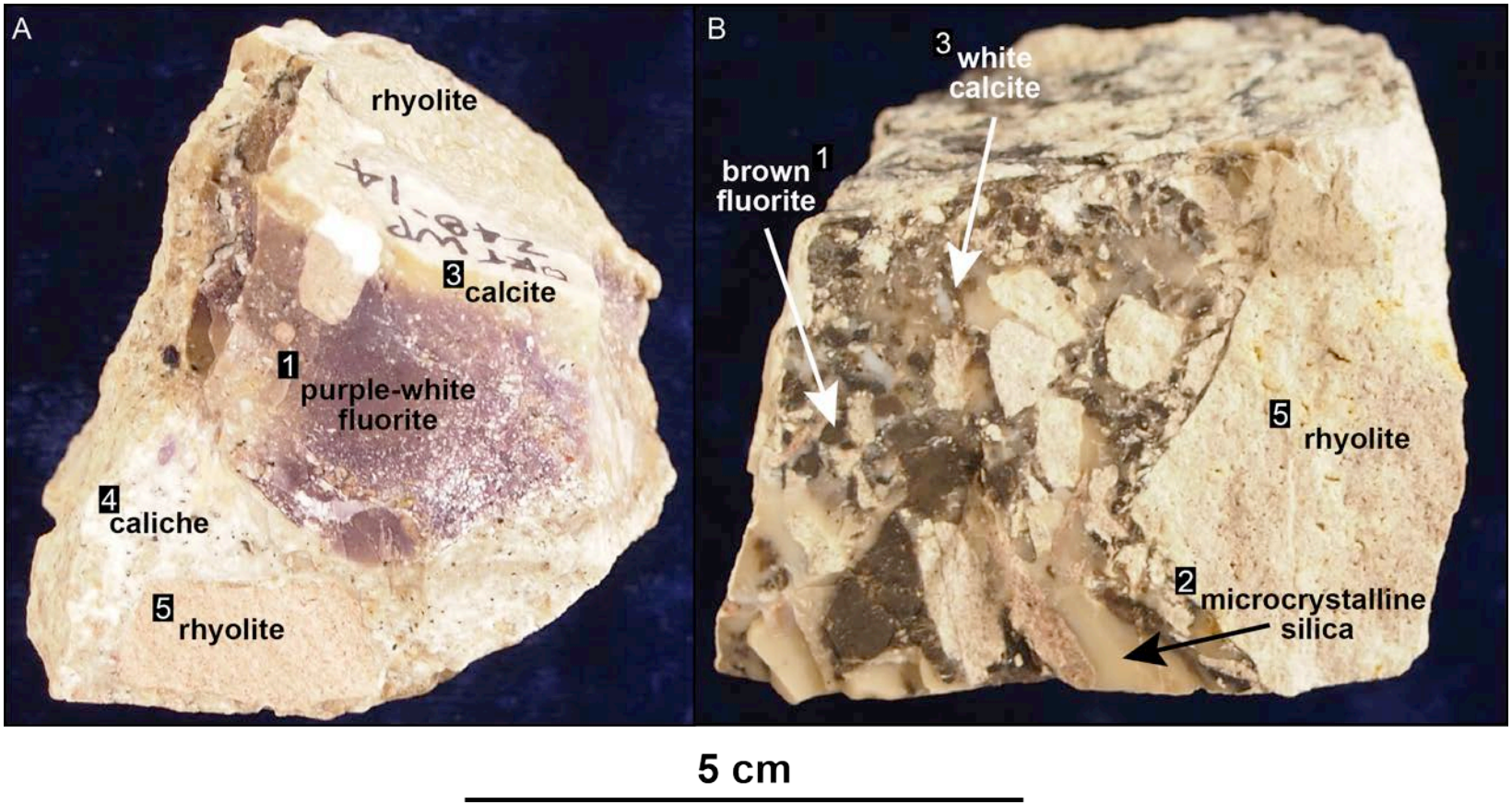

Figure 3.10: Photos of matrix supported rhyolite breccia in hand sample. The breccias are commonly cemented with multiple generations of fluorite (1), microcrystalline silica (2), calcite (3), and caliche (4). The fluorite occurs in a multitude of colors including purple, green, white, and brown. The silica has been observed as pale tan, white, brown, and an orange-brown color. The calcite is typically a pale yellow to white in color. The rhyolite clasts (5) are typically angular to subangular and range from tan, red, purple, and gray. Samples ORT248-01 and ORT256-01

Round Top Rhyolite Mineralogy & Modal Abundance

	Mineral	Modal Abundance	Mineral Formulae
Major Phases 90-95%	Potassium Feldspar	48-52%	$KAlSi_3O_8$
	Quartz	28-30%	SiO_2
	Plagioclase	8-14%	$NaAlSi_3O_8$
Accessory Phases 6-8%	Annite Biotite	4-5%	$KFe3^{2+}AlSi_3O10(OH,F)_2$ aka Trioctahedral Li-rich mica with variable Fe
	Zircon	1%	$Zr(Hf,U,Th)SiO_4$
	Magnetite-Hematite	1-2%	Fe_3O_4 to Fe_2O_3
Trace Phases 1%	Barite		$BaSO_4$
	Cassiterite		SnO_2
	Cerianite-(Ce)		$(Ce_{4+},Th)O_2$
	Changbaiite		$PbNb_2O_6$
	Columbite		$FeNbO_2$
	Cryolite		Na_3AlF_6
	Rutile Nb-rich		TiO_2
	Tantalite		$(Fe,Mn)(Ta,Nb)_2O_6$
	Thorite		$ThSiO_4$
	(W)-unknown		Nb-REE Fluoride
	(X)-unknown		Ca-Th-Pb-REE Fluoride
	Yttrocerite		$(Y,REE,LREE,Ca)F_{3-x}$
	Yttrofluorite		$(Y,HREE,Ca)F_{3-x}$

Table 3.1: Table of Round Top rhyolite confirmed mineralogy with formulae and modal abundance.

List of Minerals and Formulae Described by Other Authors*

	Mineral	Mineral Formulae
Potential Minerals	Aeschynite	$(Ce,Ca,Fe)(Ti,Nb)_2(O,OH)_6$
Minerals Identified By Other Studies*	Ancylite-(Ce)	$Sr(La,Ce)(CO_3)(OH)\bullet H_2O$
	Bastnäsite	$(Y,Ce,La,REE)CO_3F$
	Betafite	$(Ca,Na,U)_2(Nb,Ti,Ta)_2O_6(O,OH,F)$
	Cerfluorite	$(Ce,LREE,Ca)F_{3-x}$
	Cerussite	$PbCO_3$
	Coffinite	$U(SiO4)_{1-x}(OH)_{4-x}$
	Elpasolite	K_2NaAlF_6
	Fluellite	$AlF_3\bullet 4H_2O$
	Kaolinite	$Al_2Si_2O_5(OH)_4$
	Kasolite	$Pb(UO_2)\bullet H_2O$
	Thomsenolite	$NaCaAlF_6\bullet H_2O$
	Uraninite	UO_2
	Xenotime	$(Y,REE)(PO_4)$
	Zunyite	$Al_{13}Si5O_{20}(OH)_{18}Cl$
	(Y)-unknown	Ca-Th Phosphate-silicate
	(Z)-unknown	Pb-rich Mn-oxide

*Compiled from Shannon and Goodell (1986), Rubin et al. (1987), Price et al. (1990), Bloch (2010), & Hulse et al. (2012).

Table 3.2: Table of minerals with formulae identified by others. All but aeschynite are minerals identified by other authors to be present at Round Top but were not observed within the scope of this study.

Mineral	Ore Symbol
Annite biotite	ann
Barite	ba
Cassiterite	ct
Cerianite-(Ce)	crn
Changbaiite	cgb
Columbite	cmb
Cryolite	crl
Fluorite	fl
Hematitie	hem
Potassium feldspar	kfs
Magnetitie	mt
Plagioclase	pl
Quartz	qz
Rutile	rt
Tantalite	tan
Thorite	thr
Yttrocerite	ytc
Yttrofluorite	ytf
Zircon	zrn
(W)-unkown	W-unk
(X)-unknown	X-unk

Table 3.3: Table of mineral labels used for identification in petrographic and microbeam images.

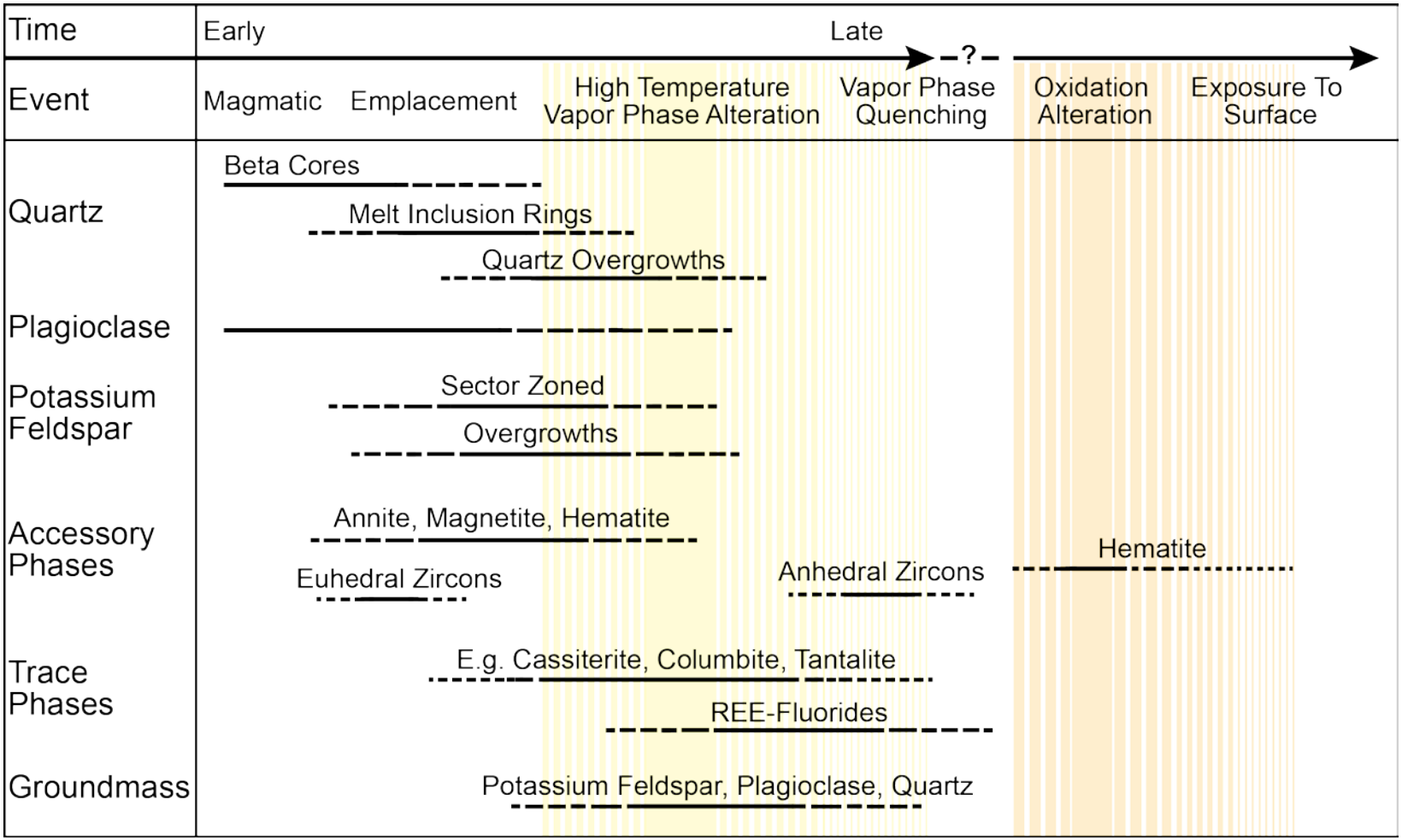

Figure 3.11: Petrogenetic sequence of the crystallization and alteration of the Round Top laccolith. Figure 3.11 full caption, next page.

Figure 3.11 continued: Crystallization of the laccolith included an early, middle, and late stage followed by high temperature vapor phase alteration (yellow) and later oxidation (orange). Early in the sequence the quartz beta cores, plagioclase laths, and euhedral accessory phases began to crystallize at depth. Emplacement of the laccolith produced disequilibrium conditions that initiated the crystallization of the sector-zoned potassium feldspars, the potassium feldspar mantles, and accessory phases, in addition to producing the concentric ring of melt inclusions within the quartz phenocrysts. With continued crystallization the late-stage quartz overgrowths, trace phases, and groundmass formed. During the finial portion of crystallization and most likely for some duration afterward, the high temperature vapor phase produced dissolution of the feldspar mineralogy and caused embayment to the outer edges of the quartz. Upon quenching, the volatile-rich vapor phase crystallized within the pore spaces of the potassium feldspar phenocrysts and groundmass, and intestinally within fractures and voids to form the REE-fluorides, trace phases, and anhedral zircons. Partial oxidation of the laccolith at a later unknown time altered a portion of the magnetite to hematite, producing the spectrum of rhyolite colors and the turbidity observed in thin section.

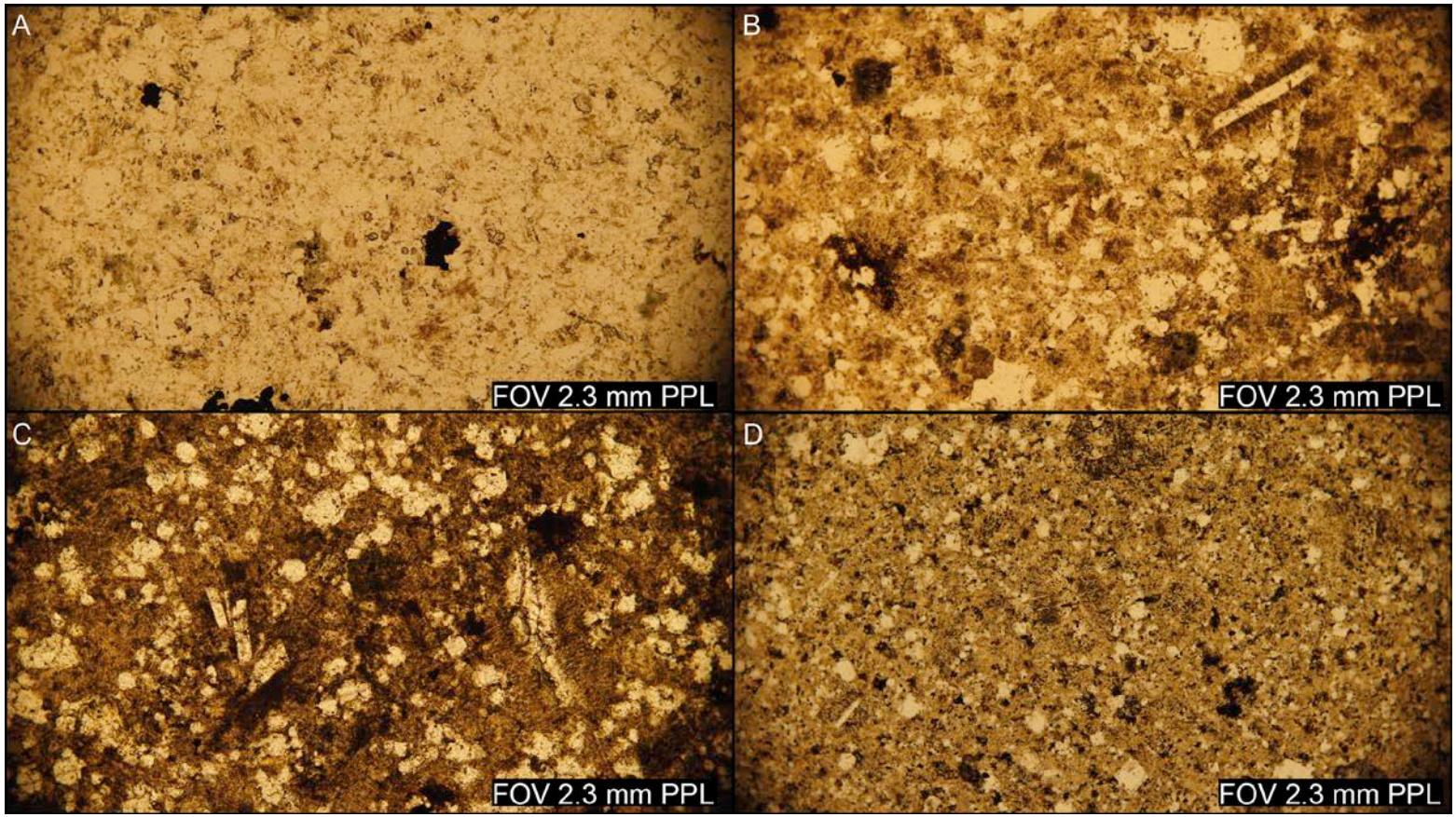

Figure 3.12: Photomicrographs of the four rhyolite types, gray, purple, red, and tan, at a common magnification in PPL. Note the increasing turbid texture when progressing from the gray rhyolite (A), to the purple rhyolite (B), to the red rhyolite (C), and decreasing slightly with the tan rhyolite (D). The turbid texture is produced from an increasing amount of iron oxide within the pore-space of the potassium feldspar portion of the groundmass. The tan (D) rhyolite most closely resembles the gray rhyolite relative to turbidity. Samples DH421, ORT255-07, and ORT44-22

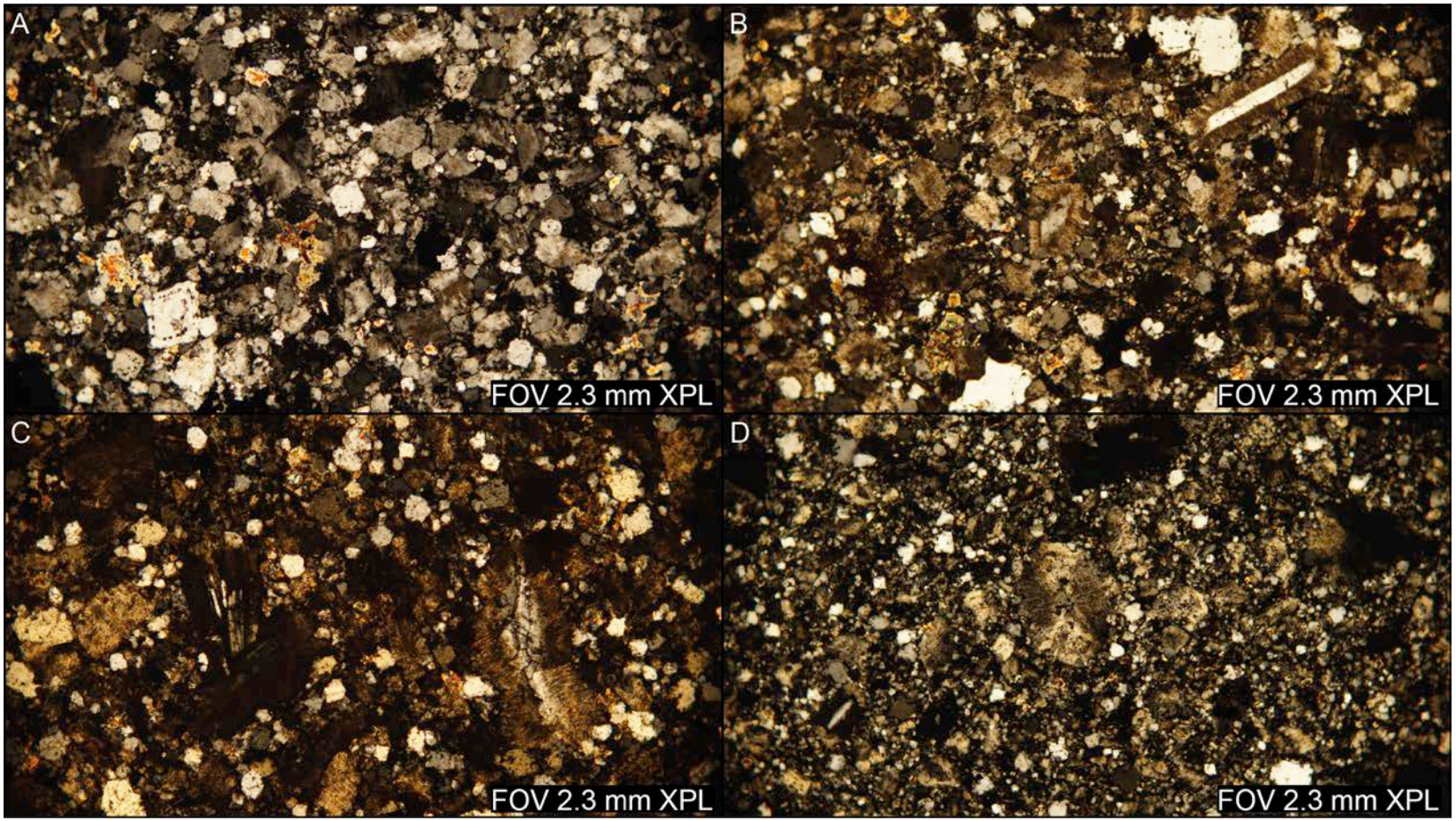

Figure 3.13: Photomicrographs of the four rhyolite types, gray, purple, red, and tan, at a common magnification in XPL. Note the increasing overall red-tint of the thin sections when progressing from gray (A) to the red (C) rhyolite. This turbidity is caused by an increasing amount of iron oxide within the pore space of the potassium feldspar groundmass. The tan rhyolite (D) is less turbid than the red rhyolite and most closely resembles the gray rhyolite in turbidity. Samples DH421, ORT255-07, and ORT44-22

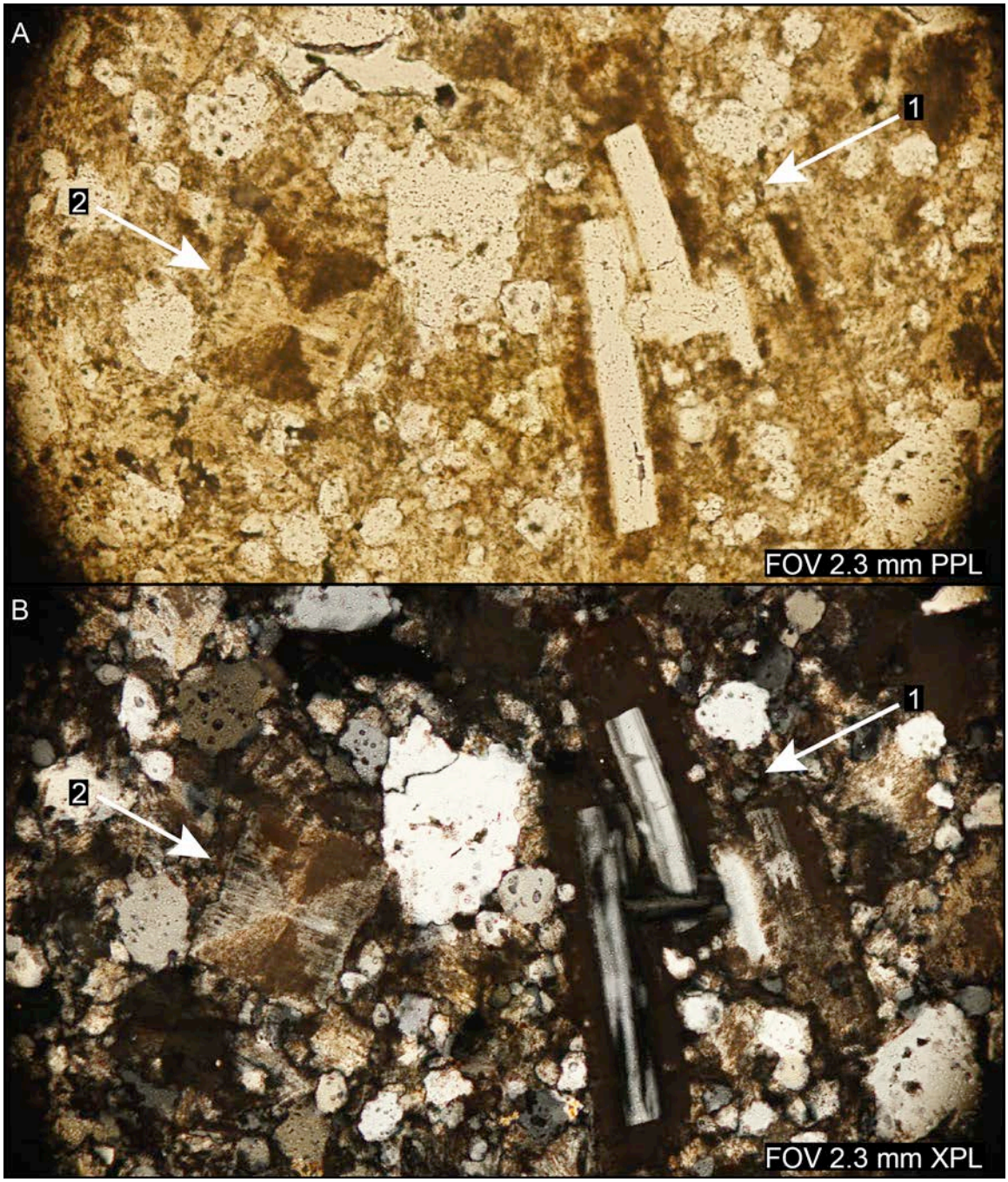

Figure 3.14: Photomicrographs examples of typical potassium feldspar phenocrysts in PPL and XPL. Potassium feldspar occurs in two forms, 1) as an overgrowth to a more sodic feldspar cores (1), and 2) as an hourglass type phenocryst (2). Sample ORT255-15

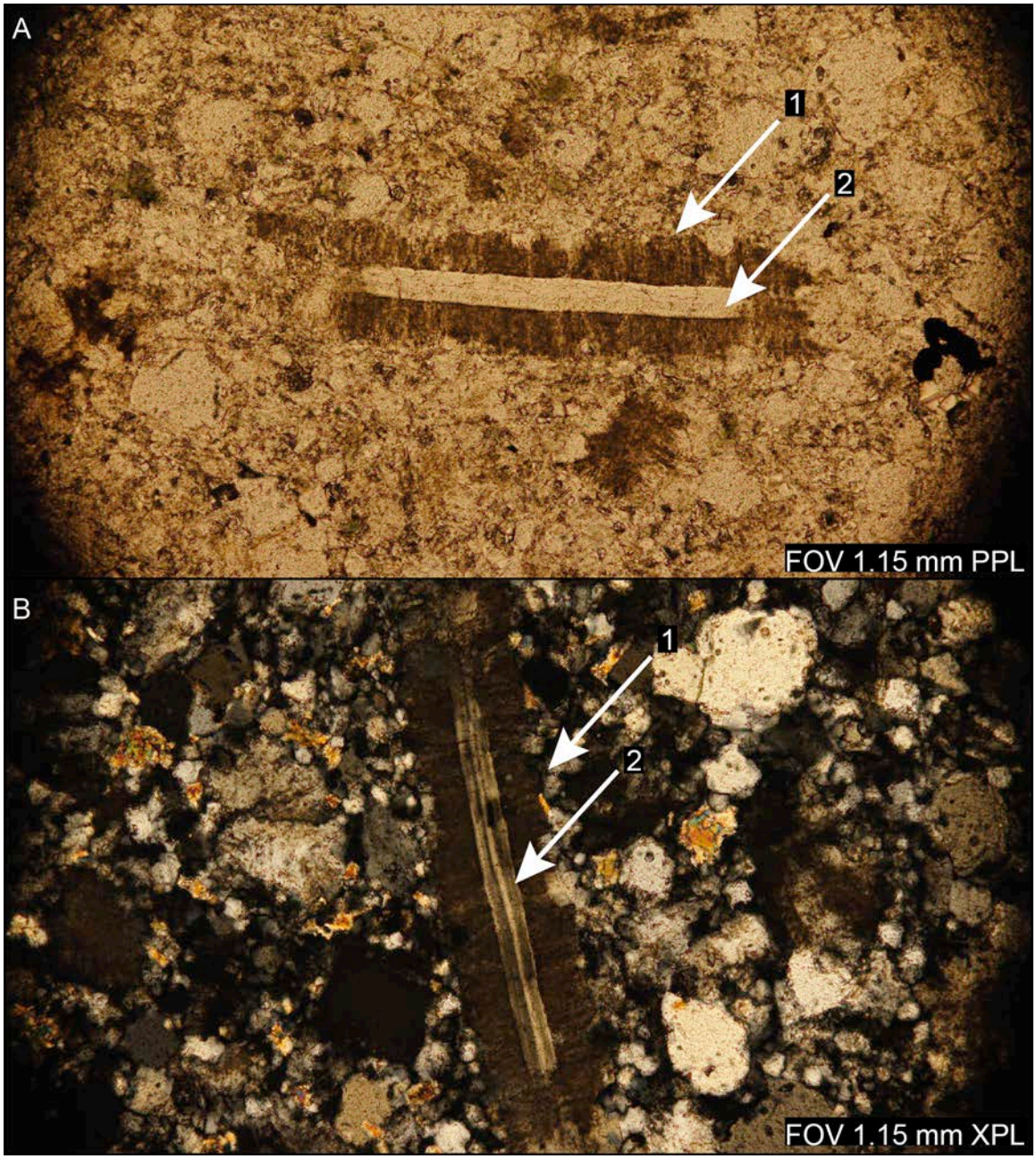

Figure 3.15: Photomicrographs of typical potassium feldspar as an overgrowth to a plagioclase feldspar core in PPL and XPL. Note the ragged nature of the exterior edges of the potassium feldspar overgrowth (1) possibly indicating later corrosion due to disequilibrium. Additionally, the transition from the plagioclase core to the potassic overgrowth is abrupt and relatively smooth with no disequilibrium textures (2). In XPL, the Carlsbad twinning of the plagioclase is apparent (B-2). Sample ORT262-02

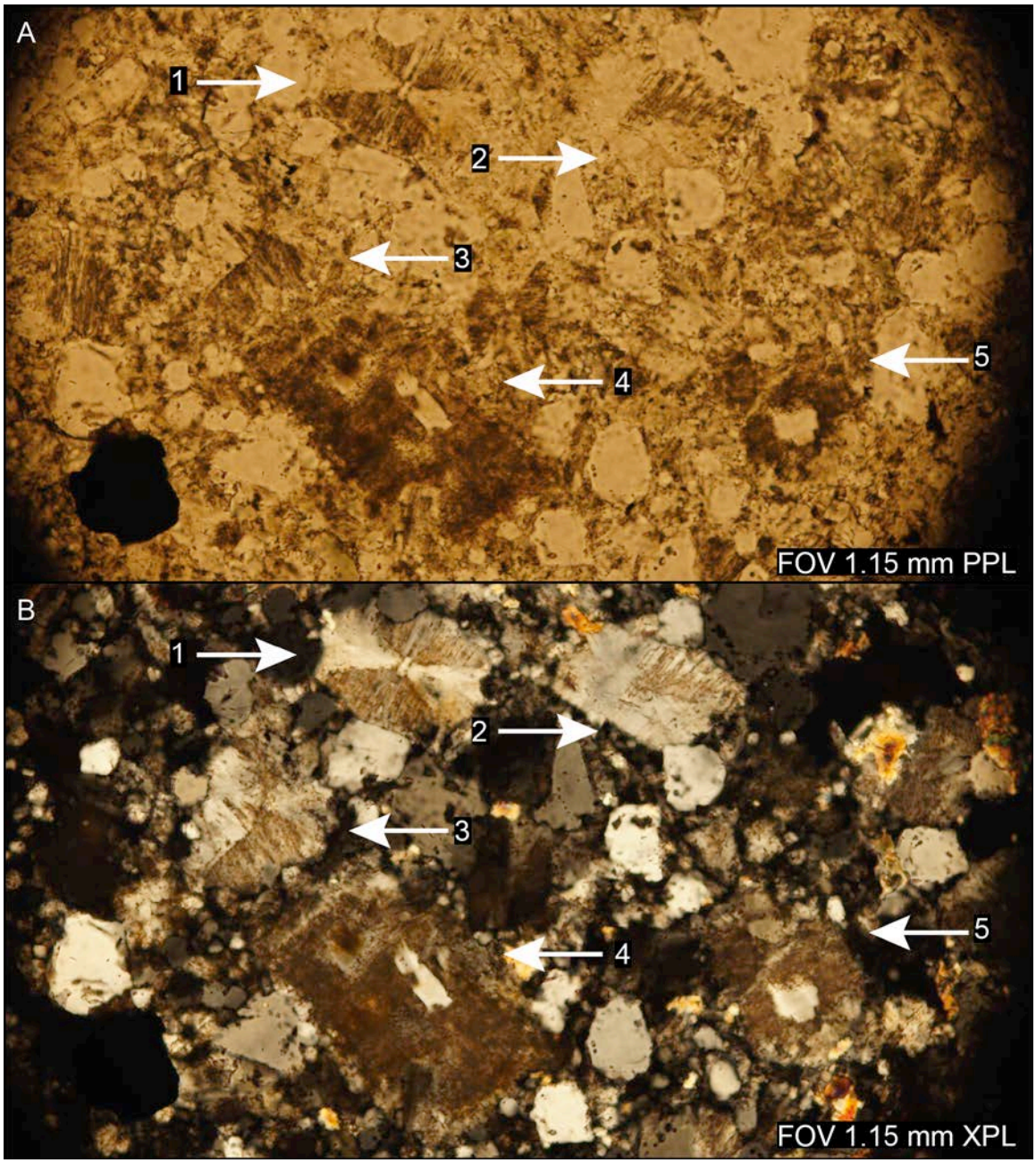

Figure 3.16: Photomicrographs of five examples of euhedral to anhedral hourglass type potassium feldspars in PPL and XPL. The hourglass structures of the feldspars may range from well formed (1), too poorly formed (2-5). The turbid texture within a portion of the hourglass results from abundant iron oxide. It is unclear why typically only part of the hourglass is turbid, but it may relate to slight compositional heterogeneities between hourglasses. Sample DH462-A

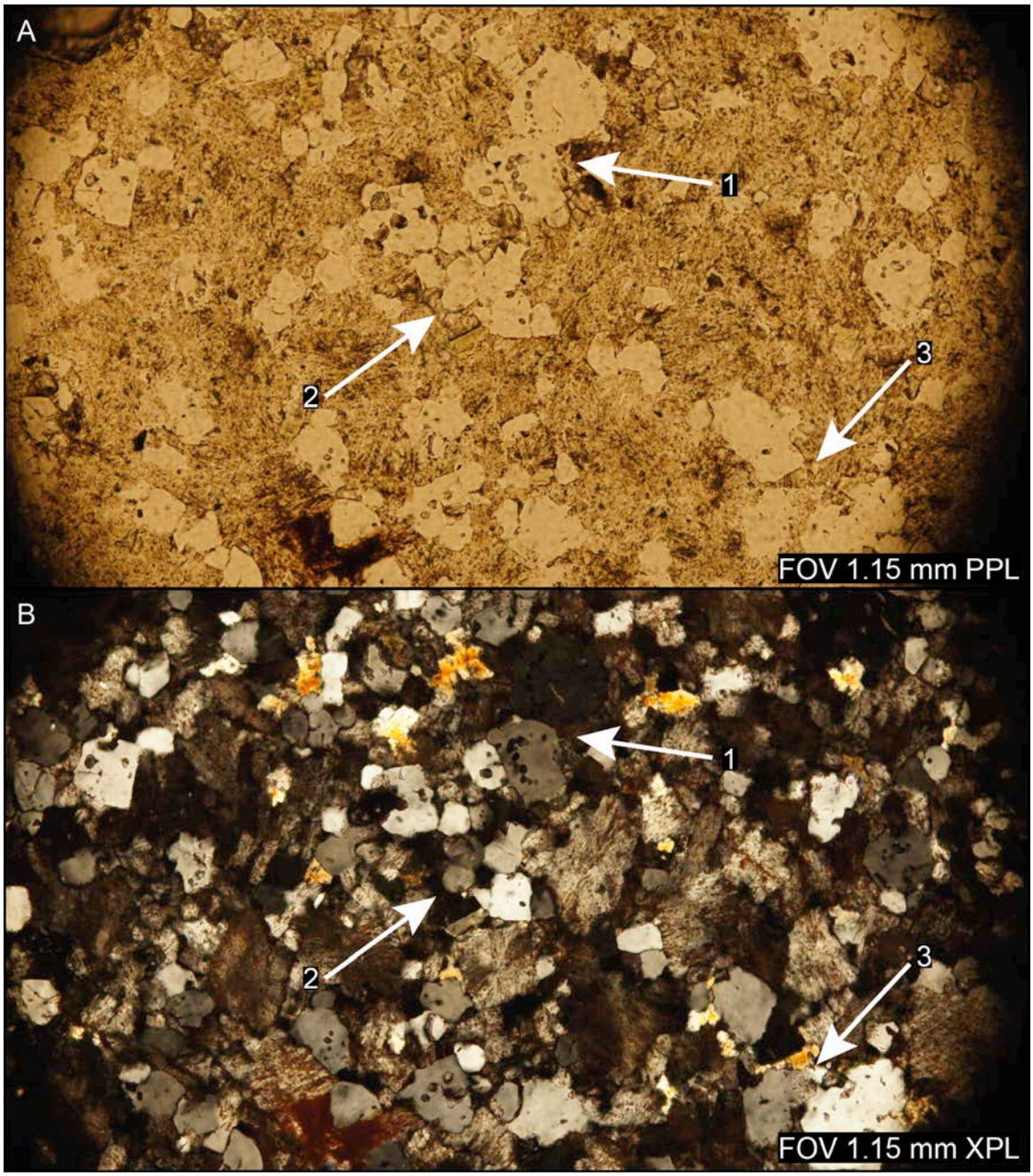

Figure 3.17: Photomicrographs of typical quartz phenocrysts and groundmass in PPL and XPL. Quartz phenocrysts commonly are subhedral to anhedral, occur in clusters or as twins (1) and display a range of melt inclusion rings (1). Quartz within the groundmass is typically subhedral to anhedral and is the second most abundant mineral in the groundmass. The quartz in XPL displays regular to undulatory extinction and displays the typical first order gray birefringence. Sample DH462-A

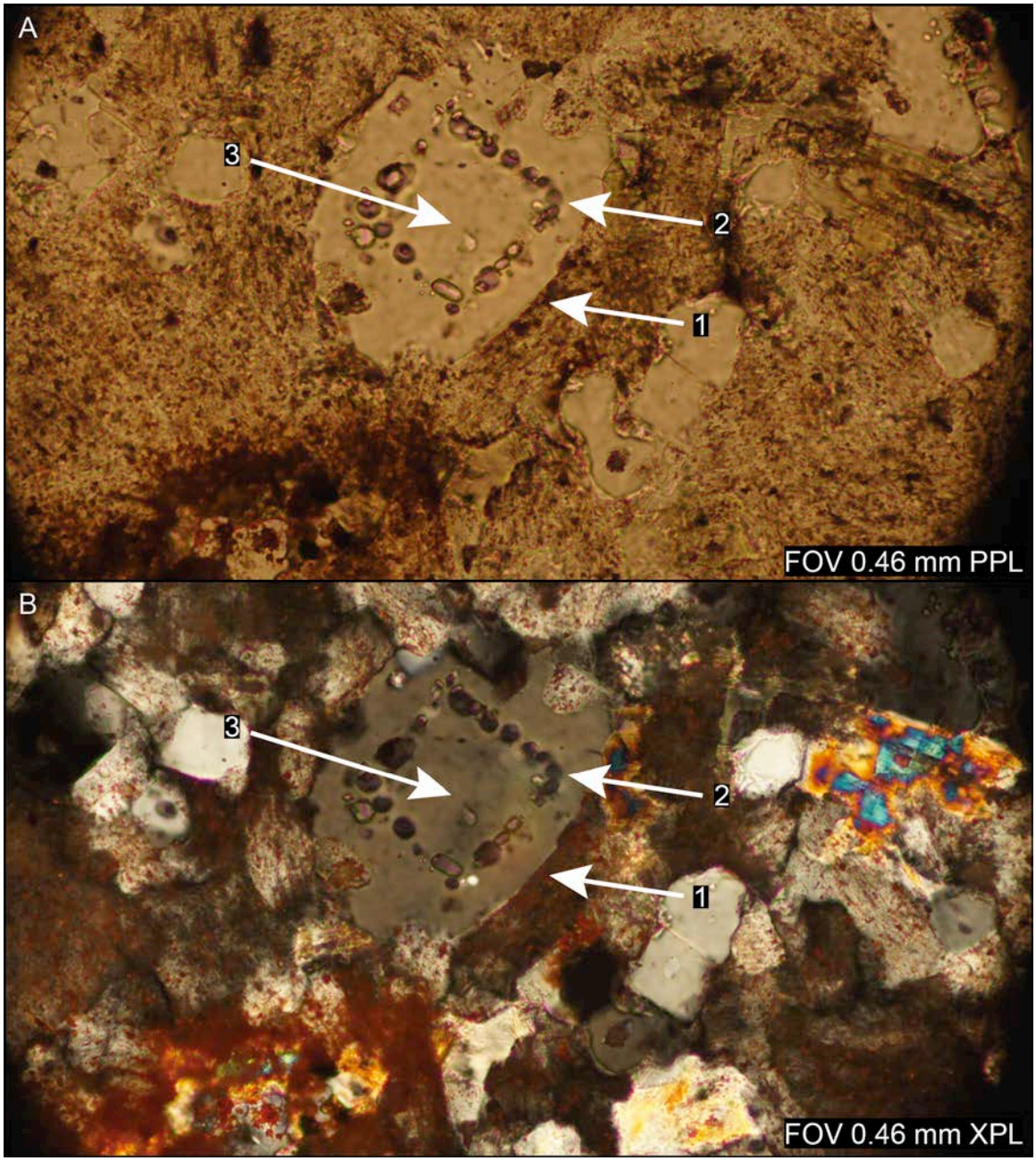

Figure 3.18: Photomicrographs of a quartz phenocryst with concentric melt inclusion ring in PPL and XPL. Quartz phenocrysts are typically comprised of an outer quartz overgrowth (1), followed by a concentric ring of melt inclusions (2) composed of sodium, potassium, and silica, and a quartz core (3). The inclusions appear purple in PPL and XPL, and are typically round to oblong in shape. No obvious vapor phase or daughter crystals have been identified within the inclusions; therefore most of these appear to be melt inclusions. Sample DH462-A

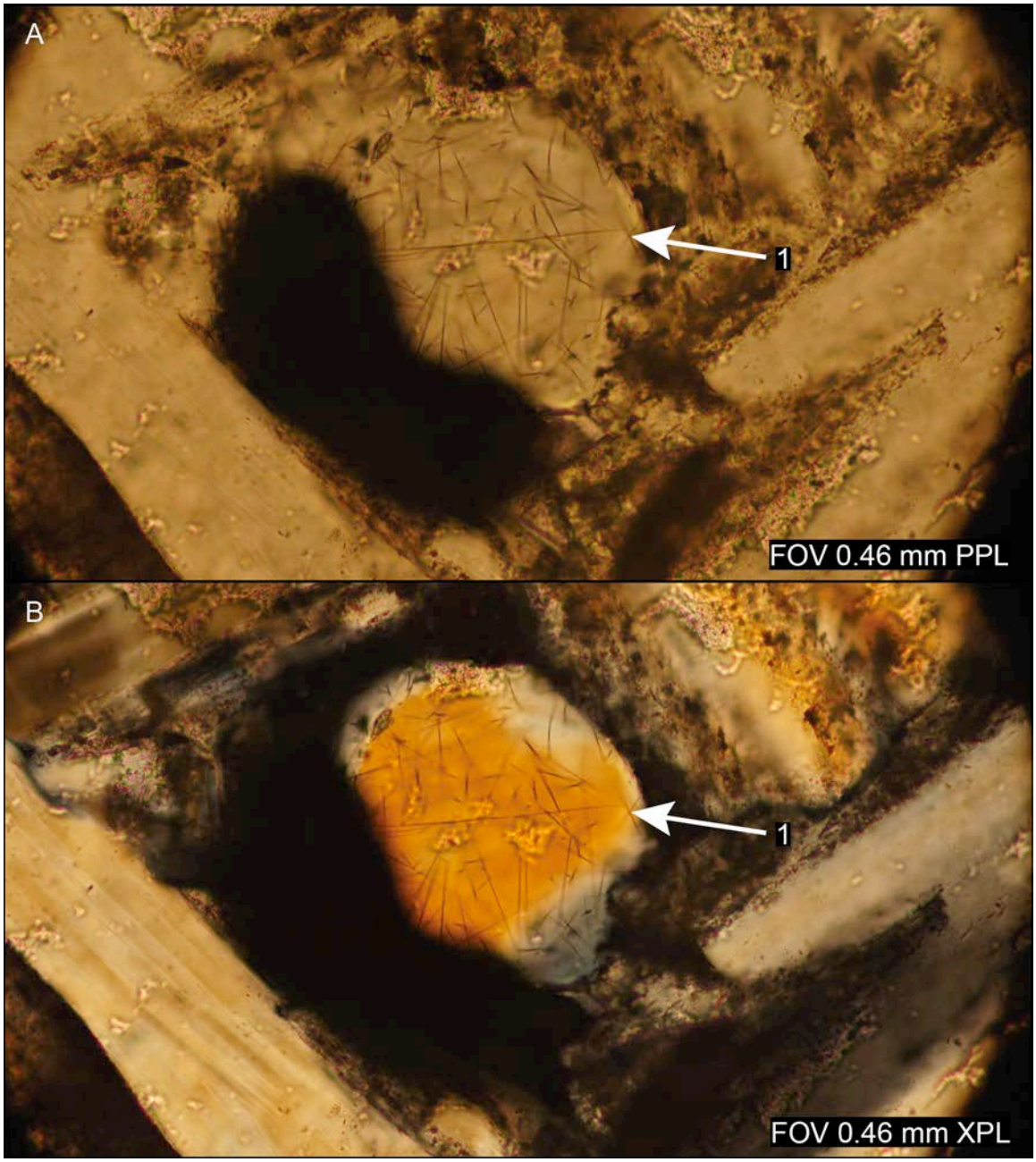

Figure 3.19: Photomicrographs of rutilated quartz phenocryst within plagioclase glomerocryst in PPL and XPL. This is the only example of rutilated quartz (1) identified within the scope of this study, and may represent an anomaly or entrapment of quartz from a secondary source. Sample DH455

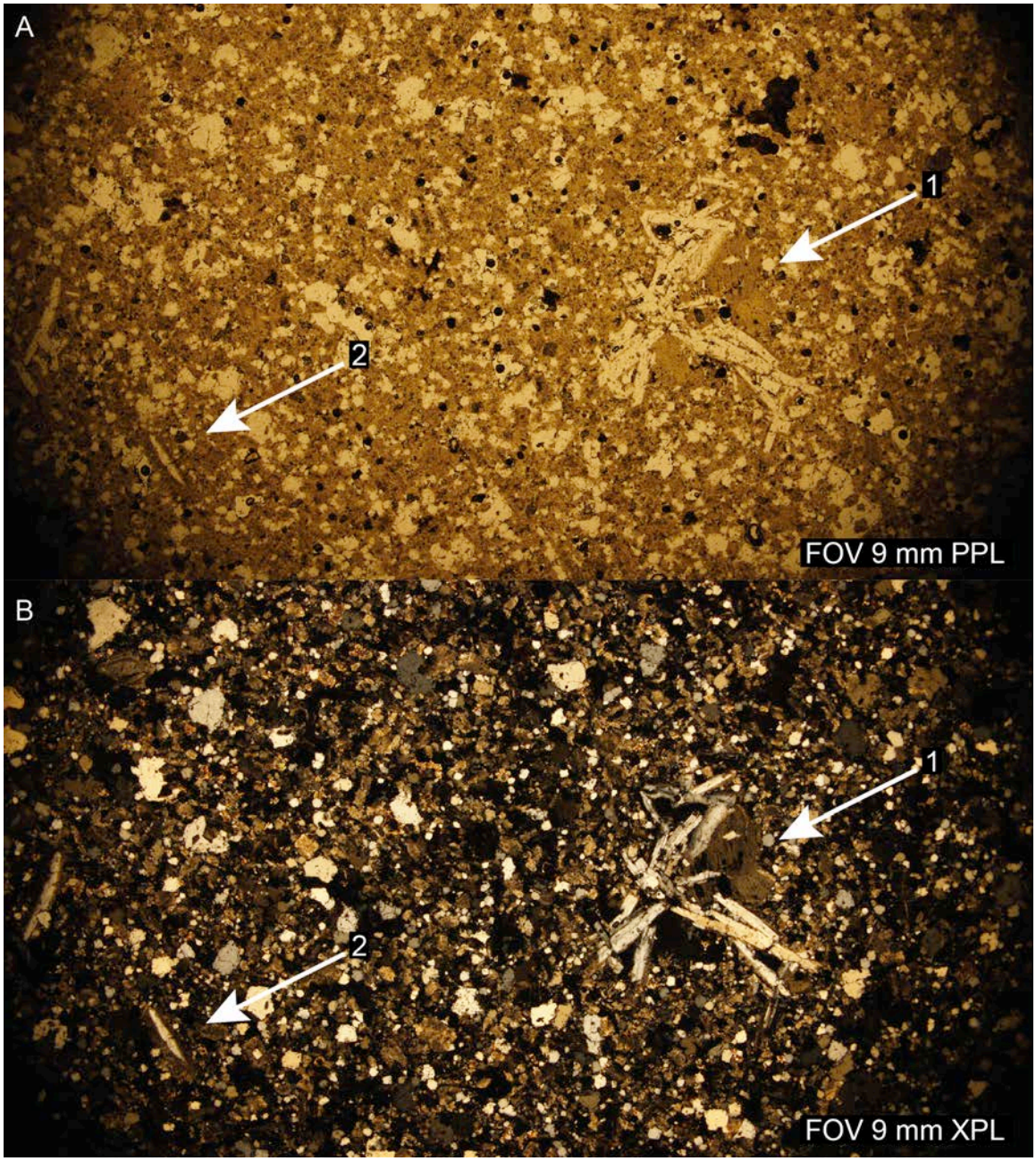

Figure 3.20: Photomicrographs of plagioclase phenocrysts in the two forms in which they occur; as clusters/glomerocrysts, and as individual phenocrysts in PPL and XPL. The glomerocrysts (1) are typically intergrown and may be greater than 1000 µm in diameter. Individual phenocrysts may range from 20-120 µm in diameter. Sample ORT266-03

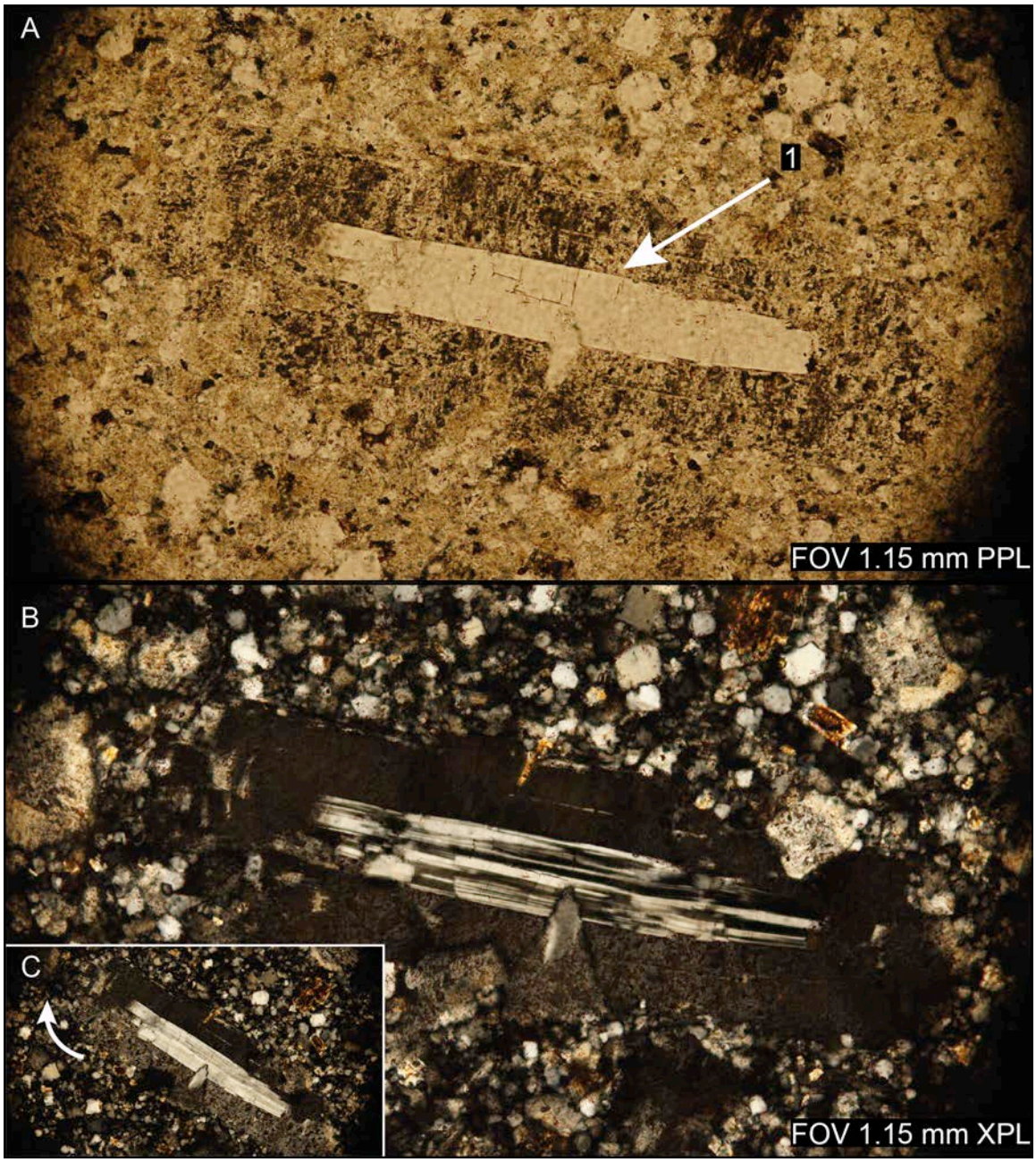

Figure 3.21: Photomicrographs of subhedral plagioclase feldspar lath in PPL and XPL. Note the boundary between the inner plagioclase core and the outer potassic rim is relatively coherent and not embayed (1). Plagioclase in XPL typically displays a range of albitic (B) and Carlsbad (C) extinction types. Sample ORT44-02

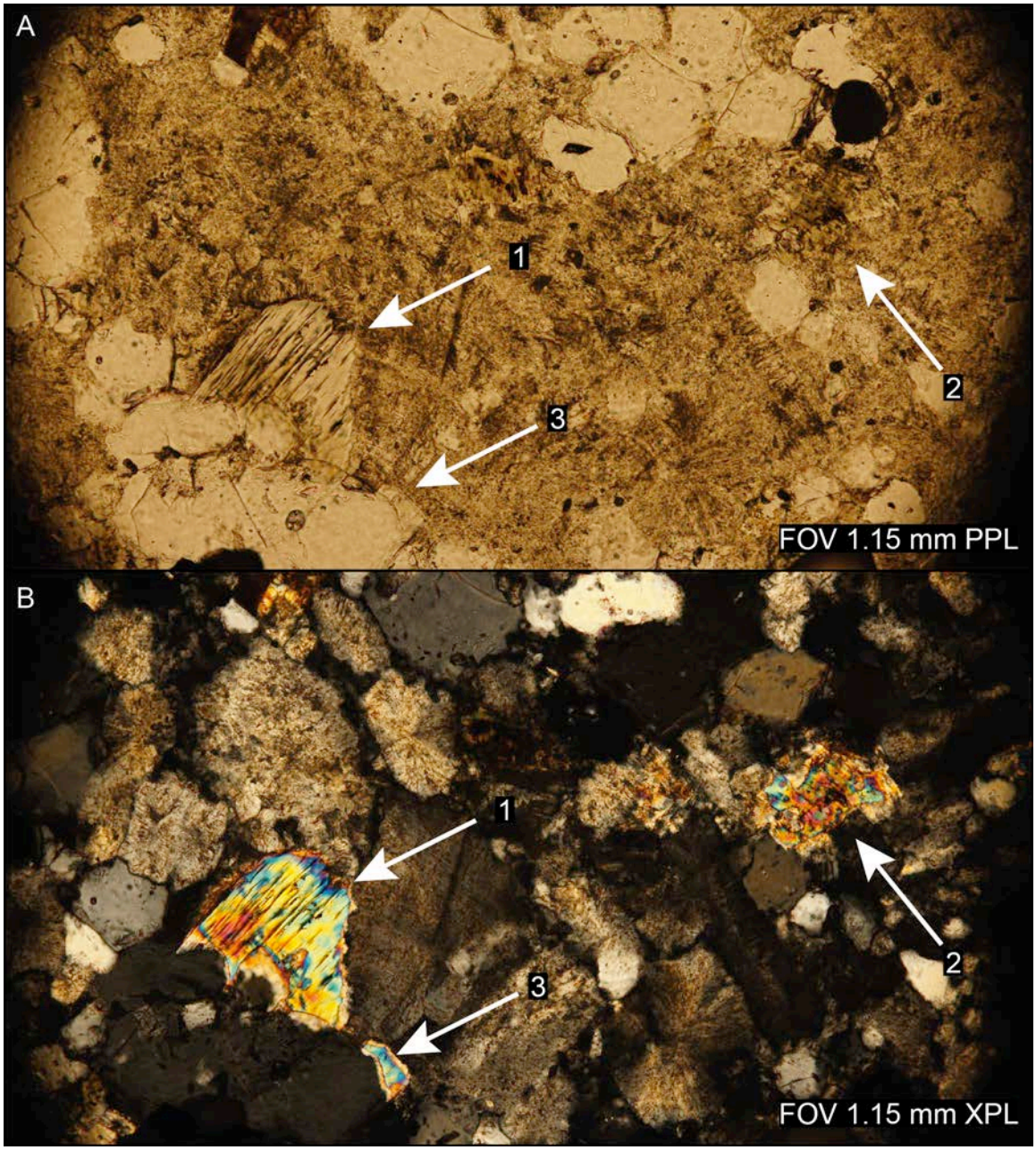

Figure 3.22: Photomicrographs of interstitial annite biotite phenocrysts in PPL and XPL. The annite is easily identifiable due to the prominent basal cleavage (1) and birds-eye extinction (2). The phenocrysts form along grain boundaries and interstitial to earlier formed minerals (3). Within PPL the phenocrysts display moderate pleochroism, transitioning form pale green to green-brown. Sample ORT266-03

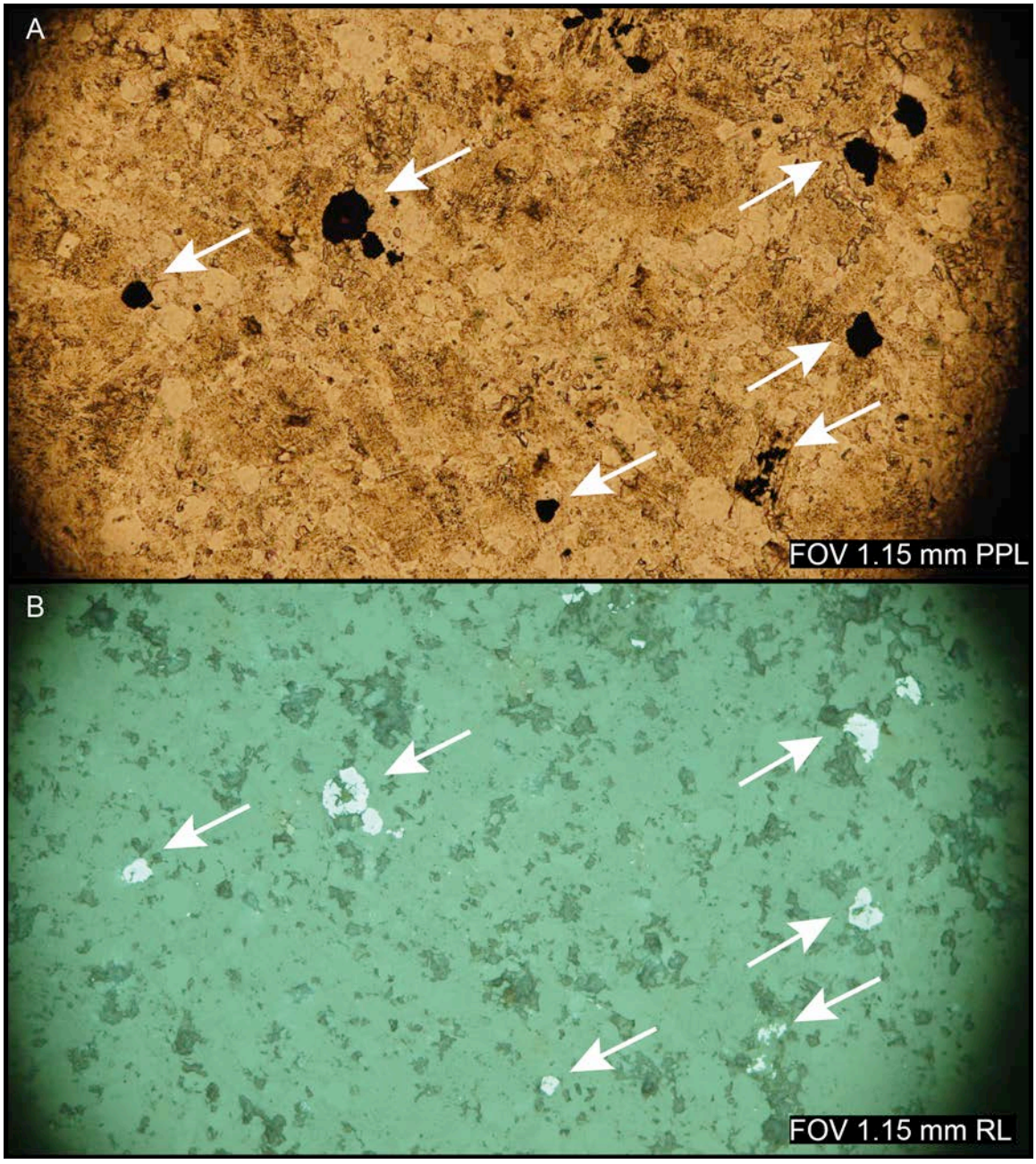

Figure 3.23: Photomicrographs of a group of subhedral to anhedral magnetite phenocrysts within gray rhyolite in PPL and RL. Note the magnetite is relatively unoxidized, but does have minor plucking due to the thin section making process. Magnetite is opaque in PPL (A) and appears as a dull gray within RL (B). Sample DH456

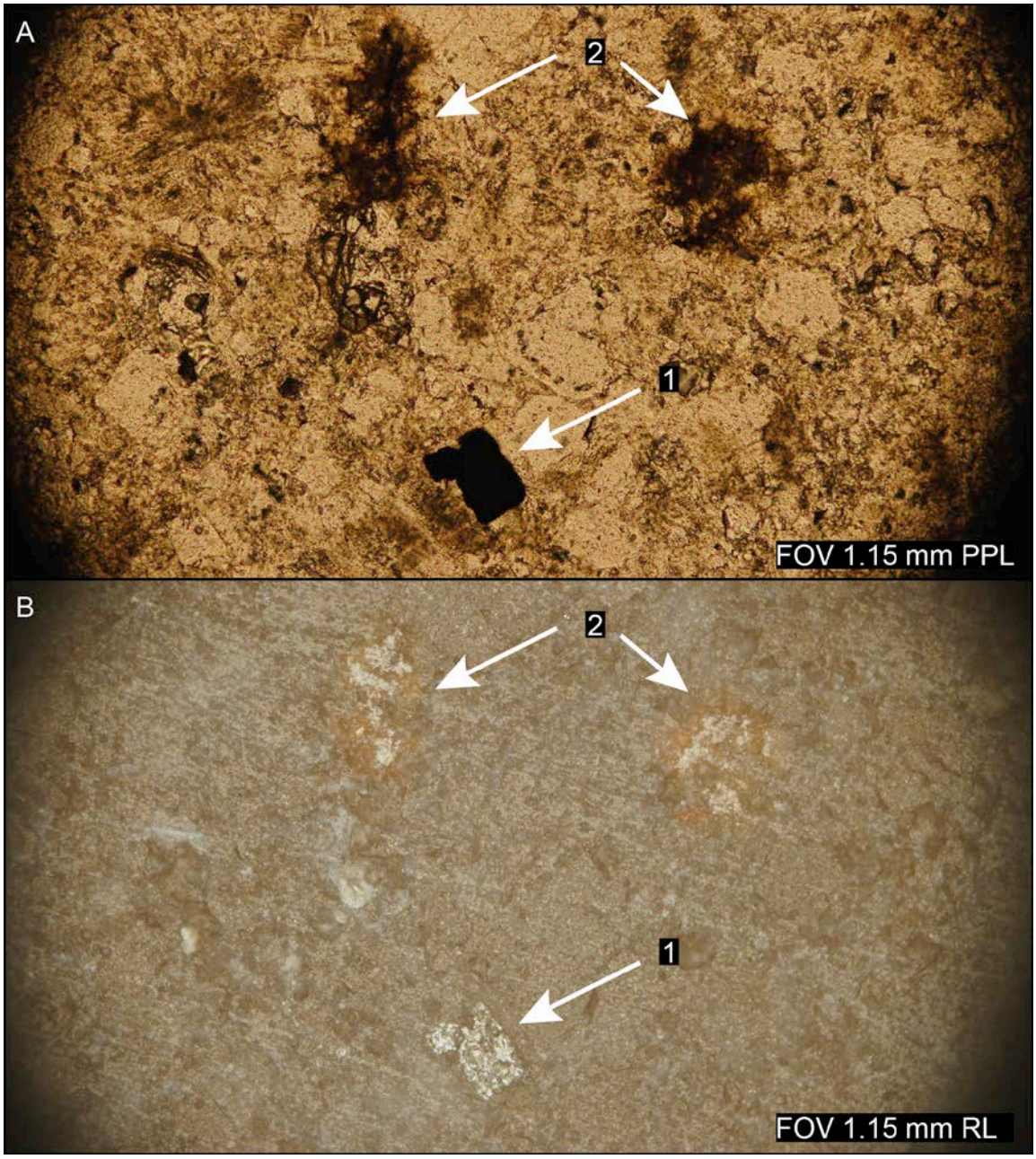

Figure 3.24: Photomicrographs of magnetite phenocrysts with varying degrees of oxidation in PPL and RL. The less oxidized magnetite (1) typically lacks the distinct red hematite halo common to the partially oxidized magnetite (1) phenocrysts. The amount of accompanying hematite may vary within the rhyolite but typically increases from gray, to purple, to red rhyolites. Magnetite phenocrysts within close proximity to one another may display a range of oxidation, as seen here. Sample ORT262-02

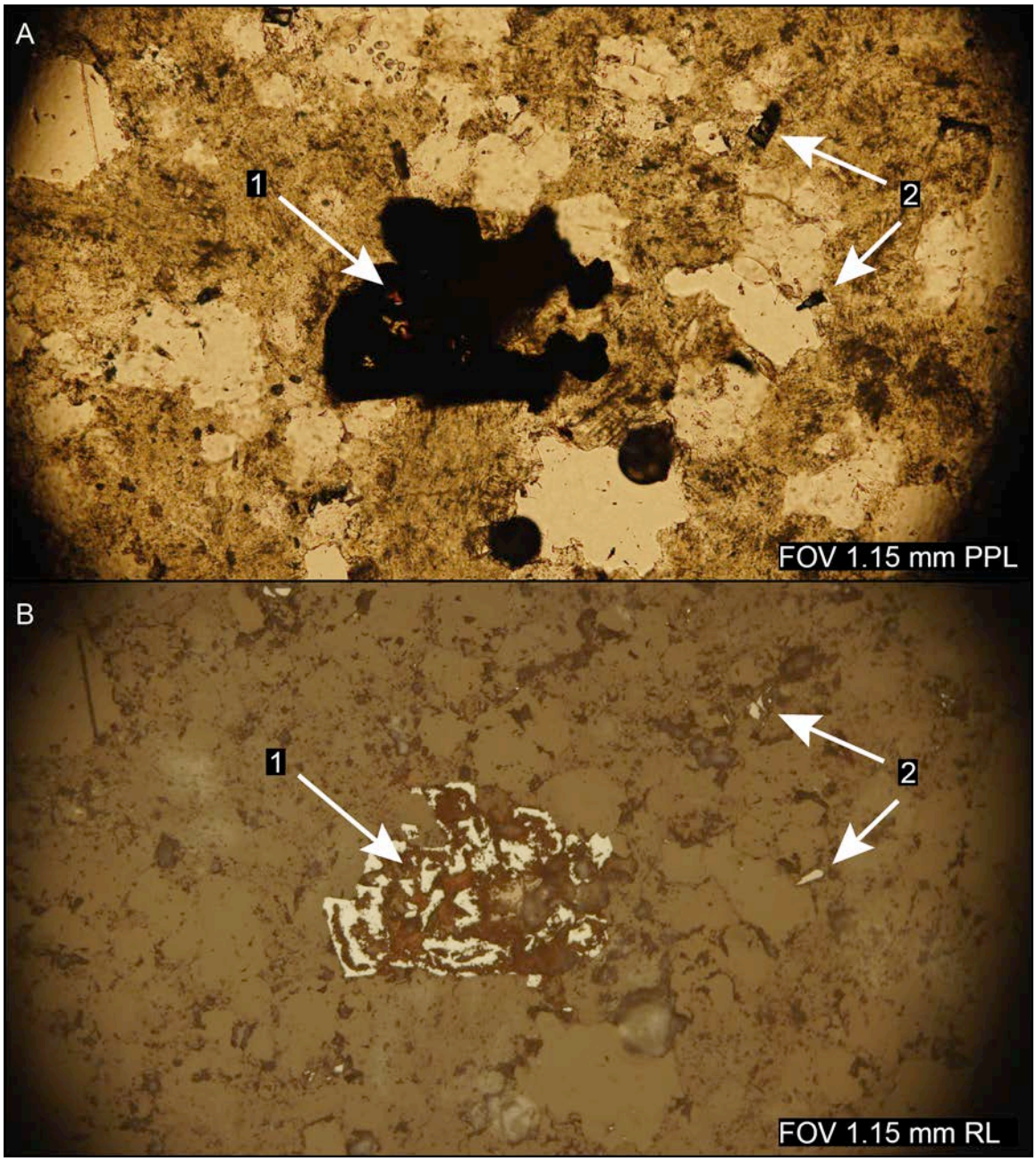

Figure 3.25: Photomicrographs of magnetite phenocryst with pock-like oxidation texture in PPL and RL. Partial oxidation of magnetite phenocrysts to hematite (1) becomes more abundant when transitioning from gray, to purple, to red rhyolites. Magnetite also occurs as microcrysts within the groundmass (2). Sample ORT266-03

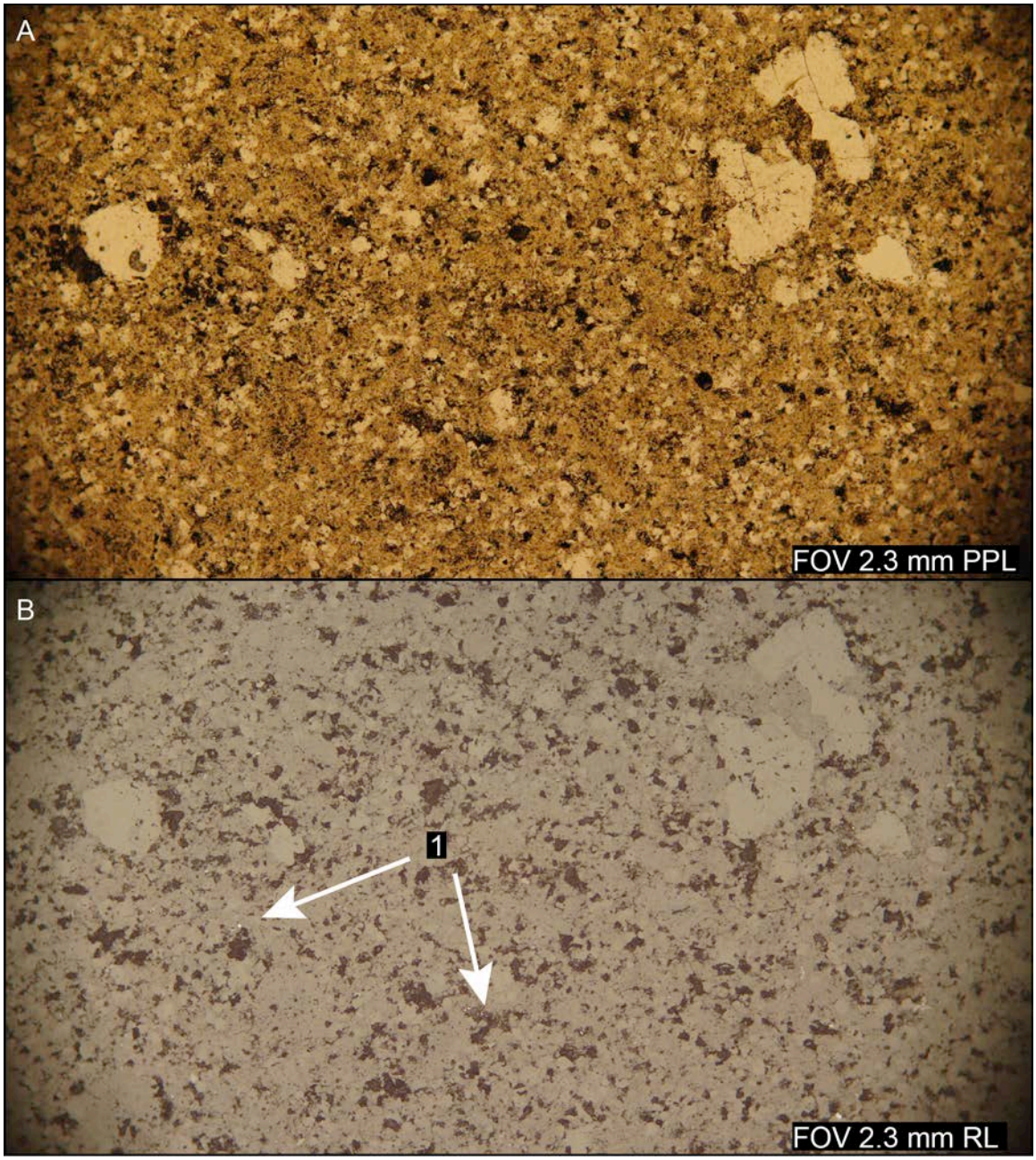

Figure 3.26: Photomicrographs of the magnetite phenocryst-poor tan rhyolite in PPL and RL. Within the tan rhyolite magnetite only occurs as microcrysts within the groundmass (1) and are visible in RL. It is unclear if the general lack of magnetite is due to subsequent alteration or if the rhyolite lacked magnetite initially at the time of formation. Sample ORT44-02

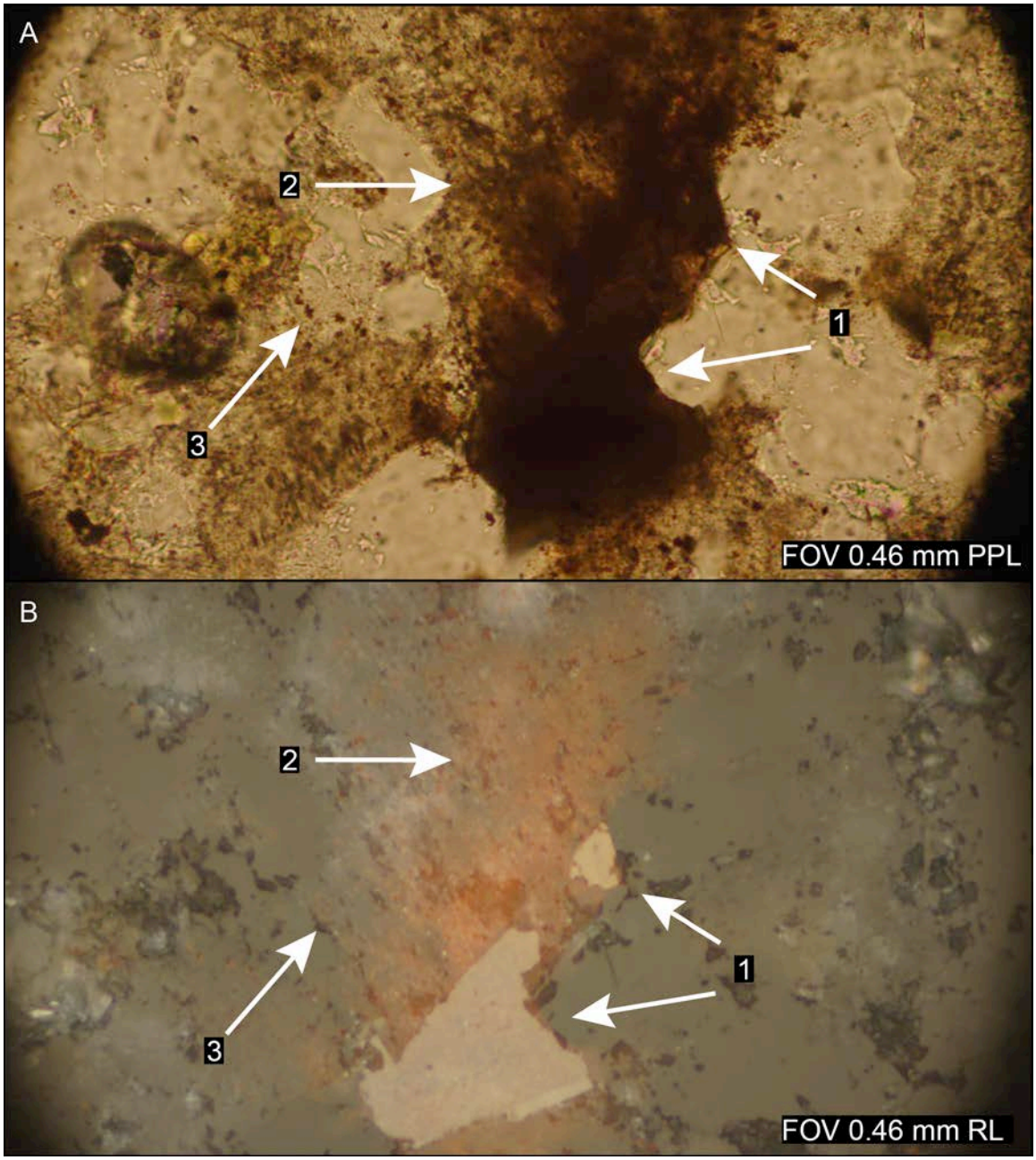

Figure 3.27: Photomicrographs of hematitic halo near magnetite phenocryst in PPL and RL. The magnetite phenocryst is often obscured by the hematite halo and only visible within RL (1). The hematite halo fills pore space within the surrounding groundmass (2 & 3), and is visible as a distinct red color in both PPL and RL. Sample ORT266-03

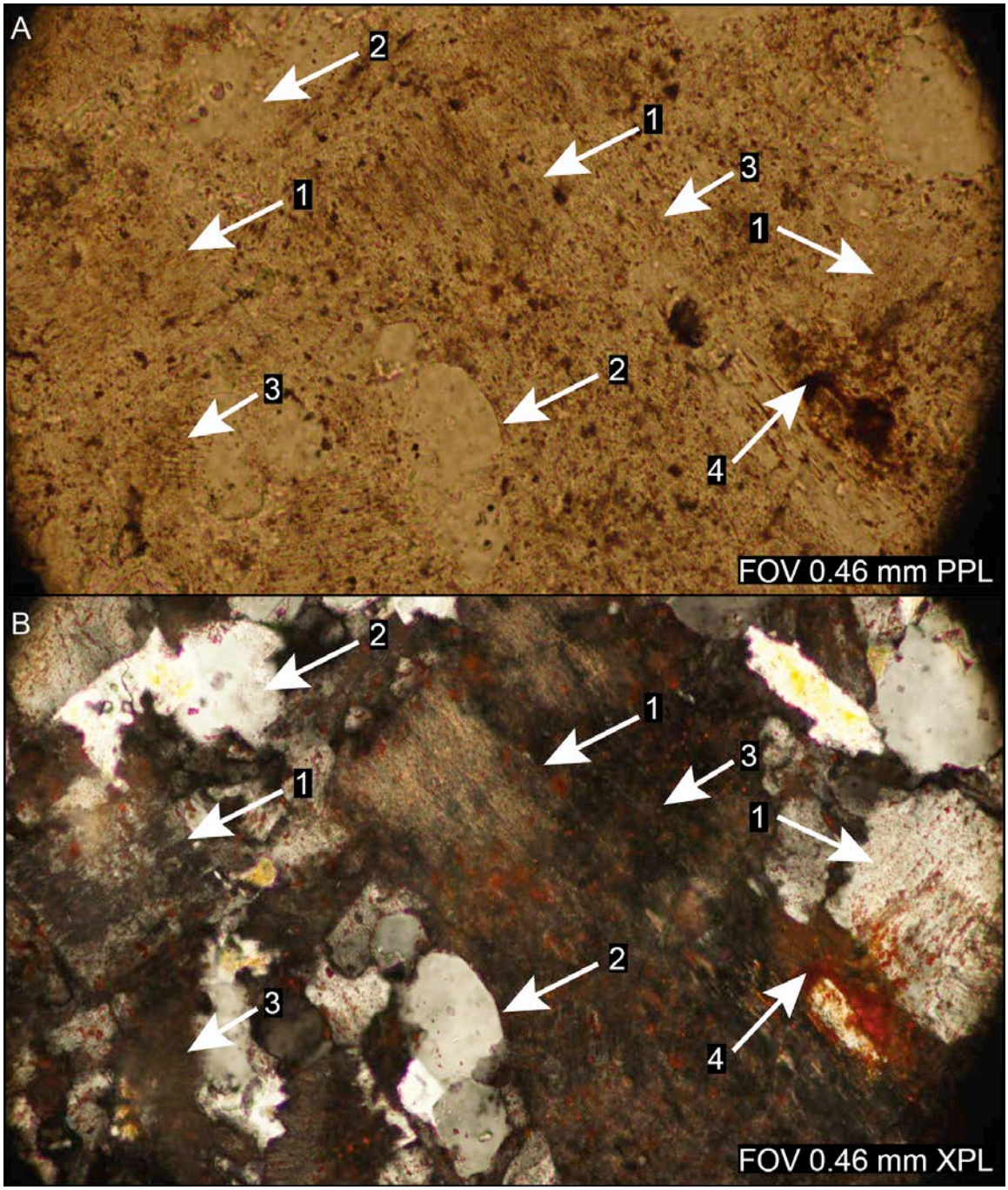

Figure 3.28: Photomicrographs of the typical rhyolite groundmass in PPL and XPL. The groundmass is composed of subhedral to anhedral potassium-rich feldspar (1), quartz (2), and sodium-rich feldspar (3). Note the abundance of red hematite dispersed throughout the groundmass (4). Individual crystals within the groundmass typically range from <10-100 μm in diameter. Sample DH421

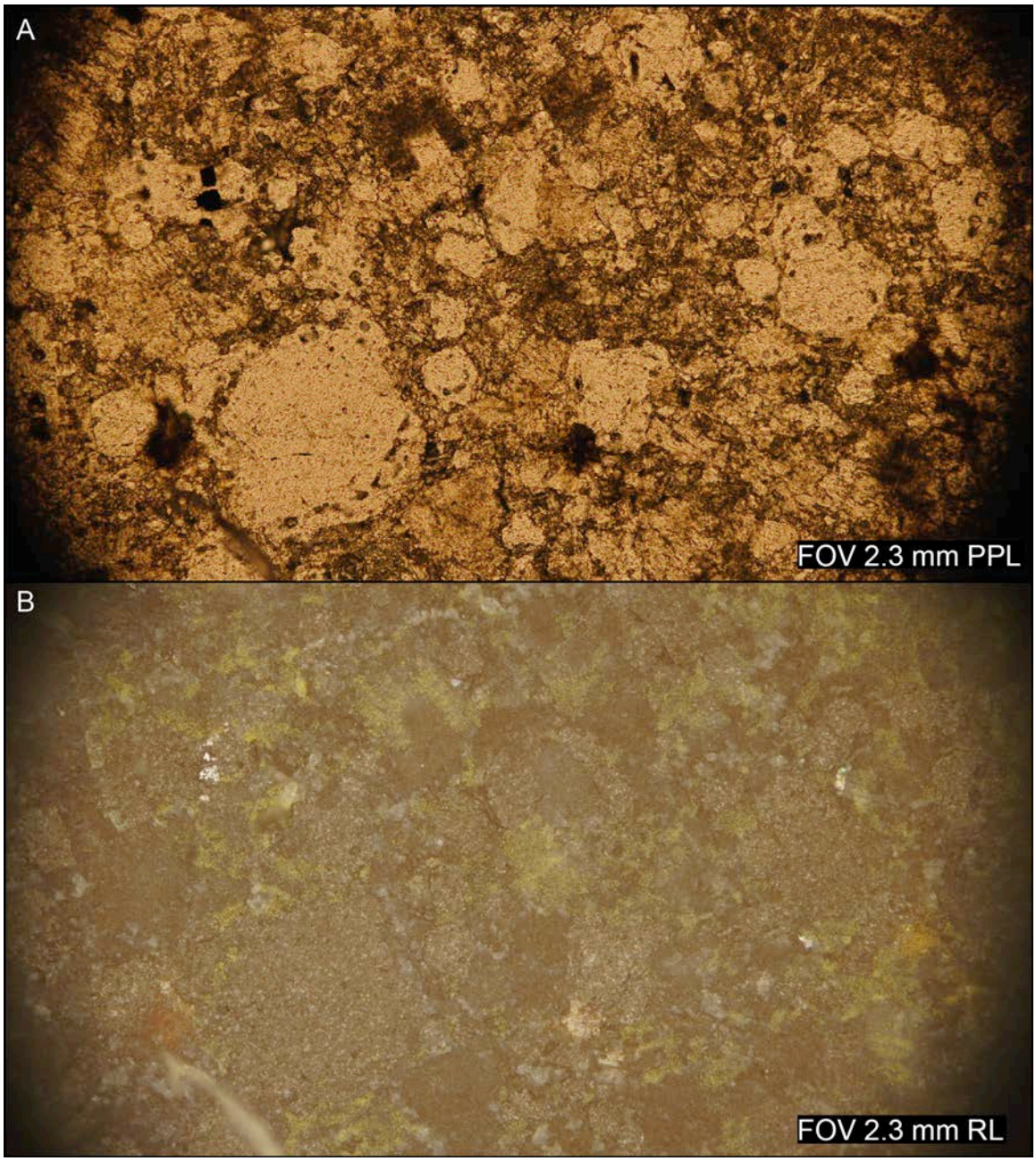

Figure 3.29: Photomicrographs of sodium cobaltinitrite stained gray rhyolite thin section in PPL and RL. The potassium-rich portions of the groundmass appear yellow when stained, and comprise approximately 20% of the total groundmass. Through staining, the lack of potassium-rich portions of the groundmass becomes apparent when compared to the purple and red stained rhyolites. Sample ORT262-02

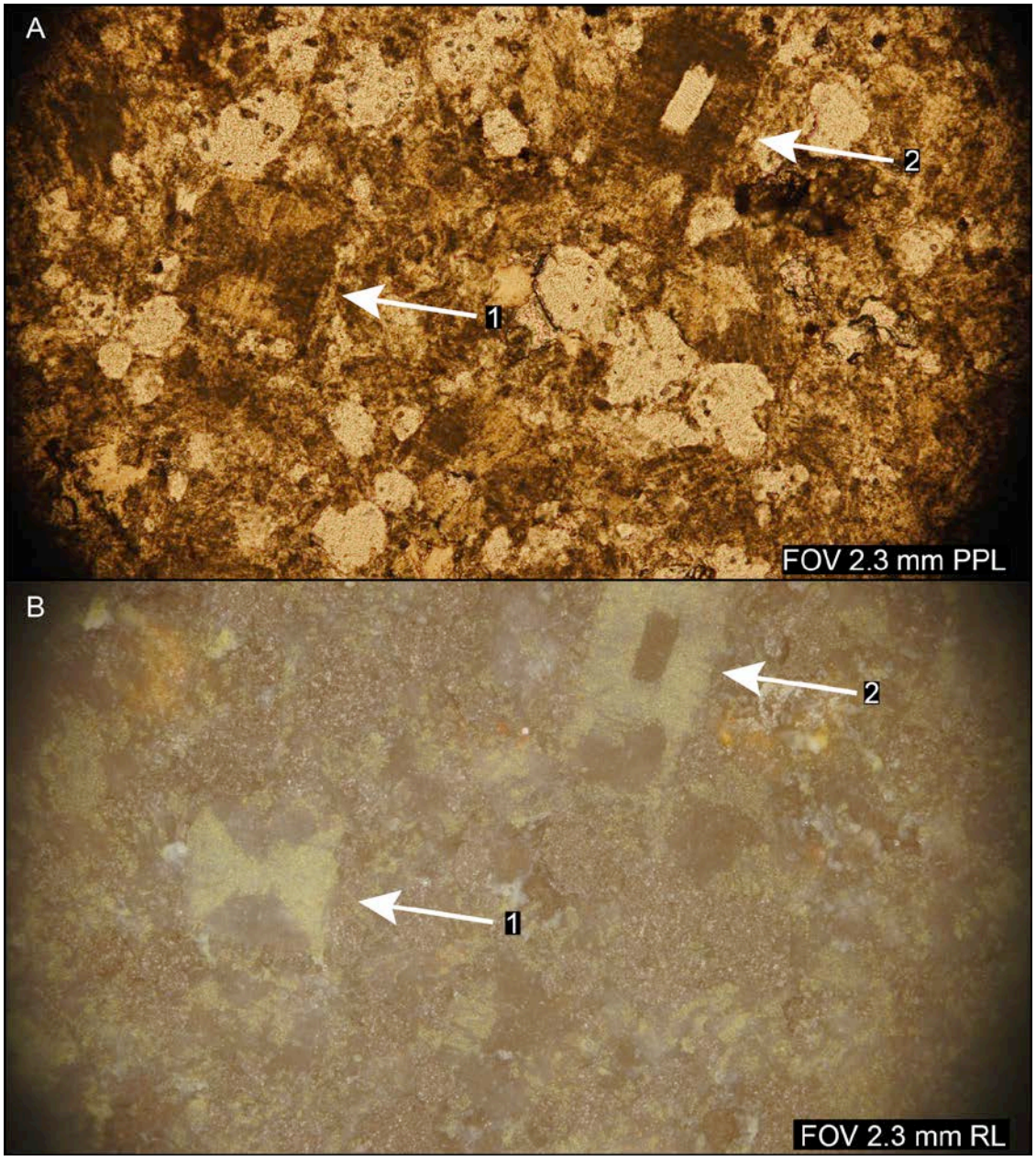

Figure 3.30: Photomicrographs of sodium cobaltinitrite stained purple rhyolite thin section in PPL and RL. The potassium-rich portions of the groundmass appear yellow and comprise approximately 30% of the total groundmass. Feldspar identification is especially aided by the staining; highlighting the potassium-rich portions of the hourglass feldspars (1), and the potassic overgrowths to sodic feldspars (2). Through staining, the moderate abundance of potassium-rich portions of the groundmass becomes apparent when compared to the gray and red stained rhyolites. Sample ORT247-01

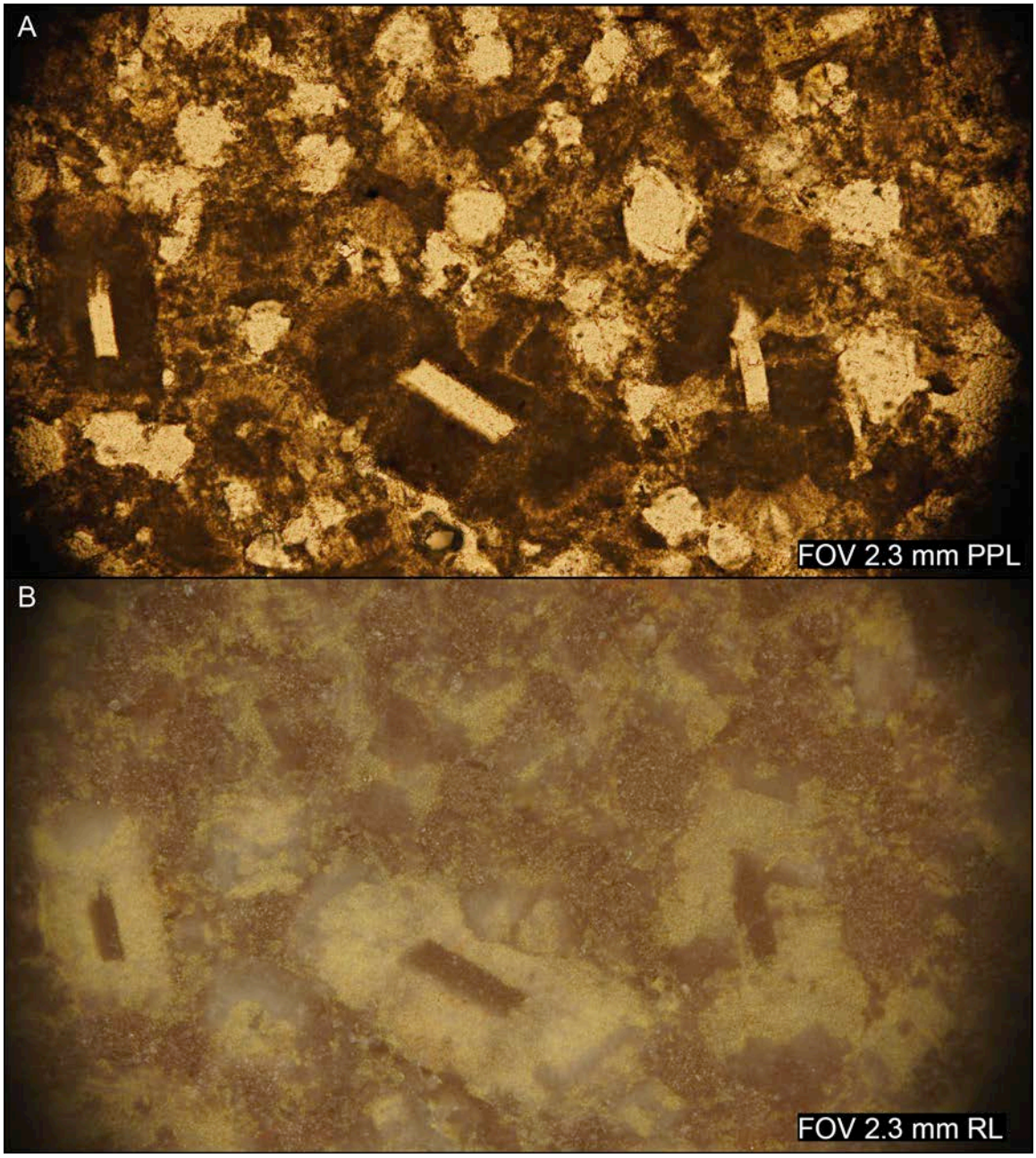

Figure 3.31: Photomicrographs of sodium cobaltinitrite stained red rhyolite thin section in PPL and RL. The potassium-rich portions of the groundmass appear yellow and comprise approximately 40% the total. Note the potassium-rich portions of the feldspar phenocrysts become highly apparent when stained. Through staining, the abundance of potassium-rich portions of the groundmass becomes apparent when compared to the gray and purple stained rhyolites. Sample DH421

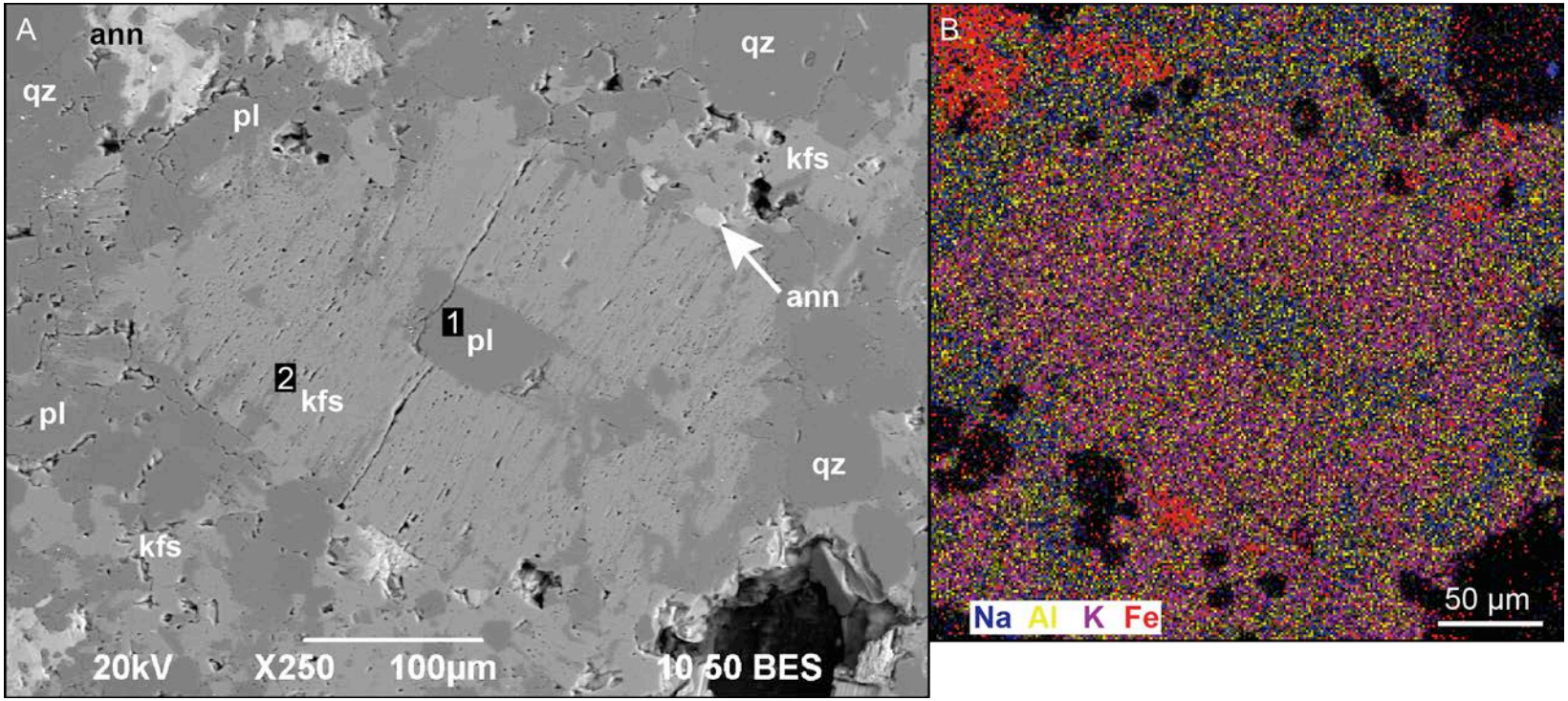

Figure 3.32: BSE image and EDS map of feldspar lath with plagioclase core and potassium feldspar overgrowth. The BSE image (A) highlights the high porosity (2) of the potassic overgrowth relative to the plagioclase core (1). Additionally, with the BSE detector the interstitial nature of the annite biotite and intermingled texture of the potassium feldspar and plagioclase groundmass is highly apparent. The crystal edges of the potassic overgrowth are highly anhedral and embayed. Portions of the overgrowth are more sodium rich and appear as a darker gray, equivalent to the interior plagioclase core. The EDS map demonstrates the abundance of potassium (purple) within the overgrowth and sodium (blue) within the core. Additionally, the EDS map demonstrates the abundance of iron (red) within both the overgrowth and core. Sample ORT264-01.24

Figure 3.33: CL image of feldspar phenocryst with a relatively small plagioclase core and large potassium overgrowth. The plagioclase core is approximately 40 µm in length and the potassic rim is approximately 50 µm at the widest point. Sample ORT264-01

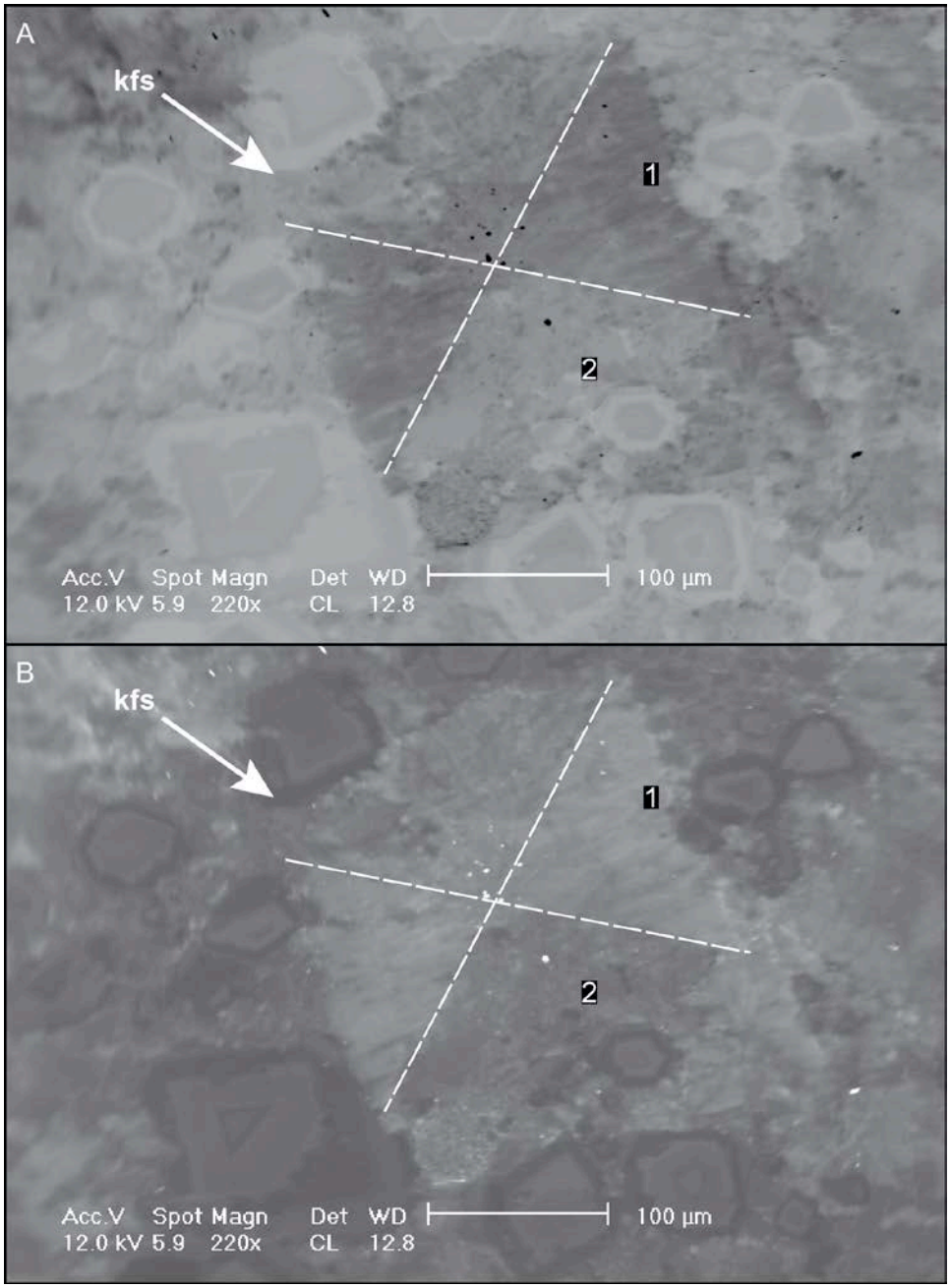

Figure 3.34: CL image of the hourglass type potassium feldspar phenocryst with distinct sector zonation. The white dashed lines denote the approximate boundaries between the two internal hourglass structures. In normal CL (A), the potassium rich portion (1) appears as a darker gray, whereas the potassium with sodium portion (2) appears as a lighter gray. Although, compositionally the feldspar is predominately potassium feldspar. Sample ORT264-01

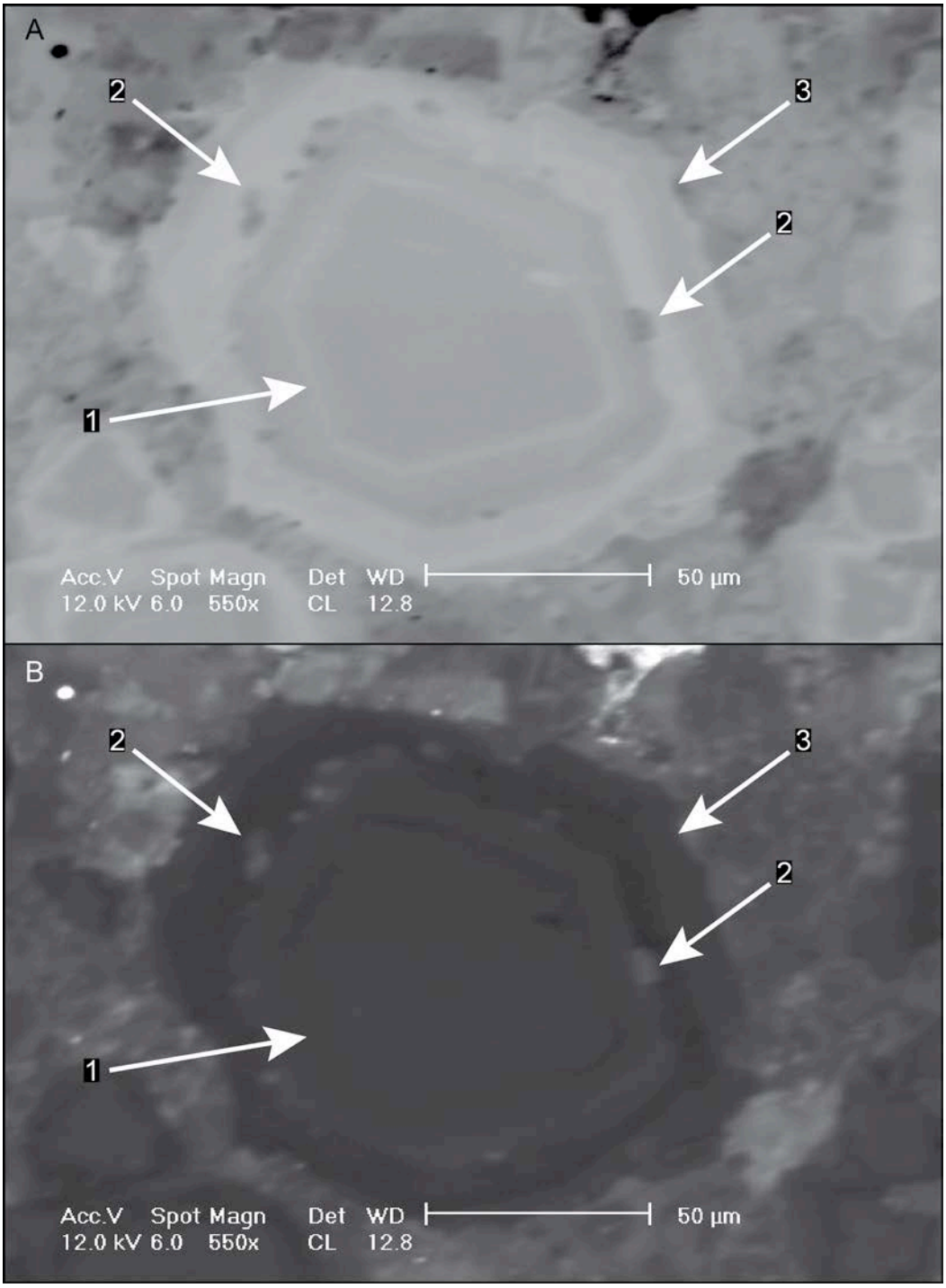

Figure 3.35: CL image of a typical three-part quartz phenocryst comprised of an inner-zoned hexagonal quartz core (1), followed by a concentric ring of melt inclusions (2), overgrown by a later stage subhedral to anhedral quartz (3). Sample ORT264-01

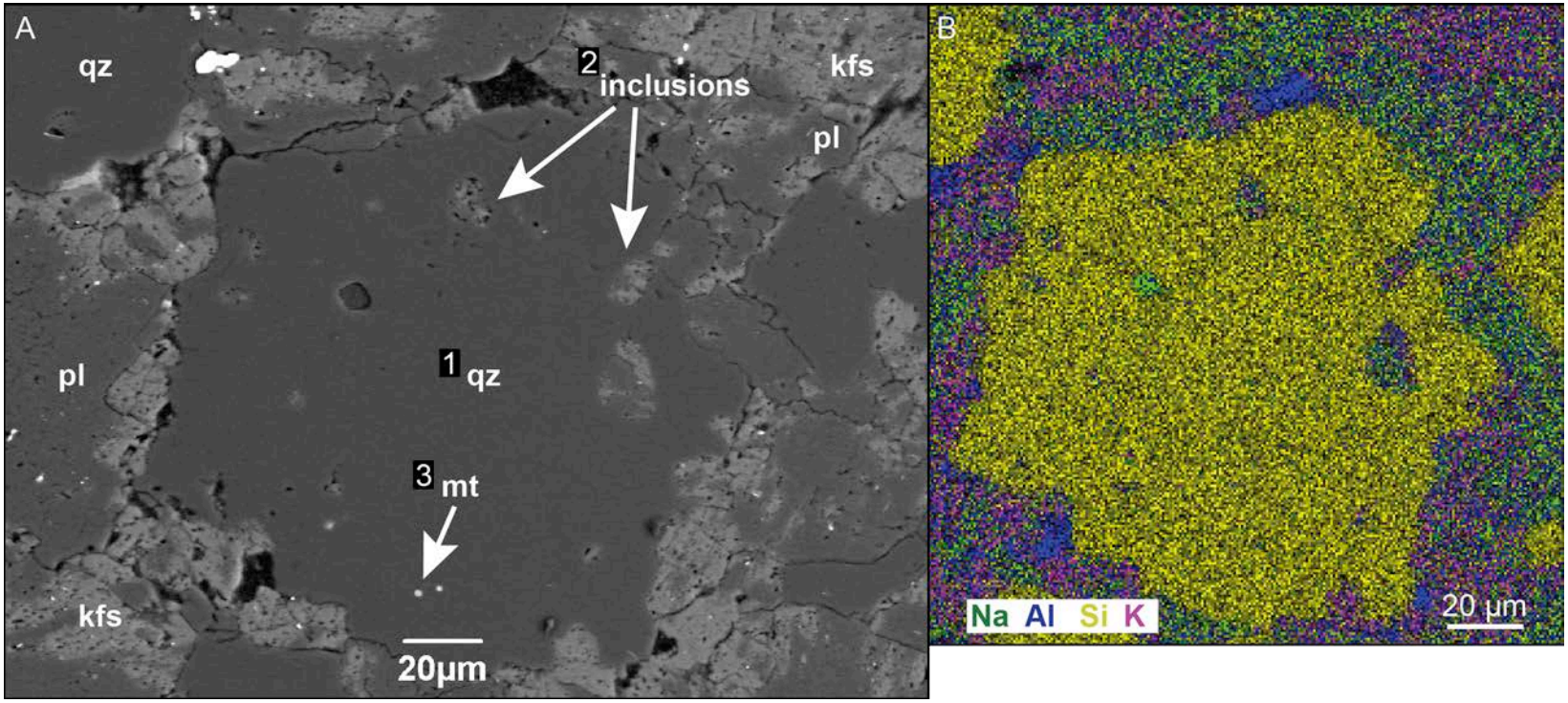

Figure 3.36: BSE image and EDS map of a typical quartz phenocryst with concentric melt inclusion ring at the quartz-to-quartz boundary. The quartz phenocrysts are typically subhedral to anhedral with highly embayed and undulatory edges. Set back from the outer edge, is typically a semi-concentric ring of inclusions (2), which are comprised of potassium, sodium, and silica (the same composition as the rhyolite groundmass). Additionally, inclusions of magnetite (3) and REE-fluorides have been identified. The EDS map highlights the mixed composition of the melt inclusions and the similarity in composition to the groundmass. Sample ORT263-04.47

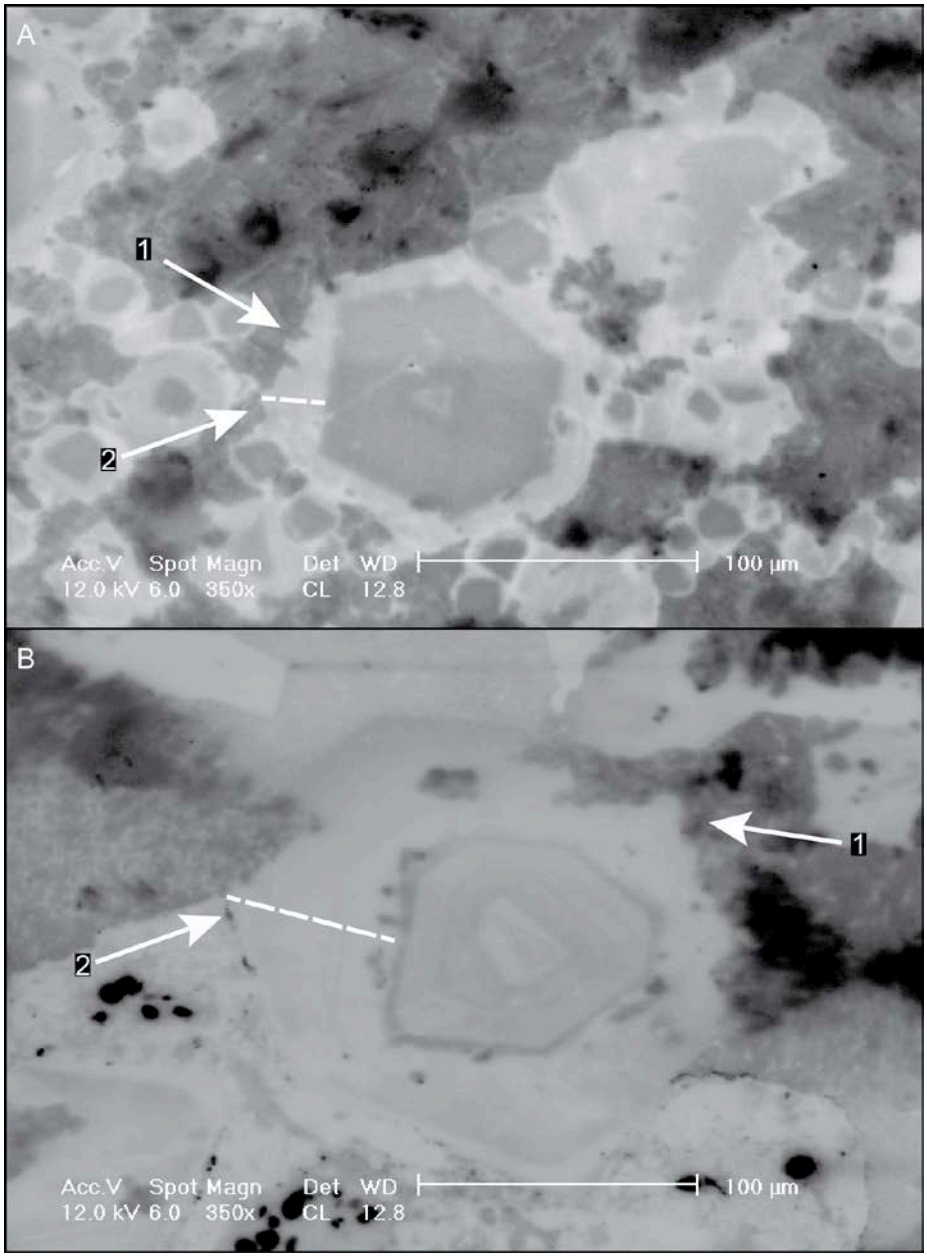

Figure 3.37: CL images of the three-part quartz phenocrysts with varying outer overgrowth thickness and zoned interior cores. The thickness of the late-stage quartz overgrowth rims vary greatly (2) and have been observed to range from 10-60 µm in diameter at the widest point for phenocrysts of approximately the same size. The outer edge of the late-stage overgrowth is typically highly embayed and undulatory (1), possibly denoting rapid crystallization and/or later corrosion of the rim due to disequilibrium. Sample ORT266-02

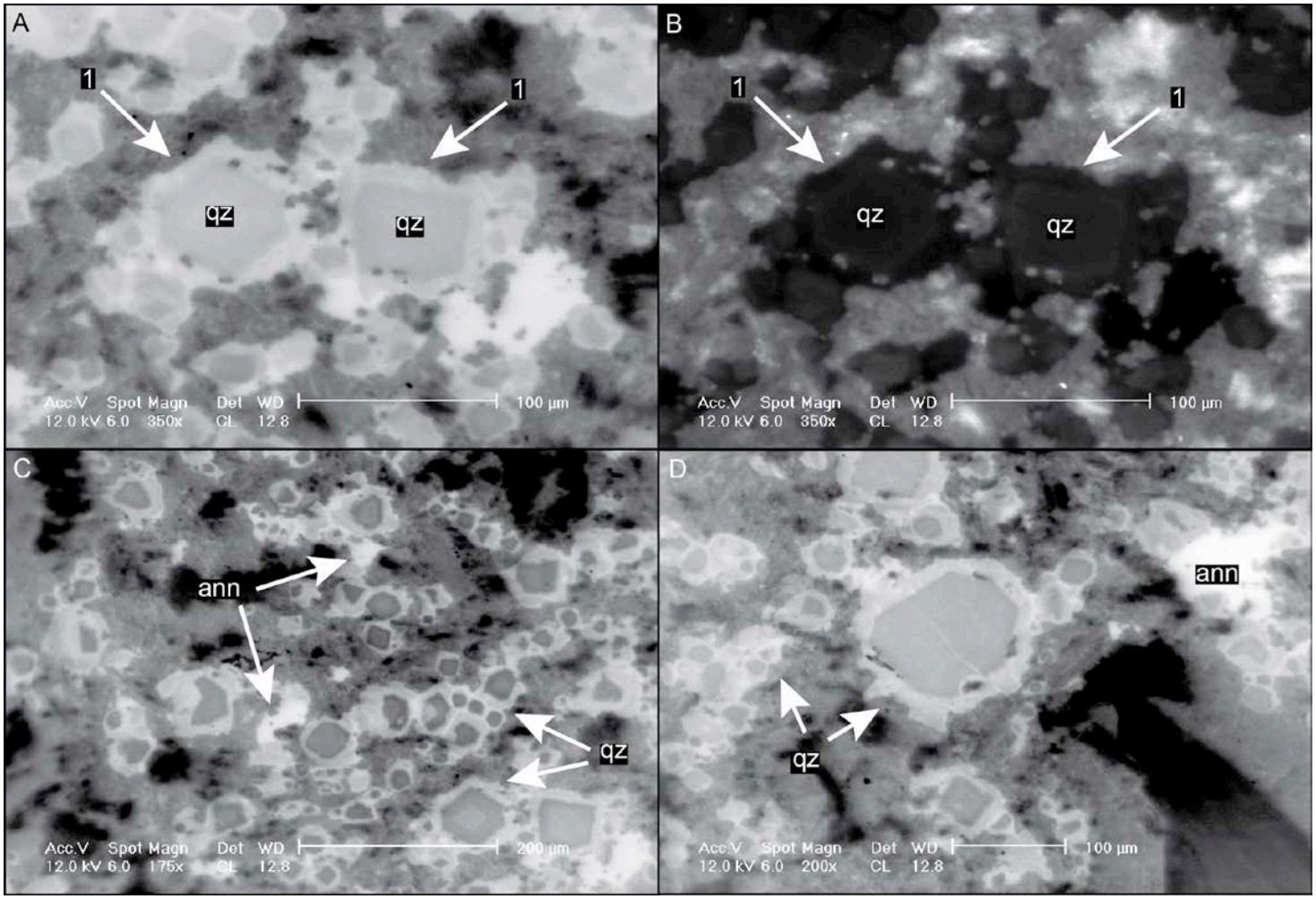

Figure 3.38: CL images of abundant quartz phenocrysts and groundmass with melt inclusions along the quartz-to-quartz boundary. Figure 3.38 full caption, next page.

Figure 3.38 continued: CL images of abundant quartz phenocrysts and within the groundmass with melt inclusions along the quartz-to-quartz boundary. A-B) The occurrence of the concentric inclusion ring is abundant and may be found in the majority of quartz phenocrysts (1). This abundance suggests that the majority of the quartz phenocrysts underwent the same petrogenesis. C-D) Quartz crystals are abundant as phenocrysts and within the groundmass Note all the quartz crystals, both those that are part of the groundmass and those that are phenocrysts display the typical three parts. Additionally, the abundance of interstitial annite is highly visible in CL. Sample ORT266-02

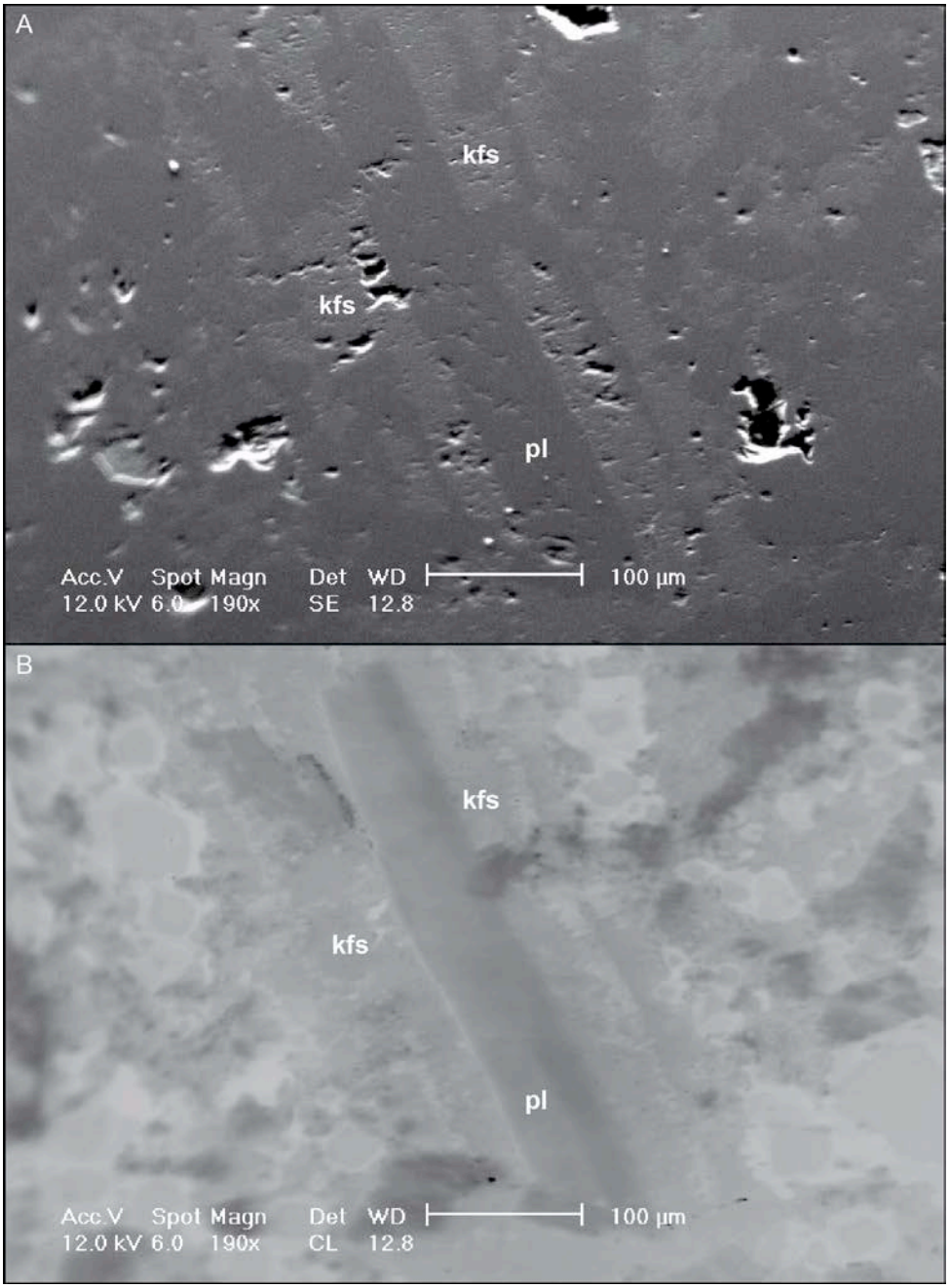

Figure 3.39: SE and CL images of a typical plagioclase feldspar phenocryst with potassium feldspar overgrowth rim. The interior plagioclase core may vary greatly in length, ranging from 20-120 µm. The overgrowth of potassium-rich feldspar suggests that the plagioclase formed first in the petrogenic sequence, and then conditions changed favoring potassium feldspar growth. Sample ORT266-02

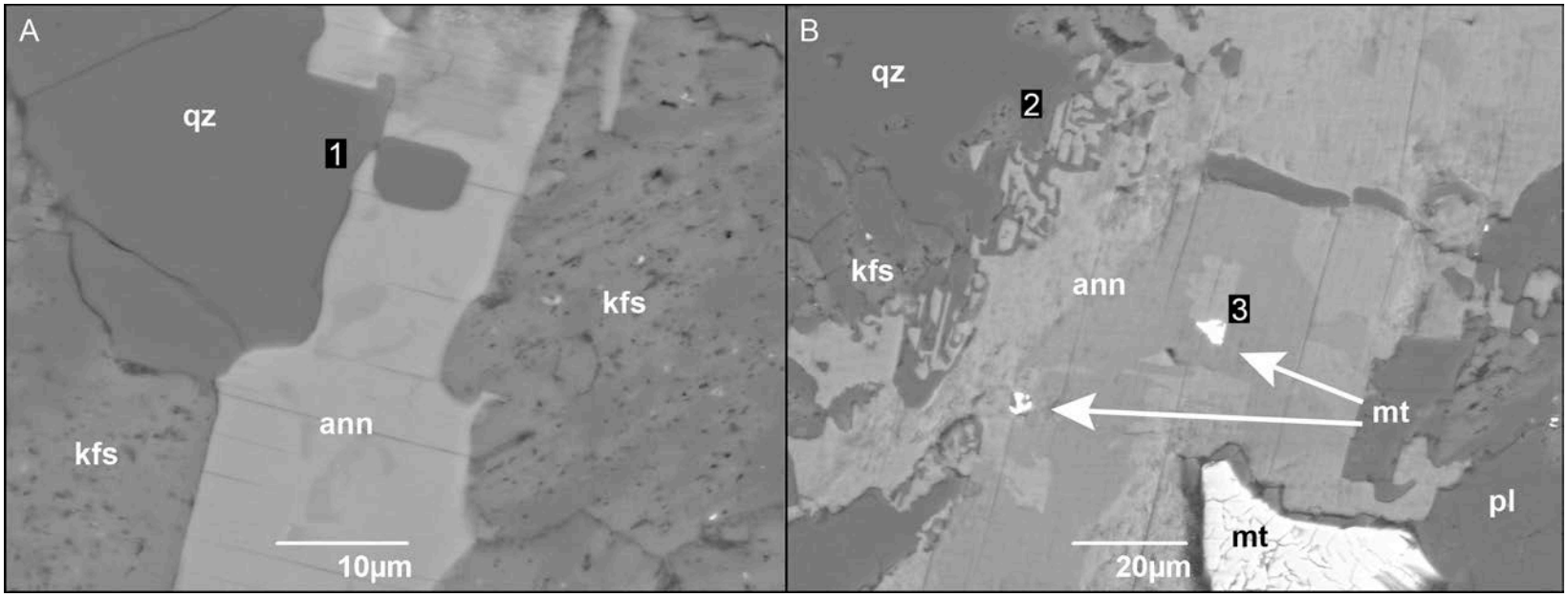

Figure 3.40: BSE images of interstitial and late-stage annite biotite. The annite is typically late-stage and anhedral, conforming to neighboring crystals (1). The annite may have clean edges (1), or unique rune-type edges as seen in (2). It is unclear as to the source of these unique edges but they potentially may reflect rapid crystallization. Additionally, some crystals display zonation (3) visible as varying shades of gray, although the compositional differences are too minor to be detected by the EDS. Magnetite and hematite are often found as inclusions or along the basal cleavage of the annite. Sample ORT263-04.40 and 41

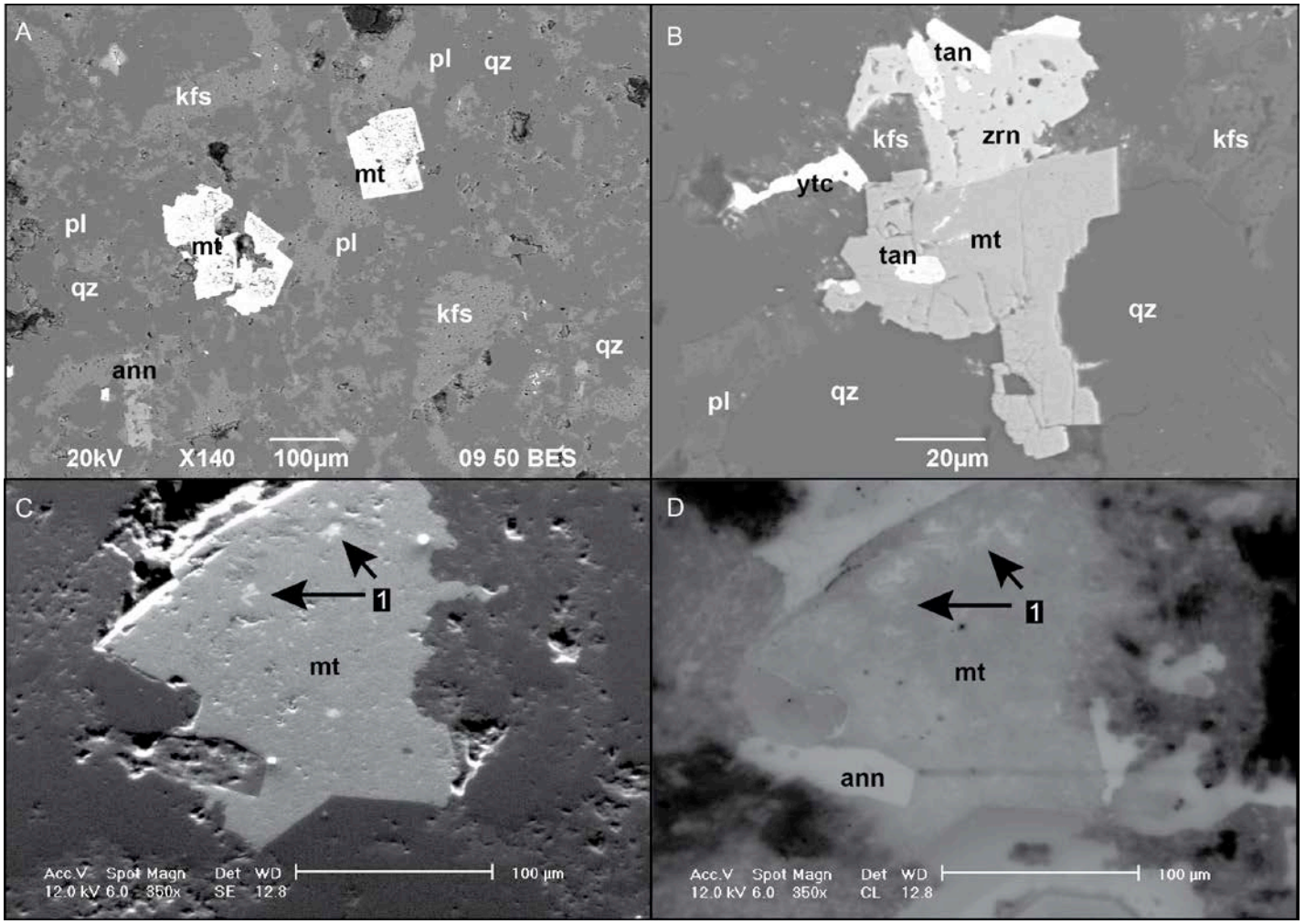

Figure 3.41: BSE, SE, and CL images of euhedral to subhedral magnetite phenocrysts with abundant inclusions. Figure 3.41 full caption, next page.

Figure 3.41 continued: A) Magnetite phenocrysts typically range from 10-150 μm in diameter and may be euhedral to subhedral. B) BSE image of a magnetite phenocryst with tantalite inclusions, in close association with zircon phenocrysts with more tantalite inclusions, and yttrocerite. The magnetite phenocrysts commonly occur in close association with other accessory and trace mineral phases, as seen here. Note the potassium feldspar groundmass close to the magnetite phenocryst with iron-oxide pore-fill, and the potassium feldspar groundmass distal to the magnetite phenocryst without pore-fill. C-D) SE and CL images of magnetite phenocrysts with amoeboid-like mineral inclusions (1). Inclusions are commonly difficult to see but may be readily viewed with the CL detector or by diminishing the brightness and with the BSE detector. The inclusions formed contemporaneously with the magnetite phenocryst. Samples ORT270-01.85 and ORT263-04.45

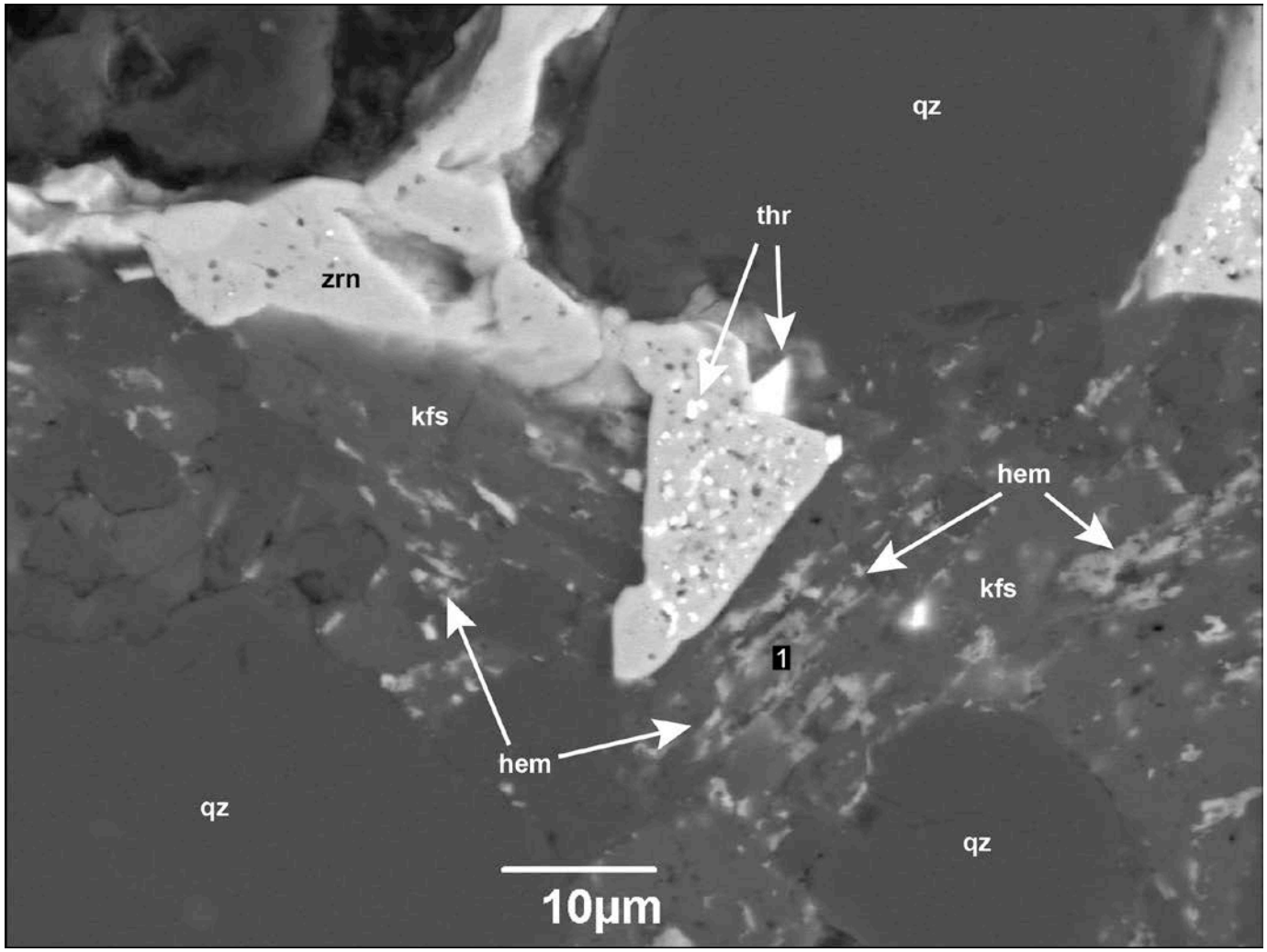

Figure 3.42: BSE image of hematitic pore-fill within the potassium feldspar groundmass. Figure 3.42 full caption, next page.

Figure 3.42 continued: The iron oxide appears as medium gray wispy inclusions within the darker gray potassium feldspar groundmass (1). This inclusionary process has only been observed within the potassium feldspar portion of the groundmass and is believed to be the cause of the turbid texture of the rhyolites. The hematitic pore-fill is not pervasive throughout the groundmass, but rather occurs as patches, typically associated with other trace and accessory phases, as seen here. Sample ORT266-02.56

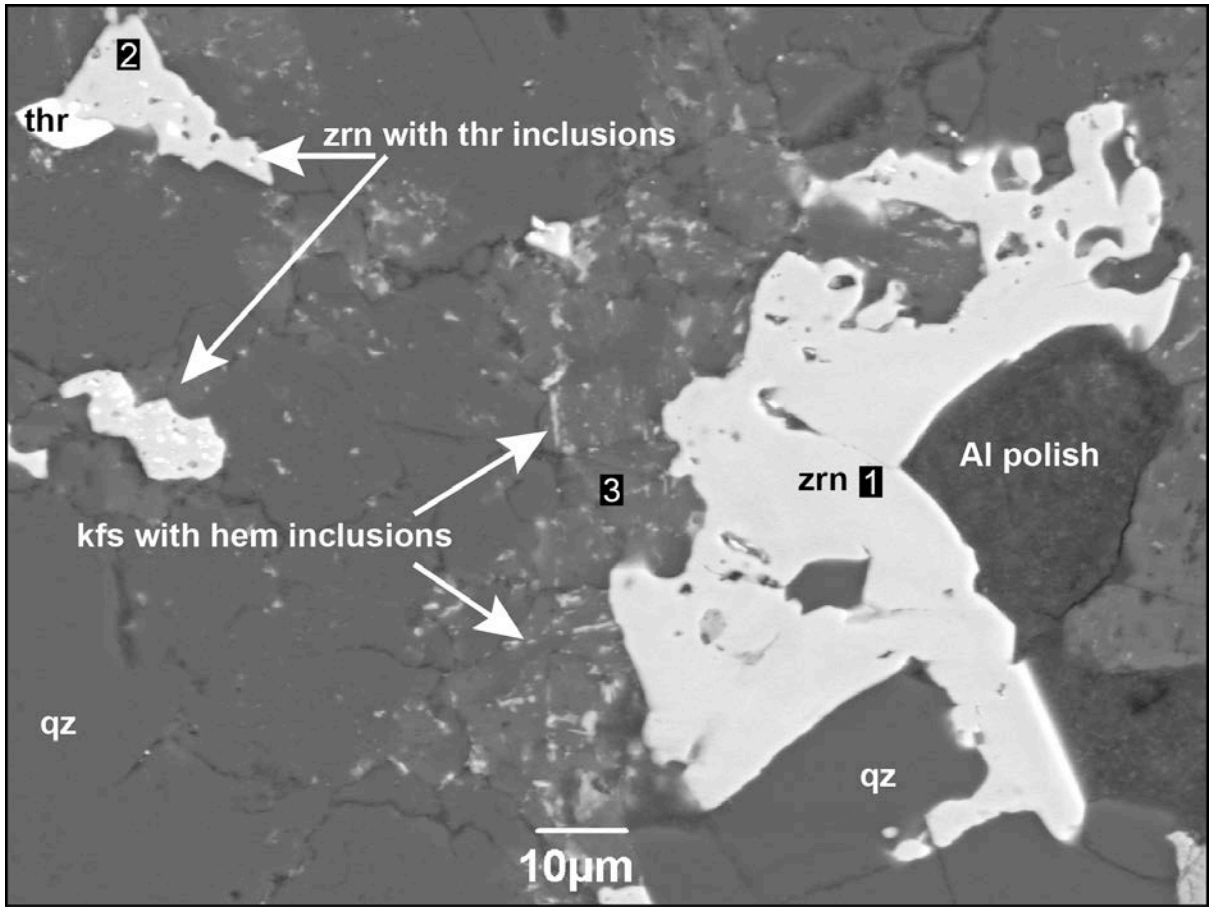

Figure 3.43: BSE image of late-stage zircons with and without thorite inclusions within an iron-rich potassium feldspar groundmass. Two populations of zircons have been identified within the Round Top rhyolites, a thorite inclusion-poor (1) and a thorite inclusion-rich (2) population as first described by Rubin et al. (1989). The zircons are late-stage as evident by their highly anhedral and somewhat interstitial nature. Note the hematitic pore fill near the zircons within the potassium groundmass (3). Sample ORT263-04.

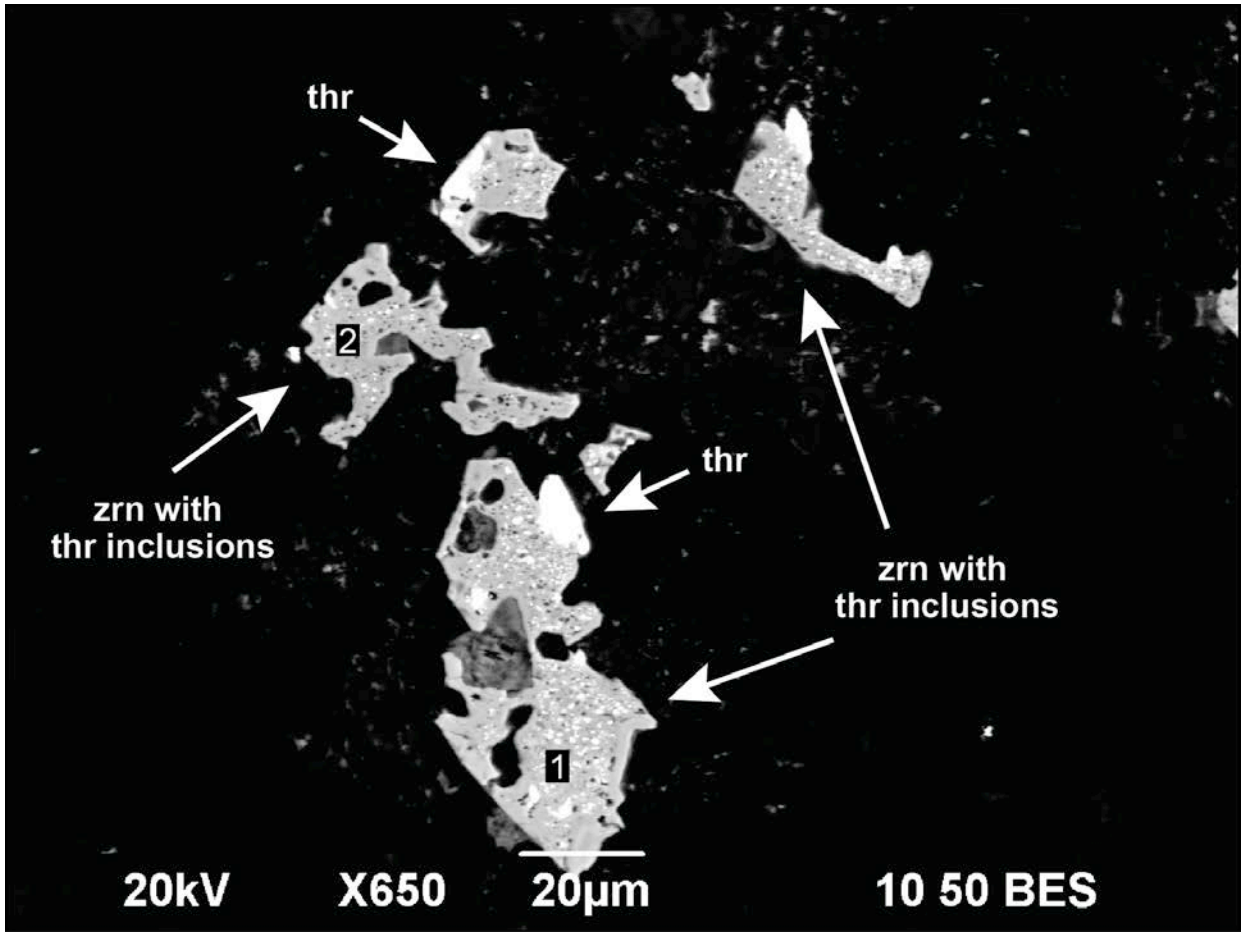

Figure 3.44: BSE image of a cluster of subhedral and anhedral zircon phenocrysts. Euhedral to subhedral zircon phenocrysts (1) are rare. Typically the zircons are anhedral (2) and display amoeboid-like morphologies with abundant embayments and thorite overgrowths. All of the zircons featured contain abundant thorite inclusions. Sample ORT266-01

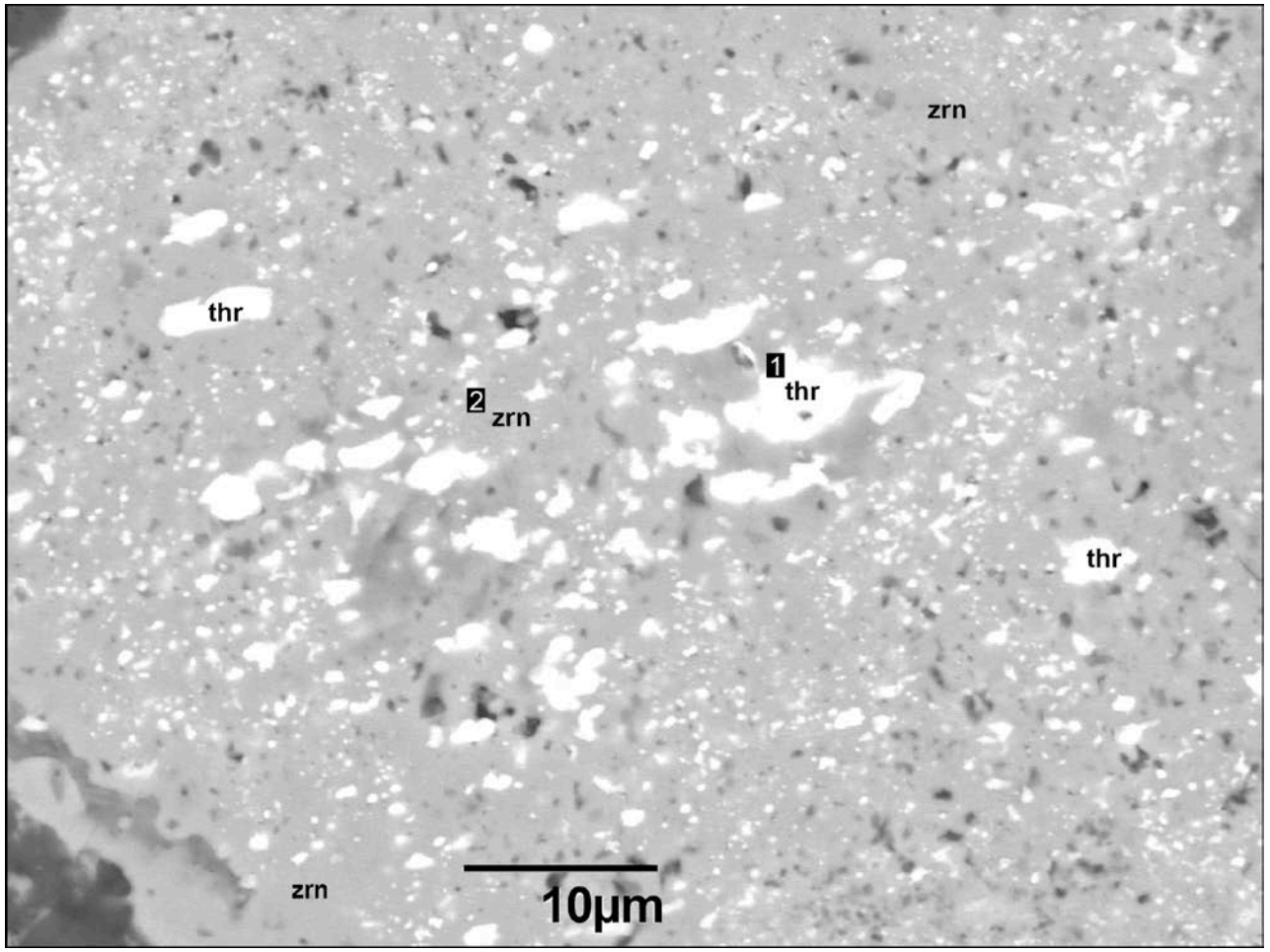

Figure 3.45: BSE image of thorite inclusions within a zircon phenocryst. The thorite inclusions range from <1-10 µm and compose approximately 20-50% of the zircon phenocryst. The darker voids presumably contained thorite inclusions at one point, but were plucked during the thin section process. Sample ORT266-02.63

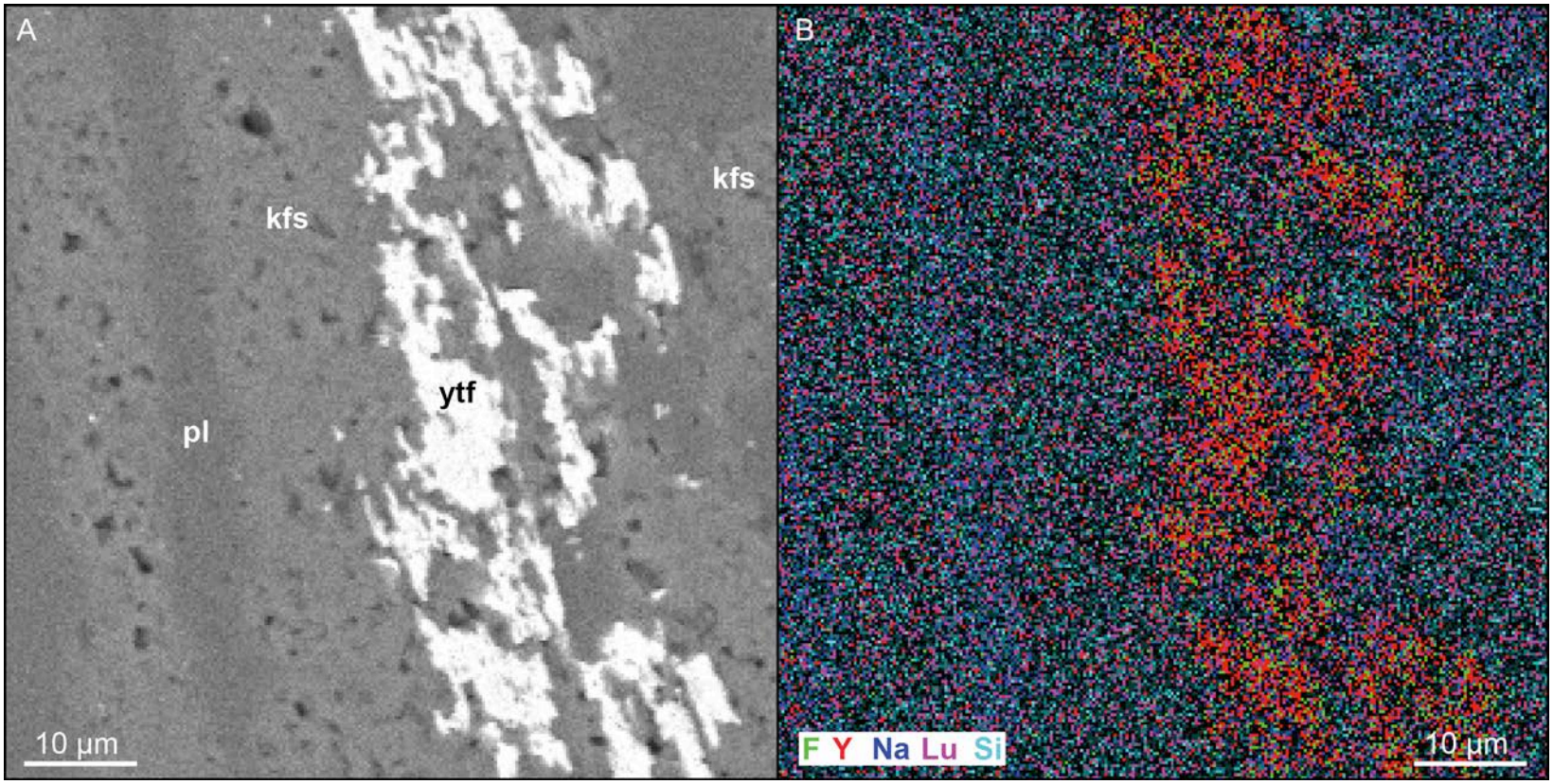

Figure 3.46: BSE image and EDS map of yttrofluorite inclusions within the outer portion of a feldspar phenocryst. A) The yttrofluorite appears to be comprised of multiple anhedral pore-filling crystals each <1-10 µm in length. The REE-fluorides most commonly occur as pore-filling type morphologies associated with the potassium portions of the rhyolite. The highly anhedral-wispy nature of the yttrofluorite suggests rapid crystallization. The combined length of the inclusions is approximately 100 µm (not fully shown). B) The EDS map highlights the patchy nature of the yttrofluorite, rich in fluorine and yttrium. Sample ORT266-02.65

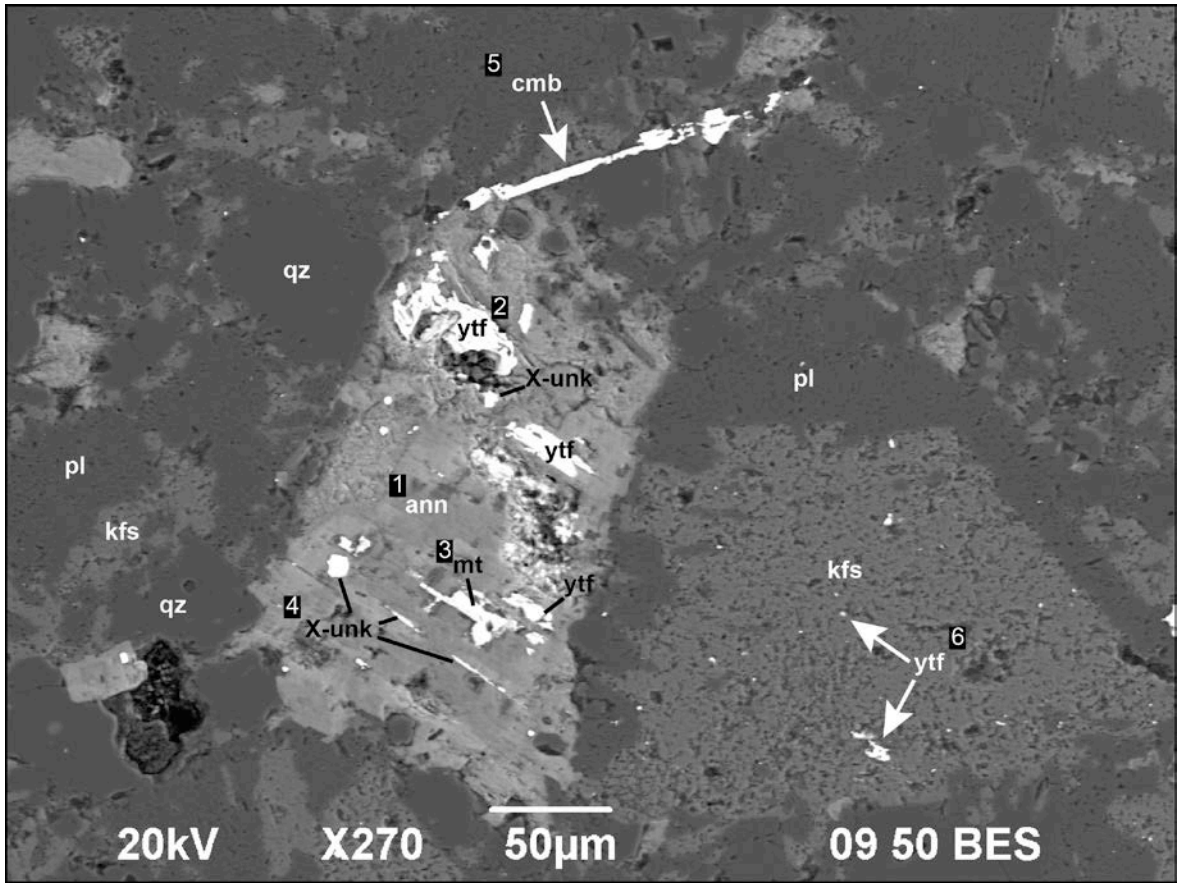

Figure 3.47: BSE image of an annite phenocryst with multiple mineral inclusions. The inclusions include yttrofluorite (2), magnetite (3), and (X)-unknown mineral (4). REE-inclusions typically partially conform to the direction of the biotite basal cleavage. Changbaiite is visible in close association with the annite phenocryst (5), as is multiple yttrofluorite inclusions (6) within the adjacent potassium feldspar phenocryst. Sample ORT270-01.81

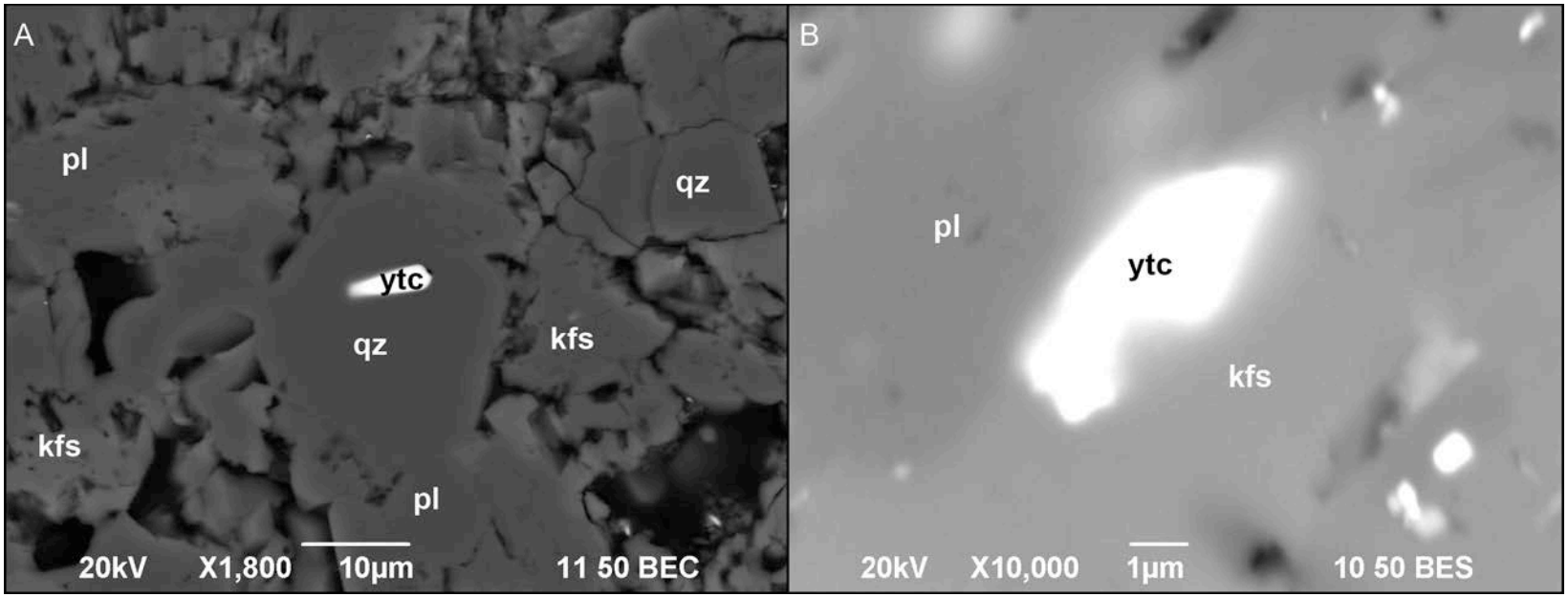

Figure 3.48: BSE images of yttrocerite inclusions within quartz and the groundmass. A) Image of late-stage anhedral yttrocerite inclusion within a quartz phenocryst. Inclusions of REE-fluorides range greatly in size and form, anywhere from 1-40 µm in diameter. It is unclear if this yttrocerite inclusion formed conterminously with the host quartz crystal or somehow became entrained at a later point. B) BSE image of late-stage yttrocerite inclusions with potassium and plagioclase feldspar groundmass. Pore-filling REE-fluorides are the most common form of the minerals. They typically are anhedral and range from <1-10 µm in diameter. They may occur as individual crystals or within clusters. Samples ORT44-20.006 and ORT264-01.20

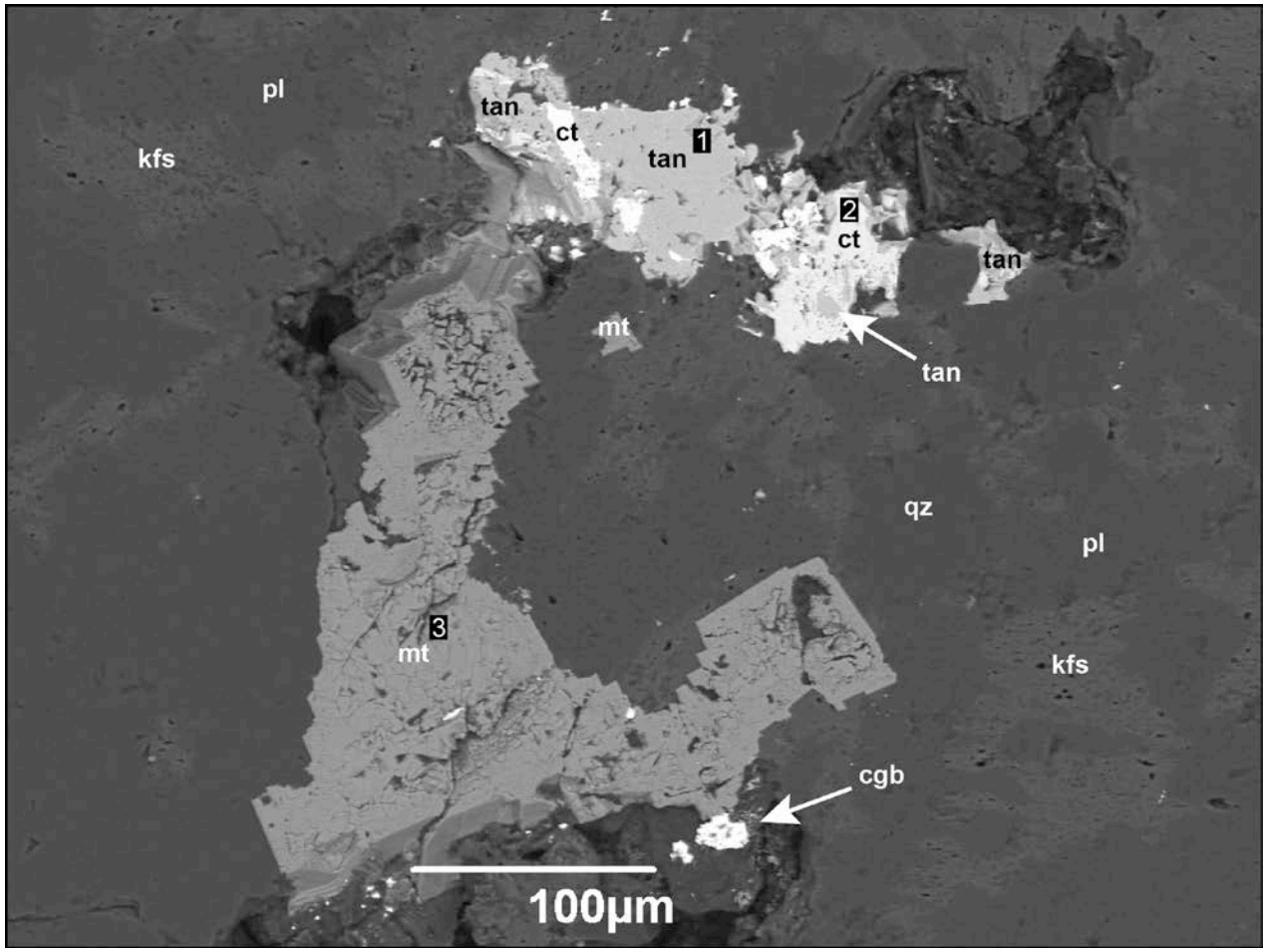

Figure 3.49: BSE image of intergrown tantalite and cassiterite, in close proximity to a magnetite phenocryst. The intergrown nature of the tantalite (1) and cassiterite (2) suggests that crystallization was contemporaneous and possibly contemporaneous with the magnetite (3). Trace phases most commonly occur in close proximity to other trace and accessory phases, as seen here. Sample ORT266-02.61

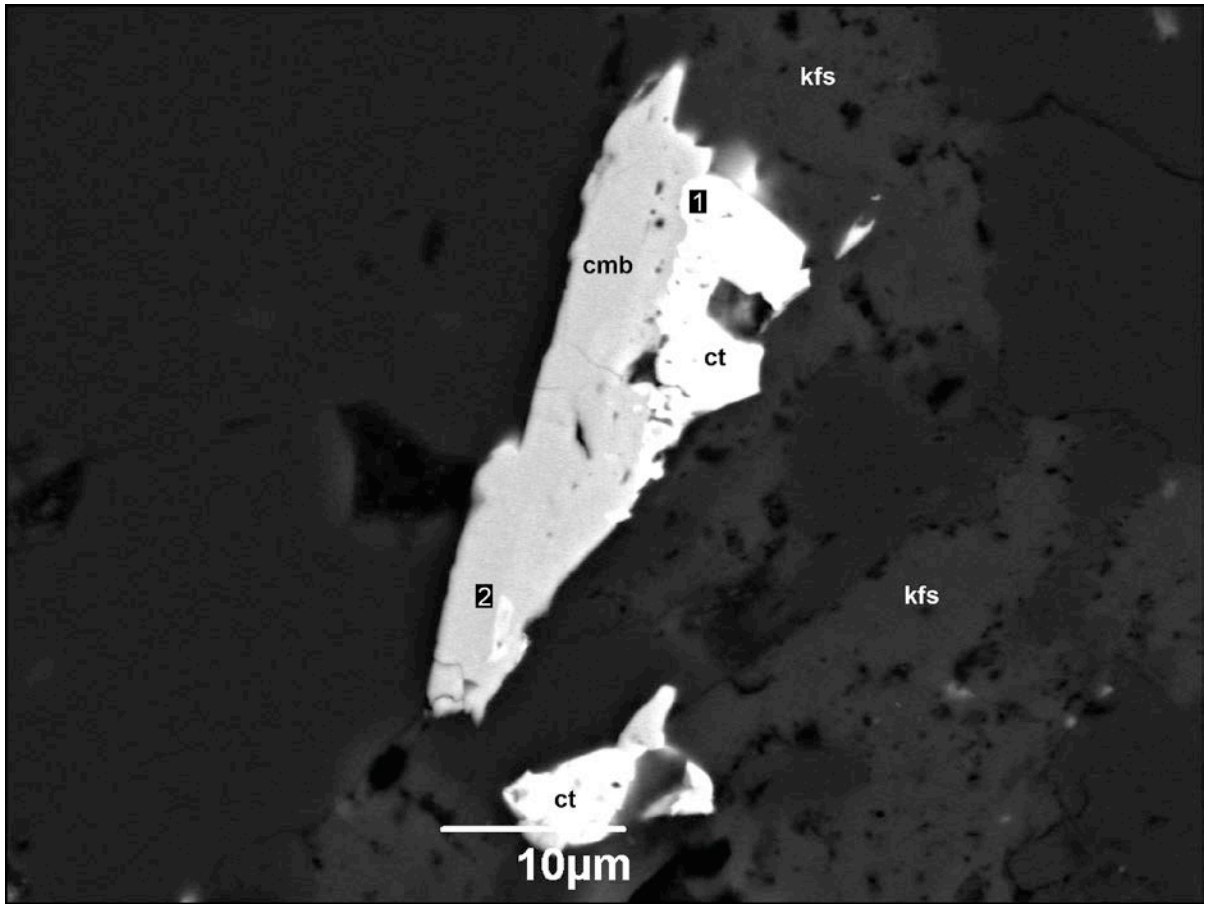

Figure 3.50: BSE image of late-stage intergrown cassiterite and columbite crystals. Note the undulatory boundary between the two grains (1) and inclusion of cassiterite within the columbite (2) representing concurrent crystallization. The trace phases are within interstitial to other crystals and within the potassium feldspar portion of the groundmass. The brightness and contrast settings have been turned down in order to be able to see the mineral relationship. Sample ORT266-02.53

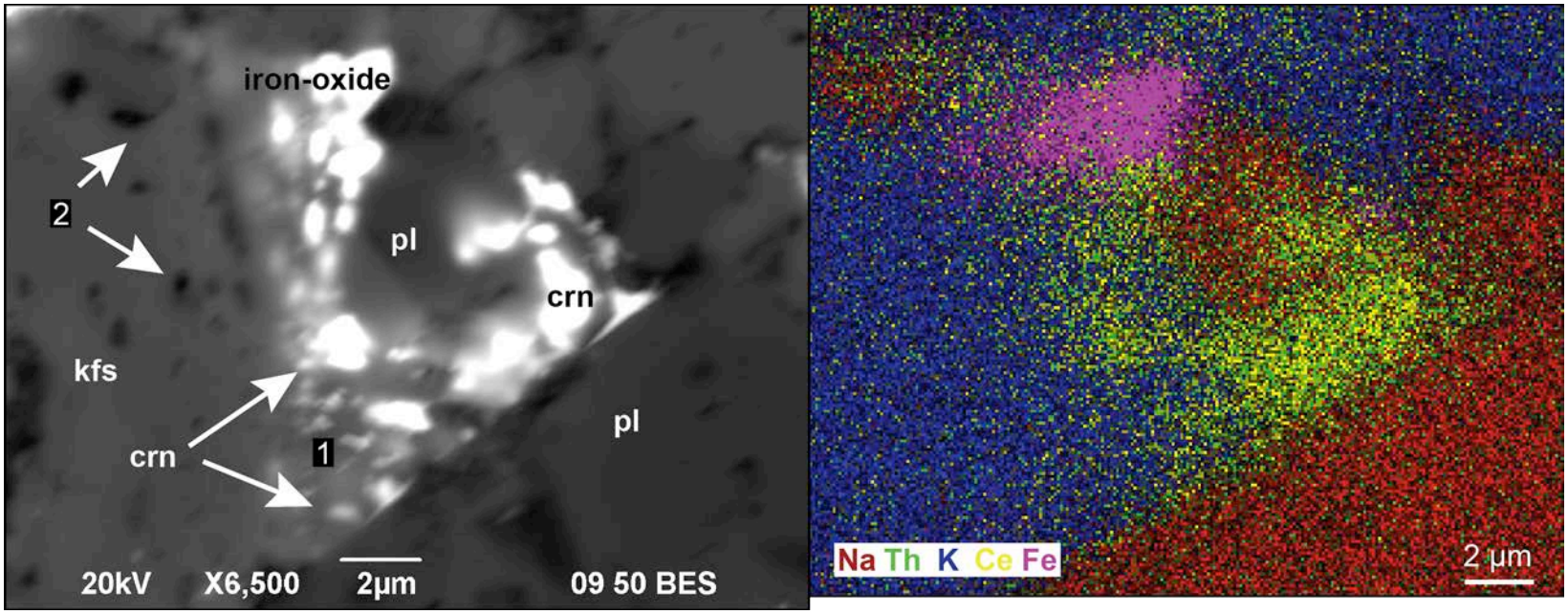

Figure 3.51: BSE image and EDS map of late-stage anhedral cerianite group. A) The cerianite group is comprised of many small cerianite crystals ranging from <1-2 µm in diameter. The cerianite appears to be filling the pore spaces of the potassium feldspar groundmass (1). The void pores (2) within the groundmass appear to be of a similar shape and size as that of the cerianite crystals. This late-stage cerianite has distinct wispy tails, which form along the boundaries of the adjacent minerals and groundmass. B) The EDS map indicates the cerianite rich In Ce and Th. An iron mineral is located at the upper portion of the map, and is potentially magnetite. Sample ORT270-01.78

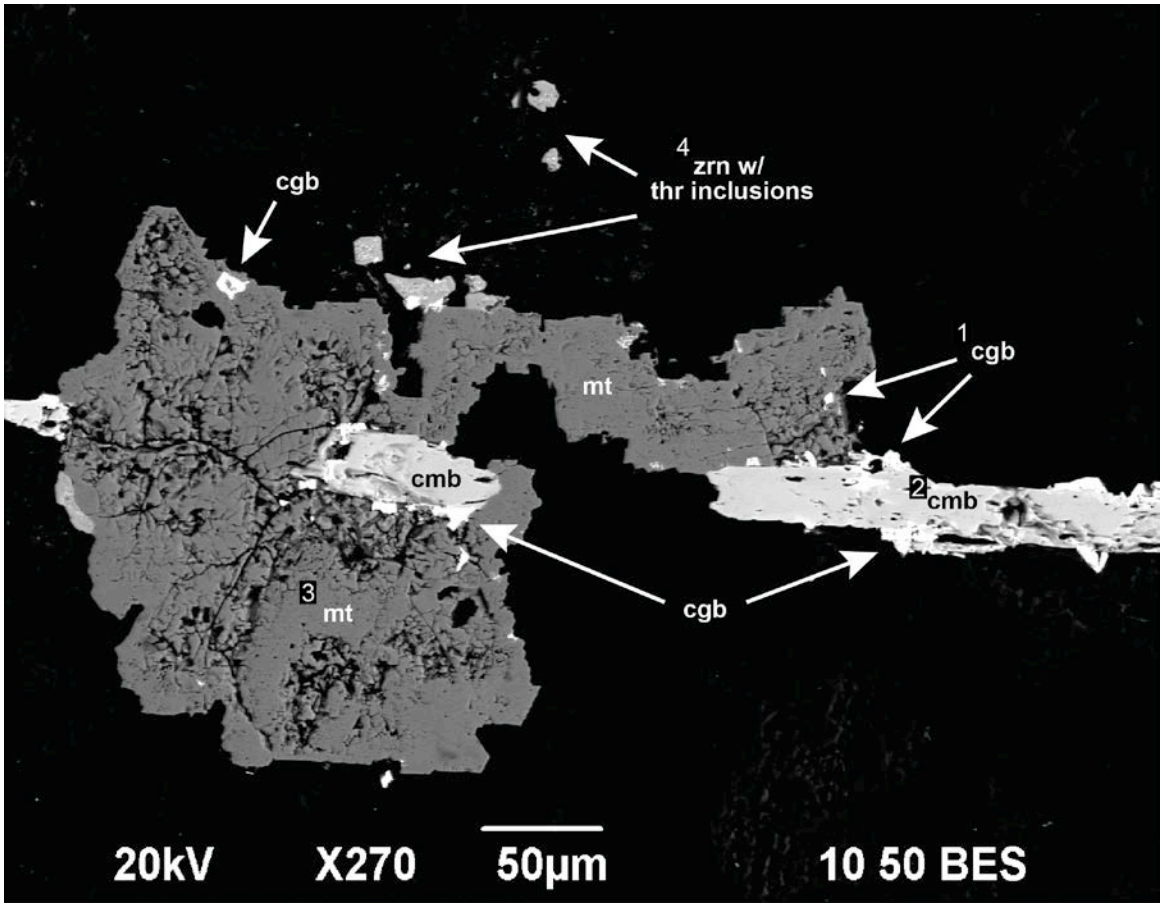

Figure 3.52: BSE image of intergrown changbaiite and columbite phenocrysts. The intergrown changbaiite (1) and columbite (2) are inclusions within a magnetite phenocryst (3) and adjacent to thorite-rich zircons (4). The intermingled nature of the phenocrysts suggests crystallization of the mineral suite was contemporaneous. The contrast and brightness on the EDS detector has been turn down in order to be able to see the individual mineral components. Sample ORT266-01.98

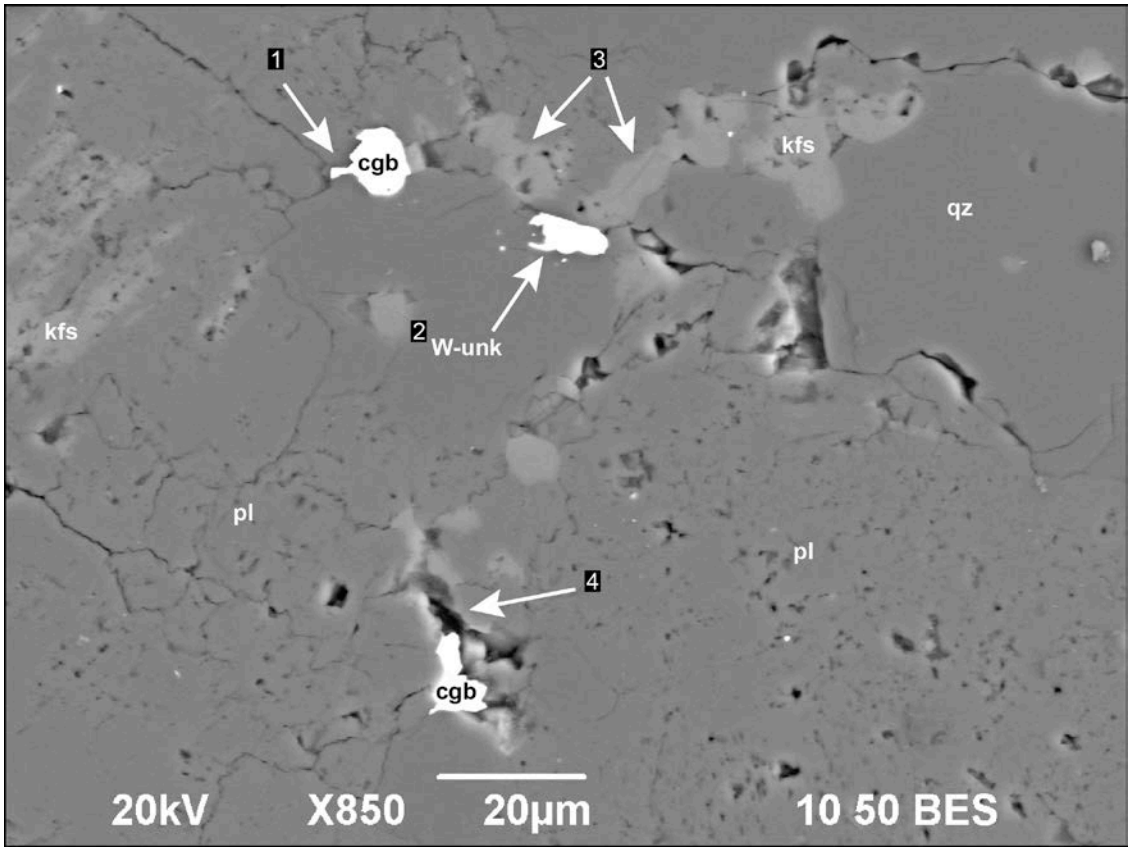

Figure 3.53: BSE image of fracture fill changbaiite and the (W)-unknown mineral. The minerals occur along the boundaries of other minerals and within microscopic fractures within the groundmass. The changbaiite and (W)-unknown minerals are anhedral and appear to have irregular, tail like edges (1 & 2). This morphology suggests late-stage crystallization, subsequent to the formation of the surrounding crystals and fractures. Additionally, is appears that potassium-rich groundmass is pervasive along the microscopic fractures (3). Large void spaces along the microscopic fractures and adjacent to the changbaiite (4), at one point potentially contained more trace phases that since have been plucked during the thin section making process. Sample ORT264-01.26

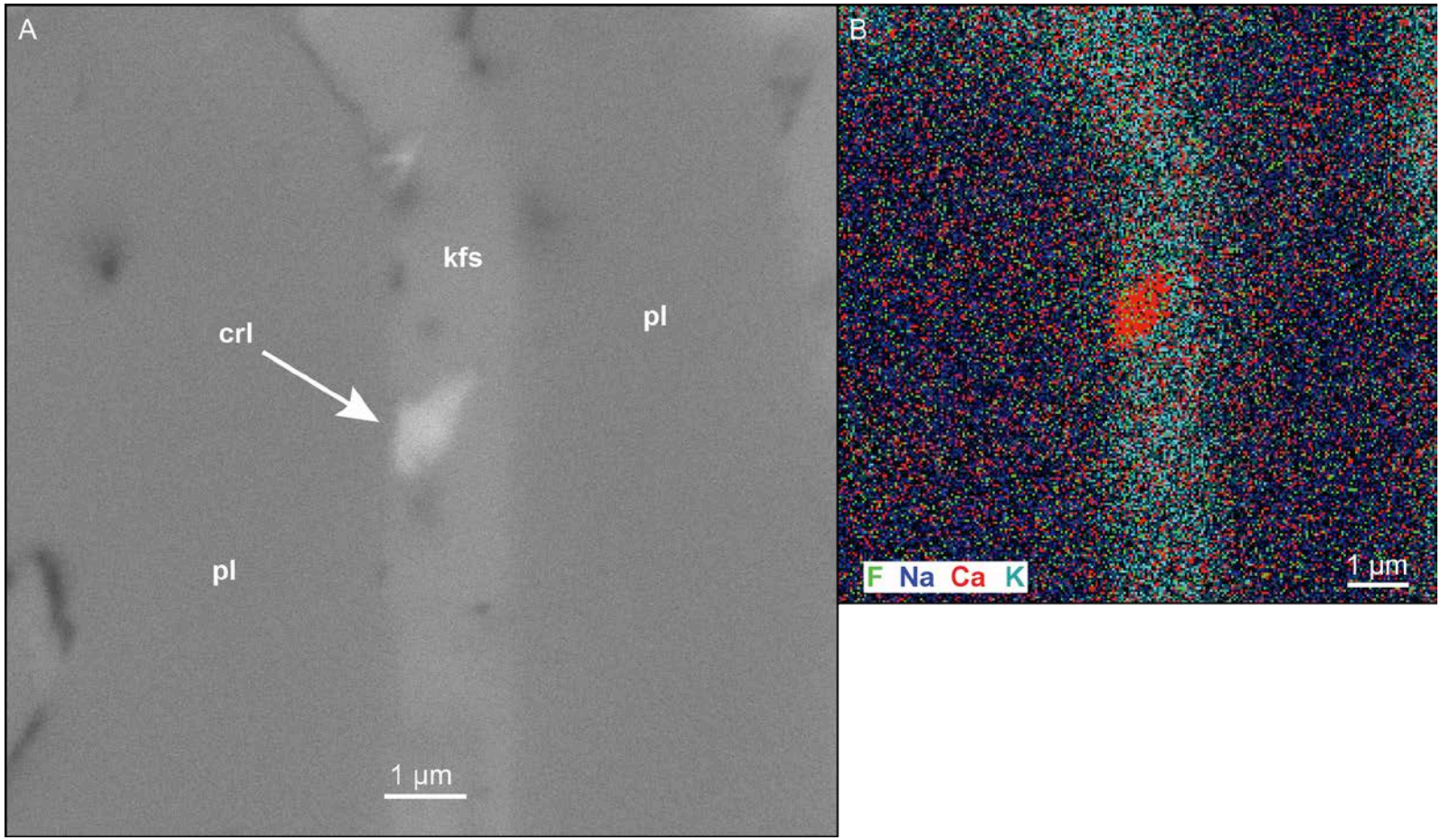

Figure 3.54: BSE image and EDS map of a cryolite inclusion within the potassium feldspar portion of the rhyolite groundmass. Only two examples of cryolite were identified within the scope of this study, and each occurred as small (~1 µm) anhedral inclusions within the groundmass. EDS analyses indicates the cryolite is rich in Ca, which may be substituting for Na. Sample ORT264-01

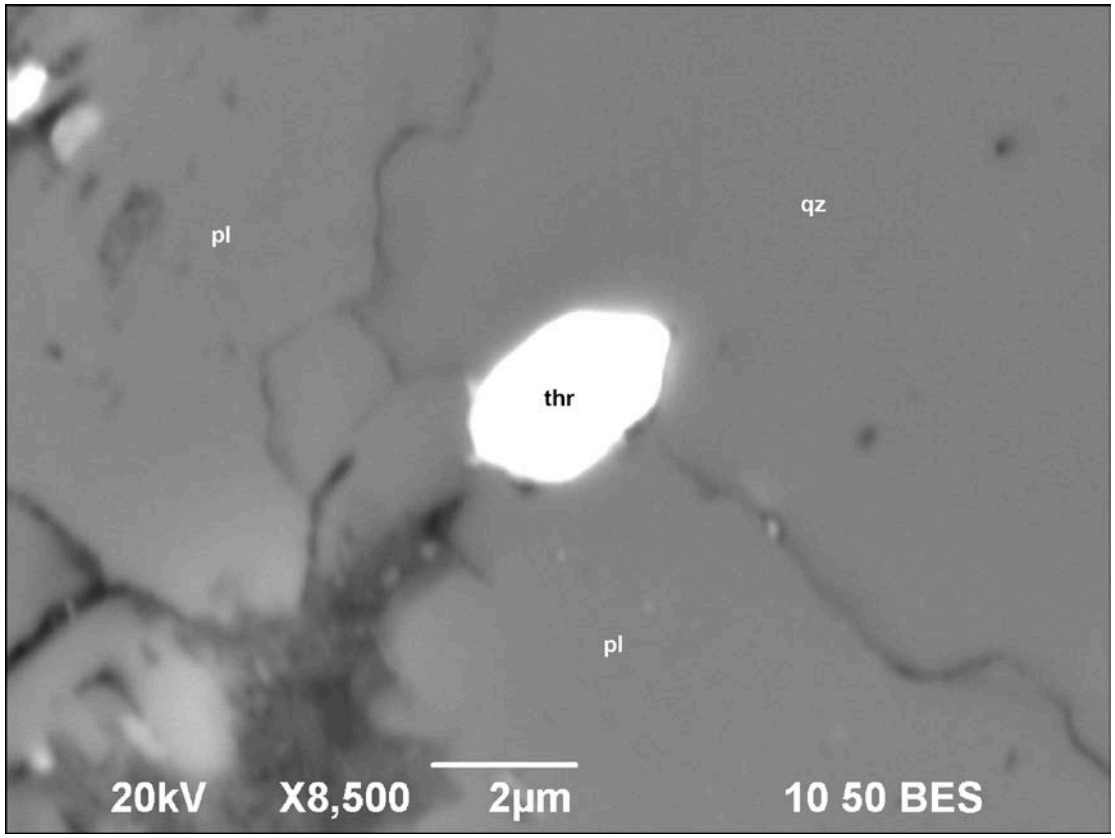

Figure 3.55: BSE image of late-stage thorite interstitial to the groundmass. Thorite occurs in two forms within the rhyolites, 1) as inclusions to and in close association with zircon phenocrysts (Figure 3.44), and 2) as individual crystals typically interstitial and along grain boundaries. Both populations of thorite are anhedral and may range from <1-10 µm in diameter. The inclusions of thorite within the zircon phenocrysts range from 20-50% of the overall host. Individual thorite crystals typically occur within the groundmass, and may be isolated from other minerals or occur in a group with other thorite crystals. Sample ORT264-01.19

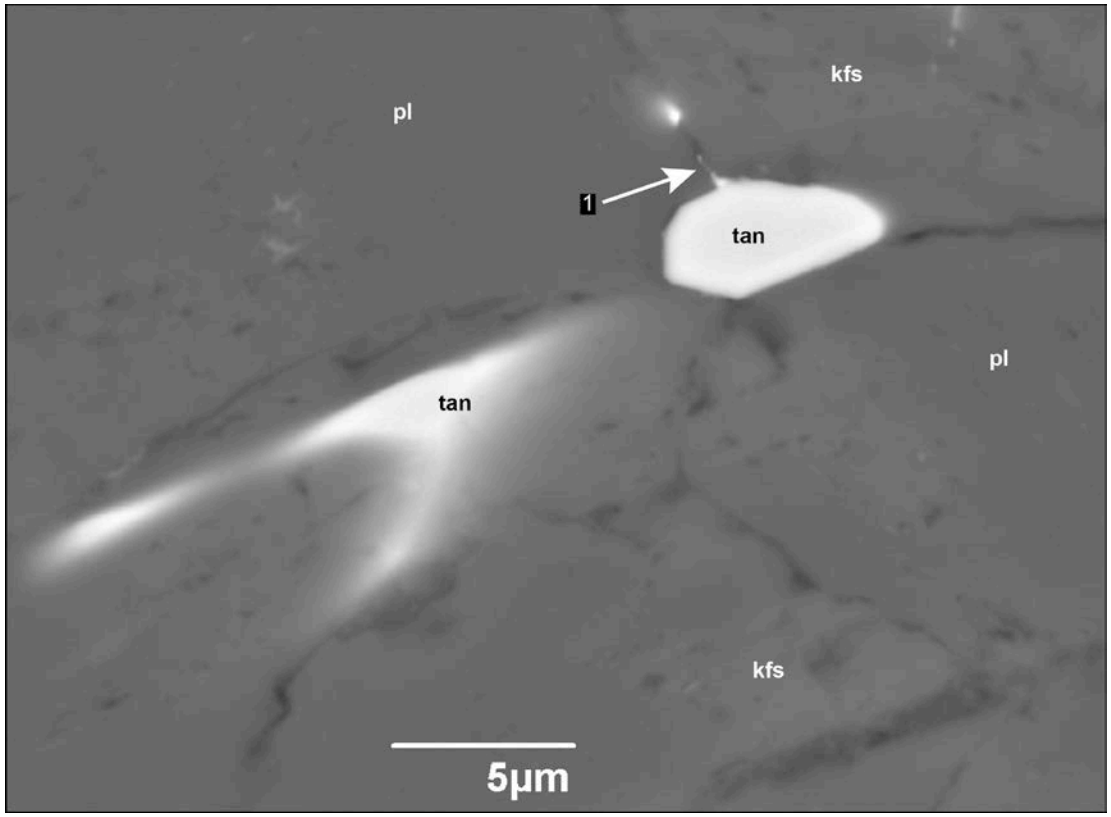

Figure 3.56: BSE image of tantalite interstitial to the potassium and plagioclase feldspar groundmass. Tantalite occurs in two forms, 1) as phenocrysts in close relation to other trace and accessory phases (Figure 3.48), and 2) as interstitial small crystals within the groundmass. The intermingled relationship to other minerals and the anhedral pore-filling type nature of the interstitial crystals suggests probable late-stage crystallization within the petrogenic sequence. When intestinal to the groundmass, the tantalite commonly forms tail-like structures (1) along the boundaries of the surrounding crystals. For these structures to form, the surrounding minerals must be present prior to the formation of the tantalite. Sample ORT263-04.50

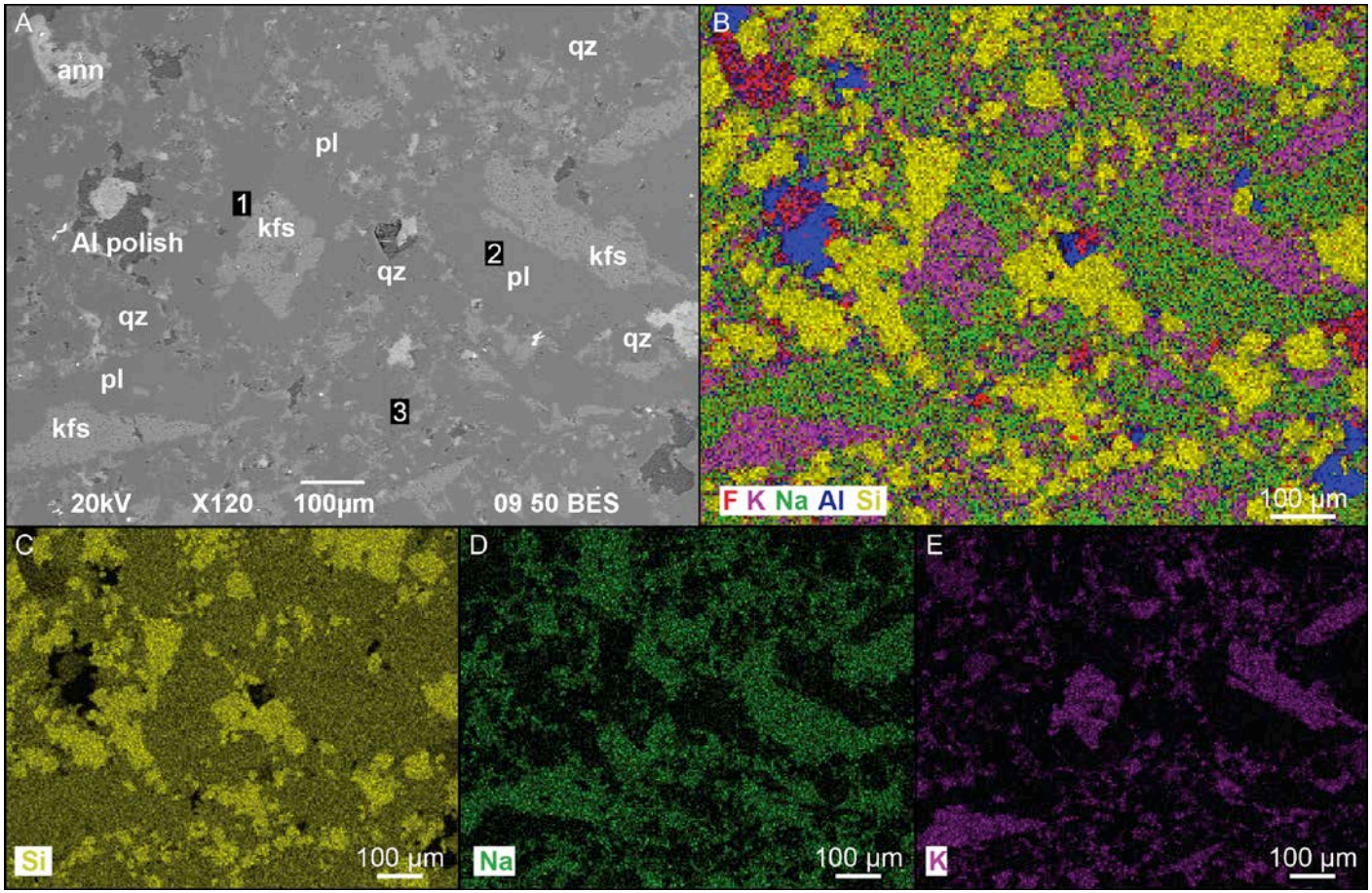

Figure 3.57: BSE image and EDS maps of the typical rhyolite groundmass, rich in potassium, sodium, and silica. A) The groundmass is comprised on subhedral to anhedral, intermingled patches of potassium feldspar (1), plagioclase feldspar (2), and quartz (3). B) Combined EDS map that shows the overall anhedral-patchy nature of the groundmass, suggesting rapid crystallization. C-E) EDS maps of the Si, Na, and K-rich portions of the groundmass. Sample ORT270-01.84

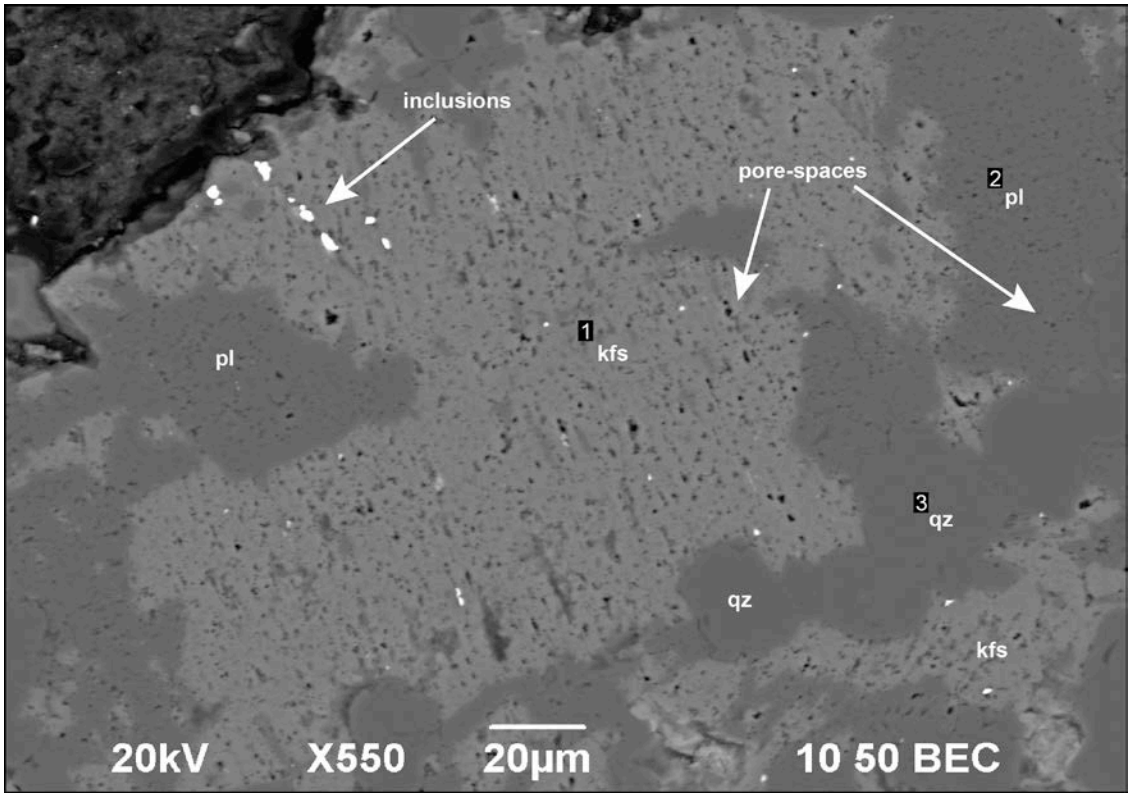

Figure 3.58: BSE image of the rhyolite groundmass composed of anhedral intermingled porous potassium feldspar and plagioclase with subhedral quartz. The potassium feldspar when viewed with the BSE detector is a light gray tone with abundant voids (1). The pores of the potassium feldspar appear to be lineated, forming along linear structures within the groundmass. The plagioclase feldspar is a medium gray tone with minor voids (2). The plagioclase contains less pore spaces then the potassium feldspar and the pores are typically smaller in size then those of the potassium feldspar. The quartz is of a similar medium gray tone to the plagioclase, but is smooth in appearance with no pores (3). The potassium portion of the groundmass commonly contains inclusions of accessory and trace minerals within the abundant pore spaces. Sample ORT266-01.105

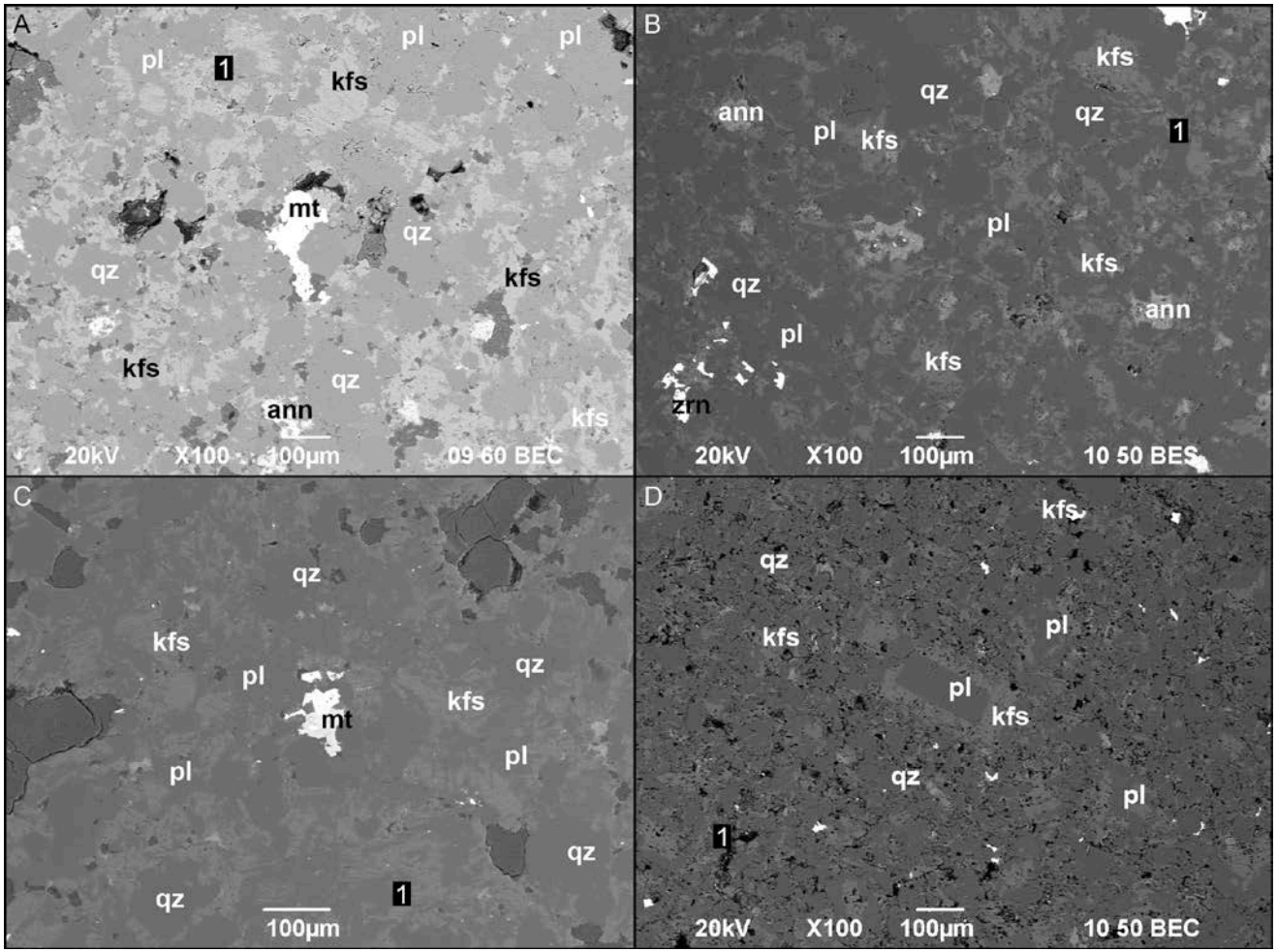

Figure 3.59: BSE images comparing the typical groundmass of the gray, purple, red and tan rhyolites. Figure 3.59 full caption, next page.

Figure 3.59 continued: The groundmass of the gray, purple, and red rhyolites is very similar compositionally and texturally and contains abundant intermingled anhedral potassium feldspar, plagioclase feldspar, and subhedral quartz. The feldspar portion of the groundmass typically appears as intermingled patches of potassium and plagioclase (1). A) BSE image of typical gray rhyolite groundmass. The gray rhyolite appears to have a slightly more quartz within the groundmass then the purple or red rhyolites. B) BSE image of typical purple rhyolite groundmass. The purple rhyolite appears to have a slightly less amount of the intermingled feldspar texture then the gray or red rhyolites. C) BSE image of typical red rhyolite groundmass. The red rhyolite appears to have slightly more of the intermingled feldspar texture then gray or purple rhyolites. D) BSE image of typical tan rhyolite groundmass. The groundmass of the tan rhyolite is more porous (1) than the other types of rhyolite, and lacks the abundant intermingled feldspars characteristic to the other three. Of the four types of rhyolite, the tan appears to have the least amount of potassium feldspar. The gray and tan rhyolites have slightly more quartz within the groundmass (25%) than the purple and red (15-20%). Samples ORT264-01.6, ORT266-01.93, ORT263-01.46, and ORT44-01.8

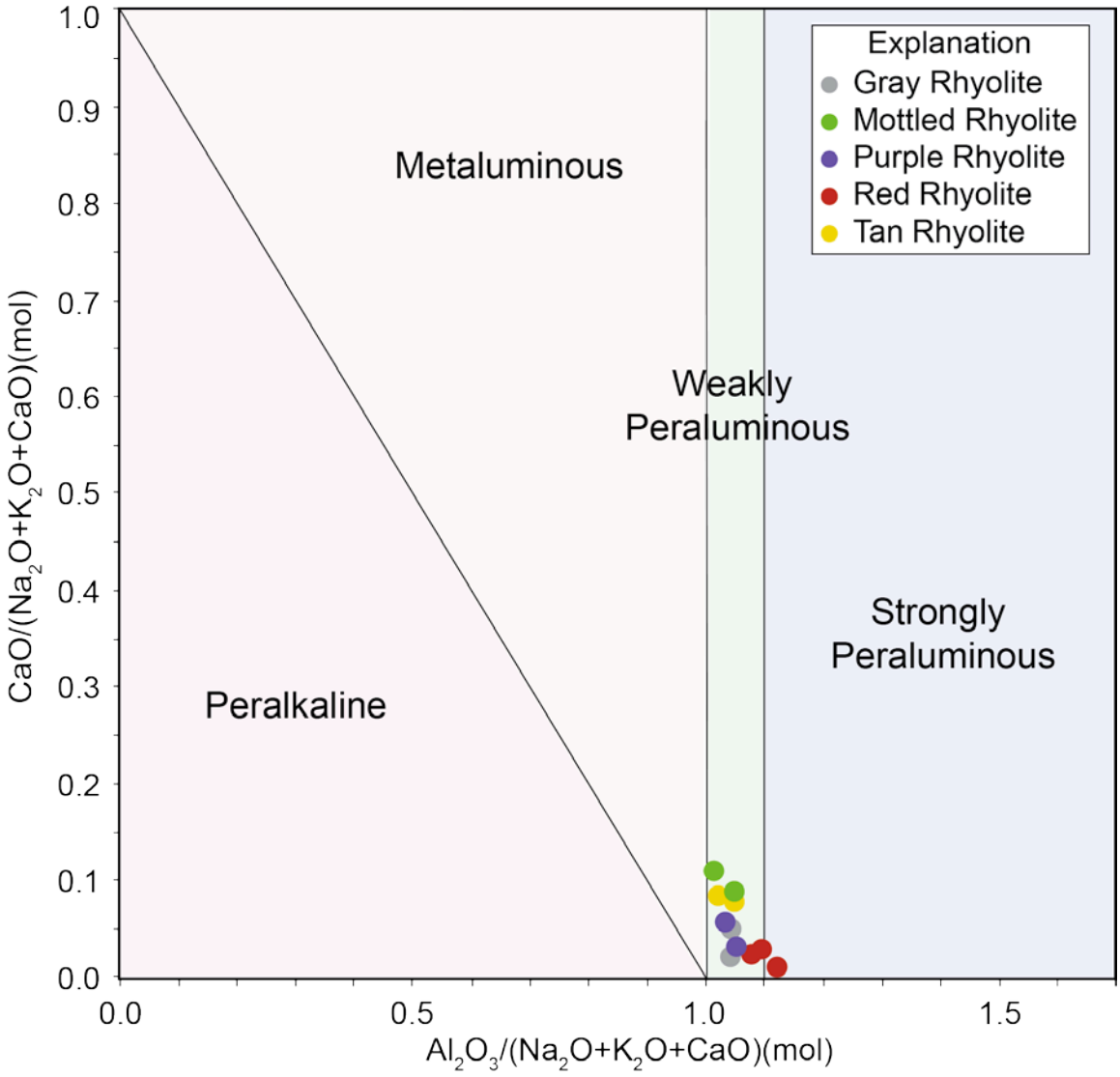

Figure 3.60: The Round Top rhyolite samples plotted against the Alumina Saturation in Igneous Rocks classification diagram as defined by Barton and Young (2002). All rhyolite samples fall within the weakly peraluminous field except for one red rhyolite sample which falls just within the strongly peraluminous field. A peraluminous classification indicates the presences of an excess of alumina over the required amount necessary to form feldspar during crystallization (i.e. Al2O3 > Na2O+K2O+CaO mol).

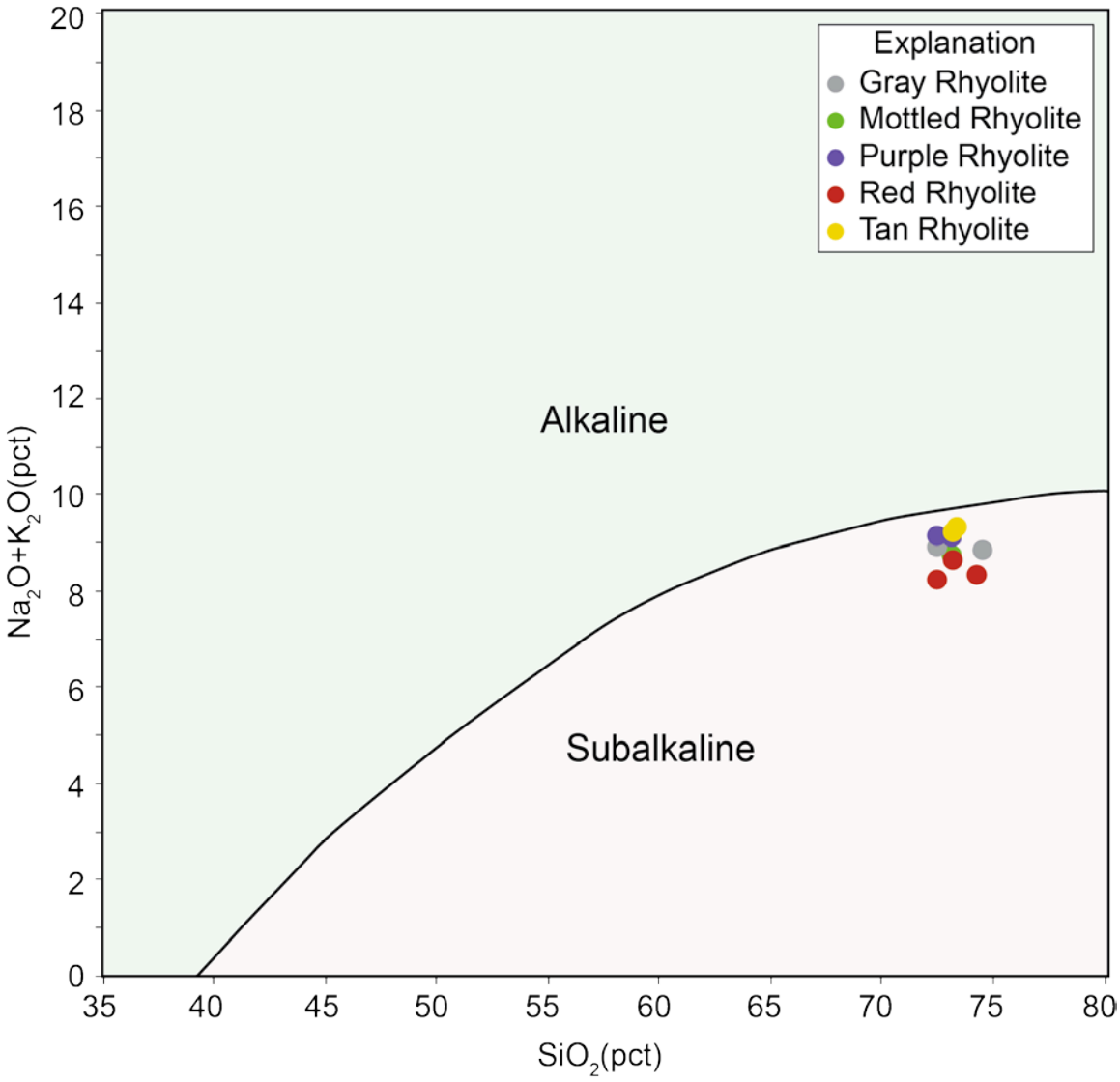

Figure 3.61: The Round Top rhyolite samples plotted against the Alkaline/Subalkaline classification diagram, boundary curve defined by Irvine and Baragar (1971). All of the rhyolite samples fall just within the subalkaline classification. The red rhyolite types are slightly less alkaline then the other varieties.

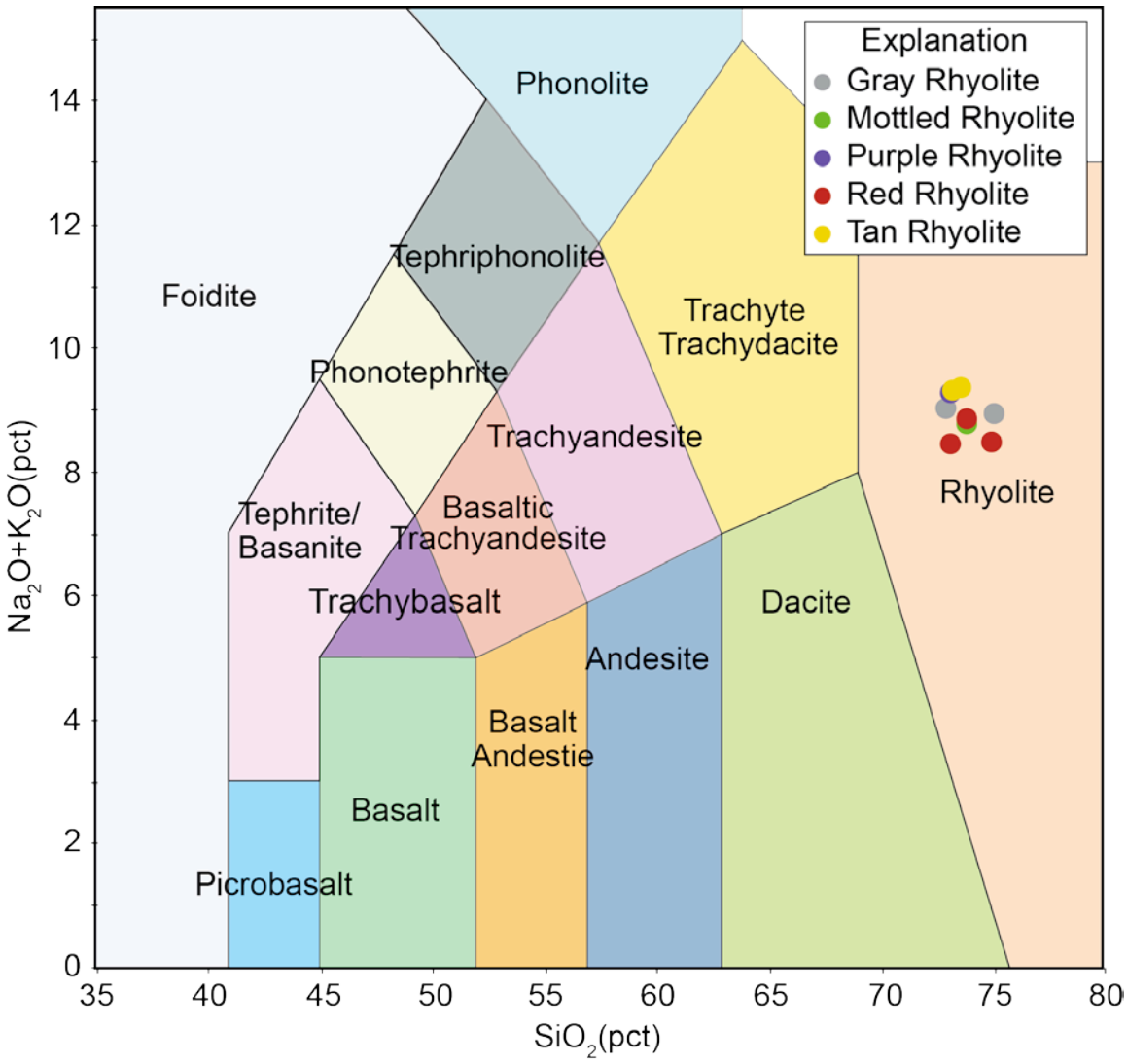

Figure 3.62: The Round Top rhyolite samples plotted against the Total Alkali vs. Silica (Na2+K2O vs. SiO2) classification diagram for igneous rocks as defined by LeMaitre et al. (1989).

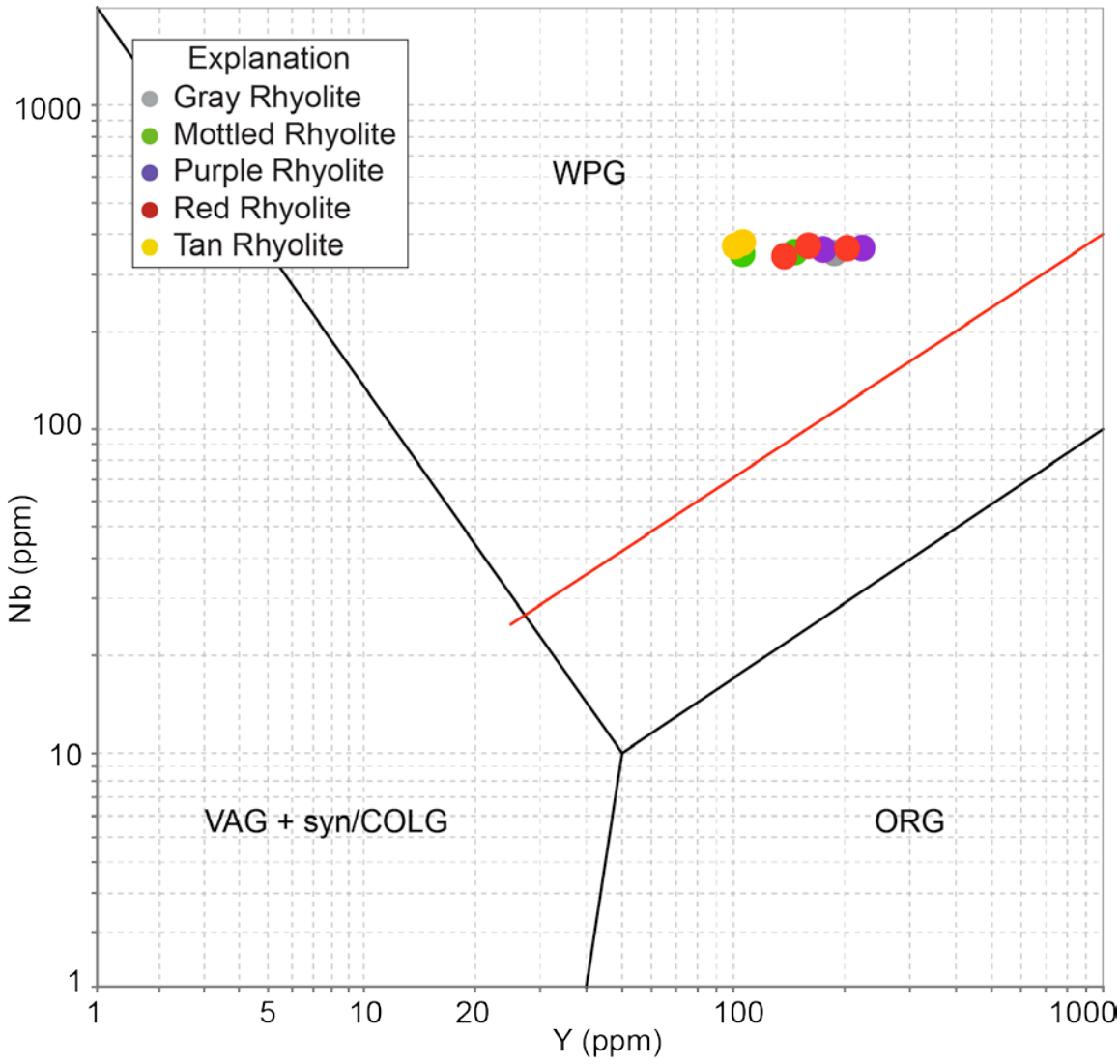

Figure 3.63: The Round Top rhyolite samples plotted against the Granite Nb/Y discrimination diagram as define by Pearce et al. (1984). All of the rhyolite samples fall within the Within Plate Granite (WPG) field denoting a continental provenance of the magma. The other fields are the Volcanic Arc Granite (VAG), Syncollisional Granite (syn-COLG), and Ocean Ridge Granite (ORG). The red line is the boundary for ORG from anomalous ridges.

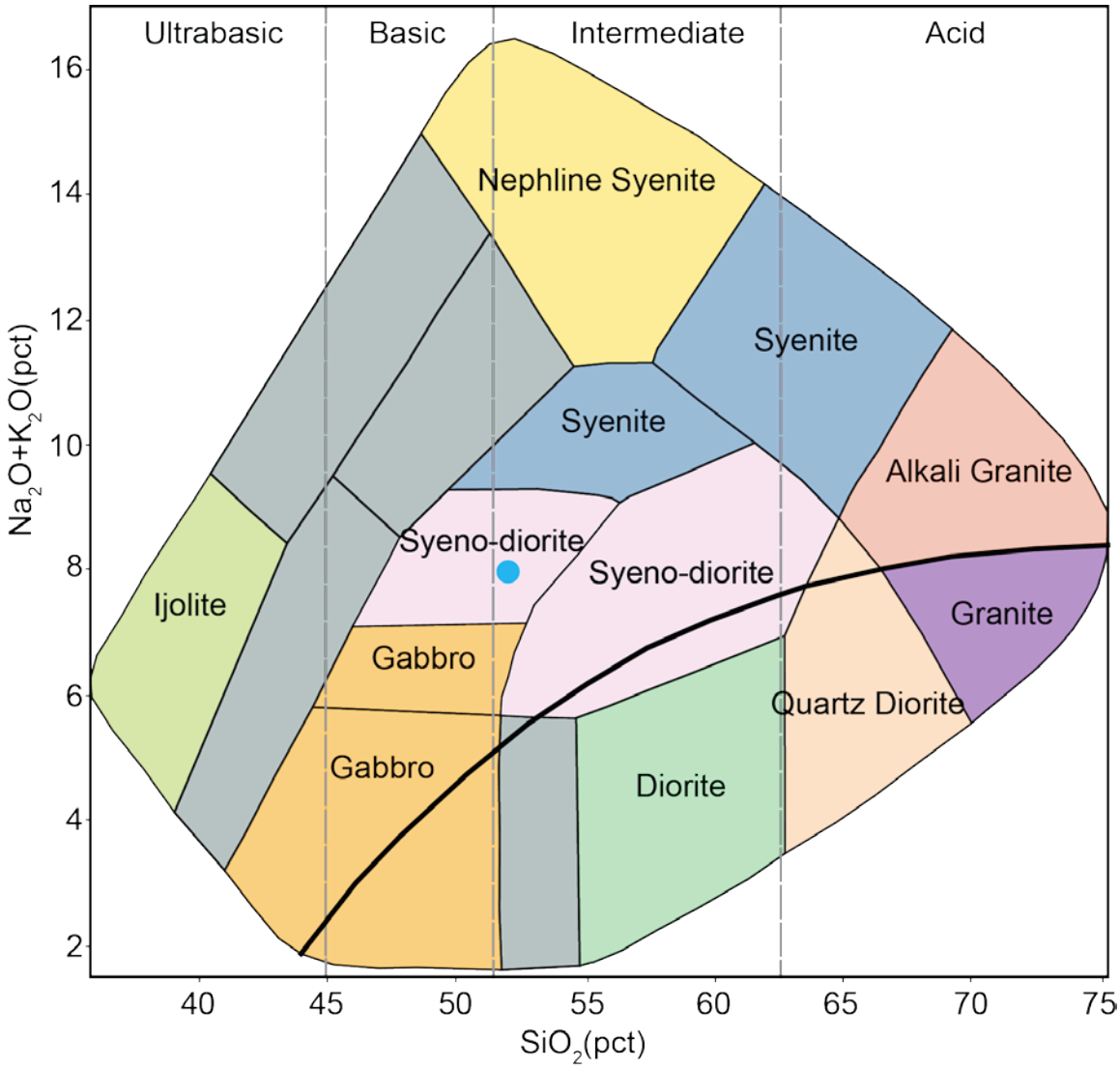

Figure 3.64: The Round Top sill sample plotted against the TAS Plutonic classification diagram (Cox et al. 1979, adapted by Wilson 1989). The sill that underlays the Round Top laccolith at the northern end is classified as a syeno-diorite. Granite Provenance Classification Diagram.

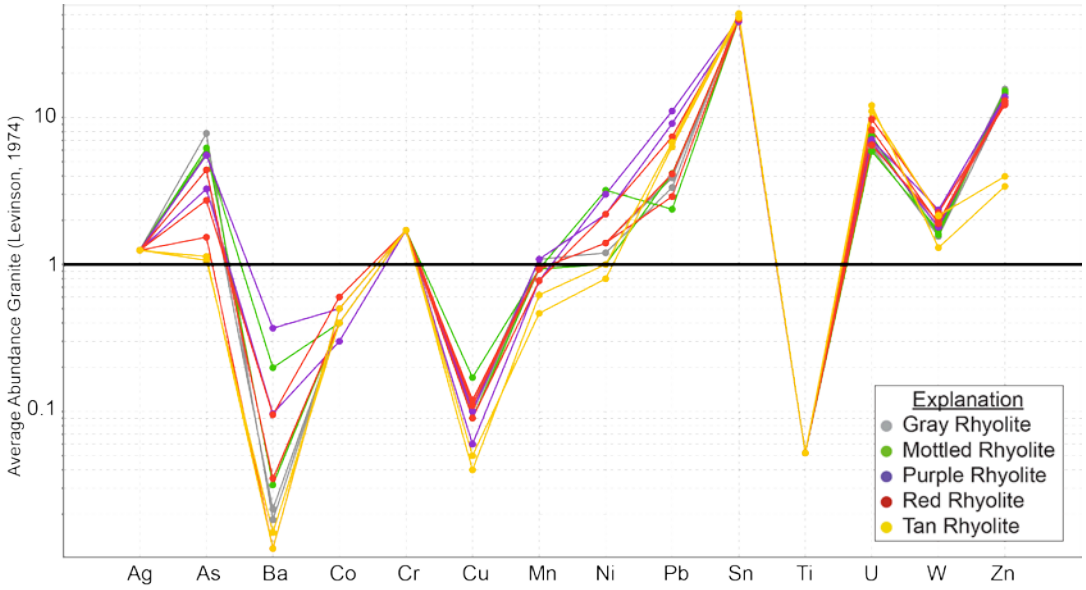

Figure 3.65: Spider diagram of the Round Top rhyolite samples versus the average elemental abundance of granite, as defined by Levinson (1974). Relative to the average granite, the rhyolites are enriched in As, Cr, Ni, Pb, Sn, U, W, and Zn. They are depleted in Ba, Co, Cu, Mn, and Ti.

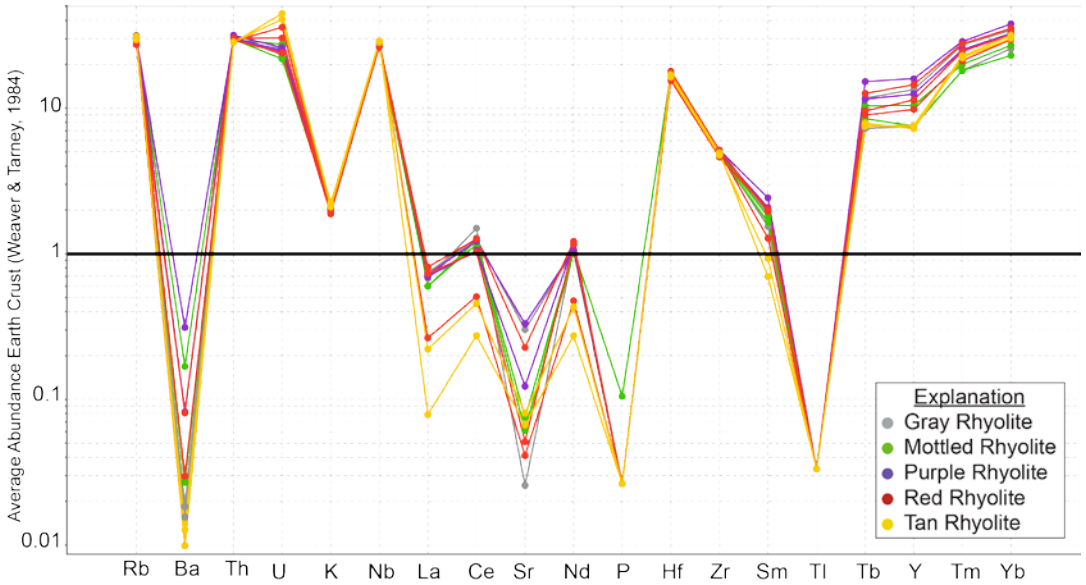

Figure 3.66: Spider diagram of the Round Top rhyolite samples versus the average elemental abundance of continental crust, as defined by Weaver and Tarney (1984). Relative to the average continental crust, the rhyolites are enriched in Rb, Th, U, K, La, Hf, Zr, Sm, Tb, Y, Tm, and Y. They are depleted in Ba, La, Sr, Nd, P, and Tl.

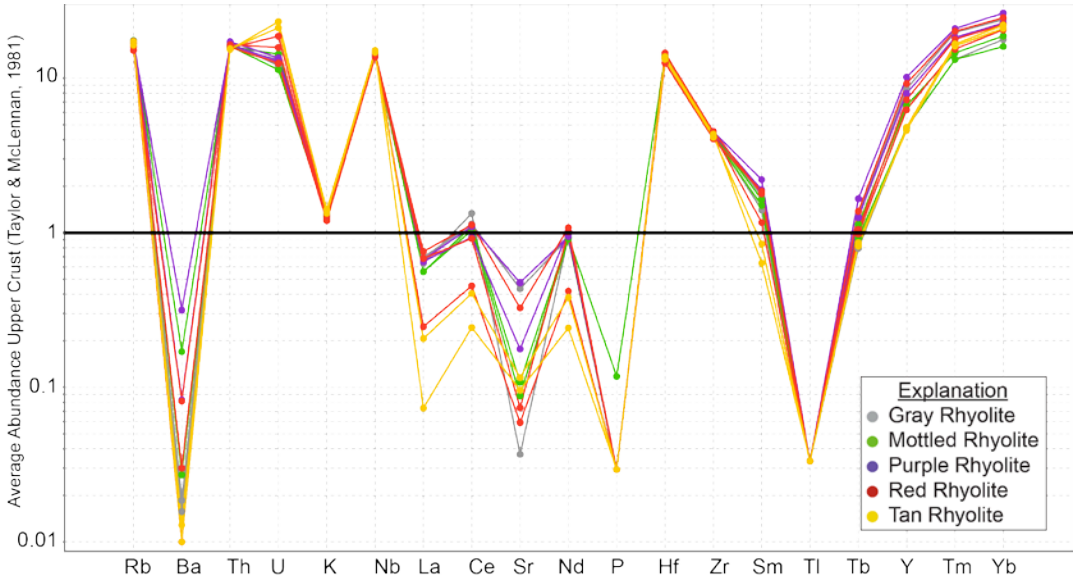

Figure 3.67: Spider diagram of the Round Top rhyolite samples versus the average elemental abundance of the upper crust, as defined by Taylor and McLennan (1981). Relative to the upper crust, the rhyolites are enriched in Rb, Th, U, K, Nd, Hf, Zr, Sm, Tb, Y, Tm, and Yb. They are depleted in Ba, La, Ce, Sr, Nd, P, and Tl.

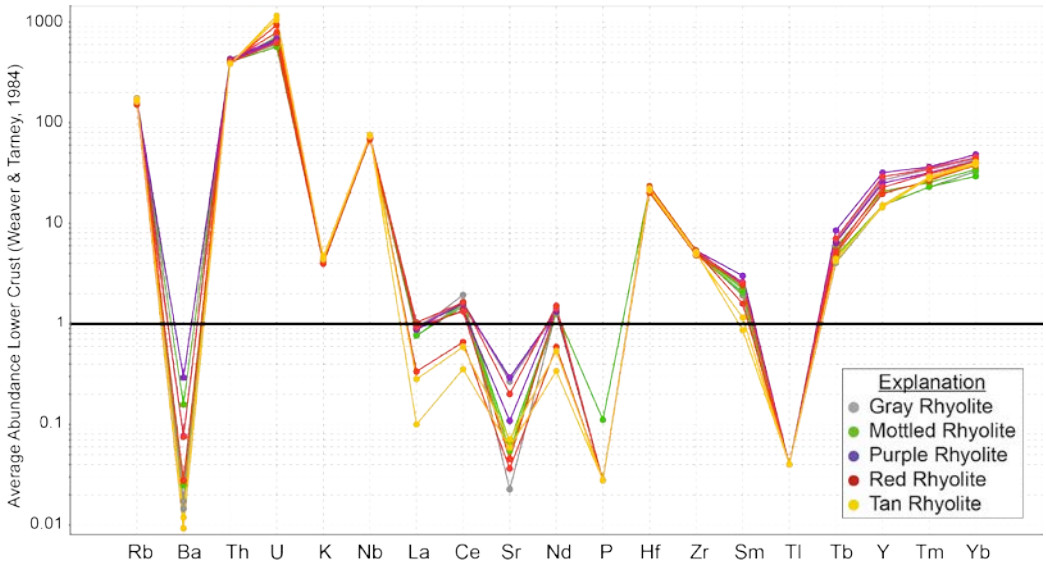

Figure 3.68: Spider diagram of the Round Top rhyolite samples versus the average elemental abundance of the lower crust, as defined by Weaver and Tarney (1984). Relative to the lower crust, the rhyolites are enriched in Rb, Th, U, K, Nb, Ce, Nd, Hf, Zr, Sm, Tb, Y, Tm, and Yb. They are depleted in Ba, La, Ce, Sr, Nd, P, and Tl.

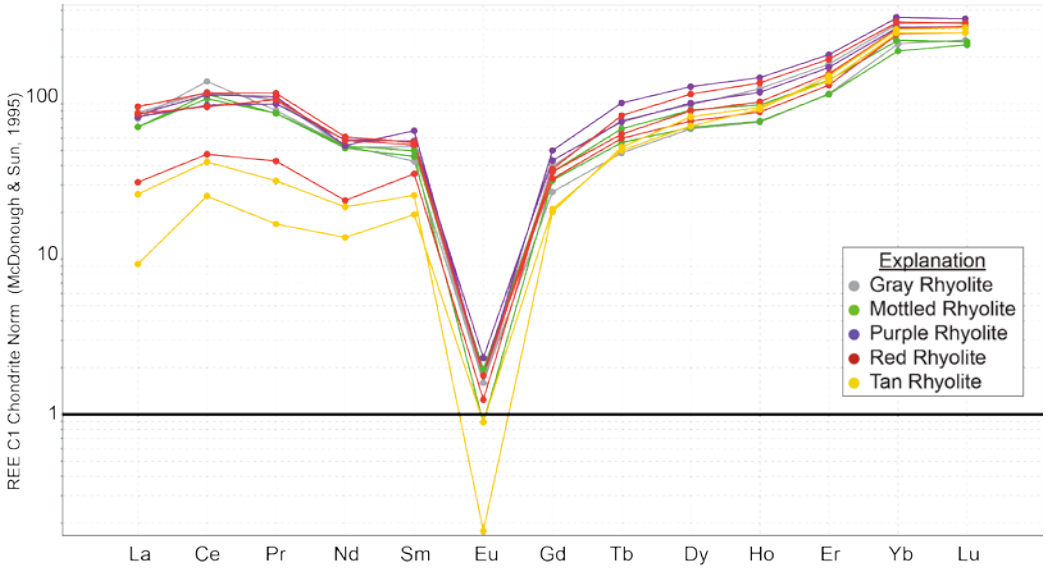

Figure 3.69: Spider diagram of the Round Top rhyolite samples versus the average chondrite elemental abundance, as defined by McDonough and Sun (1995). Relative to a chondrite, the rhyolites are enriched in La, Ce, Pr, Nd, Sm, Gd, Tb, Dy, Ho, Er, Yb, and Lu. They are depleted in Eu.

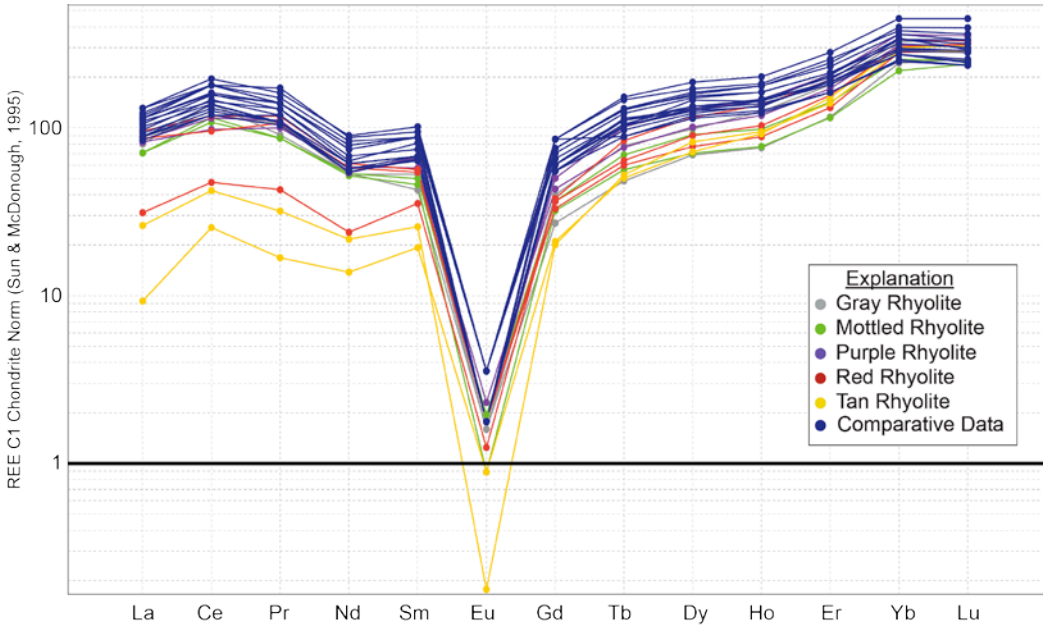

Figure 3.70: Spider diagram of the Round Top rhyolite samples versus data from previous studies, chondrite normalized as defined by McDonough and Sun (1995). All of the Round Top rhyolites except for the tan samples and one red sample closely conform to the REE trends produced by Price et al. (1990) and Rubin et al. (1993).

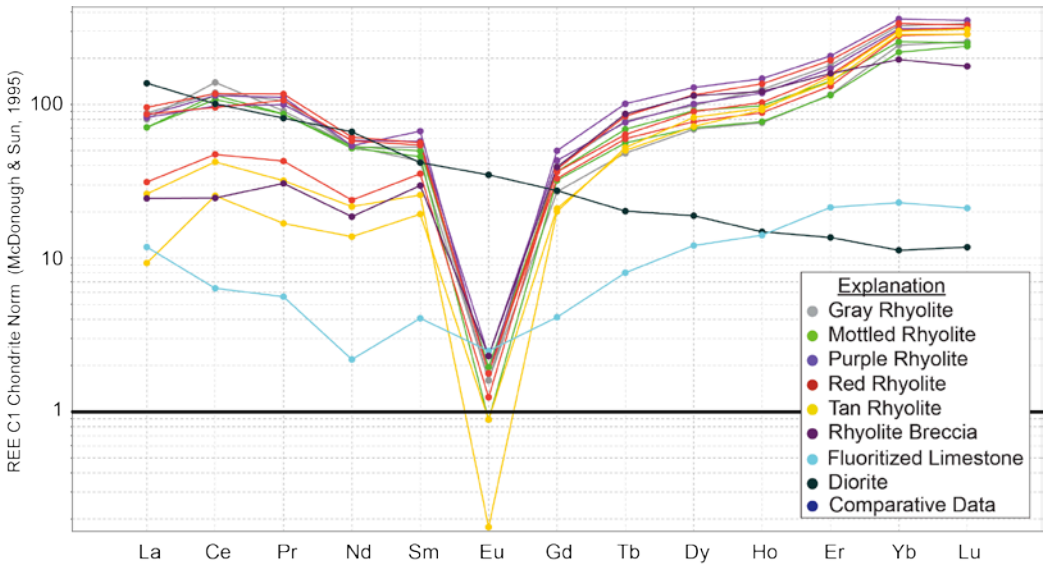

Figure 3.71: Spider diagram of all of the Round Top samples, including the rhyolite breccia, fluoritized limestone, and diorite sill, chondrite normalized to McDonough and Sun (1995). The rhyolite breccia closely follows the trend of the tan and one red rhyolite sample. The fluoritized limestone demonstrates an overall depletion in REEs relative to the rhyolite samples, and has a greater depletion in middle REEs versus HREEs and LREEs. The diorite sill is enriched in LREEs over HREEs producing a negative slope.

	SiO_2	Fe_2O_3	Sr	Th	U	Zr	Y	La	Ce	Pr	Nd	Sm	Eu	Gd	Tb	Dy	Ho	Er	Tm	Yb	Lu	Li	FeO	F
SiO_2	1.00																							
Fe_2O_3	-0.14	1.00																						
Sr	-0.77	0.29	1.00																					
Th	-0.55	0.55	0.85	1.00																				
U	-0.02	-0.71	-0.27	-0.67	1.00																			
Zr	0.20	0.04	0.12	0.33	-0.42	1.00																		
Y	-0.62	0.48	0.67	0.72	-0.34	0.46	1.00																	
La	-0.12	0.79	0.48	0.75	-0.86	0.13	0.34	1.00																
Ce	0.00	0.70	0.36	0.69	-0.87	0.09	0.19	0.92	1.00															
Pr	-0.17	0.80	0.53	0.79	-0.86	0.17	0.41	0.99	0.90	1.00														
Nd	-0.06	0.77	0.37	0.69	-0.89	0.10	0.26	0.98	0.92	0.98	1.00													
Sm	-0.31	0.75	0.61	0.87	-0.82	0.30	0.61	0.92	0.79	0.95	0.90	1.00												
Eu	-0.13	0.48	0.30	0.54	-0.67	0.24	0.42	0.67	0.52	0.67	0.69	0.73	1.00											
Gd	-0.54	0.64	0.65	0.87	-0.64	0.43	0.89	0.63	0.51	0.69	0.60	0.86	0.60	1.00										
Tb	-0.63	0.37	0.66	0.74	-0.33	0.49	0.97	0.30	0.18	0.37	0.23	0.61	0.38	0.90	1.00									
Dy	-0.64	0.27	0.62	0.62	-0.14	0.40	0.95	0.16	0.04	0.23	0.09	0.48	0.37	0.81	0.97	1.00								
Ho	-0.68	0.19	0.66	0.60	-0.07	0.42	0.95	0.08	-0.06	0.15	-0.01	0.39	0.29	0.75	0.94	0.97	1.00							
Er	-0.69	0.13	0.66	0.55	0.02	0.39	0.91	0.00	-0.15	0.07	-0.09	0.31	0.23	0.69	0.89	0.94	0.99	1.00						
Tm	-0.70	0.13	0.69	0.52	0.09	0.32	0.87	0.01	-0.18	0.08	-0.10	0.28	0.21	0.62	0.82	0.87	0.95	0.98	1.00					
Yb	-0.59	0.05	0.65	0.46	0.14	0.38	0.82	-0.05	-0.24	0.02	-0.16	0.23	0.24	0.54	0.76	0.83	0.91	0.95	0.98	1.00				
Lu	-0.60	0.09	0.70	0.49	0.13	0.33	0.78	0.01	-0.20	0.07	-0.12	0.24	0.18	0.51	0.71	0.76	0.86	0.91	0.97	0.98	1.00			
Li	0.21	0.17	-0.24	-0.07	-0.10	0.19	0.15	0.02	-0.07	0.01	0.07	0.04	0.56	0.09	0.01	0.08	0.09	0.14	0.13	0.21	0.17	1.00		
FeO	-0.39	0.87	0.55	0.67	-0.55	-0.19	0.44	0.73	0.70	0.75	0.69	0.68	0.31	0.57	0.33	0.25	0.21	0.20	0.21	0.14	0.21	0.04	1.00	
F	-0.58	-0.01	0.67	0.56	-0.33	0.29	0.38	0.21	0.25	0.23	0.14	0.26	0.00	0.37	0.43	0.31	0.40	0.39	0.37	0.30	0.33	-0.42	0.16	1.00

Strong	≥0.70 (+ or -)
Moderate	0.50-0.69 (+ or -)
Moderately Weak	0.30-0.49 (+ or -)
Weak	≤0.29 (+ or -)

Table 3.4 Correlation chart of major oxides and elements for the Round Top rhyolite samples. Orange color denotes relatively strong correlations, blue moderate, purple moderately weak, and no color denotes weak correlation. Correlation based on Pearson correlation coefficient as provided by Microsoft Excel.

CHAPTER 4: DISCUSSION, CONCLUSIONS, AND FUTURE WORK

Discussion

SUMMARY

Based on REE enrichment trends first described by Shannon and Goodell (1986; Figure 2.5), Round Top is the second to last emplaced laccolith in a series of five, which comprise the Sierra Blanca group. The magma from which the group formed underwent an extensive process of evolution and enrichment, facilitated by a long-lived tectonic regime. Continued evolution of the magmatic source produced the unusual enrichment of REEs, F, U, and Be characteristic of Round Top.

The Round Top laccolith consists of four intermingled rhyolite types that vary in color, mineralogy, texture, and alteration, but are comagmatic. Geochemical analyses indicate all rhyolite types are weakly to strongly peraluminous and subalkaline, but have undergone varying degrees of oxidation, producing variations in color and texture. The variations observed in the mottled textures and rhyolite colors are the product of incomplete oxidation of the laccolith by secondary fluids. The color variations occur due to differing proportions of hematite within the pore spaces of the potassium feldspar groundmass. The hematite was sourced from the oxidation of magnetite within

the rhyolite, and was subsequently deposited within the open pore spaces of the feldspar produced by early dissolution. The tan rhyolite has been locally subjected to intense alteration independent to that of the rest of the laccolith that has converted the potassium feldspar to clay.

The REE concentrations and whole-rock geochemistry between the rhyolite types are similar, but not exact. All are approximately equally enriched in HREEs, demonstrate a strong negative europium anomaly, and a positive REE enrichment slope. Due to the higher degree of alteration that the tan rhyolite has undergone, geochemical analyses indicate depletion in many elements relative to the other rhyolite types. This is especially evident with the LREEs, where the tan is depleted by almost half an order of magnitude. It is unclear what type or types of rhyolite the tan variation was prior to bleaching.

Petrographic and microbeam studies indicate early, middle, and late stages of crystallization, followed by alteration by a high temperature vapor phase and subsequent oxidization. The Round Top rhyolites are composed of 48-52% potassium feldspar, 28-30% quartz, 8-14% plagioclase feldspar, 4-5% annite biotite, 2-3% opaques dominantly magnetite-hematite, 1% zircon, and 1% trace phases, including REE-fluoride minerals. Microbeam studies indicate the trace phases include tantalite, columbite, cerianite-(Ce), thorite, changbaiite, cryolite, cassiterite, yttrocerite, yttrofluorite, and two unidentified minerals.

LACCOLITH EMPLACEMENT AND MORPHOLOGY

The Round Top magma was emplaced into upper Cretaceous fine-grained siliciclastic strata, presumably near the timing of the formation of the adjacent Sierra Blanca laccolith, 36 Ma (Henry & McDowell, 1986). With continued injection, the magmatic body increased in volume displacing the overlying sediments. This emplacement style formed the domed convex structure of the current laccolith. The undulatory and irregular basal contact between the laccolith, Cretaceous strata, and diorite sill suggest the magma was injected along bedding plans at multiple depths. The rhyolitic magma most likely utilized the preexisting conduit of the diorite sill during emplacement, although enclaves of the preexisting mafic sill have not been documented within the rhyolite. Therefore, it is possible that the laccolith was emplaced along a different conduit that happened to overlie the diorite sill locally.

The abundance of disequilibrium textures and the anhedral mineralogy of many of the crystals throughout the laccolith suggest emplacement of the magmatic material was abrupt. The hourglass sector zonation of the potassium feldspar phenocrysts is an unusual disequilibrium texture that occurs as the result of different crystal faces preferentially attracting different compositions during formation, indicating rapid crystallization and disequilibrium growth (Shelley, 1992; Vernon, 2004). Additionally, the pristine outer edge of many of the interior plagioclase laths and interior quartz cores indicate corrosion or disequilibrium of the phenocrysts did not occur prior to the formation of the

overgrowths. Thus, the change in magmatic conditions was rapid: as dissolution or embayment would have occurred if the interior portions of the phenocrysts were exposed to a metastable environment for a prolonged period. The three-part quartz phenocrysts indicate transition from euhedral beta quartz formation to the rapid crystallization of anhedral quartz and entrainment of surrounding magmatic material that later formed the melt inclusions. The uniform occurrence of these disequilibrium textures throughout all of the rhyolite types suggests that the change in pressure-temperature conditions affected the entirety of the laccolith, and discounts the possibility that the laccolith consists of multiple magmatic emplacement events.

The highly fractured nature of the laccolith facilitated the movement of the primary and secondary fluids responsible for alteration and oxidation, as evident by the abundance of rhyolite breccias and cemented fractures. These fractures are the result of rapid cooling and subsequent shrinking of the laccolith after emplacement, perhaps later enhanced by normal faulting related to Basin and Range extension.

The laccolith is composed of discrete packages of four rhyolite types, which are dispersed throughout the igneous body. This preferential location between the occurrences of gray, purple, and red rhyolite suggests portions of the laccolith were more strongly oxidized than others, and may represent preferential fluid pathways, variations in the fracture system, and/or heterogeneity in the strength or volume of the oxidizing fluids.

MINERALOGY

The petrogenetic sequence of the Round Top laccolith includes early, middle, and late crystallization stages, which were subjected to concurrent alteration from a volatile-rich vapor phase and later partial oxidation of the laccolith by circulating fluids (Figure 3.11). Given the observed mineralogical relationships between the major, accessory, and trace phases, early crystallization included the formation of the larger phenocrysts within the magma chamber and progressed through emplacement. Crystallization and alteration ceased with the quenching of the vapor phase. During the final stages of crystallization, interaction with the volatile-rich vapor phase produce the alteration textures now observed within the feldspars and quartz overgrowths. At an unknown time after crystallization, interaction with oxidizing fluids partially altered the laccolith to form the gray, purple, red, and mottled rhyolite types.

Crystallization of the major phases began within the magma chamber, forming the plagioclase feldspar laths (that would later become the cores to the larger feldspar phenocrysts), and the hexagonal, higher temperature core portions of the quartz phenocrysts. Emplacement of the magma from depth to the current stratigraphic position within the Cretaceous strata was relatively rapid, which inhibited significant crystallization during transport as evident by the fine grained and uniform nature of the groundmass. During the emplacement of the laccolith, as temperature and pressure conditions decreased, the subhedral to euhedral, hourglass-type potassium feldspar phenocrysts, the potassium feldspar

overgrowths, the smaller accessory phases, and the larger constitutes of the groundmass (potassium feldspar, plagioclase, quartz, and annite) began to crystallize. Interaction of these minerals with the circulating high temperature volatile-rich vapor phase produced the dissolution textures observed with the feldspar and quartz populations. As new magma ceased to be emplaced and the laccolith cooled, the volatile-rich vapor phase quenched to form the trace and late-stage phases. These late-stage phases occur interstitial to and within the potassium feldspar pores, and include cerianite-(Ce), tantalite, changbaiite, cassiterite, yttrocerite, yttrofluorite, and the (X) and (W)-unknowns. The intimate association of the REE-fluoride minerals and other trace phases with the magnetite, zircon, and groundmass, suggests the timing of crystallization between all phases was relatively close.

The different stages of crystallization and subsequent alteration by the high temperature vapor phase must have occurred with a high degree of overlap and within a relatively short duration, as evident by the many inclusions of mineral phases from one stage within another. The emplacement of the magma body would have shifted the pressure and temperature conditions of the system very rapidly, causing disequilibrium growth and subsequent mantling of the plagioclase by the potassium feldspars and the quartz overgrowths. The abundance of volatiles within the vapor phase potentially acted to buffer the formation of crystals until later within the petrogenetic sequence, as is observed in other systems with abundant F and Li (Vernon, 2004). The partial oxidation of

portions of the laccolith occurred subsequent to the quenching of the vapor phase but prior to exhumation of the laccolith to surface.

Rubin et al. (1989, 1993) suggested that the two zircon populations of the Round Top rhyolite (thorite-rich and thorite-poor) indicate dissolution and recrystallization of a portion of the zircons during subsequent hydrothermal alteration of the laccolith. This is unlikely given the nature of fluid that would be necessary to conduct such selective remobilization. It is unclear as to how an acidic fluid (such as those associated with hydrothermal alteration and with the acidity necessary to dissolve zircon), could preferentially dissolve zircon while not dissolving adjacent quartz, potassium feldspar, and plagioclase phenocrysts. Therefore, the two populations of zircon most likely represent one population that is in varying stages of thorite exsolution.

ALTERATION – CAUSE FOR VARIATIONS IN RHYOLITE COLOR AND TEXTURE

At the time of crystallization and just subsequent to, the laccolith was subjected to a relatively uniform degree of alteration prior to undergoing oxidation. This alteration caused the partial dissolution and formation of the semi-linear pores spaces within the potassium feldspar phenocrysts, overgrowths, and feldspar groundmass, in addition to forming the embayments to the quartz overgrowths. Dissolution of the feldspars must have occurred prior to the crystallization of the late stage minerals in order to produce the inclusionary relationship observed between the two groups. The strong correlation of the

REE-minerals to the potassium feldspar portion of the rhyolite suggests the availability of open pore space was a significant factor in the retention of the REE-fluorides, and therefore this close mineralogical relationship should be considered in future economic endeavors. The ubiquitous nature of the quartz embayment and feldspar dissolution suggests the vapor phase alteration was pervasive throughout the entirety of the laccolith.

Subsequent to the pervasive vapor phase alteration, selective oxidation of the laccolith occurred to produce the gray, purple, red, and mottled rhyolites. The different forms of rhyolite represent varying degrees of oxidation and turbidity; the gray rhyolite is the least oxidized, with the purple, red, and tan representing greater degrees of oxidation. Mineralogically, the amount of hematitic pore-fill within the potassium feldspar portions of the groundmass increases from the gray, purple, and red rhyolites. Consequently, the increasing hematite abundance is the primary cause for the subsequent increase in the turbidity observed in thin section. The unique mottled textures formed as fluids migrated through the laccolith, percolating outward from fractures and oxidizing the surrounding wallrock. If exposure to the oxidizing fluids had persisted, the mottled rhyolites would have continued to oxidize, becoming red rhyolite. It is unclear as to how the highly geometric mottled textures formed, but these may be due to microfractures within the rock.

The depletion in LREEs, the kaolinization of the potassium feldspar, and the localized occurrence of the tan rhyolite suggest that this limited portion of the

laccolith was subjected to a form of alteration different to that of the rest of the laccolith, and may be due to prolonged interaction with hydrothermal fluids.

GEOCHEMISTRY

The positive slope of the REE spider diagrams, the strong negative Eu-anomaly, and high silica content suggests the Round Top magma underwent a high degree of enrichment prior to emplacement, possibly due to crystal fractionation. Schilling & Winchester (1967) estimated the average crustal abundances of La and Lu from a depth of 0-10 km as F_{La}=0.53 and F_{Lu}=0.029, where F_{La} and F_{Lu} are the fraction of the element within the total REE group for a given depth. The strong HREE to LREE enrichment observed within all of the rhyolite samples indicates a high degree of evolution in order to achieve a reversal in relative abundance compared to that of the typical continental crust, as defined by Schilling & Winchester (1967). During crystallization Eu is predominately controlled by plagioclase (especially within felsic melts) as Eu^{2+} is relatively easily substituted for Ca^{2+} (Rollinson, 1993). Therefore a strong negative Eu-anomaly indicates the removal of Ca-rich feldspars from the magmatic source prior to emplacement, most likely due to crystal fractionation and/or retainment of these feldspars during partial melting of a source material (Rollinson, 1993). To achieve the low concentrations of Eu observed within the Round Top rhyolites, the magma must have undergone substantial removal of the Ca-rich plagioclase prior to emplacement.

The correlation of the REEs+Y to F suggest that the REEs+Y were concentrated within the volatile-rich vapor phase portion of the magmatic system and not within the silica-rich melt, at the time of crystallization. Fe_2O_3 and FeO additionally demonstrate positive correlations to the REEs+Y, potentially indicating a remobilizing relationship between the late oxidizing fluids with the initial F-REE-Y minerals. The weak association of Zr to both F and SiO_2 may additionally be the result of later overprinting by the subsequent oxidization of the laccolith, prolonging the question of provenance for the two populations of zircon first noted by Rubin et al. (1989).

All of the rhyolite sample types demonstrate a correlation of F to oxidization: samples with more equivalent F concentrations are typically more oxidized. Overprinting by the later oxidizing fluids may have effectively stripped fluorine from the rhyolite while simultaneously oxidizing the iron minerals, thus forming the more equivalent concentrations of F in those samples that have been subjected to a higher degree of oxidation. Similarly, the rhyolite types that are most oxidized contain the most disparate Zr concentrations, suggesting the oxidizing fluids are either adding or stripping Zr during the oxidizing processes. This correlation is complementary to the hydrothermal zircon hypothesis put forth by Rubin et al. (1989). However, the difference in concentration of Zr within all of the rhyolites ranges from only 969 ppm to 1,085 ppm, and therefore may only be representative of inherent geochemical heterogeneity across the laccolith, reflected at a scale of 100-960 g samples analyzed. Additionally, rhyolite

samples with high Sr values typically contain low silica content, suggesting that the same mechanism that controlled F content of the rhyolites additionally controlled the Sr values.

MAGMA EVOLUTION AND EMPLACEMENT

A laccolith is an unusual feature within the spectrum of magmatic events, and the mechanisms that control the formation and distribution of such oddities are still poorly understood. The specific controls necessary to form a highly HREE-enriched laccolithic deposit, such as that of Round Top, are even less understood. A number of geologic events must have occurred at favorable moments in the geologic past to culminate in such a manner as to allow for the Round Top laccolith to occur in its current state. The peraluminous composition of the Round Top rhyolite differs from the more peralkaline to metaluminous composition of other rhyolitic bodies within the Trans-Pecos region, suggesting a difference in the process responsible for their formation (Barker, 1980; Rubin et al., 1987; Price et al., 1990).

To produce the Round Top laccolith, regional circumstances must have been favorable for the formation and evolution of the continentally sourced, highly enriched silicic magma to rise and mature from depth. The complex tectonic history of the Trans-Pecos region has undoubtedly played a key role in the development of this magmatic source. The periodic episodes of compression punctuated by abrupt stress orientation changes and subsequent regional

extension, all overprinted with multiple generations of faulting and volcanism, most likely created a geologic setting favorable to complex magmatic evolution. The Round Top magma must have undergone an advanced process of crystal fractionation/differentiation in order to form the enriched laccolithic material not equally matched within the Trans-Pecos region. The prior emplacement of the three more voluminous Sierra Blanca laccoliths concentration the Round Top magma in incompatible elements, forming the geochemical characteristic now considered desirable as an economic resource. To form the laccolith, emplacement of this magmatic material must have stalled during ascension in order to prevent eruption of the magma to the surface. The entrapment of the magma within the Cretaceous strata was most likely controlled by buoyancy and density contrasts between the Cretaceous overburden and the upwelling viscous silicic magma. The high fluorine content and volatile-rich nature of the magma additionally contributed to the stalling of the igneous material by altering the viscosity of the igneous fluids. Fluorine, as with water, has been identified as a mechanism to decrease the viscosity of volatile-rich silicic magmas (Giordano et al., 2004; Vernon, 2004). This changed the final fate of the Sierra Blancas from that of an intrusive pluton to that of a near surface laccolitic group. The convex shape and domal peaks that characterize the group suggest an emplacement of moderate force, causing mild deformation of the surrounding sediments as magma pooled and uplifted the overlying layers. Crystallization of the magma began at depth to give rise to the larger, more euhedral phenocrysts observed

within the rhyolites. Further crystallization produced the potassium feldspar mantles, phenocrysts, and feldspar groundmass that were subsequently altered by the circulating high temperature vapor. The enclosing Cretaceous strata would have produced an ideal environment to trap residual magmatic volatiles, thus facilitating the dissolution of the feldspar. As the laccolith cooled, the vapor phase quenched to form the late-stage minerals, including the abundant trace phases and REE-fluorides. Crystallization of the laccolith as a whole was relatively rapid, as the rhyolite is uniformly aphanitic.

Subsequent erosion of the Cretaceous overburden over the past 36 Ma exposed a large portion of Round Top to the surface. The highly fragmented and blocky nature of the laccolith reflects the cooling and shrinking of the magma, later exaggerated by Basin and Range faulting. The abundant cementation of fractures and cracks within the laccolith by multiple generations of fluorite, calcite, caliche, and microcrystalline silica indicate a prolonged period of remobilization and precipitation, facilitated by the circulating oxidizing fluids.

Fluid movement along fractures and within the rhyolitic body over time led to the partial oxidation of portions of the laccolith. These oxidizing fluids percolated through the rock, exploiting the extensive fracture system that transects the laccolith. Interaction with these fluids caused the magnetite phenocrysts to oxidize, producing abundant hematite. The variation in rhyolite type is the product of increasing proportions of hematitic fill within the micropores in the feldspar groundmass: forming the spectrum of gray, purple, red, and

mottled rhyolites. The origin of the more highly geometric mottled textures is unknown, but may potentially be related to rhyolitic microfractures. The mineralogical, geochemical, and textural attributes characteristic to Round Top are the product of a series of unique geologic events that collectively formed this anomalous laccolith, and potentially others yet to be discovered in Trans-Pecos Texas.

Conclusion

The Round Top laccolith represents the last emplaced portion of a highly evolved magmatic system, enriched in incompatible elements including REEs, U, Be, and F. A prolonged magmatic enrichment history coupled with favorable tectonic and regional events allowed for the emplacement and formation of the Sierra Blanca laccolith group. Round Top, being one of the youngest of the laccolith group, was additionally enriched in incompatible elements relative to the other laccoliths. The concentration of F, U, Be, and REEs that partially define this unique deposit are derived from a highly evolved magmatic progression, including extensive crystal fractionation. Based on the observed evidence within this report and the culmination of information from previous studies, the primary conclusions formulated as to the formation and unique enrichment of the Round Top laccolith are as follows.

- Morphological reconstruction through RC chip drill hole data demonstrates a complex intermingled relationship between rhyolite types at depth, suggesting the laccolith is not of a layered sequence but rather was formed from one magmatic event.
- Whole-rock and trace geochemical analyses confirm that the Round Top rhyolite is peraluminous and subalkaline, although there appears to be a range in the peraluminous degree, from weak to strong. All of the rhyolite samples are subalkaline, but compositionally are very close to being

alkaline.

- The Round Top rhyolites are composed of 48-52% potassium feldspar, 28-30% quartz, 8-14% plagioclase feldspar, 4-5% annite biotite, 2-3% opaques dominantly magnetite-hematite, 1% zircon, and 1% trace phases including REE-fluoride minerals.
- Mineralogical and geochemical similarities between the rhyolite types suggest a cogenetic origin, emplacement history, and mineral paragenesis. These features indicate the rhyolite varieties are all of one type of rhyolite that has been subsequently oxidized by varying degrees.
- The variation in rhyolite color and the occurrence of mottled rhyolite textures are the product of selective alteration produced by the migration of oxidizing fluids. The gray rhyolite represents the rock type that has had the least interaction with these oxidizing fluids, whereas the red represents that which has had the most.
- The high temperature vapor phase alteration of the feldspar mineralogy was essential to the retention and formation of the REE minerals within the laccolith, as it developed the pervasive open pore space that was then occupied by the crystallizing minerals.
- REE minerals are late-stage and subhedral to anhedral. They predominately occur within the pore spaces of the potassium feldspar groundmass and phenocrysts. Although, they additionally occur as crystals associated with other accessory and trace phases, as inclusions

within other phases, along grain boundaries, and along fractures and within voids.

- HREE enrichment is in agreement with previous studies, and is similar between all of the rhyolite types, including gray, purple, red, tan, and mottled.
- LREE enrichment is similar between the gray, purple, red, and mottled rhyolite types. The tan rhyolite type diverges from this trend in that it is less enriched in LREEs by almost half an order of magnitude. The tan rhyolite has been subjected to localized alteration independent to that of the other rhyolite types.
- Differences in geochemistry between rhyolite types (specifically in F content) most likely represent innate heterogeneity in the concentration of the volatile-rich vapor phase at the time of crystallization. The discrepancies in Sr content either represent this same heterogeneity, or as Sr is fairly mobile, they may represent remobilization due to migrating fluids.

Exploration for deposits of a similar nature to that of Round top should focus on identifying regions and igneous suites that closely resemble that of the Sierra Blancas. Future deposits will be situated within long-lived, complex tectonic regimes, that have been subjected to regional compression and extension punctuated by subduction induced bimodal volcanism. The enrichment in the rhyolite that comprises Round Top is the result of the prolonged removal of

compatible elements from source magma chamber through the emplacement of earlier laccoliths. With the emplacement of each sequential laccolith, the source magma became more enriched in incompatible elements, evident by the associated increasing HREE concentrations. Exploration should focus on locating felsic laccolith groups not yet exposed to the surface, as these are more likely to be less affected by remobilizing secondary oxidation and erosion. The emplacement of Round Top as a laccolith (versus that of an extrusive rhyolitic flow) facilitated the retention of the volatile-rich vapor phase within the magma, forming the abundant REE-minerals now considered economically desirable. Additionally, the retention of the high temperature vapor phase produced the pores within the feldspars, creating the necessary open space later occupied by the quenched volatile phase. Future exploration should concentrate on identifying the last emplaced laccolithic member of a group, as this will most likely have the highest concentration of incompatible elements and a high potential for the retention of a volatile-rich vapor phase, and therefore may be of economic interest.

Future Research

A number of questions have arisen during the scope of this research that, if answered, would provide insight and clarity to this complicated deposit. Future work to be conducted could include:

- A more extensive documentation of the unique mineralogical characteristics and their significance to the formation of the laccolith, especially focusing on the implications and causes for the dual zircon population and irregularities in Sr concentrations.
- More research is needed to understand the mechanisms and controls instrumental in the emplacement of the Sierra Blanca laccoliths, including such questions as to what impact did the anomalous fluorine content have on the emplacement of the laccolith? Why were five laccoliths of differing volumes, all emplaced at approximately the same stratigraphic level?
- Further geochemical analyses and data interpretation are needed to better understand the provenance of the laccolithic magma responsible for Round Top and the unique associated geochemistry.
- Sr-isotopic analysis would be ideal as a means to compare the concentration variations observed between the rhyolite sample pairs, and may possibly aid in identifying the nature of the alteration fluids.

- Mineralogical work could be conducted using crystallization rates of the feldspars as a means to estimate the emplacement depth, temperature, and rate of cooling of the laccolith post emplacement.
- Additionally, more work is needed to identify the origin and significance of the unique mottled rhyolite textures observed throughout the laccolith.

Appendix A

Sample List

Waypoint ID	Collection Date	Northing	Westing	Elevation (ft)
244	13-Mar-12	N31 16 57.2	W105 27 39.3	4832
245	13-Mar-12	N31 16 55.8	W105 27 38.3	4863
246	13-Mar-12	N31 17 00.4	W105 28 02.0	4969
247	13-Mar-12	N31 17 00.7	W105 28 07.7	4965
248	13-Mar-12	N31 16 27.4	W105 28 52.1	4883
249	13-Mar-12	N31 16 24.5	W105 28 48.6	4872
250	14-Mar-12	N31 16 31.1	W105 29 00.4	4710
251	14-Mar-12	N31 16 31.1	W105 29 00.4	4706
252	14-Mar-12	N31 16 31.0	W105 29 00.2	4712
253	14-Mar-12	N31 16 34.7	W105 29 00.1	4857
254	14-Mar-12	N31 16 34.9	W105 29 00.4	4847
255	14-Mar-12	N31 16 24.6	W105 28 48.9	4870
256	14-Mar-12	N31 16 27.4	W105 28 51.8	4901
257	14-Mar-12	N31 17 05.0	W105 27 55.5	5122
258	14-Mar-12	N31 17 01.6	W105 28 01.1	5023
259	15-Mar-12	N31 11 57.3	W105 26 52.6	4657
260	15-Mar-12	N31 16 51.5	W105 28 43.1	5127
261	15-Mar-12	N31 16 50.3	W105 28 45.6	5242
262	15-Mar-12	N31 16 43.8	W105 28 54.0	5233
263	15-Mar-12	N31 16 44.1	W105 28 55.7	5231
264	15-Mar-12	N31 16 47.1	W105 28 52.0	5246
265	15-Mar-12	N31 16 51.6	W105 28 43.5	5150
266	15-Mar-12	N31 16 56.1	W105 28 37.2	5082
267	15-Mar-12	N31 16 56.4	W105 28 40.2	4995
268	15-Mar-12	N31 16 55.7	W105 28 41.7	4921
269	15-Mar-12	N31 17 11.8	W105 27 58.0	5106
270	15-Mar-12	N31 16 44.5	W105 28 11.0	5114
271	15-Mar-12	N31 16 57.7	W105 28 09.8	4904
272	16-Mar-12	N31 16 57.0	W105 27 35.2	4991
273	16-Mar-12	N31 16 59.9	W105 27 30.2	4826
274	16-Mar-12	N31 16 56.5	W105 27 38.4	4866
27	20-Aug-12	N31 15 38.6	W105 25 35.9	5591
28	20-Aug-12	N31 15 38.4	W105 25 36.5	5587
32	20-Aug-12	N31 15 38.1	W105 25 37.0	5584
33	20-Aug-12	N31 16 46.3	W105 28 58.7	5092
34	20-Aug-12	N31 16 48.6	W105 28 55.8	5108
35	20-Aug-12	N31 16 49.0	W105 28 55.3	5102
36	20-Aug-12	N31 16 51.5	W105 28 49.1	5128

Table A.1: Location of sample collection points by waypoint number.

Waypoint ID	Collection Date	Northing	Westing	Elevation (ft)
37	20-Aug-12	N31 16 51.4	W105 28 49.2	5144
38	20-Aug-12	N31 16 44.0	W105 28 54.0	5266
40	20-Aug-12	N31 16 44.2	W105 28 55.9	5240
41	20-Aug-12	N31 16 44.4	W105 28 57.3	5210
43	20-Aug-12	N31 16 56.7	W105 28 40.1	4984
44	20-Aug-12	N31 16 55.6	W105 28 41.7	4915
45	20-Aug-12	N31 17 00.9	W105 28 02.3	5010
46	20-Aug-12	N31 16 11.1	W105 28 11.2	4836

Position Format /lon hddd°mm'ss.s"
Datum WGS 84
Measurement US

Table A.1 continued: Location of sample collection points by waypoint number. Locations shown on Figures 3.1-3.3.

Drill Hole ID	Collection Date	Northing	Westing	Elevation (ft)	Depth (ft)	Dip
DH244	17-Mar-12	N31 16 48.9	W105 28 55.2	5066.77	312.50	-90
DH248	17-Mar-12	N31 16 51.4	W105 29 01.0	4779.02	205.00	-90
DH287	17-Mar-12	N31 16 28.7	W105 28 04.6	5122.80	305.00	-90
DH421	17-Mar-12	N31 16 24.4	W105 28 47.9	4897.85	740.00	-90
DH446	17-Mar-12	N31 16 53.5	W105 28 27.6	5190.00	230.00	-90
DH455	17-Mar-12	N31 16 46.0	W105 28 32.6	5431.59	305.00	-90
DH456	17-Mar-12	N31 16 43.2	W105 28 41.2	5561.63	800.00	-90
DH461	17-Mar-12	N31 16 38.2	W105 28 29.6	5722.59	1180.00	-90
DH462A	17-Mar-12	N31 16 40.4	W105 28 35.8	5669.95	1020.00	-90
				Total footage	5097.50	

Position Format	Lat/lon hddd°mm'ss.s"
Datum	WGS 84
Measurement	US

Table A.2: Location of RC chip drill holes. Sample locations shown on Figure 3.4.

TS Num.	Sample ID	Northing	Westing	Slide Size	Comments	Sodium Cobaltinitrite Staining 1/2 Slide	Description
1	ORT270-02	N31 16 44.5	W105 28 11.0	27x46mm	No Polish	x	Rhyolite - red
2	ORT266-02	N31 16 56.1	W105 28 37.2	27x46mm	No Polish	x	Rhyolite - purple with visible hematite
3	ORT268-18	N31 16 55.7	W105 28 41.7	27x46mm	No Polish		Fluorite - purple
4	OLRT258-01	N31 17 01.6	W105 28 01.1	27x46mm	No Polish		Sandstone - tan
5	OLRT247-01	N31 17 00.7	W105 28 07.7	27x46mm	No Polish	x	Rhyolite - purple
6	ORT262-02	N31 16 43.8	W105 28 54.0	27x46mm	No Polish	x	Rhyolite - gray
7	ORT255-15	N31 16 24.6	W105 28 48.9	27x46mm	No Polish	x	Rhyolite - red with manganese oxides
8	ORT263-04	N31 16 44.1	W105 28 55.7	27x46mm	No Polish	x	Rhyolite - purple
9	ORT249-21	N31 16 24.5	W105 28 48.6	27x46mm	No Polish		Microsilica - white
10	OLRT246-01	N31 17 00.4	W105 28 02.0	27x46mm	No Polish	x	Rhyolite breccia - brown
11	OLRT272-06	N31 16 57.0	W105 27 35.2	27x46mm	No Polish	x	Rhyolite - red
12	ORT249-07	N31 16 24.5	W105 28 48.6	27x46mm	No Polish		Fluorite breccia - purple & white
13	ORT249-12	N31 16 24.5	W105 28 48.6	27x46mm	No Polish		Rhyolite breccia - purple & white
14	ORT266-01	N31 16 56.1	W105 28 37.2	27x46mm	No Polish	x	Rhyolite - purple with visible hematite
15	ORT270-03	N31 16 44.5	W105 28 11.0	27x46mm	No Polish	x	Mottled rhyolite - tan & purple striped
16	ORT263-03	N31 16 44.1	W105 28 55.7	27x46mm	No Polish	x	Mottled rhyolite - gray & purple spotted
17	OLRT272-07	N31 16 57.0	W105 27 35.2	27x46mm	No Polish	x	Mottled rhyolite - red & tan striped
18	ORT270-01	N31 16 44.5	W105 28 11.0	27x46mm	No Polish	x	Rhyolite - purple with visible hematite
19	OLRT272-02	N31 16 57.0	W105 27 35.2	27x46mm	No Polish	x	Rhyolite - tan
20	ORT248-22	N31 16 27.4	W105 28 52.1	27x46mm	No Polish		Rhyolite breccia - purple & white
21	ORT261-02	N31 16 50.3	W105 28 45.6	27x46mm	No Polish		Fluorite - brown & colorless
22	ORT267-09	N31 16 56.4	W105 28 40.2	27x46mm	No Polish	x	Diorite - black
23	ORT270-04	N31 16 44.5	W105 28 11.0	27x46mm	No Polish		Limestone - fluoritized with manganese oxides

Table A.3: Thin section sample locations and descriptions

TS Num.	Sample ID	Northing	Westing	Slide Size	Comments	Sodium Cobaltinitrite Staining 1/2 Slide	Description
24	ORT253-04	N31 16 34.7	W105 29 00.1	27x46mm	No Polish	x	Rhyolite - purple
25	ORT264-01	N31 16 47.1	W105 28 52.0	27x46mm	No Polish	x	Rhyolite - gray
26	ORT266-03	N31 16 56.1	W105 28 37.2	27x46mm	SEM Polish	x	Mottled rhyolite - gray & purple spotted
27	ORT263-02	N31 16 44.1	W105 28 55.7	27x46mm	SEM Polish		Mottled rhyolite - gray & red spotted
28	ORT256-01	N31 16 27.4	W105 28 51.8	50x75mm	SEM Polish		Rhyolite breccia - tan & purple
29	ORT256-11	N31 16 27.4	W105 28 51.8	50x75mm	SEM Polish		Rhyolite breccia - red & purple
30	ORT249-05	N31 16 24.5	W105 28 48.6	50x75mm	SEM Polish		Fluorite - purple
31	ORT44-20	N31 16 55.6	W105 28 41.7	27x46mm	Double Polish		Rhyolite - tan
32	ORT44-22	N31 16 55.6	W105 28 41.7	27x46mm	Double Polish		Rhyolite - tan
33	DH421	N31 16 24.4	W105 28 47.9	27x46mm	Double Polish		Mixed rhyolites
34	DH462A	N31 16 40.4	W105 28 35.8	27x46mm	Double Polish		Mixed rhyolites
35	DH446 DH455	N31 16 53.5 N31 16 46.0	W105 28 27.6 W105 28 32.6	27x46mm	Double Polish		Mixed rhyolites
36	DH456	N31 16 43.2	W105 28 41.2	27x46mm	Double Polish		Mixed rhyolites
37	DH461	N31 16 38.2	W105 28 29.6	27x46mm	Double Polish		Mixed rhyolites
38	DH244 DH248 DH287	N31 16 48.9 N31 16 51.4 N31 16 28.7	W105 28 55.2 W105 29 01.0 W105 28 04.6	27x46mm	Double Polish		Mixed rhyolites
39	ORT264-01	N31 16 47.1	W105 28 52.0	27x46mm	Double Polish		Rhyolite - gray
40	ORT263-04	N31 16 44.1	W105 28 55.7	27x46mm	Double Polish		Rhyolite - red with visible hematite
41	ORT266-01	N31 16 56.1	W105 28 37.2	27x46mm	Double Polish		Rhyolite - gray with visible hematite
42	ORT270-01	N31 16 44.5	W105 28 11.0	27x46mm	Double Polish		Rhyolite - purple with visible hematite
43	ORT266-02	N31 16 56.1	W105 28 37.2	27x46mm	Double Polish		Rhyolite - purple with visible hematite

Position Format Lat/lon hddd°mm'ss.s"
Datum WGS 84
Measurement US

Table A.3 continued: Thin section sample locations and descriptions .Sample locations shown on Figures 3.1-3.3.

Thin Section ID	Sample ID	Northing	Westing	Rock Type	Analysis
18	ORT270-01	N31 16 44.5	W105 28 11.0	Rhyolite - purple	SEM
27	ORT263-02	N31 16 44.1	W105 28 55.7	Mottled rhyolite - red & gray spotted	SEM
29	ORT256-11	N31 16 27.4	W105 28 51.8	Rhyolite breccia	SEM
31	ORT44-20	N31 16 55.6	W105 28 41.7	Rhyolite - tan	SEM
39	ORT264-01	N31 16 47.1	W105 28 52.0	Rhyolite - gray	SEM & ESEM
40	ORT263-04	N31 16 44.1	W105 28 55.7	Rhyolite - red	SEM & ESEM
41	ORT266-01	N31 16 56.1	W105 28 37.2	Rhyolite - purple	SEM
43	ORT266-02	N31 16 56.1	W105 28 37.2	Rhyolite - purple with visible hematite	SEM

Position Format	Lat/lon hddd°mm'ss.s"
Datum	WGS 84
Measurement	US

Table A.4: Microbeam analyses sample locations and descriptions. Sample locations shown on Figures 3.1-3.3.

Sample Num.	Sample ID	Northing	Westing	Rock Type	Associated Thin Section Num.
1	ORT262-01	N31 16 43.8	W105 28 54.0	Gray Rhyolite	-
2	ORT37-01	N31 16 51.4	W105 28 49.2	Gray Rhyolite	-
3	ORT263-02	N31 16 44.1	W105 28 55.7	Mottled Rhyolite	27
4	ORT270-03	N31 16 44.5	W105 28 11.0	Mottled Rhyolite	15
5	ORT266-01	N31 16 56.1	W105 28 37.2	Purple Rhyolite	14
6	ORT41-01	N31 16 44.4	W105 28 57.3	Purple Rhyolite	-
7	ORT270-02	N31 16 44.5	W105 28 11.0	Red Rhyolite	1
8	ORT33-02	N31 16 46.3	W105 28 58.7	Red Rhyolite	-
9	ORT46-01	N31 16 11.1	W105 28 11.2	Red Rhyolite	-
10	ORT44-20	N31 16 55.6	W105 28 41.7	Tan Rhyolite	31
11	ORT44-21	N31 16 55.6	W105 28 41.7	Tan Rhyolite	-
12	ORT43-04	N31 16 56.7	W105 28 40.1	Diorite	-
13	ORT270-14	N31 16 44.5	W105 28 11.0	Fluoritized LS	-
14	ORT248-13	N31 16 27.4	W105 28 52.1	Rhyolite Breccia	-

Position Format	Lat/lon hddd°mm'ss.s"
Datum	WGS 84
Measurement	US

Table A.5: Geochemical sample locations and type. Sample locations shown on Figures 3.1-3.3.

Sample Num.	Thin Section Num.	Sample Type	Method			Minerals Identified																				
			Microscope	SEM	CL	ann	ba	ct	cm	cgb	ces	cmb	crl	fl	hem	kfs	mt	pl	qz	rt	tan	thr	ytc	ytf	zrn	W-unk	X-unk
DH244	38-1	Rhyolite - tan	x	–	–	x	–	–	–	–	–	–	–	–	x	x	x	x	x	–	–	–	–	–	–	–	–
DH248	38-3	Rhyolite - tan	x	–	–	x	–	–	–	–	–	–	–	–	x	x	x	x	x	–	–	–	–	–	–	–	–
DH287	38-4	Rhyolite - purple	x	–	–	x	–	–	–	–	–	–	–	–	x	x	x	x	x	–	–	–	–	–	–	–	–
DH421	33-1	Rhyolite - red w/ hem	x	–	–	x	–	–	–	–	–	–	–	–	x	x	x	x	x	–	–	–	–	–	–	–	–
DH421	33-2	Rhyolite - gray w/ hem	x	–	–	x	–	–	–	–	–	–	–	–	x	x	x	x	x	–	–	–	–	–	–	–	–
DH421	33-3	Rhyolite - purple w/ hem	x	–	–	x	–	–	–	–	–	–	–	–	x	x	x	x	x	–	–	–	–	–	–	–	–
DH421	33-4	Rhyolite - tan w/ visible hem	x	–	–	x	–	–	–	–	–	–	–	–	x	x	x	x	x	–	–	–	–	–	–	–	–
DH446	35-1	Rhyolite - gray	x	–	–	x	–	–	–	–	–	–	–	–	x	x	x	x	x	–	–	–	–	–	–	–	–
DH446	35-2	Rhyolite - purple w/ hem	x	–	–	x	–	–	–	–	–	–	–	–	x	x	x	x	x	–	–	–	–	–	–	–	–
DH446	35-3	Rhyolite - tan	x	–	–	x	–	–	–	–	–	–	–	–	x	x	x	x	x	–	–	–	–	–	–	–	–
DH455	35-4	Rhyolite - gray	x	–	–	x	–	–	–	–	–	–	–	–	x	x	x	x	x	x	–	–	–	–	–	–	–
DH456	36-1	Rhyolite - gray w/ hem	x	–	–	x	–	–	–	–	–	–	–	–	x	x	x	x	x	–	–	–	–	–	–	–	–
DH456	36-2	Rhyolite - tan	x	–	–	x	–	–	–	–	–	–	–	–	x	x	x	x	x	–	–	–	–	–	–	–	–
DH456	36-3	Rhyolite - purple w/ hem	x	–	–	x	–	–	–	–	–	–	–	–	x	x	x	x	x	–	–	–	–	–	–	–	–
DH456	36-4	Rhyolite - gray	x	–	–	x	–	–	–	–	–	–	–	–	x	x	x	x	x	–	–	–	–	–	–	–	–
DH461	37-1	Rhyolite - purple	x	–	–	x	–	–	–	–	–	–	–	–	x	x	x	x	x	–	–	–	–	–	–	–	–
DH461	37-2	Rhyolite - gray	x	–	–	x	–	–	–	–	–	–	–	–	x	x	x	x	x	–	–	–	–	–	–	–	–
DH461	37-3	Rhyolite - red w/ hem	x	–	–	x	–	–	–	–	–	–	–	–	x	x	x	x	x	–	–	–	–	–	–	–	–

Table A.6: List of minerals identified by sample.

Sample Num.	Thin Section Num.	Sample Type	Method			Minerals Identified																				
			Microscope	SEM	CL	ann	ba	ct	crn	cgb	ces	cmb	crl	fl	hem	kfs	mt	pl	qz	rt	tan	thr	ytc	ytf	zrn	W-unk	X-unk
DH461	37-4	Rhyolite - tan	X	-	-	X	-	-	-	-	-	-	-	-	X	X	X	X	X	-	-	-	-	-	-	-	-
DH462-A	34-1	Rhyolite - purple/gray mottled	X	-	-	X	-	-	-	-	-	-	-	-	X	X	X	X	X	-	-	-	-	-	-	-	-
DH462-A	34-2	Rhyolite - red w/ hem	X	-	-	X	-	-	-	-	-	-	-	-	X	X	X	X	X	-	-	-	-	-	-	-	-
DH462-A	34-3	Rhyolite - purple w/ hem	X	-	-	X	-	-	-	-	-	-	-	-	X	X	X	X	X	-	-	-	-	-	-	-	-
DH462-A	34-4	Rhyolite - tan	X	-	-	X	-	-	-	-	-	-	-	-	X	X	X	X	X	-	-	-	-	-	-	-	-
OLRT247-01	5	Rhyolite - brown/purple	X	-	-	X	-	-	-	-	-	-	-	-	X	X	X	X	X	-	-	-	-	-	-	-	-
ORT255-07	7	Rhyolite - red w/ hem	X	-	-	X	-	-	-	-	-	-	-	-	X	X	X	X	X	-	-	-	-	-	-	-	-
ORT256-11	29	Rhyolite breccia	-	X	-	X	X	X	-	-	X	-	-	X	X	X	X	X	X	-	X	-	-	-	-	-	-
ORT262-02	6	Rhyolite - gray	X	-	-	X	-	-	-	-	-	-	-	-	X	X	X	X	X	-	-	-	-	-	-	-	-
ORT263-02	27	Rhyolite - red/gray mottled	-	X	-	X	-	-	-	X	-	-	-	-	X	X	X	X	X	-	-	X	-	-	X	-	-
ORT263-04	8	Rhyolite - red	-	X	-	X	-	-	-	X	-	X	-	-	X	X	X	X	X	-	X	X	X	-	X	-	-
ORT264-01	25	Rhyolite - gray	-	X	X	X	-	-	-	X	-		X	-	X	X	X	X	X	-	-	X	X	-	X	X	-
ORT266-01	14	Rhyolite - purple	-	X	-	X	-	X	X	X	-	X	-	-	X	X	X	X	X	-	-	X	X	X	X	-	-
ORT266-02	2	Rhyolite - purple w/ hem	X	X	X	X	-	X	-	X	-	X	-	-	X	X	X	X	X	-	X	X	X	X	X	-	-
ORT266-03	26	Rhyolite - purple w/ hem	X	-	-	X	-		-	-	-		-	-	X	X	X	X	X	-	-	-	-	-	-	-	-
ORT270-01	18	Rhyolite - purple	-	X	-	X	-	X	X	-	-	X	-	-	X	X	X	X	X	-	-	X	-	X	X	-	X
ORT270-02	1	Rhyolite - red	X	-	-	X	-		-	-	-	-	-	-	X	X	X	X	X	-	-	-	-	-	-	-	-
ORT44-20	31	Rhyolite - tan	-	X	-	X	-	X	-	-	-	-	-	-	X	X	X	X	X		X	X	X	-	X	-	-
ORT44-22	32	Rhyolite - tan	X	-	-	X	-	-	-	-	-	-	-	-	X	X	X	X	X	-	-	-	-	-	-	-	-

Table A.6 continued: List of minerals identified by sample. Corresponding mineral names for abbreviations are located in Table 3.3, (x) = observed, (-) = not observed.

Appendix B

Chemical Analysis

Oxides	ORT262-01	ORT37-01	ORT263-02	ORT270-03	ORT266-01	ORT41-01	ORT270-02
SiO_2	74.50	73.17	73.69	73.62	73.52	73.25	73.25
Al_2O_3	13.31	13.51	13.49	13.50	13.75	13.59	13.33
Fe_2O_3	1.60	1.64	1.57	1.68	1.53	1.62	2.16
MgO	0.07	0.27	0.03	0.03	0.11	0.19	0.10
CaO	0.10	0.25	0.42	0.51	0.14	0.26	0.13
Na_2O	4.82	4.99	4.69	4.82	4.92	4.93	4.69
K_2O	4.28	4.16	4.32	4.20	4.40	4.37	4.03
TiO_2	0.02	0.02	0.02	0.02	0.02	0.02	0.02
P_2O_5	<0.01	<0.01	<0.01	0.02	<0.01	<0.01	<0.01
MnO	0.07	0.06	0.06	0.06	0.05	0.07	0.06
Cr_2O_3	<0.002	<0.002	<0.002	<0.002	<0.002	0.002	<0.002
LOI	0.8	1.5	1.3	1.1	1.1	1.2	1.8
TOT/C	<0.02	<0.02	0.03	0.04	<0.02	<0.02	<0.02
TOT/S	<0.02	<0.02	<0.02	<0.02	<0.02	<0.02	0.06
Sum	99.53	99.52	99.56	99.54	99.50	99.49	99.57
FeO	0.55	0.59	0.54	0.55	0.51	0.59	0.75

Oxides	ORT33-02	ORT46-01	ORT44-20	ORT44-21	ORT43-04	ORT270-14	ORT248-13
SiO_2	74.31	73.62	73.69	73.78	52.07	4.00	14.50
Al_2O_3	13.28	13.91	13.84	13.98	17.18	0.61	9.94
Fe_2O_3	1.79	1.69	0.75	0.90	7.48	0.49	0.33
MgO	0.03	0.10	0.05	0.04	3.70	0.49	0.07
CaO	0.12	0.04	0.41	0.40	6.02	64.97	50.67
Na_2O	4.82	4.83	4.95	4.75	5.16	0.25	0.65
K_2O	3.95	4.20	4.42	4.67	2.81	0.11	0.63
TiO_2	0.02	0.02	0.02	0.02	1.15	0.03	<0.01
P_2O_5	0.02	<0.01	<0.01	<0.01	0.57	<0.01	<0.01
MnO	0.06	0.05	0.03	0.04	0.16	0.04	0.05
Cr_2O_3	<0.002	<0.002	<0.002	<0.002	0.002	0.002	<0.002
LOI	1.2	1.1	1.5	1.0	3.2	5.4	12.4
TOT/C	<0.02	<0.02	<0.02	<0.02	0.08	0.09	0.08
TOT/S	<0.02	<0.02	0.03	<0.02	0.02	0.10	0.04
Sum	99.56	99.55	99.62	99.62	99.48	76.43	89.27
FeO	0.50	0.51	0.36	0.44	2.80	0.29	0.30

Table B.1: Chemical analyses from outcrop samples – Oxides (wt.%).

Element	ORT262-01	ORT37-01	ORT263-02	ORT270-03	ORT266-01	ORT41-01	ORT270-02
Ni ppm	<20	<20	<20	<20	<20	<20	<20
Sc ppm	1	<1	<1	1	<1	<1	<1
Ba ppm	11	13	19	119	221	58	7
Be ppm	47	42	35	39	26	55	10
Co ppm	0.4	0.4	0.4	0.4	0.5	0.3	0.5
Cs ppm	61.7	55.6	60.2	60.6	39.0	50.8	40.0
Ga ppm	70.8	70.9	67.5	70.1	71.0	70.0	72.1
Hf ppm	81.3	81.4	77.4	81.3	79.8	78.0	72.7
Nb ppm	363.3	350.4	347.9	352.3	359.1	362.8	368.8
Rb ppm	1895.9	1843.4	1927.5	1906.9	1882.0	1915.6	1756.6
Sn ppm	151	142	138	139	141	135	140
Sr ppm	12.9	151.8	30.9	37.9	61.9	166.7	114.2
Ta ppm	58.7	57.7	57.2	58.3	57.3	59.6	57.3
Th ppm	168.1	176.4	167.8	169.0	173.1	181.0	172.4
U ppm	32.8	30.1	35.8	28.3	32.1	33.8	39.5
V ppm	13	<8	<8	<8	12	10	12
W ppm	3.6	3.1	3.2	3.4	3.6	4.7	3.8
Zr ppm	1045.9	1059.6	1002.7	1040.7	1049.6	1084.2	968.5
Mo ppm	0.9	0.5	0.7	0.4	0.6	0.6	0.8
Cu ppm	1.1	1.0	0.9	1.7	0.6	1.0	1.2
Pb ppm	66.8	77.8	83.3	47.5	221.4	182.1	58.0
Zn ppm	624	516	604	581	546	553	501
Ni ppm	0.6	0.7	0.5	1.6	1.5	1.1	0.7
As ppm	11.7	6.6	9.3	8.6	8.3	4.9	2.3
Cd ppm	<0.1	<0.1	<0.1	<0.1	<0.1	<0.1	<0.1
Sb ppm	1.5	1.4	1.3	1.5	1.9	1.3	1.7
Bi ppm	2.0	1.9	2.0	2.8	2.5	2.7	2.5
Ag ppm	<0.1	<0.1	<0.1	<0.1	<0.1	<0.1	<0.1
Au ppb	<0.5	<0.5	<0.5	<0.5	<0.5	<0.5	<0.5
Hg ppm	<0.01	<0.01	<0.01	<0.01	<0.01	<0.01	<0.01
Tl ppm	1.2	2.3	1.2	1.3	1.3	1.8	1.5
Se ppm	<0.5	0.7	<0.5	<0.5	<0.5	<0.5	<0.5
Li %	0.05	0.04	0.03	0.05	0.06	0.04	0.05
F %	0.22	0.90	0.40	0.48	0.31	0.55	0.24

Table B.2: Chemical analyses from outcrop samples – Element.

Element	ORT33-02	ORT46-01	ORT44-20	ORT44-21	ORT43-04	ORT270-14	ORT248-13
Ni ppm	<20	<20	<20	<20	<20	<20	<20
Sc ppm	<1	<1	1	1	13	<1	8
Ba ppm	57	21	9	7	2294	54	160
Be ppm	12	17	19	6	13	3898	205
Co ppm	0.6	0.4	0.4	0.5	19.0	2.3	1.7
Cs ppm	46.5	50.4	42.9	43.5	83.7	9.3	8.4
Ga ppm	67.8	70.8	67.2	66.0	18.8	1.7	14.7
Hf ppm	84.4	79.2	77.0	79.7	4.5	0.3	12.3
Nb ppm	342.1	362.2	368.0	377.6	9.5	1.1	58.8
Rb ppm	1663.1	1856.7	1801.3	1901.5	129.8	31.3	265.3
Sn ppm	140	143	144	153	<1	1	23
Sr ppm	25.8	20.7	40.5	33.6	1062.5	1771.1	783.6
Ta ppm	59.0	58.9	60.6	61.6	0.6	0.1	9.4
Th ppm	166.6	164.9	161.0	162.4	8.2	0.8	35.3
U ppm	31.2	46.7	58.0	52.9	2.4	124.0	364.6
V ppm	<8	10	<8	<8	180	25	23
W ppm	3.9	4.5	2.6	4.3	1.1	6.3	1.1
Zr ppm	1082.6	1052.1	999.3	1038.1	171.6	10.3	165.8
Mo ppm	0.4	0.4	0.3	0.4	0.2	0.9	0.8
Cu ppm	1.1	0.9	0.5	0.4	24.4	1.2	1.3
Pb ppm	82.8	148.1	126.3	134.9	6.6	389.0	353.3
Zn ppm	520	487	136	159	43	158	152
Ni ppm	0.7	1.1	0.4	0.5	5.9	<0.1	<0.1
As ppm	4.1	6.6	1.6	1.7	0.7	33.3	50.5
Cd ppm	<0.1	<0.1	<0.1	<0.1	1.5	3.0	<0.1
Sb ppm	1.1	1.8	0.5	0.6	<0.1	0.5	0.3
Bi ppm	2.2	1.3	0.6	0.4	<0.1	0.2	0.8
Ag ppm	<0.1	<0.1	<0.1	<0.1	<0.1	<0.1	<0.1
Au ppb	<0.5	<0.5	<0.5	<0.5	1.7	0.8	7.3
Hg ppm	<0.01	<0.01	<0.01	<0.01	<0.01	<0.01	<0.01
Tl ppm	1.2	1.5	1.5	1.7	<0.1	0.3	1.1
Se ppm	<0.5	<0.5	<0.5	<0.5	<0.5	2.4	0.9
Li %	0.05	0.05	0.04	0.05	<0.01	<0.01	<0.01
F %	0.23	0.24	0.29	0.39	0.11	34.27	19.33

Table B.2 continued: Chemical analyses from outcrop samples – Element.

REE	ORT262-01	ORT37-01	ORT263-02	ORT270-03	ORT266-01	ORT41-01	ORT270-02
Y	104.5	187.7	105.7	146.5	175.0	223.2	159.5
La	19.0	20.8	16.8	16.8	19.5	20.1	22.7
Ce	85.3	73.0	66.1	70.5	59.9	70.0	72.0
Pr	8.42	9.81	8.04	8.04	9.27	10.31	10.85
Nd	24.5	24.1	23.7	24.4	26.7	24.6	28.0
Sm	6.31	7.82	6.78	7.37	8.52	9.92	8.34
Eu	0.09	0.09	0.05	0.11	0.13	0.10	0.10
Gd	5.38	7.90	6.38	7.27	8.59	9.95	7.25
Tb	1.74	2.82	2.03	2.49	2.76	3.65	2.30
Dy	16.94	24.21	17.33	22.38	24.82	31.71	22.10
Ho	4.15	6.83	4.22	5.36	6.47	8.04	5.62
Er	18.57	28.82	18.37	22.73	27.39	33.12	25.01
Tm	4.37	6.51	4.35	4.80	6.05	6.91	5.88
Yb	39.13	52.56	35.22	41.26	50.09	58.01	48.95
Lu	6.31	8.26	5.89	6.17	7.69	8.67	7.76

REE	ORT33-02	ORT46-01	ORT44-20	ORT44-21	ORT43-04	ORT270-14	ORT248-13
Y	137.3	203.0	101.0	106.1	20.8	24.5	188.8
La	20.5	7.4	6.2	2.2	32.6	2.8	5.8
Ce	58.6	29.0	25.9	15.6	61.9	3.9	15.1
Pr	9.87	3.97	2.96	1.56	7.56	0.52	2.84
Nd	26.5	10.9	9.9	6.3	30.3	1.0	8.5
Sm	8.04	5.24	3.81	2.86	6.19	0.60	4.39
Eu	0.10	0.07	<0.02	0.05	1.96	0.14	0.13
Gd	6.56	7.55	4.00	4.18	5.47	0.82	7.77
Tb	2.16	3.03	1.89	1.81	0.73	0.29	3.13
Dy	19.00	28.38	20.27	17.67	4.64	2.97	28.01
Ho	4.83	7.44	5.17	5.03	0.81	0.77	6.63
Er	21.06	30.99	22.45	24.19	2.18	3.42	25.45
Tm	5.08	6.64	5.33	5.49	0.30	0.58	4.78
Yb	45.19	54.16	46.15	48.38	1.81	3.70	31.56
Lu	7.06	8.09	7.04	7.58	0.29	0.52	4.36

Table B.3: Chemical analyses from outcrop samples – REE (ppm).

Element	Count	Minimum (ppm)	Maximum (ppm)	Mean (ppm)	Median (ppm)	Standard Deviation (ppm)
Ce	2430	15.7	1100.0	79.8	80.7	23.5
Dy	2430	1.5	199.0	31.0	32.0	6.5
Er	2430	1.0	143.5	32.4	33.5	6.1
Eu	2430	0.0	9.0	0.2	0.1	0.2
Gd	2430	1.4	134.0	10.3	10.5	3.0
Hf	2430	1.5	463.0	85.1	87.1	15.2
Ho	2430	0.3	45.0	7.8	8.1	1.6
La	2430	7.5	457.0	20.3	20.1	9.3
Lu	2430	0.2	18.7	8.8	9.1	1.5
Nb	2430	4.8	1800.0	375.7	384.0	65.7
Nd	2430	7.3	510.0	28.5	28.6	10.5
Pr	2430	2.0	138.0	10.4	10.5	2.9
Sm	2430	1.6	138.5	10.4	10.5	3.0
Sn	2430	1.0	381.0	137.0	141.0	24.0
Ta	2430	0.4	143.5	65.9	67.7	10.8
Tb	2430	0.2	28.1	3.5	3.6	0.8
Th	2430	3.6	314.0	176.0	181.0	27.8
Tm	2430	0.2	24.3	7.1	7.3	1.3
U	2430	2.5	1000.0	49.7	43.0	40.5
Y	2430	10.1	1245.0	217.4	225.0	45.3
Yb	2430	1.0	140.0	56.4	58.2	9.5

Table B.4: Select minimum and maximum concentrations values from TRER. Data table modified from Hulse et al. (2013).

	Rubin (1993)	Price et al. (1990)						Price et al. (1990)							Price et al. (1990)	
	Round Top	Grey rhyolite, relatively unaltered, low Sr						Gray rhyolite, apparently unaltered, high Sr							Pink rhyolite, weathered	
wt%	J85-55*	RT4-96	RT3-130	RT337-310	J85-55*	RT287-200	RT1-230.5	J87-73	J87-72	RT336-200	RT283-182.5	RT5-169	RT2-34	RT201-355	J87-70	J87-74
SiO_2	73.60	70.48	70.50	70.56	72.47	72.53	73.15	69.34	70.10	70.90	71.55	71.94	71.97	72.72	72.65	73.15
TiO_2	0.02	0.02	0.02	0.03	0.02	0.03	0.02	0.03	0.03	0.02	0.04	0.02	0.02	0.02	0.03	0.02
Al_2O_3	13.89	13.43	13.73	13.52	13.68	13.49	13.71	13.43	13.62	13.19	13.26	13.55	13.99	13.69	13.42	13.82
Fe_2O_3	0.73	-	-	-	-	-	-	-	-	-	-	-	-	-	-	-
FeO	0.70	-	-	-	-	-	-	-	-	-	-	-	-	-	-	-
FeO Total	-	2.97	2.91	2.95	1.34	2.57	1.72	3.58	3.43	3.08	2.19	2.80	2.50	2.58	2.07	1.52
MnO	0.08	0.08	0.08	0.08	0.08	0.08	0.08	0.10	0.09	0.08	0.08	0.08	0.08	0.07	0.06	0.06
MgO	0.01	0.01	0.01	0.04	0.01	0.01	0.01	0.17	0.22	0.05	0.12	0.14	0.45	0.20	0.06	0.03
CaO	0.08	0.02	0.03	0.06	0.08	0.02	0.03	0.67	1.32	1.62	1.16	0.33	0.15	0.44	0.60	1.14
Na_2O	6.58	7.42	6.72	6.89	6.48	6.29	5.34	5.74	5.51	5.29	5.44	5.61	5.74	5.56	5.27	5.33
K2O	4.29	4.07	4.20	4.04	4.22	4.12	4.20	4.02	4.23	3.90	4.32	4.09	4.13	4.09	4.13	3.66
P_2O_5	0.01	<0.01	<0.01	<0.01	<0.01	<0.01	<0.01	<0.01	<0.01	<0.01	<0.01	<0.01	<0.01	<0.01	<0.01	<0.01
H_2O^+	0.13	0.20	0.12	0.25	0.13	0.14	0.39	0.59	0.82	0.43	0.31	0.41	0.41	0.55	1.01	0.59
CO_2	0.00	<0.04	<0.04	<0.04	0.00	<0.04	<0.04	<0.04	<0.04	0.04	0.04	<0.04	0.04	<0.04	<0.04	<0.04
F	1.30	1.68	0.17	1.97	1.94	1.38	0.31	1.72	1.63	1.33	1.18	1.24	1.57	1.32	0.42	1.06

Appendix B.5: Table of data from Price et al. (1990) and Rubin et al. (1993) utilized for geochemical comparison.

	Rubin (1993)	Price et al. (1990)						Price et al. (1990)							Price et al. (1990)	
	Round Top	Grey rhyolite, relatively unaltered, low Sr						Gray rhyolite, apparently unaltered, high Sr							Pink rhyolite, weathered	
ppm	J85-55*	RT4-96	RT3-130	RT337-310	J85-55*	RT287-200	RT1-230.5	J87-73	J87-72	RT336-200	RT283-182.5	RT5-169	RT2-34	RT201-355	J87-70	J87-74
Li	440	480	470	520	460	500	490	470	470	470	510	510	520	480	380	590
Be	170	58	31	45	180	14	19	57	46	26	18	14	13	100	24	13
Zn	610	590	580	630	610	620	590	590	620	580	630	600	580	550	570	510
Rb	1,960	1700	2000	1600	2000	2000	2200	1800	1900	1500	1800	1700	2000	2000	1700	1600
Sr	28	14	12	40	32	7	7	290	230	120	140	90	220	100	62	79
Y	220	200	200	240	200	230	200	280	310	250	240	280	230	220	220	240
Zr	1,040	1000	1100	1200	1000	1100	1100	1100	1200	1000	1100	1100	1100	1100	1100	1200
Nb	340	350	400	420	340	410	370	380	370	380	400	410	390	380	380	370
Mo	<5	3	4	2	2	<1	2	5	4	3	1	3	3	2	3	2
Ba	<10	8	8	6	5	12	8	10	19	15	22	14	14	7	210	17
La	23	20	21	25	22	21	21	27	31	29	28	31	26	27	27	24
Ce	90.0	73	84	96	80	73	77	110	120	110	110	110	88	97	99	85
Pr	11.0	9.6	10	13	10	11	10	13	15	14	13	16	12	12	13	10
Nd	28.0	25	28	34	25	28	26	36	41	38	36	40	31	29	34	26
Sm	10.0	9.5	10	13	9.7	10	10	13	15	13	13	14	11	12	13	9.4
Eu	0.1	0.1	0.1	0.1	0.1	0.1	0.1	0.2	0.2	0.2	0.2	0.2	0.1	0.1	0.2	0.1
Gd	11.0	17	12	15	11	12	11	15	17	15	14	17	12	12	13	11
Tb	3.7	3.2	3.7	4.6	3.5	4.0	3.2	4.7	5.5	4.7	4.4	5.3	3.8	4.1	4.0	3.7
Dy	36.0	29	32	39	30	33	28	40	46	38	37	42	33	32	31	31
Ho	7.8	6.9	7.6	9.7	7.4	8.0	6.7	9.7	11	8.9	8.9	10	7.9	8.1	7.9	7.3
Er	33.0	26	29	37	30	30	26	39	45	34	34	41	30	32	30	31
Tm	6.7	5.3	6.0	7.8	6.0	6.0	5.4	8.1	9.1	6.9	6.9	8.1	5.9	5.7	5.9	6.7
Yb	55.0	41	44	58	48	44	40	64	72	54	51	61	44	47	46	54
Lu	7.2	5.8	6.3	8.2	7.1	6.1	5.8	9.7	11	7.8	7.4	8.9	6.0	7.1	6.9	8.2
Hf	17	-	-	-	-	-	-	-	-	-	-	-	-	-	-	-
Ta	35	40	39	42	35	38	38	47	43	26	31	36	37	42	41	51
Pb	320	280	320	300	320	300	250	320	290	210	290	250	240	260	250	200
Th	230	200	200	220	230	210	170	250	210	190	230	210	180	190	190	220
U	54	38	66	54	54	35	36	51	21	46	56	40	28	33	23	44
V	-	7	6	<5	<5	<5	<5	<5	<5	5	5	<5	<5	6	11	7
Ni	-	32	29	42	<5	21	16	29	26	27	22	25	23	23	23	14
Cu	-	68	51	89	13	45	37	49	46	40	62	52	45	56	49	40
Cs	-	62	75	53	83	51	49	93	86	67	58	56	48	49	69	66
Ba	<10	8	8	6	5	12	8	10	19	15	22	14	14	7	210	17

Appendix B.5 continued: Table of data from Price et al. (1990) and Rubin et al. (1993) utilized for geochemical comparison.

wt.%	Average	Standard Deviation	2σ
SiO_2	71.73	1.23	2.46
TiO_2	0.02	0.01	0.01
Al_2O_3	13.59	0.21	0.42
Fe_2O_3	0.73	0.00	0.00
FeO	0.70	0.00	0.00
FeO Total	2.55	0.64	1.29
MnO	0.08	0.01	0.02
MgO	0.10	0.12	0.23
CaO	0.48	0.53	1.05
Na_2O	5.95	0.66	1.31
K2O	4.11	0.15	0.31
P_2O_5	0.01	0.00	0.00
H_2O^+	0.41	0.25	0.50
CO_2	0.02	0.02	0.04
F	1.26	0.53	1.06

ppm	Average	Standard Deviation	2σ
Li	485.00	43.01	86.02
Be	51.75	51.74	103.48
Zn	591.25	30.18	60.36
Rb	1841.25	188.48	376.95
Sr	91.94	85.22	170.43
Y	235.00	31.22	62.45
Zr	1096.25	62.94	125.87
Nb	380.63	23.31	46.62
Mo	2.79	1.01	2.03
Ba	25.00	49.68	99.36
La	25.19	3.50	7.01
Ce	93.88	14.44	28.89
Pr	12.04	1.88	3.77
Nd	31.56	5.28	10.56
Sm	11.60	1.78	3.56
Eu	0.14	0.05	0.10
Gd	13.44	2.21	4.41
Tb	4.13	0.66	1.32
Dy	34.81	4.95	9.91
Ho	8.36	1.18	2.36
Er	32.94	5.10	10.21
Tm	6.66	1.07	2.14
Yb	51.44	8.69	17.38
Lu	7.47	1.42	2.84
Hf	17.00	0.00	0.00
Ta	38.81	5.74	11.47
Pb	275.00	37.91	75.83
Th	208.13	20.68	41.36
U	42.44	12.46	24.93
V	6.71	1.91	3.81
Ni	25.14	6.62	13.24
Cu	49.47	15.98	31.97
Cs	64.33	14.01	28.02
Ba	25.00	49.68	99.36

Table B.5 continued: Average, standard deviation, and 2-sigma for Price et al. (1990) and Rubin et al. (1993) utilized for geochemical comparison.

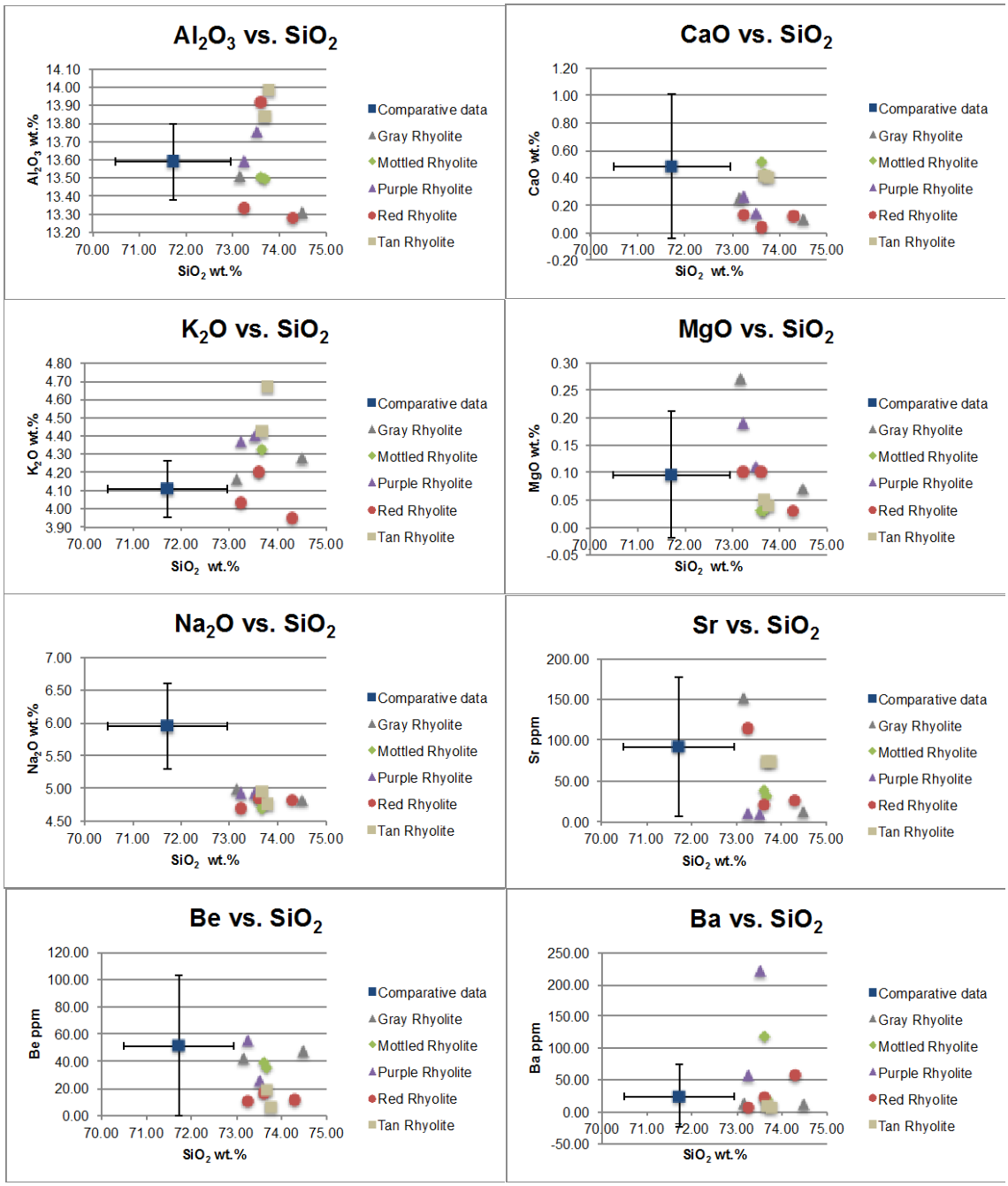

Appendix B.6: Harker diagrams and bivariate plots.

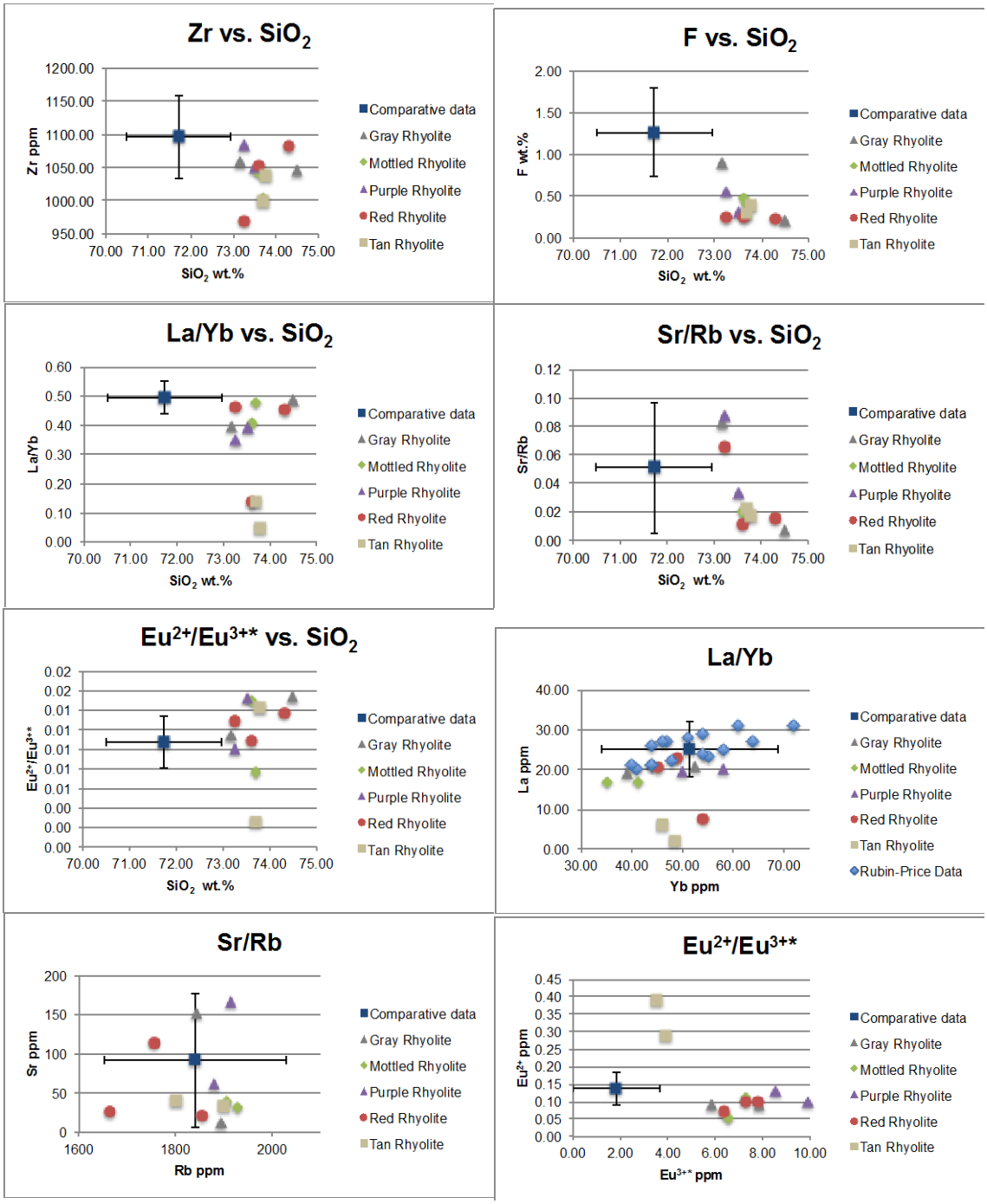

Appendix B.6 continued: Harker diagrams and bivariate plots.

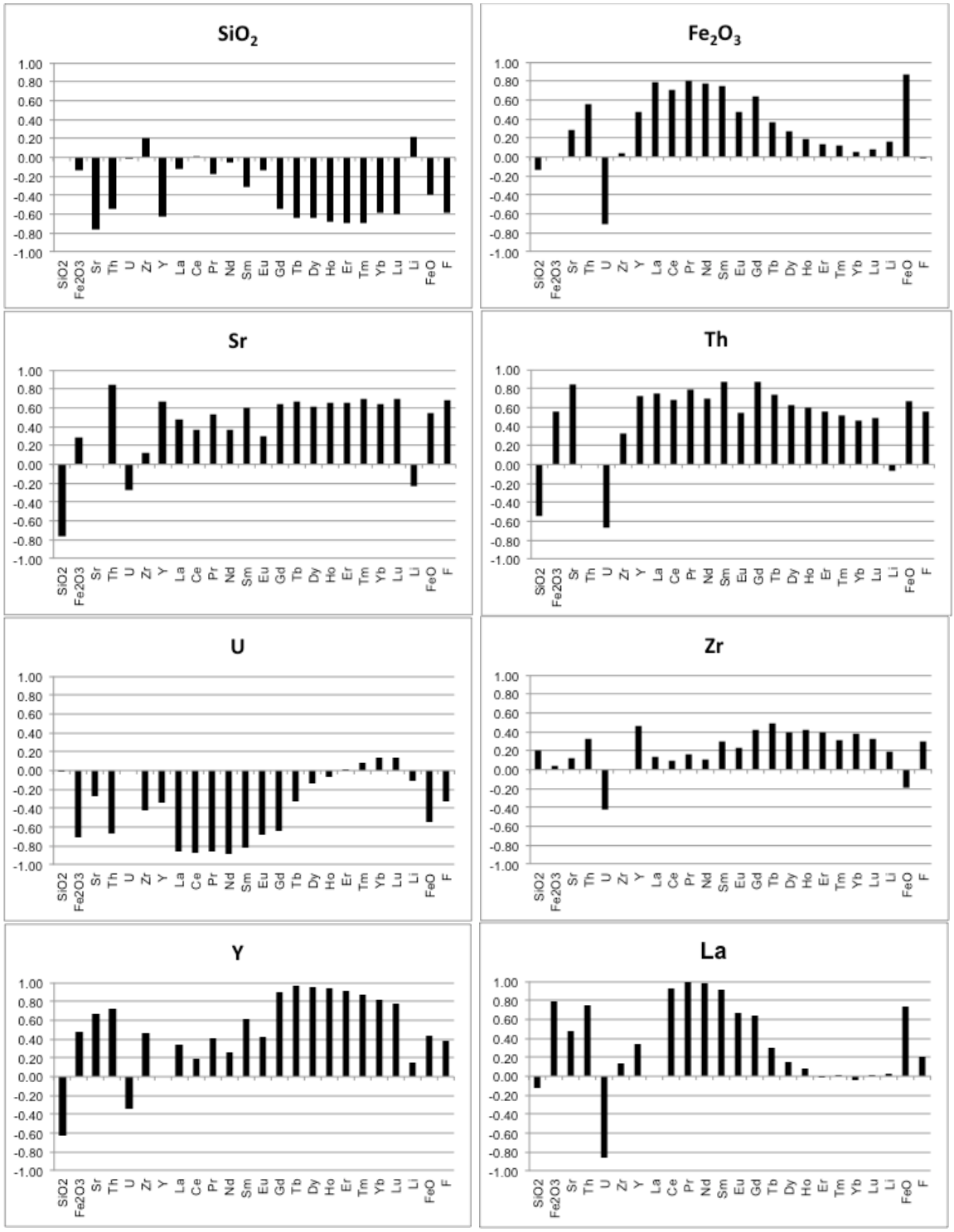

Appendix B.7: Correlation charts for the Round Top rhyolites by major oxide or element.

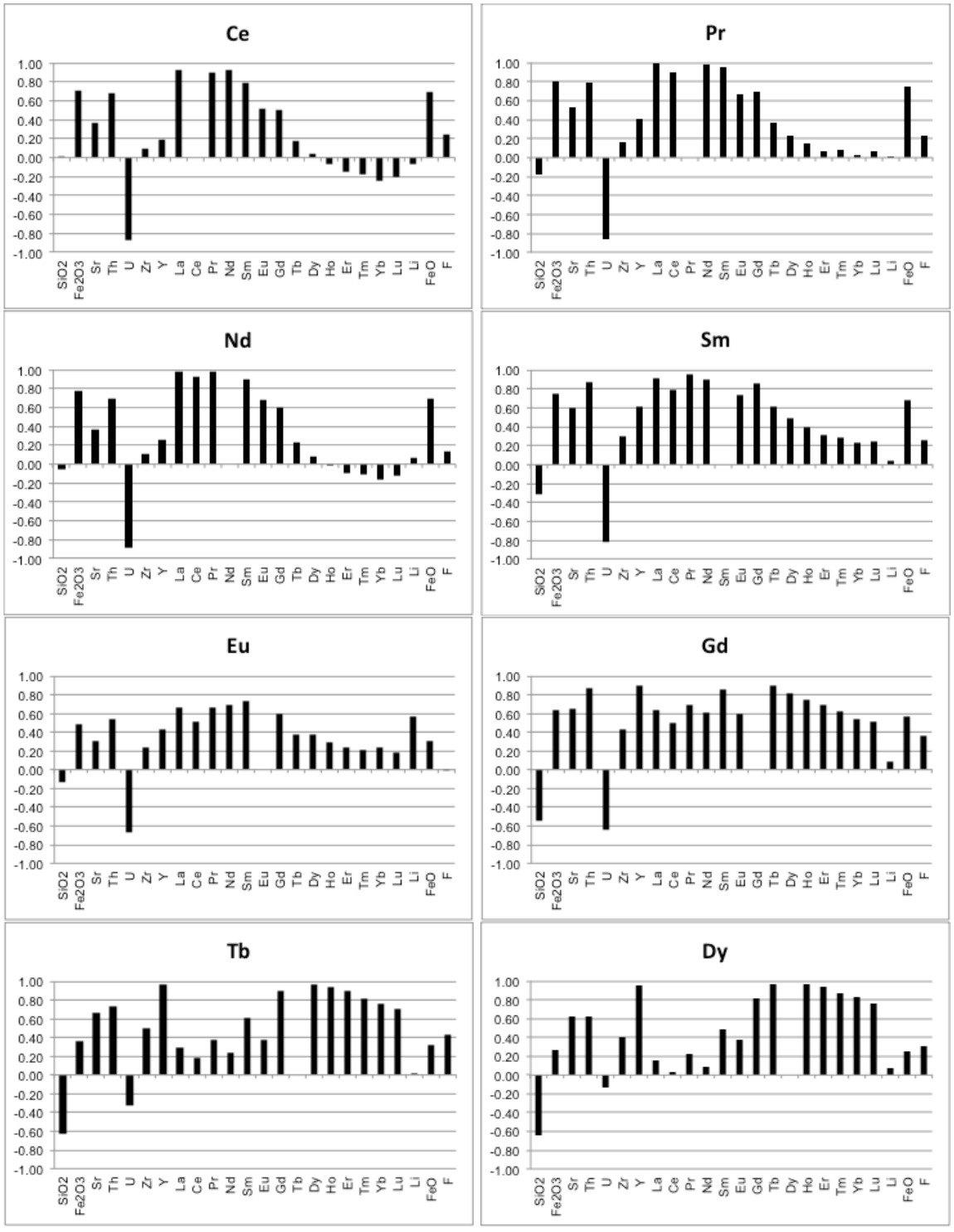

Appendix B.7 continued: Correlation charts for the Round Top rhyolites by major oxide or element.

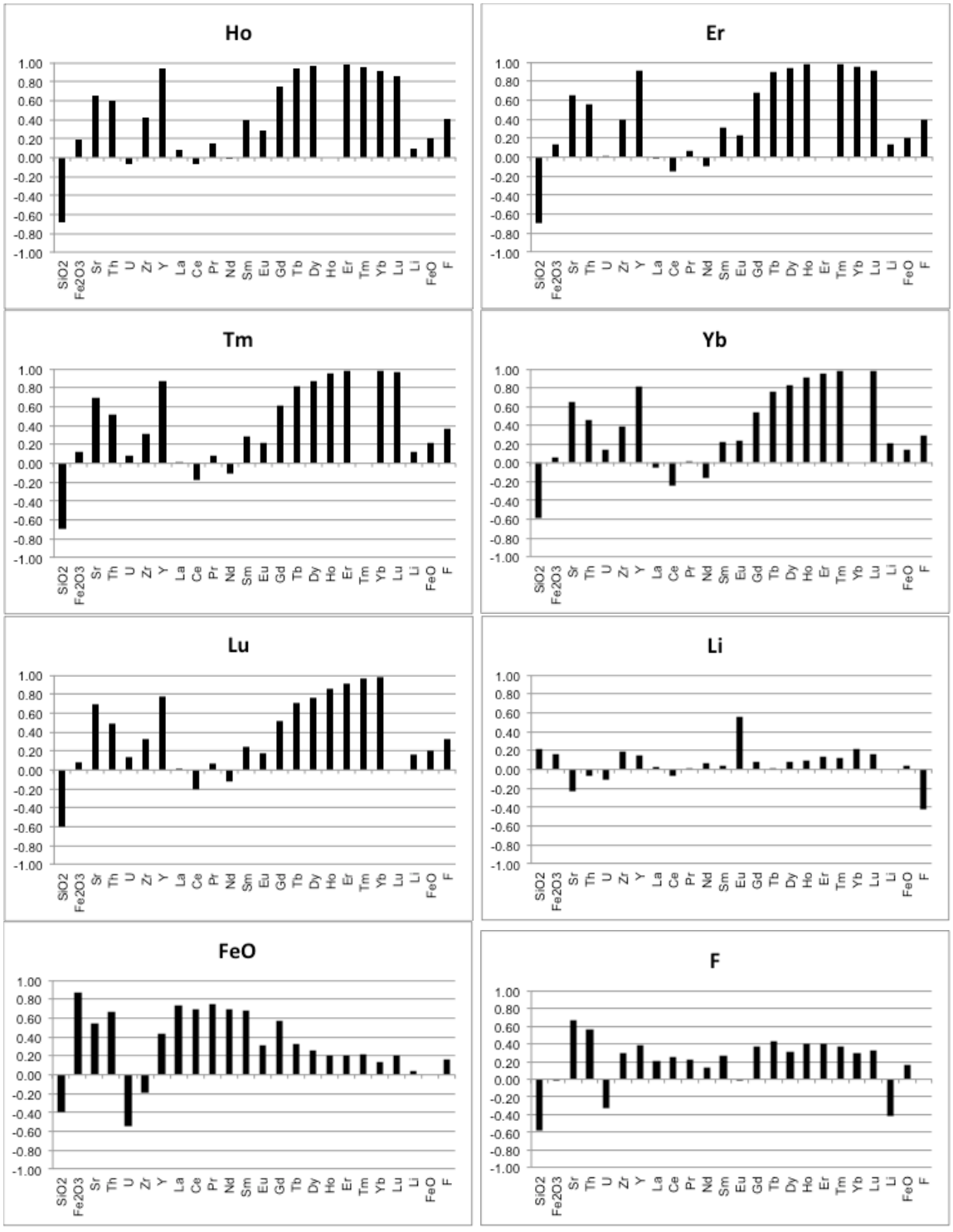

Appendix B.7 continued: Correlation charts for the Round Top rhyolites by major oxide or element.

References

2013, Texas Rare Earth Resources Corporation, *in* Media, B., ed., Volume 2013, Blender Media.

2014a, Southern Regional Climate Center, Volume 2013, Louisiana State University.

2014b, US Climate Data, *in* SpA, B., ed., Climate Sierra Blanca - Texas, Volume 2013, Belsoft SpA.

June 1988, Cyprus Sierra Blanca Inc. Beryllium Project.

Albritton, C. C., Jr., and Smith, J. F., Jr., 1965, Geology of the Sierra Blanca area, Hudspeth County, Texas: U. S. Geological Survey : Reston, VA, United States, 1044-9612.

Barker, D. S., 1977, Northern Trans-Pecos magmatic province: Introduction and comparison with the Kenya rift: Geological Society of America Bulletin, v. 88, no. 10, p. 1421-1427.

-, 1987, Tertiary alkaline magmatism in Trans-Pecos Texas: Geological Society Special Publications, v. 30, p. 415-431.

Befus, K. S., Hanson, R. E., Lehman, T. M., and Griffin, W. R., 2008, Cretaceous basaltic phreatomagmatic volcanism in West Texas: Maar complex at Peña Mountain, Big Bend National Park: Journal of Volcanology and Geothermal Research, v. 173, no. 3–4, p. 245-264.

Blatt, H., and Tracy, R. J., 1997, Petrology; igneous, sedimentary, and metamorphic, United States, W. H. Freeman and Company : New York, NY, United States, 199.

Breyer, J. A., Busbey, A. B., III, Hanson, R. E., Befus, K. E., Griffin, W. R., Hargrove, U. S., and Bergman, S. C., 2007, Evidence for Late Cretaceous volcanism in Trans-Pecos Texas: Journal of Geology, v. 115, no. 2, p. 243-251.

Corry, C. E., 1988, Laccoliths; mechanics of emplacement and growth, Volume 220: United States, Geological Society of America (GSA) : Boulder, CO, United States.

Cox, K. G., Bell, J. D., and Pankhurst, R. J., 1979, The interpretation of igneous rocks, London, George Allen & Unwin.

Gilmer, A. K., Kyle, J. R., Connelly, J. N., Mathur, R. D., and Henry, C. D., 2003, Extension of Laramide magmatism in southwestern North America into Trans-Pecos Texas: Geology [Boulder], v. 31, no. 5, p. 447-450.

Giordano, D., Romano, C., Dingwell, D. B., Poe, B., and Behrens, H., 2004, The combined effects of water and fluorine on the viscosity of silicic magmas: Geochimica et Cosmochimica Acta, v. 68, no. 24, p. 5159-5168.

Goodell, P. C., Gomez, A., and Kyger, N., 2013, Round Mountain, Texas, Laccolith Can Be A Reliable Source of HREE For US Industry and Defense: Geological Society of America Abstracts with Programs, v. 45, no. 7, p. 501.

Henderson, P., 1984, Rare earth element geochemistry Developments in geochemistry, Netherlands, Elsevier Sci. Publ. Co. : Amsterdam, Netherlands.

Henry, C. D., and McDowell, F. W., 1986, Geochronology of magmatism in the Tertiary volcanic field, Trans-Pecos Texas: Guidebook - Bureau of Economic Geology, University of Texas at Austin, v. 23, p. 99-122.

Henry, C. D., and Price, J. G., 1984, Variations in caldera development in the Tertiary volcanic field of Trans-Pecos Texas: Journal of Geophysical Research, v. 89, no. B10, p. 8765-8786.

Henry, C. D., Price, J. G., and James, E. W., 1991, Mid-Cenozoic stress evolution and magmatism in the southern Cordillera, Texas and Mexico; transition from continental arc to intraplate extension: Journal of Geophysical Research, v. 96, no. B8, p. 13.

Henry, C. D., Price, J. G., and Miser, D. E., 1989, Geology and Tertiary igneous activity of the Hen Egg Mountain and Christmas Mountains quadrangles, Big Bend region, Trans-Pecos Texas: University of Texas at Austin, Bureau of Economic Geology : Austin, TX, United States, 0082335X.

Hulse, D. E., Newton, I., M. Claiborne, , and Malhotra, D., 2013, NI 43-101 Preliminary Economic Assessment Round Top Project Sierra Blanca, Texas: Texas Rare Earth Resources and Gustavson Associates.

Hulse, D. E., Newton, I., M. Claiborne, , Malhotra, D., and Black, Z. J., 2012, NI 43-101 Preliminary Economic Assessment Round Top Project Sierra Blanca, Texas: Texas Rare Earth Resources and Gustavson Associates.

King, P. B., 1949, Regional geologic map of parts of Culberson and Hudspeth counties, Texas: U. S. Geological Survey : Reston, VA, United States.

Levinson, A. A., 1974, Introduction to Exploration Geochemistry, Applied Publ. Ltd.

Long, K. R., Van Gosen, B. S., Foley, N. K., and Cordier, D., 2010, The principal rare earth elements deposits of the United States; a summary of domestic deposits and a global perspective: U. S. Geological Survey : Reston, VA, United States.

Matthews, W. K., III, and Adams, J. A. S., 1986, Geochemistry, age, and structure of the Sierra Blanca and Finlay Mountain intrusions, Hudspeth County, Texas: Guidebook - Bureau of Economic Geology, University of Texas at Austin, v. 23, p. 207-224.

Maxwell, R. A., Lonsdale, J. T., Goldich, S. S., and Smith Jr., J. F., 1949, West Texas Geological Society Guidebook Field Trip No. 1, West Texas Geological Society, Marathon region, Big Bend region, Green Valley-Paradise Valley region, Sierra Blanca region, Texas.

McAnulty, W. N., 1971, A glimpse of some of the geology and mineral resources of the Sierra Blanca-Van Horn area, Hudspeth and Culberson counties, Texas, El Paso Geol. Soc.

-, 1980, Geology and mineralization of the Sierra Blanca peaks, Hudspeth County, Texas: Guidebook - New Mexico Geological Society, no. 31, p. 263-266.

McDonough, W. F., and Sun, S. s., 1995, The composition of the Earth: Chemical Geology, v. 120, no. 3–4, p. 223-253.

Muehlberger, W. R., 1980, Texas Lineament revisited: Guidebook - New Mexico Geological Society, no. 31, p. 113-121.

Negron, L., Clague, J., Gorski, D., Amaya, M., and Pingitore, N. E., 2013, Fluorescein Dye Penetration in Round top Rhyolite (Hudspeth County, Texas, USA) to Reveal Micro-permeability and optimize Grain Size for Heavy REE Heap Leach: American Geophysical Union Abstract.

Nesse, W. D., 2000, Introduction to mineralogy, United States, Oxford University Press : New York, NY, United States.

Pingitore, N., Clague, J., and Gorski, D., 2013, A Unique Yttrofluorite-Hosted Giant Heavy Rare Earth Deposit: Round Top Mountain: American Geophysical Union Abstract.

-, 2014, Round Top Mountain rhyolite (Texas, USA), a massive, unique Y-bearing-fluorite-hosted heavy rare earth element (HREE) deposit: Journal of Rare Earths, v. 32, no. 1, p. 90-96.

Price, J. G., Henry, C. D., Barker, D. S., and Parker, D. F., 1987, Alkalic rocks of contrasting tectonic settings in Trans-Pecos Texas: Special Paper - Geological Society of America, v. 215, p. 335-346.

Price, J. G., Rubin, J. N., Henry, C. D., Pinkston, T. L., Tweedy, S. W., and Koppenaal, D. W., 1990, Rare-metal enriched peraluminous rhyolites in a continental arc, Sierra Blanca area, Trans-Pecos Texas; chemical modification by vapor-phase crystallization: Special Paper - Geological Society of America, v. 246, p. 103-120.

Rollinson, H. R., 1993, Using geochemical data; evaluation, presentation, interpretation, United Kingdom, Longman Scientific & Technical : Harlow, United Kingdom.

Rubin, J. N., Henry, C. D., and Price, J. G., 1989a, Hydrothermal zircons and zircon overgrowths, Sierra Blanca Peaks, Texas: American Mineralogist, v. 74, no. 7-8, p. 865-869.

-, 1993, The mobility of zirconium and other 'immobile' elements during hydrothermal alteration: Chemical Geology, v. 110, no. 1-3, p. 29-47.

Rubin, J. N., Price, J. G., Henry, C. D., and Koppenaal, D. W., 1987, Cryolite-bearing and rare metal-enriched rhyolite, Sierra Blanca Peaks, Hudspeth County, Texas: American Mineralogist, v. 72, no. 11-12, p. 1122-1130.

Rubin, J. N., Price, J. G., Henry, C. D., and Kyle, J. R., 1990, Geology of the beryllium-rare earth element deposits at Sierra Blanca, West Texas: Guidebook Series [Society of Economic Geologists [U. S.], v. 8, p. 191-203.

Rubin, J. N., Price, J. G., Henry, C. D., Pinkston, T. L., Tweedy, S. W., Koppenaal, D. W., Peterson, S. B., Harlan, H. M., Miller, W. T.,

Thompson, R. J., Grabowski, R. B., Laybourn, P. D., Schrock, G. E., Johnson, A., Staes, D. G., Gaines, R. V., and Miller, F. H., 1989b, Mineralogy of beryllium deposits near Sierra Blanca, Texas: Process Metallurgy, v. 5, p. 601-614.

Schilling, J. G., and Winchester, J. W., 1967, Rare-earth fractionation and magmatic processes, 1967.

Shannon, W. M., 1986, Lithogeochemical characterization of intrusive rocks comprising the Quitman-Sierra Blanca igneous complex, Hudspeth County, Texas.

Shannon, W. M., and Goodell, P. C., 1986, Lithogeochemistry of intrusive rocks of the Quitman-Sierra Blanca igneous complex, Hudspeth County, Texas: Guidebook - Bureau of Economic Geology, University of Texas at Austin, v. 23, p. 225-236.

Shelley, D., 1992, Igneous and metamorphic rocks under the microscope; classification, textures, microstructures and mineral preferred-orientations, United Kingdom, Chapman & Hall : London, United Kingdom.

Taylor, S. R., McLennan, S. M., Armstrong, R. L., and Tarney, J., 1981, The Composition and Evolution of the Continental Crust: Rare Earth Element Evidence from Sedimentary Rocks [and Discussion]: Philosophical Transactions of the Royal Society of London. Series A, Mathematical and Physical Sciences, v. 301, no. 1461, p. 381-399.

Vernon, R. H., 2004, A practical guide to rock microstructure, United Kingdom, Cambridge University Press : Cambridge, United Kingdom.

Weaver, B. L., and Tarney, J., 1984, Empirical approach to estimting the composition of the continental crust: Nature [London], v. 310, no. 5978, p. 575-577.

Wilson, J. A., 1980, Geochronology of the Trans-Pecos Texas volcanic field: Guidebook - New Mexico Geological Society, no. 31, p. 205-211.

Wilson, M., 1989, Igneous petrogenesis, London, Unwin Hyman.

Vita

L. Christine O'Neill was born in Sacramento, California in 1985. She attended California State University of Sacramento where she first discovered her passion for geology, and later obtained her Bachelors of Science in geology. Christine went on the complete a Masters of Science at the University of Texas at Austin in economic geology and to pursue a career in minerals exploration.

Permanent email: LCONeill@utexas.edu

This thesis was typed by L. Christine O'Neill.